JYU DISSERTATIONS 444

Henri Hänninen

Deep Inelastic Scattering in the Dipole Picture at Next-to-Leading Order

UNIVERSITY OF JYVÄSKYLÄ
FACULTY OF MATHEMATICS
AND SCIENCE

JYU DISSERTATIONS 444

Henri Hänninen

Deep Inelastic Scattering in the Dipole Picture at Next-to-Leading Order

Esitetään Jyväskylän yliopiston matemaattis-luonnontieteellisen tiedekunnan suostumuksella
julkisesti tarkastettavaksi Ylistönrinteen salissa FYS1
lokakuun 29. päivänä 2021 kello 12.

Academic dissertation to be publicly discussed, by permission of
the Faculty of Mathematics and Science of the University of Jyväskylä,
in Ylistönrinne, auditorium FYS1, on October 29, 2021, at 12 o'clock.

JYVÄSKYLÄN YLIOPISTO
UNIVERSITY OF JYVÄSKYLÄ

JYVÄSKYLÄ 2021

Editors
Ilari Maasilta
Department of Physics, University of Jyväskylä
Päivi Vuorio
Open Science Centre, University of Jyväskylä

ISBN 978-951-39-8893-7 (PDF)
URN:ISBN:978-951-39-8893-7
ISSN 2489-9003

Permanent link to this publication: http://urn.fi/URN:ISBN:978-951-39-8893-7

Abstract

This thesis studies gluon saturation in hadronic matter at high energy by calculating next-to-leading order (NLO) corrections to inclusive and diffractive deep inelastic scattering cross sections in the Color Glass Condensate (CGC) effective field theory.

We demonstrate that the large soft gluon logarithm is correctly factorized into the Balitsky–Kovchegov (BK) renormalization group equation by accurately connecting the NLO scattering kinematics to the rapidity scale of the dipole amplitude in the scattering. This brings the perturbative expansion under control and enables us to do precision comparisons between theory and data. We fit the initial condition of the BK evolution equation to HERA inclusive deep inelastic scattering data by combining of the NLO accuracy inclusive cross sections with beyond leading order BK evolution prescriptions. This results in the state-of-the-art accuracy comparison between CGC theory and HERA data, and determination of the dipole amplitude initial shape which is a necessary input for all NLO CGC phenomenology. In the introductory part of this thesis, the effect of the NLO BK equation on the fits is assessed, and an alternative form for the NLO loop correction to the inclusive cross sections is derived which enables the consistent setting of the dipole amplitude rapidity scale in the NLO corrections.

The underlying mechanism of diffraction in particle scattering is still unknown, with multiple competing pictures. Diffraction is studied in this thesis in the CGC formalism, and we calculate the tree-level $q\bar{q}g$ NLO contribution to the diffractive deep inelastic scattering structure functions where the $q\bar{q}g$ Fock state scatters off the target and becomes the diffractively produced system. This contribution has previously been known in the literature only in leading $\log(Q^2)$ accuracy valid at large Q^2, and only for the structure function F_T^D. The $q\bar{q}g$ contribution to both structure functions F_T^D and F_L^D are presented in full NLO accuracy.

Tiivistelmä

Tässä väitöskirjassa tutkitaan hadronisen aineen gluonikyllästymistä korkealla energialla laskemalla toisen kertaluvun häiriöteorian korjauksia kaikenkattavaan ja diffraktiiviseen syvän epäelastisen sironnan vaikutusalaan efektiivisessä värilasikondensaatti-kenttäteoriassa.

Näytämme, että suuri matalan pitkittäisliikemäärän gluoneista johtuva logartmi faktorisoituu oikein Balitsky–Kovchegov (BK) -renormalisaatioryhmäyhtälöön, kun toisen kertaluvun sironnan kinematiikka yhdistetään tarkasti sironnan dipoliamplitudin rapiditeettiskaalaan. Tämä tuo häiriöteorian sarjakehitelmän hallintaan ja mahdollistaa tarkkuusvertaamisen teorian ja kokeellisten tulosten välillä. Sovitamme BK-evoluutioyhtälön alkuehdon HERA-kokeen syvän epäelastisen sironnan kokonaisvaikutusalan mittaustuloksiin yhdistämällä toisen kertaluvun tarkkuuden vaikutusalalaskun yli johtavan kertaluvun tarkkuuden BK-evoluutio yhtälöiden kanssa. Tämä tuottaa huipputarkkuuden yhteensopivuustestin värilasikondensaatti-teorian ja mittaustulosten välillä, sekä määrityksen dipoliamplitudin evoluution alkumuodolle, joka on välttämätön syöte hiukkastörmäysten kuvaamiseen värilasikondensaatti-teoriassa. Tässä väitöskirjan johdanto-osassa arvioidaan toisen kertaluvun tarkkuuden BK-yhtälön vaikutusta sovitustuloksiin, ja johdetaan vaihtoehtoinen muoto toisen kertaluvun silmukkakorjaukselle syvän epäelastisen sironnan kokonaisvaikutusalaan, mikä mahdollistaa johdonmukaisen rapiditeettiskaalan asettamisen toisen kertaluvun korjauksissa.

Hiukkassironnassa tapahtuvan diffraktion perustavaa mekanismia ei vielä tunneta syvällisesti ja kilpailevia kuvia prosessille on useita. Diffraktiota tutkitaan tässä väitöskirjassa värilasikondensaatti-teoriassa, jossa laskemme toisen kertaluvun puutason $q\bar{q}g$-korjauksen diffraktiivisen syvän epäelastisen sironnan rakennefunktioihin, missä $q\bar{q}g$ Fock-tila siroaa kohtiosta ja muodostaa diffraktiivisen systeemin. Kyseinen osuus vaikutusalasta on aiemmin tunnettu vain johtavan $\log(Q^2)$ tarkkuudessa ja vain F_T^D-rakennefunktiolle. Tämä $q\bar{q}g$-korjaus esitetään sekä F_T^D- että F_L^D-rakennefunktioille täydessä toisen kertaluvun tarkkuudessa.

Author Henri Hänninen
Department of Physics
University of Jyväskylä
Finland

Supervisors Prof. Tuomas Lappi
Department of Physics
University of Jyväskylä
Finland

Dr. Heikki Mäntysaari
Department of Physics
University of Jyväskylä
Finland

Reviewers Prof. Anna Staśto
Department of Physics
Penn State University
USA

Prof. Bo-Wen Xiao
School of Science and Engineering
The Chinese University of Hong Kong
China

Opponent Prof. Krzysztof Golec-Biernat
Division of Theoretical Physics
Institute of Nuclear Physics PAN
Poland

Preface

The research reported in this thesis has been carried out at the University of Jyväskylä from April 2017 to September 2021. This work was supported by the European Union's Horizon 2020 research and innovation programme by the European Research Council (ERC, grant agreement No. ERC-2015-CoG-681707), and in the very final stages by the Academy of Finland (project 321840). The computing resources provided by CSC – IT Center for Science in Espoo, Finland, and the Finnish Grid and Cloud Infrastructure (persistent identifier urn:nbn:fi:research-infras-2016072533) were crucial for the completion of this work.

I have been delighted and fortunate to have had the opportunity to work in the excellent supervision of Prof. Tuomas Lappi and Dr. Heikki Mäntysaari, both of whom I thank for their expert guidance and support. Secondly, I thank Dr. Guillaume Beuf for all the enlightening discussions and correspondence that helped making many aspects of this thesis possible. I also wish to thank Dr. Bertrand Ducloué, Dr. Yair Mulian, Dr. Risto Paatelainen, and Dr. Yan Zhu for fruitful collaboration. I am also thankful to Prof Kari J. Eskola, Prof. Tero Heikkilä, and Prof. Kimmo Kainulainen for their lessons in theoretical physics and for their guidance. I thank Prof. Anna Staśto and Prof. Bo-Wen Xiao for reviewing this manuscript, and Prof. Krzysztof Golec-Biernat who has agreed to act as my opponent.

Friends and colleagues have had an important, if less direct, part in the realization of this thesis. Special thanks go to Kalle Kansanen and Mikko Kuha for sharing this journey of becoming a young scientist and for their friendship. I had the privilege to begin this journey, in the beforetimes, in the grad student office YFL 353 known as Holvi. I thank the Holvi collaborators Lotta Jokiniemi, Mikko Kivekäs, Mikko Kuha, Miha Luntinen, Topi Löytäinen, Petja Paakkinen, Jani Penttala, Pekka Pirinen, and Oskari Saarimäki for the engaging and inspiring ~~working environment~~ group chat. I also thank Toni Ikonen, Joonas Niinikoski, and Timo Schultz for the adventures into advanced mathematics and the camaraderie during the tumultuous first years under the accelerated physics study programme.

I thank my mother and father for their support in all my endeavors. My father's book recommendations of Gamow's and Feynman's works are among the earliest memories of interest in, and excitement about, theoretical physics. I also thank my grandfather Osmo for always nurturing my interest in the natural sciences. Finally, with the deepest appreciation, I thank Laura, Petrus, and Aurora for their love and support.

Henri Hänninen, September 2021, Jyväskylä

List of Publications

This thesis consists of an introductory part and of the following publications:

[I] **Deep inelastic scattering in the dipole picture at next-to-leading order**
B. Ducloué, H. Hänninen, T. Lappi and Y. Zhu, Phys. Rev. D **96**.9 (2017) 094017, arXiv: 1708.07328 [hep-ph].

[II] **One-loop corrections to light cone wave functions: the dipole picture DIS cross section**
H. Hänninen, T. Lappi and R. Paatelainen, Annals Phys. **393** (2018) 358–412, arXiv: 1711.08207 [hep-ph].

[III] **Color Glass Condensate at next-to-leading order meets HERA data**
G. Beuf, H. Hänninen, T. Lappi and H. Mäntysaari, Phys. Rev. D **102** (2020) 074028, arXiv: 2007.01645 [hep-ph].

The author performed the numerical calculations, drew the figures, and participated in the writing and editing of the manuscript for the Article [I]. For the Article [II], the author performed the numerical implementation and comparison of the cross sections calculated in [II] to the ones calculated in Refs. [1, 2]. For the Article [III], the author implemented and performed the fits, drew the figures, and wrote the first draft. The implementation used was based on a software component written by collaborator H. Mäntysaari. Chapter 5 of this thesis is related to work done in collaboration with G. Beuf, T. Lappi, Y. Mulian, and H. Mäntysaari, which is in preparation for publication.

Contents

Chapter 1

Introduction

There are some things we know about the proton [3]. Since its discovery just over 100 years ago by Rutherford [4, 5], we have learned that it is not an elementary particle which means it has an internal structure. Thus, the known properties of the proton must arise from this internal structure. For example the charge, mass, size, and spin of the proton somehow emerge from this structure and the interactions of the constituents of the proton.

We have learned that the proton is composed of three elementary particles called quarks: two up quarks and one down quark. These quarks interact with each other via the strong nuclear force, which is mediated by a massless electric-chargeless gauge boson called the gluon. Quarks, gluons, and their interactions are described by the quantum field theory Quantum Chromodynamics (QCD). QCD predicts that the gluons exchanged between the quarks can temporarily split into new quark-antiquark pairs, which can produce further gluon emissions and splittings. Thus the proton is expected to have a background presence of quarks and gluons on top of the three valence quarks. The densities of these sea quarks and gluons depend on the energy scale the proton is studied at, and these densities have been determined experimentally as the parton distribution functions. Since the gluons and sea quark-antiquark pairs do not have net electric charge, the charge $+1e$ of the proton is indeed the sum of the charges of the up and down quarks.

How about the rest mass of the proton, does it compose straightforwardly from the rest masses of the up and down quarks? Well, yes, to the extent that around *one percent* of the proton mass is from the rest masses of the three quarks. The remaining 99% of the mass arises from the dynamics — movement and confinement — of the quarks and gluons [6]. A qualitative theory understanding of the decomposition of the missing mass has been known [6, 7], but only recently quantitative theory calculations for these components of the mass have been calculated with lattice QCD [8]. The proton mass arises from four

contributions: the quark condensate ($\sim 9\%$), the quark energy ($\sim 32\%$), the gluonic field strength ($\sim 37\%$), and the anomalous gluonic contribution ($\sim 23\%$). The first and smallest of the contributions arises from the masses of the valence and sea quarks, and only this contribution would vanish if the quarks were massless. The quark energy and gluonic field strength contributions arise from the kinetic energies of the quarks and gluons, and the final anomalous component is a quantum effect [6].

Well maybe the size of the proton as a charged composite particle is uncomplicated to measure and understand? Yes, in the sense that in the last decade there has been more than a 7σ disagreement on the charge radius of the proton [9]. This so-called proton radius puzzle originates from a 4% difference between a newer experiment using muonic hydrogen spectroscopy and older measurements done with regular hydrogen spectroscopy and low-energy electron-proton scattering, both of which were in agreement previously. New experiments are being planned to understand the origin of the discrepancy and to settle the correct charge radius [9].

Surely at least the spin of the proton is comprised as the sum of the spins of the three valence quarks? Alas, no. With global QCD analyses of spin-dependent data — such as longitudinally polarized proton-proton collision data [10, 11] — it has been determined that the quark spin contribution is roughly 30% of the proton spin [10, 11]. The remaining spin arises from gluons and the orbital angular momentum of the quarks and gluons, the determination of which has been more uncertain. Current estimates for the quark and gluon contributions are $\sim 30\% - 40\%$, and $\sim 26\% - 52\%$, respectively, which fall short to produce the proton spin of $\frac{1}{2}$ [10–12]. Both new experimental data of polarized beams, and improved theory understanding of the high-energy behavior of these spin contributions [12–14] will be needed to find the remaining spin.

The work done for this thesis is concerned with the theoretical understanding of the internal structure of the proton at high energy. In this energetic regime QCD predicts that more and more gluons are emitted by the quarks and gluons in the proton. However, as the gluon density rises dramatically with growing energy, at some point the reabsorption of gluons becomes preferred over new emissions, which halts the increase of the gluon density. This phenomenon is known as *saturation*, and in this work it is studied in the Color Glass Condensate (CGC) effective field theory, which describes QCD at very high energies. The CGC formalism has been used to describe strong interactions in a large variety of scattering processes in e+p, e+A, p+A, and A+A collisions [15–20]. Further, it has the power to *ab initio* describe thermalization in heavy ion collisions, and the initial conditions of thermalized quark gluon plasma. The collective high-density behavior of gluons described in the CGC has been discovered to have a surprising connection to gravity, which has recently been proposed as the

CGC–Black Hole correspondence [21]. More specifically regarding this thesis, state-of-the-art next-to-leading order (NLO) accuracy theory results for proton structure functions are evaluated numerically and used for data comparison. Furthermore, a new analytical calculation of diffractive proton structure functions in NLO accuracy is presented. These accuracy improvements of the CGC framework theory calculations are necessary to rise to the challenge brought on by the upcoming Electron-Ion Collider (EIC), which will provide state-of-the-art precision measurements of the structure of the proton and nuclei [22–24].

The internal structure of this thesis is as follows. Chapter 2 reviews the basics of Color Glass Condensate effective field theory needed to describe particle scattering processes. The following chapters discuss the extension of CGC formalism calculations both analytically and numerically to next-to-leading order in perturbative QCD. In Chapter 3 are discussed the recent NLO accuracy CGC framework results for the inclusive deep inelastic scattering (DIS) structure functions of the proton. Chapter 4 considers the application of these proton structure functions to make comparisons between theory and experimental data. The calculation of diffractive DIS structure functions at NLO in the CGC formalism is explored in Chapter 5. Finally, in Chapter 6 we conclude on the work done for this thesis, including previously unpublished results. The Articles [**I**], [**II**], and [**III**] are joined as appendices to the thesis.

Chapter 2

The Color Glass Condensate effective field theory

2.1 Proton structure at high energy

The structure of the proton as seen by a probe particle in a scattering — and more generally the physical picture of any scattering process — can vary dramatically in different reference frames and gauges [25]. In the introduction we considered the proton in the parton model where it consisted of quarks and gluons. The parton model picture is valid in the infinite momentum frame. In a perturbation theory calculation of a probe scattering off the parton model proton, the perturbative expansion takes place on the target side of the scattering which amounts to seeing more partonic detail[1] at higher orders in perturbation theory. In this picture saturation arose as a limit on the occupation number of quarks and gluons in the proton. In the picture of CGC on the other hand, it manifests as a unitarity limit on the scattering from the target. The CGC effective field theory has been established as a well-suited theory tool to study saturation phenomena in QCD [17, 18].

The CGC formalism considers scattering processes in a different picture built on light-front quantization of the probe particle, and the target is seen as a collective force field of its constituents [26, 27]. In this case the incoming probe particle becomes perturbatively calculable which gives it a picture of internal structure [26], for example a virtual photon consists of color-neutral states of partons and leptons. Simultaneously, the target proton or nucleus is seen to be composed of a strong color-field, which contains the non-perturbative QCD physics of the scattering. These color-fields emerge from the large density of

[1] For example in deep inelastic scattering, quarks are seen at leading order whereas gluons start to be seen at next-to-leading order.

gluons present in the target at high energy. The gluon occupation number is much larger than the commutators between the gluon creation and annihilation operators, which permits the semiclassical description of the color-fields [18]. Thus the probe particle sees the target as an incredibly strong color-field, which is Lorentz contracted into a thin pancake. At high energy where saturation manifests, the target system enters a non-linear weakly-coupled regime of QCD and the energy evolution of the color-field becomes calculable in perturbation theory.

This chapter first discusses in Sec. 2.2 the description of the projectile particle in light-front perturbation theory. Scattering off the target color-field and the energy dependence of this scattering process are described in Secs. 2.3 and 2.4.

2.2 Light-front perturbation theory

To begin delving into the mathematics of the Color Glass Condensate, we must first consider the coordinate system that is conventionally used. Instead of the familiar frame of Minkowskian flat spacetime with the metric $g = \mathrm{diag}(1,-1,-1,-1)$, light-front perturbation theory (LFPT) calculations are done in coordinates where the t- and z-axes are on the light-front; this is expressed by the light-front metric [27]:

$$\tilde{g} = \begin{pmatrix} 0 & 0 & 0 & 1 \\ 0 & -1 & 0 & 0 \\ 0 & 0 & -1 & 0 \\ 1 & 0 & 0 & 0 \end{pmatrix}. \tag{2.1}$$

Together with the light-front metric, the components of a four-vector x^μ are

$$\begin{aligned} x &\coloneqq (x^+, \mathbf{x}, x^-), \\ x^\pm &\coloneqq \frac{1}{\sqrt{2}}(x^0 \pm x^3), \\ \mathbf{x} &\coloneqq (x^1, x^2), \end{aligned}$$

i.e. the time and x^3-components of x^μ are mixed, and the transverse components are unchanged. With the above, the inner product under the light-front metric is: $x \cdot y = x_\mu y_\nu \tilde{g}^{\mu\nu} = x^+ y^- + x^- y^+ - \mathbf{x} \cdot \mathbf{y}$. In these light-front coordinates, the x^+ component is called light-front time, the x^- component is light-front position and in momentum space the k^- component is light-front energy [27].

Next, we will collect the essential definitions and conventions of the LFPT calculations done in Refs. [1, 2], which will be used throughout this thesis and especially in the calculations performed in Ch. 5. The required definitions are used

in LFPT calculations that are performed in the mixed space of transverse positions $\mathbf{x}$, as seen above, and of longitudinal momenta k^+; this phase space comes up in the Fourier transformation of transverse momenta: $(\mathbf{k}, k^+) \to (\mathbf{x}, k^+)$. For a total and rigorous definition of the full light-front quantization and light-front perturbation theory calculation rules and conventions, we refer the reader to the Refs. [II, 1, 2].

We begin by considering the description of the physical state of a photon on the light-front, which is the probe particle in the scattering processes considered in this thesis. Specifically, in Chs. 3 and 5 we discuss calculations of virtual photon-proton scattering cross sections using the formalism reviewed in this chapter. In light-front perturbation theory the photon state is written as a Fock state expansion using light-front wavefunctions (LFWF)[2] $\tilde{\Psi}_{\gamma^*_\lambda \to X}$ as follows:

$$\begin{aligned}\left|\gamma^*_\lambda(q^+, \mathbf{q}; Q^2)_H\right\rangle = \sqrt{Z_{\gamma^*_\lambda}}\Bigg\{&\text{Non-QCD Fock states} \\ &+ \widetilde{\sum_{q_0\bar{q}_1 \text{ F. states}}} \tilde{\Psi}_{\gamma^*_\lambda \to q_0\bar{q}_1} \tilde{b}^\dagger_0 \tilde{d}^\dagger_1 \left|0\right\rangle \\ &+ \widetilde{\sum_{q_0\bar{q}_1 g_2 \text{ F. states}}} \tilde{\Psi}_{\gamma^*_\lambda \to q_0\bar{q}_1 g_2} \tilde{b}^\dagger_0 \tilde{d}^\dagger_1 \tilde{a}^\dagger_2 \left|0\right\rangle + \cdots \Bigg\}, \end{aligned} \tag{2.2}$$

for a photon with four-momentum q and virtuality $Q^2 = -q^2$. The subscript H denotes that the dressed state is in the Heisenberg picture [1]. The non-QCD basis states are composed of colorless particles such as photons and leptons and so can be neglected, since they will not scatter off the color-field of the target — this will be discussed in the next section. The remaining two expansion contributions that are shown start at different orders in perturbation theory: the quark-antiquark contributions denoted by $q\bar{q}$ start at the order of the electromagnetic coupling e, and the quark-antiquark-gluon ($q\bar{q}g$) contributions at order eg, where g is the coupling of the strong interaction. Thus only the former contributes at leading order (LO) in the perturbative expansion, and the latter starts at next-to-leading order (NLO). The remaining terms in the Fock basis expansion that are shortened to dots ($\cdots$) start only at order eg^2, i.e. next-to-next-to-leading order (NNLO), and do not contribute to the calculations discussed in this thesis. The photon LFWF normalization is of the order $Z_{\gamma^*} = 1 + \mathcal{O}(e^2)$, and so can be dropped [2].

The LFWFs are calculated using conventional quantum mechanical perturbation theory, the light-front rules for which can be found in Refs. [II, 1, 2], and in a more pedagogical detail in Refs. [27, 28]. For example, the LFWF for the

[2]For conciseness, this is shortened to wavefunction many times in this thesis.

virtual photon splitting into a quark-antiquark dipole is calculated as:

$$\tilde{\Psi}_{\gamma^*_\lambda \to q_0\bar{q}_1} = \frac{\langle q_0\bar{q}_1|\, \hat{V}_I(0)\, |\gamma^*\rangle}{k^-_{\gamma^*} - k^-_{q_0\bar{q}_1} + i\varepsilon} + \cdots\,, \tag{2.3}$$

where $\hat{V}_I(0)$ is the interaction operator at the moment of the scattering $x^+ = 0$, $k^-_{\gamma^*}$ and $k^-_{q_0\bar{q}_1}$ are the light-front energies of the incoming $|\gamma^*\rangle$ and outgoing $|q\bar{q}\rangle$ states, and beyond leading order contributions are represented by the dots.

The $|q\bar{q}\rangle$ and $|q\bar{q}g\rangle$ contribution expressions of Eq. (2.2) are further composed as follows. The creation operators of the quark, antiquark and gluon are $\tilde{b}^\dagger, \tilde{d}^\dagger$, and $\tilde{a}^\dagger$, respectively, using the shorthand $\tilde{b}^\dagger_0 \coloneqq \tilde{b}^\dagger(k^+_0, \mathbf{x}_0, h_0, \alpha_0)$. The notation $\widetilde{\sum}$ denotes the sum over the quantum numbers of each parton in the Fock state and a phase-space integration [1]:

$$\widetilde{\sum_{q_0\bar{q}_1 \text{ F. state}}} \coloneqq \sum_{h_0,\alpha_0,f_0} \sum_{h_1,\alpha_1,f_1} \prod_{i=0}^{1} \left[\int_{-\infty}^{\infty} \frac{\mathrm{d}k^+_i}{2\pi} \frac{\theta(k^+_i)}{2k^+_i} \int \mathrm{d}^2\mathbf{x}_i \right], \tag{2.4}$$

$$\widetilde{\sum_{q_0\bar{q}_1 g_2 \text{ F. state}}} \coloneqq \sum_{h_0,\alpha_0,f_0} \sum_{h_1,\alpha_1,f_1} \sum_{\lambda_2,a_2} \prod_{i=0}^{2} \left[\int_{-\infty}^{\infty} \frac{\mathrm{d}k^+_i}{2\pi} \frac{\theta(k^+_i)}{2k^+_i} \int \mathrm{d}^2\mathbf{x}_i \right], \tag{2.5}$$

where h_i are helicities of the quarks and antiquarks, α_i their colors, and f_i their flavors. For the gluon we have its polarization λ_2 and color a_2. Any additional internal partons present in the $|q\bar{q}\rangle$ and $|q\bar{q}g\rangle$ Fock states, such as a gluon loop and corresponding internal quark propagators, will need sums and integrals of their own.

Finally, the two light-front wavefunctions shown in Eq. (2.2) are defined as

$$\widetilde{\Psi}_{\gamma^*_\lambda \to q_0\bar{q}_1} = (2q^+)2\pi\delta(k^+_0 + k^+_1 - q^+) e^{i\frac{\mathbf{q}}{q^+}\cdot(k^+_0\mathbf{x}_0 + k^+_1\mathbf{x}_1)} \mathbf{1}_{\alpha_0\alpha_1} \widetilde{\psi}_{\gamma^*_\lambda \to q_0\bar{q}_1} \tag{2.6}$$

$$\widetilde{\Psi}_{\gamma^*_\lambda \to q_0\bar{q}_1 g_2} = (2q^+)2\pi\delta(k^+_0 + k^+_1 + k^+_2 - q^+) e^{i\frac{\mathbf{q}}{q^+}\cdot(k^+_0\mathbf{x}_0 + k^+_1\mathbf{x}_1 + k^+_2\mathbf{x}_2)} \times t^{a_2}_{\alpha_0\alpha_1} \widetilde{\psi}_{\gamma^*_\lambda \to q_0\bar{q}_1 g_2}, \tag{2.7}$$

where one defines the *reduced wavefunctions* $\widetilde{\psi}_{\gamma^*_\lambda \to q_0\bar{q}_1}$ and $\widetilde{\psi}_{\gamma^*_\lambda \to q_0\bar{q}_1 g_2}$ by factorizing out the color factors and the photon transverse momentum $\mathbf{q}$ dependence. Here we note the only difference in convention to Refs. [1, 2]: the factorization of $(2q^+)$ is new, and will allow for neater calculations in Ch. 5. The reduced wavefunctions contain the perturbative physics of the virtual photon fluctuating into a given Fock state, such as the $q\bar{q}$ or $q\bar{q}g$ states.

The (anti-)commutation relations for the quark, antiquark and gluon creation

and annihilation operators are in the mixed-space [1]:

$$\left\{b(k_0^+,\mathbf{x}_0,h_0,\alpha_0),b^\dagger(k_1^+,\mathbf{x}_1,h_1,\alpha_1)\right\} = (2k_0^+)(2\pi)\delta(k_0^+-k_1^+) \times \delta^{(2)}(\mathbf{x}_0-\mathbf{x}_1)\delta_{h_0,h_1}\delta_{\alpha_0,\alpha_1}, \tag{2.8}$$

$$\left\{d(k_0^+,\mathbf{x}_0,h_0,\alpha_0),d^\dagger(k_1^+,\mathbf{x}_1,h_1,\alpha_1)\right\} = (2k_0^+)(2\pi)\delta(k_0^+-k_1^+) \times \delta^{(2)}(\mathbf{x}_0-\mathbf{x}_1)\delta_{h_0,h_1}\delta_{\alpha_0,\alpha_1}, \tag{2.9}$$

$$\left[a(k_0^+,\mathbf{x}_0,\lambda_0,a_0),a^\dagger(k_1^+,\mathbf{x}_1,\lambda_1,a_1)\right] = (2k_0^+)(2\pi)\delta(k_0^+-k_1^+) \times \delta^{(2)}(\mathbf{x}_0-\mathbf{x}_1)\delta_{\lambda_0,\lambda_1}\delta_{a_0,a_1}. \tag{2.10}$$

These will be needed in Ch. 5 to calculate an overlap of Fock states.

To apply the above Fock state decomposition of the virtual photon to calculations of scattering processes in the CGC formalism, we need to understand how the *bare* quark, antiquark, and gluon scatter off the color-field of the target. The fact that only bare particles take part in the scattering off the color-field is a fundamental feature of the CGC formalism, which was originally developed in Ref. [26] in the context of an electromagnetic field. This is discussed in the next section.

2.3 Dipole amplitude

In the high-energy limit where gluon densities in hadronic matter grow to be enormous, QCD is described by the Color Glass Condensate effective field theory (EFT). At this limit the density of the gluons is so substantial that other structures of the proton or nucleus are overshadowed by their presence; so much so that the strong interactions of the target are described in the CGC formalism by strong semiclassical color-fields instead of individual gluons. For reviews of the CGC EFT, see for example Refs. [15–19]. To compute the cross section of a particle scattering off this strong color-field of the target, one must have an understanding of how the individual Fock basis states interact with the color-field.

Early calculations using light-front perturbation theory did not have precise theory tools to describe the scattering of the $q\bar{q}$ and $q\bar{q}g$ Fock states off the target, and so phenomenologically motivated models were used. One of the most well-known models is the GBW model of the dipole amplitude by Golec-Biernat and Wusthoff, which describes the scattering of a quark-antiquark dipole off the target color-field. It is [29, 30]

$$\sigma_{\mathrm{GBW}}(x_{\mathrm{Bj}},\mathbf{r}) = \sigma_0\left[1-e^{-\frac{1}{4}Q_{\mathrm{s}}^2(x_{\mathrm{Bj}})\mathbf{r}^2}\right], \quad Q_{\mathrm{s}}^2(x_{\mathrm{Bj}}) \coloneqq Q_0^2\left(\frac{x_0}{x_{\mathrm{Bj}}}\right)^\lambda, \tag{2.11}$$

where σ_0 is related to the target size, $\mathbf{r}$ is the transverse size of the quark-antiquark dipole, x_{Bj} is the Bjorken-x, and Q_s is the saturation scale. These quantities and the success of the GBW model are discussed in more detail in Ch. 3.

The progress towards precision theory calculations of the dipole amplitude needed two key advancements. One is the semiclassical approximation by Hebecker et al. [31–35] in which the dipole amplitude is described as the correlator of color-fields. The other realization, that evolved through the works of McLerran et al. [36–38], Jalilian-Marian et al. [39–42], Balitsky [43], Kovchegov [44, 45], and Iancu et al. [46–49], is that the saturation of low-transverse-momentum gluon density can be given a microscopic picture in terms of gluon fields. This gluon saturation prevents the unrealistic growth of the gluon density at large energy. These ideas would lead to the framework which became called the Color Glass Condensate.

Now, the scattering of a quark or an antiquark off the color-field proceeds as follows. As the quark propagates into the x^+-direction through the color-field it can interact with the field multiple times. In each of these interactions with the field, the transverse displacement of the quark is suppressed at high energy: the displacement is of the order $\Delta x_\perp \sim L k_\perp / E$, where L is the size of the target along the quark path, $k_\perp$ the change of transverse momentum in the interaction, and E the energy of the quark in the target rest frame. The approximation that the displacement in the transverse position of the quark can neglected, is known as the eikonal approximation. The propagator that takes the quark through the color-field including arbitrarily many interactions is known as the Wilson line [43], which is in the eikonal approximation[3] [2, 28]:

$$U_R(\mathbf{x}) = \mathscr{P} e^{-ig \int_{-\infty}^{\infty} \mathrm{d}x^+ T_R^a \mathscr{A}_a^-(x^+, \mathbf{x})} \,. \tag{2.12}$$

Here the path-ordering operator $\mathscr{P}$ enforces the path ordering in the integral over the particle path, and T_R^a are the color generators. The identifier R is either F or A for the fundamental or adjoint representations of $SU(N_\mathrm{c})$ which depends on the particle: F for the quarks and A for the gluon. Lastly, $\mathscr{A}_a^-(x^+, \mathbf{x})$ is the semiclassical color-field of the target. Thus, in the eikonal approximation, the quark only picks up a rotation in color phase space in the scattering. The propagation of a gluon through the target proceeds analogously, and only affects the representation of the Wilson line (2.12) produced, as mentioned above.

With the Wilson line we can quantify the effect of the scattering on the bare quark, antiquark or gluon state. This is formulated using the eikonal scattering

[3] The Wilson line has been derived without the eikonal approximation as well [16, 43], which amounts to permitting non-trivial quark paths in the resulting path integral.

operator $\hat{S}_E$: it acts on the creation operators of the quark, antiquark, and gluon as:

$$\hat{S}_E\, \tilde{b}^\dagger(k^+, \mathbf{x}, h, \alpha) = U_F(\mathbf{x})_{\beta\alpha}\, \tilde{b}^\dagger(k^+, \mathbf{x}, h, \beta)\, \hat{S}_E, \tag{2.13}$$

$$\hat{S}_E\, \tilde{d}^\dagger(k^+, \mathbf{x}, h, \alpha) = \left[U_F^\dagger(\mathbf{x})\right]_{\alpha\beta}\, \tilde{d}^\dagger(k^+, \mathbf{x}, h, \beta)\, \hat{S}_E, \tag{2.14}$$

$$\hat{S}_E\, \tilde{a}^\dagger(k^+, \mathbf{x}, \lambda, a) = U_A(\mathbf{x})_{ba}\, \tilde{a}^\dagger(k^+, \mathbf{x}, \lambda, b)\, \hat{S}_E. \tag{2.15}$$

The Fock vacuum is invariant under the action of the eikonal scattering operator: $\hat{S}_E\,|0\rangle = |0\rangle$.

The above can be applied to describe the scattering of the Fock basis states discussed in the previous section. This allows us to formulate the scattering amplitude of the quark-antiquark dipole off the color-field in terms of Wilson lines:

$$S_{01} \coloneqq \frac{1}{N_\mathrm{c}} \operatorname{Tr}\left(U_F(\mathbf{x}_0) U_F^\dagger(\mathbf{x}_1)\right), \tag{2.16}$$

where $\mathbf{x}_0$ and $\mathbf{x}_1$ are the transverse positions of the quark and antiquark, and N_c is the number of colors. To be able to compute observables depending on S_{01}, one must average over the color charge density configurations of the target [2, 50]. In terms of scattering observables, this amounts to the replacement $S_{01} \to \langle S_{01} \rangle$, where the angle brackets denote the average over the classical gluon field configurations. Often S_{01}, which is technically a scattering matrix that includes the case that nothing happens in the scattering, is substituted with an alternative definition that subtracts the identity operator corresponding to no scattering:

$$N_{01} \coloneqq 1 - S_{01}. \tag{2.17}$$

This is called the *dipole amplitude*, and it is the forward elastic scattering amplitude of the dipole scattering off the color-field. It is a non-perturbative quantity and as such cannot be calculated from the first principles using QCD perturbation theory. However, it has an implicit dependence on the scattering energy which is calculable perturbatively; this is discussed in more detail in the next section. The scattering amplitude of the quark-antiquark dipole will be used in the following chapters of this thesis to compute cross sections of electron-proton scattering processes.

We have thus far discussed only the scattering of quarks, gluons, and Fock basis states from the target color-field, which were described by the Wilson lines and the dipole amplitude. However, this means that in the Color Glass Condensate formalism the dipole amplitude is a universal component of scattering processes. Any scattering process where the projectile can be decomposed in the QCD Fock state basis of quarks and gluons is then described by the dipole amplitude and analogous higher order correlators related to larger Fock states.

The process dependent questions then include but are not limited to the calculation of the coefficient functions in the Fock state decomposition, such as we saw for the photon (2.2). Currently, the determination of the dipole amplitude requires a comparison to data — which is the topic of Article [III] and is discussed in Ch. 4 — but once it is known it can be used to make predictions for other scattering processes. For example, determining the dipole amplitude with a fit to electron-proton total cross section data allows one to make theory predictions of a number other observables, such as the longitudinal F_L, diffractive F_2^D, charm F_2^c, and bottom F_2^b structure functions of the proton, exclusive production of vector mesons, and deeply virtual Compton scattering [17]. This of course requires theory calculations of the scattering processes in the CGC formalism, which are plentiful — see Refs. [15–20] for reviews of phenomenological studies of different observables.

2.4 Perturbative energy evolution of the dipole amplitude

The derivation of the energy dependence of the dipole amplitude begins by considering an emission of a gluon from the quark-antiquark Fock state before the scattering. At higher energy the viable phase space for a gluon emission from the $q\bar{q}$-dipole grows larger, i.e. the emission becomes more likely. The emitted gluon can either be considered to be a part of the scattering $q\bar{q}g$ Fock state, or it can be taken to be a part of the dense gluon population of the target. The requirement that these two pictures of the same scattering lead to a single description of the scattering process eventually yields the leading order Balitsky–Kovchegov (BK) equation [43, 44], which in the large-N_c approximation is:

$$\frac{\partial \langle S_{01} \rangle_Y}{\partial Y} = \int \mathrm{d}^2\mathbf{x}_2 \mathscr{K}_{\mathrm{BK}}(\mathbf{x}_0, \mathbf{x}_1, \mathbf{x}_2)[\langle S_{02} \rangle_Y \langle S_{21} \rangle_Y - \langle S_{01} \rangle_Y]. \tag{2.18}$$

The leading order kernel

$$\mathscr{K}_{\mathrm{BK}} = \frac{N_c \alpha_s}{2\pi^2} \frac{\mathbf{x}_{01}^2}{\mathbf{x}_{12}^2 \mathbf{x}_{02}^2} \tag{2.19}$$

is proportional to the probability to emit a gluon at $\mathbf{x}_2$ from the quark-antiquark dipole of size $\mathbf{x}_{01}$, where the notation used is $\mathbf{x}_{ij} \coloneqq \mathbf{x}_i - \mathbf{x}_j$. The evolution of the dipole scattering amplitude is parametrized in the evolution variable Y, which will be discussed in a moment. The coupling α_s is fixed in the LO BK equation.

Implementing running coupling into the BK equation corresponds to a partial inclusion of NLO effects, which are taken as a part of the running coupling prescription. With the addition of the running coupling corrections according

to the widely used Balitsky prescription [51], the kernel becomes

$$K_{\mathrm{BK}}(\mathbf{x}_0,\mathbf{x}_1,\mathbf{x}_2) = \frac{N_\mathrm{c}\alpha_\mathrm{s}(\mathbf{x}_{01}^2)}{2\pi^2}\left[\frac{\mathbf{x}_{01}^2}{\mathbf{x}_{12}^2\mathbf{x}_{02}^2} + \frac{1}{\mathbf{x}_{02}^2}\left(\frac{\alpha_\mathrm{s}(\mathbf{x}_{02}^2)}{\alpha_\mathrm{s}(\mathbf{x}_{12}^2)} - 1\right) + \frac{1}{\mathbf{x}_{12}^2}\left(\frac{\alpha_\mathrm{s}(\mathbf{x}_{12}^2)}{\alpha_\mathrm{s}(\mathbf{x}_{02}^2)} - 1\right)\right]. \quad (2.20)$$

In comparison to the LO BK equation with fixed coupling, with the Balitsky running coupling the BK equation leads to a slower Y-evolution of the dipole amplitude, which is more consistent with experimental data. The effect of the Balitsky prescription in phenomenological applications is further discussed in Sec. 3.2.2, and in Ch. 4 in regards to the work done in Article [III].

Once the BK equation is applied to phenomenology, i.e. used to drive the energy evolution of the dipole amplitude which then is used to calculate observables, the relation of the evolution variable to the kinematics of the dipole becomes important. Generally, the evolution variable must be proportional to the logarithm of the squared center-of-mass energy, however at NLO the precise definition of the variable begins to matter. At leading order the evolution variable Y is a rapidity-like quantity conventionally defined as

$$Y \coloneqq \ln\left(\frac{q^+}{P^+}\right) = \ln\frac{W^2}{Q_0^2}, \quad (2.21)$$

where q^+ is the plus-momentum of the incoming $q\bar{q}$-dipole, P^+ is a plus-momentum scale related with the target, Q_0^2 is a non-perturbative momentum-scale characteristic to the target, and $W^2 = 2q^+P_0^-$ is the center-of-mass energy of the dipole-target system. Evolution in Y is known as the projectile momentum fraction or rapidity picture, or alternatively the plus-momentum ordering picture — the latter refers to the fact that in Y-evolution the successive gluon emissions are strongly ordered by their plus-momenta. Many leading order phenomenological studies have used also the definition $Y = \ln\frac{1}{x_\mathrm{Bj}}$, which becomes problematic beyond leading order since the evolution is in this case parameterized in target momentum fraction — this is discussed further in a moment. At NLO with the additional gluon in the Fock state, the above definition (2.21) of Y becomes inaccurate. Taking into account the plus-momentum of the gluon becomes crucial, and the evolution rapidity is defined as

$$Y \coloneqq \ln\left(\frac{k_2^+}{P^+}\right) = \ln z_2 + \ln\frac{q^+}{P^+}, \quad (2.22)$$

where k_2^+ is the longitudinal momentum of the emitted gluon. The momentum fraction of the gluon is defined as $z_2 \coloneqq \frac{k_2^+}{q^+}$. This z_2-dependence of Y has a key

role in NLO phenomenology, which is the main point in Article [I] and will be discussed in Sec. 3.3.

Even though this projectile momentum fraction picture is a rather natural way to parametrize the BK evolution — in the sense that the longitudinal momenta of the quarks and gluons in the Fock state stay constant in the scattering off the color-field — it is not quite problem free. In the derivation of the BK equation successive gluon emissions from the projectile dipole are considered, and their lifetimes should be strongly ordered: each daughter gluon should have a shorter lifetime than its parent. However, without further work the Y evolution includes emissions which violate this lifetime hierarchy, which leads to an instability of the evolution. For a more in-depth discussion of the challenges with Y evolution, we refer the reader to Ref. [52].

To cure the time-ordering problem in Y-evolution, different techniques have been used to include related higher-order corrections to the BK equation — this has been done by resumming radiative corrections which are enhanced by double transverse logarithms to all orders. In [53] this resummation produces a BK equation non-local in Y with a kinematical constraint that enforces the ordering; in later parts of this thesis this will be called the KCBK equation, following the convention of [III]. Another approach [54] resums these same corrections in a way that produces a local BK equation. This formulation has further been improved [55], by including a resummation of terms enhanced by single transverse logarithms, which arise from DGLAP physics and one-loop running coupling corrections; this formulation will be called the ResumBK equation, as in [III]. These resummations are able to capture a substantial subset of the NLO contributions to the BK equation [56], and in Ref. [57] it was shown that the two approaches resumming the double-log contributions produce very comparable evolutions of the dipole amplitude — the difference between the resummation prescriptions should be of the order of $\mathcal{O}(\alpha_{\mathrm{s}}^2)$.

In Ref. [52] an alternative approach is proposed to resolve some of the issues with the Y-formulation of the BK equation. Their approach recasts the BK equation as a function of the target momentum fraction. This naturally enforces proper time-ordering in the evolution, since the ordering of the emissions in the minus-momentum is equivalent with their ordering in lifetime. The new formulation of the BK evolution in the target rapidity η, which is defined by [52]

$$\eta \coloneqq Y - \rho = Y - \ln \frac{Q^2}{Q_0^2} = \ln \frac{W^2}{Q^2} = \ln \frac{1}{x_{\mathrm{Bj}}}, \tag{2.23}$$

is derived by performing this change of variables from Y to η, which is a non-perturbative operation that mixes terms of all orders in the perturbative expansion. The target rapidity formulation of the BK equation was found to have a milder instability caused by large double logarithms of a different kind, which

arise in the collinear emission limit of the gluon. An all-order resummation of these contributions was performed, and this resummed formulation will be discussed later in this thesis under the name TBK as in Article [**III**].

The derivation of the NLO corrections to the BK equation considers two gluon emissions from the incoming dipole, which scatter off the target via multiple gluon exchange. The NLO BK equation has been derived both in Y [58, 59] and η [52] evolution pictures, and the former has been solved numerically including resummations as discussed above [56, 60]. Calculations of scattering processes in the CGC formalism at full NLO accuracy require the usage of an NLO accuracy evolution equation — the usage of the NLO BK in such calculations is discussed in Ch. 4.

While the BK equation was derived first, it was later discovered that it corresponds to a large-N_c mean-field approximation of a more general evolution equation: the JIMWLK (Jalilian-Marian, Iancu, McLerran, Weigert, Leonidov and Kovner) equation [39–42, 46–49]. The JIMWLK equation describes the energy dependence of the probability distribution of the Wilson lines. Next-to-leading order corrections have been derived to the JIMWLK equation [61, 62], and analogous resummations of higher order corrections to those of the BK equation discussed above have been studied as well [63]. A recent analysis performs detailed comparisons of numerical solutions of the JIMWLK equation, studying the effects of the numerical implementation and running coupling prescriptions [64]. The JIMWLK equation has been used in phenomenology to describe scattering processes, some studies are discussed in Sec. 3.2.2.

Chapter 3

Deep Inelastic Scattering

3.1 Probing the internal structure of the proton

We begin with an overview of deep inelastic scattering (DIS), which probes the hadronic structure of a nucleon or an atomic nucleus with a high-energy lepton. DIS had an important role in the early development of QCD, the first experiments taking place at the Stanford Linear Accelerator Center (SLAC) [65, 66] contemporaneously with the development of the parton model in the late 1960s. More recently the high-energy precision measurements of electron-proton DIS at DESY-HERA [67–79] have sparked a keen interest in the low-x_{Bj} physics of proton structure.

As a specific example, Fig. 3.1 shows the deep inelastic scattering of an electron off a proton, where the electron-proton interaction takes place as the exchange of a highly virtual photon γ^*. In the parton model, the virtual photon kicks out a parton from the proton as it scatters breaking up the target and therefore probing its structure. The lepton is a particularly suitable probe particle since it does not have internal structure: the lepton current can be separated from the hadronic part, providing a clear window into the hadronic structure. From the theory point of view we are left to describe the virtual photon-proton scattering. See Ref. [28] for an in-depth discussion of DIS and a derivation of the parton model using light-front perturbation theory.

The kinematics of the virtual photon-proton deep inelastic scattering is completely described by two quantities[1] — the virtuality of the photon Q^2, and the Bjorken-x — which are defined as:

$$Q^2 := -q^2 = -(k - k')^2, \tag{3.1}$$

[1] Electron-proton DIS has a third parameter — the inelasticity y — which will be discussed in Ch. 4.

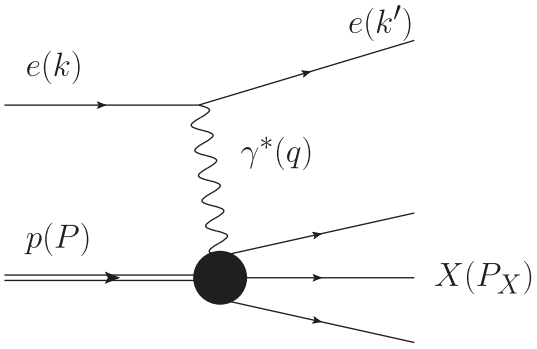

Figure 3.1: Deep inelastic scattering of an electron off a proton.

$$x_{\mathrm{Bj}} \coloneqq \frac{Q^2}{2P\cdot q} = \frac{Q^2}{W^2+Q^2-M^2} \simeq \frac{Q^2}{W^2+Q^2} \simeq \frac{Q^2}{W^2}, \tag{3.2}$$

where $W^2 \coloneqq (P+q)^2$ is the center-of-mass energy[2], and the momenta are illustrated in Fig. 3.1. The first of the approximative equalities is valid at large enough energies where the proton mass M^2 can be neglected, and the second in the proper high-energy regime, $W^2 \gg Q^2$, also known as the Regge limit. From Eq. (3.2) we see why the low-x_{Bj} regime corresponds to the high-energy limit. In the laboratory frame one has $Q^2 = 2EE'(1-\cos\theta)$, where E, E' are the initial and final energy of the electron, and θ the scattering angle. This tells us that Q^2 is a measurable quantity, and therefore x_{Bj} is as well.

These quantities can receive further interpretation. Since the virtual photon can interact with partons inside the proton with transverse momentum at most of the order $\mathbf{k}^2 \sim Q^2$, this means through the Heisenberg uncertainty principle that the partons are localized on a scale $\mathbf{r}^2 \sim 1/Q^2$ [80]. Thus Q^2 gives the resolution at which the target structure is probed. On the other hand in the infinite momentum frame, compared to the large virtuality Q^2, the virtuality of the parton inside the target can be taken to be negligible and so the parton is on-shell. If we then assume the parton carries a fraction of the target momentum $k^\mu = xP^\mu$, we have for the real outgoing parton after the interaction:

$$(xP^\mu + q^\mu)^2 = k'^2 = 0, \tag{3.3}$$

which yields,

$$x = \frac{Q^2}{2P\cdot q} \equiv x_{\mathrm{Bj}}, \tag{3.4}$$

i.e. the kinematically defined Bjorken-x can be interpreted as the momentum fraction of the hit parton in the frame where the proton longitudinal momentum is very large.

[2]Not to be confused with the electron-proton c.o.m. energy $s = (P+k)^2$.

The total virtual photon-proton cross section can be written in the high-energy limit as [28]:

$$\sigma_{\text{tot}}^{\gamma^* p} = \frac{(2\pi)^2 \alpha_{\text{em}}}{Q^2} F_2(x, Q^2), \tag{3.5}$$

which is also called the (fully) inclusive cross section, as in inclusive of all processes that produce any final state.[3] The proton structure function F_2 encodes the unknown information about the internal structure of the proton. It is related to the structure functions F_T and F_L:

$$F_2(x, Q^2) = F_T(x, Q^2) + F_L(x, Q^2), \tag{3.6}$$

where the photon polarization specific structure functions are related to the corresponding total $\gamma^*_{L,T} p$ cross sections as:

$$F_{T,L}(x, Q^2) = \frac{Q^2}{(2\pi)^2 \alpha_{\text{em}}} \sigma_{L,T}^{\gamma^* p}(x, Q^2). \tag{3.7}$$

Here L and T are referring to the longitudinal and transverse polarizations of the virtual photon. The longitudinal structure function F_L is sensitive to the gluonic structure of the proton, since in the case that the proton only contained spin-1/2 particles, the Callan-Gross relation would state that $F_L \equiv 0$ [28].

3.2 DIS in dipole picture at leading order

In contrast to the description of deep inelastic scattering in the previous section, in the high-energy regime a different picture of the scattering can be constructed. At low-x_{Bj} the target is full of low momentum fraction gluons that form semi-classical gluon fields, which flatten into a shockwave due to Lorentz contraction. In this high-energy regime, DIS is described as the scattering of the virtual photon from the color-field of the target. In the target rest frame this proceeds by the incoming — color-chargeless — virtual photon fluctuating into a Fock state which has color-charged constituents that then can scatter off the color-field of the target. This is the dipole picture of DIS, which builds on the ideas of Bjorken, Kogut, and Soper [26] who conceptualized scattering at high-energy as the scattering from a force-field, originally the electromagnetic field.

The leading contributing state in the dipole picture of DIS is the quark-antiquark pair that the photon can form in a QED pair production, depicted in Fig. 3.2. Then, in the spirit of a leading order calculation in the high-energy

[3] This is in contrast with the exclusive cross sections that *exclusively* consider a single process producing a specific final state, such as the production of a given particle, like a vector meson.

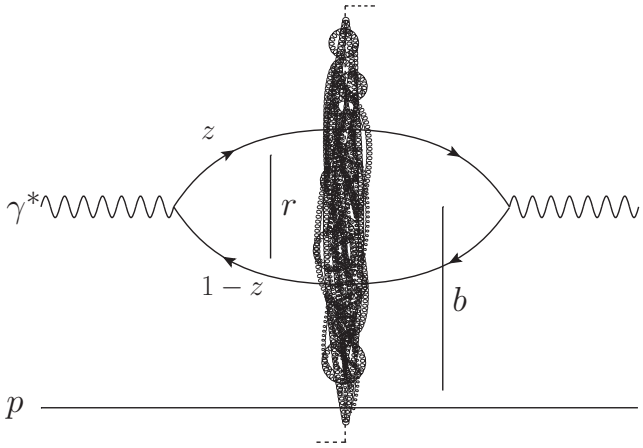

Figure 3.2: Deep inelastic scattering at leading order in the dipole picture. The diagram depicts the calculation of the elastic scattering amplitude $\mathscr{M}^{\text{fwd}}_{\gamma^*_\lambda \to \gamma^*_\lambda}$, to be used with the optical theorem (3.10) to get the total cross section.

limit, the transverse positions of the quark and antiquark can be taken to be fixed in the scattering off the shockwave. This is justified since the relative transverse momentum the quarks pick up in the scattering is suppressed in powers of the scattering energy [28]. This assumption of transverse immobility is the so-called eikonal approximation. Thus, in the eikonal approximation, the quark-dipole only picks up a color rotation in the scattering off the color-field, as described in Sec. 2.3. The optical theorem [2] then connects this elastic scattering amplitude to the inclusive cross section for the virtual photon-proton scattering.

One of the first dipole model depictions of DIS was derived by Nikolaev and Zakharov [81]. In their wake, the process has been calculated in light-front perturbation theory [82]. Many of the Color Glass Condensate framework based theory descriptions of saturation phenomenology in HERA DIS data are based on the dipole picture of DIS, for reviews see Refs. [15–18].

One final thing to consider is when the dipole picture of DIS is valid. Specifically, when is it a good depiction of photon-proton DIS — how small does x_{Bj} need to be —, and is the dipole picture related to gluon saturation in the proton. In the target rest frame, the formation time of the quark-antiquark dipole is $\tau_{q\bar{q}} \sim \frac{1}{m_p x_{\text{Bj}}}$ which much longer than the typical interaction time $\tau_{\text{int.}} \sim R_p$ when x_{Bj} is small [28, 84]; The quantities m_p and R_p are the mass and radius of the proton. Thus the dipole picture only requires the limit $x_{\text{Bj}} \ll 1$. This ties into the manifestation of saturation physics which takes place at high-energy, which is equivalent with the very small x_{Bj} required by the dipole picture. Consequently, the dipole picture is well suited to be combined with a theory description of saturation, as is done in the Color Glass Condensate effective field theory. To

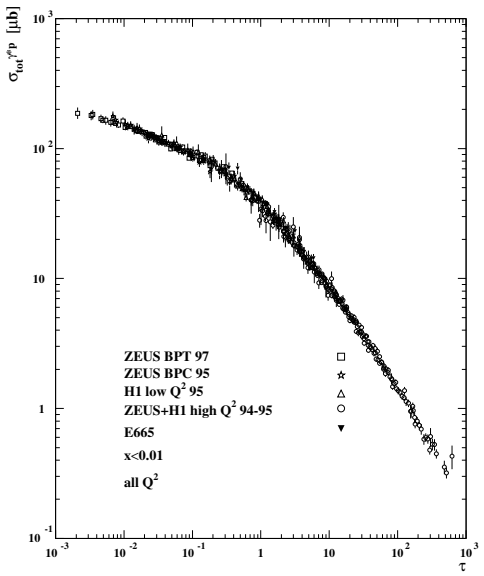

Figure 3.3: Geometric scaling of the photon-proton inclusive HERA data as the function of $\tau := Q^2/Q_s^2(x)$ [83]. Reprinted figure with permission from A. M. Stasto, K. Golec-Biernat, and J. Kwiecinski, Phys. Rev. Lett., 86, 596, 2001. Copyright (2001) by the American Physical Society.

get more insight into the correct regime in x_{Bj}, we look at the HERA $\gamma^* p$ data shown in Fig. 3.3. The plot shows that the inclusive photon-proton cross section scales as the function of $\tau := Q^2/Q_s^2(x)$, where $Q_s^2(x)$ is an emergent semi-hard scale, the saturation scale, in the scattering. This scaling phenomenon is called geometric scaling, which can be indicative of non-linear saturation physics [85], though there are other possible mechanisms [17]. Based on empirical observations such as the geometric scaling, $x_{\mathrm{Bj}} \lesssim 0.01$ is conventionally taken to be the valid regime of the dipole picture. A further point supporting the applicability of the dipole picture to $\gamma^* p$ DIS is that it works phenomenally well: HERA data is described very well at low x_{Bj} — important analyses will be discussed in Sec. 3.2.2.

3.2.1 Inclusive deep inelastic scattering cross section at leading order

Let us discuss the high-level steps to be taken in the calculation of the leading order inclusive virtual photon-proton DIS cross sections. First we need to pick out the relevant contributions to the dressed virtual photon Fock state — discussed in Sec. 2.2 — that contribute at leading order. Only the quark-antiquark

state contributes and so at leading order:

$$\left|\gamma_\lambda^*(q^+,\mathbf{q};Q^2)_H\right\rangle = \sqrt{Z_{\gamma_\lambda^*}}\left\{\widetilde{\sum_{\substack{q_0\bar{q}_1\\ \text{F. states}}}} \tilde{\Psi}_{\gamma_\lambda^*\to q_0\bar{q}_1}\tilde{b}_0^\dagger\tilde{d}_1^\dagger\left|0\right\rangle + \text{negl. Fock states}\right\}. \quad (3.8)$$

One then calculates the forward elastic scattering amplitude for the virtual photon-shockwave scattering, which is defined in light-front quantization as [2]:

$$\left\langle\gamma_\lambda^*(q')_H\right|\left(\hat{S}_E-1\right)\left|\gamma_\lambda^*(q)_H\right\rangle = (2q^+)2\pi\delta(q'^+-q^+)i\mathcal{M}^{\text{fwd}}_{\gamma_\lambda^*\to\gamma_\lambda^*}, \quad (3.9)$$

where $\hat{S}_E$ is the scattering operator that acts on the creation operators of the quark and antiquark. With the forward elastic scattering amplitude, one can then use the optical theorem [2] to relate the amplitude to the total inclusive cross section of the virtual photon-proton scattering:

$$\sigma^{\gamma_\lambda^* p\to X} = 2\,\text{Im}\,\mathcal{M}^{\text{fwd}}_{\gamma_\lambda^*\to\gamma_\lambda^*} = 2\,\text{Re}\left(-i\mathcal{M}^{\text{fwd}}_{\gamma_\lambda^*\to\gamma_\lambda^*}\right). \quad (3.10)$$

The last missing piece are the wavefunctions $\tilde{\Psi}_{\gamma_\lambda^*\to q_0\bar{q}_1}$ for the virtual photon splitting into a quark-antiquark dipole, which have been computed in light-front perturbation theory by many authors, see for example Refs. [82, 86][4]. The squares of these wavefunctions can be interpreted as the probability for the virtual photon to fluctuate into the quark-antiquark dipole. Summed over helicities and photon transverse polarizations, they are [87]

$$\left|\Psi_{\gamma_T^*\to q\bar{q}}\right|^2 = \frac{2N_c}{\pi}\alpha_{\text{em}}e_f^2\left\{\left[z^2+(1-z)^2\right]\varepsilon^2\text{K}_1^2(\varepsilon r)+m_f^2\text{K}_0^2(\varepsilon r)\right\}, \quad (3.11)$$

$$\left|\Psi_{\gamma_L^*\to q\bar{q}}\right|^2 = \frac{8N_c}{\pi}\alpha_{\text{em}}e_f^2Q^2z^2(1-z)^2\text{K}_0^2(\varepsilon r), \quad (3.12)$$

where $\varepsilon^2 = z(1-z)Q^2+m_f^2$, $z := \frac{k^+}{q^+}$ is the longitudinal momentum fraction of the quark, r is the size of the $q\bar{q}$ dipole as shown in Fig. 3.2, f and m_f are the flavor and mass of the quark, and K_0, K_1 are modified Bessel functions of the second kind.

Following the outlined calculation one derives the total virtual photon-proton deep inelastic scattering cross sections, which are [28, 87]:

$$\sigma_{L,T}^{\gamma^* p}(x,Q^2) = \sum_f\int\text{d}^2\mathbf{r}\int_0^1\frac{\text{d}z}{4\pi}\left|\Psi_{\gamma_{L,T}^*\to q\bar{q}}\right|^2\sigma_{q\bar{q}}(x,r), \quad (3.13)$$

[4]For a D-dimensional derivation, see Refs. [II, 1]. Dimensional regularization of the LO result is necessary in the derivation of the complete NLO wavefunctions.

where $r \coloneqq \|\mathbf{r}\|$, and the quark-antiquark dipole scattering amplitude is defined as

$$\sigma_{q\bar{q}}(x, r) = \int \mathrm{d}^2\mathbf{b}\, 2\left[1 - \mathrm{Re}\, S(x, r, \mathbf{b})\right], \tag{3.14}$$

and $S(x, r, \mathbf{b})$ is the scattering matrix for the dipole-gluon shockwave scattering, where $\mathbf{b}$ is the transverse separation of the $q\bar{q}$ dipole from the target, as shown in Fig. 3.2. Sec. 2.3 discusses how the scattering matrix arises in the calculation of the scattering amplitude (3.9). In Eq. (3.13) we see the explicit factorization between the virtual photon wavefunction and the dipole amplitude — the cross section is composed of two independent pieces, a piece with the perturbative QED physics, and a piece with the non-perturbative QCD physics. This feature of the LO dipole picture cross sections is called dipole factorization.

3.2.2 Comparisons of leading order DIS cross sections and measurements

Some of the most exhaustive searches for saturation effects have been done by studying deep inelastic scattering. These analyses rely on the dipole picture of DIS [81, 82] and introduce theory description of saturation effects through the dipole amplitude, which the DIS cross sections depend on. The description of these saturation effects can be roughly divided in two eras: pre-BK and BK era. In this section we discuss some of the key saturation physics analyses and data comparisons done using LO dipole picture DIS structure functions.

The first analysis of DIS data incorporating saturation physics was done using the GBW model by Golec-Biernat and Wusthoff [29] — an analytic parametrization of the dipole amplitude, discussed in Sec. 2.3 — and it achieved a reasonably good description of the old HERA data [67–70]. This model was modified to include DGLAP evolution [88], which improved the description of the total DIS cross sections, especially at large Q^2. Another analytic model was constructed by Iancu, Itakura and Munier (IIM) [89] to improve upon on the success of GBW by including features of BK evolution [43, 44]. The IIM model has been updated to include impact parameter dependence, leading to the bCGC model [87, 90]. These updated models provide improved agreement with the then new and much more accurate HERA data [71–73], in comparison to the simple GBW model.

One more important analytic parametrization to capture saturation effects is the Impact Parameter Saturation (IP-Sat) model proposed by Kowalski and Teaney [91]. In the IP-Sat model the dipole amplitude evolution is induced by the LO DGLAP Q^2-evolution of the gluon distribution, and the x_{Bj}-dependence is parametrized. The original IP-sat implementation provided a good description of HERA data in a much wider Q^2-range than the GBW model was capable of. Since then, the model has been updated [92] with more precise data [74], and

another work [93] updates the model with the most recent HERA data [74–77], and performs a comparison between Impact Parameter models with and without saturation, finding that they are comparably capable of describing the available data.

The BK era was brought about by the AAMS and AAMQS global fits [94, 95], which were the first fits to use the BK equation to drive the small-x dependence of the dipole amplitude. This was an important upgrade in terms of theory precision, since now the only non-perturbative input would be the dipole amplitude at the initial scale of the BK evolution. Using the translationally invariant running coupling BK [51, 96], the AAMQS fits found remarkably good agreement with the inclusive structure functions. A similar analysis using the running coupling BK was done with a slightly different parametrization [97], and in [98] energy conservation corrections are implemented to the running coupling BK, yielding excellent agreement with inclusive data.

Steps have been taken to improve the theoretical precision of the BK approach by including important beyond leading order contributions to the BK equation. One approach [99] enhances the momentum space BK equation by including contributions from DGLAP evolution, which together with a consistency constraint on real gluon emissions produce a large part of higher order corrections. A good description of HERA data was found by an analysis [100] using this evolution equation incorporating aspects of both BK and DGLAP evolutions.

Another approach to enhance the BK equation is the resummation of beyond leading order contributions to the evolution that are enhanced by large logarithms of $1/x_{\mathrm{Bj}}$ — see the discussion of different approaches in Sec. 2.4. The first of such improved BK equations to be used in data analysis is the ResumBK[5] [55], where they find a good description of HERA data even at fairly high-Q^2. The resummation of the single transverse log -enhanced contributions has a minor effect on the fit quality, yielding slightly higher values of χ^2, but nevertheless too small a change to be considered in the accuracy of the analysis. A study [57] comparing the ResumBK and KCBK [53] formulations of the double log resummed BK evolutions found both approaches equally capable of describing HERA DIS data well, and that more theoretical work is needed to distinguish a preferred prescription of resummation and running coupling in the BK equation. A more recent data comparison [101] fits inclusive HERA data using BK evolution which is formulated as a function of the target rapidity [52] (TBK in [III]), as opposed to the projectile rapidity picture used in the above prescriptions. The effects of the resummations of the single and double trans-

[5]ResumBK, KCBK and TBK are acronyms coined in [III] for the formulations of BK evolution derived in Refs. [55], [53], and [52], respectively.

verse log enhanced contributions are considered comprehensively, and they find that the inclusion of the single log resummation has a substantial effect on the fit quality in this scheme — an excellent description of the HERA data is found when both resummations are included, even up to reasonably high Q^2.

Another branch of BK evolution improvements implements some form of impact parameter dependence. In [102] a comparison to HERA data is done with a fairly good agreement, however a full fit was not performed due to the computational cost involved with the impact parameter dependent BK. Similar work has been done using the leading order JIMWLK evolution [103], where a quite good description of the inclusive HERA data was found at small and moderate Q^2. Recent work incorporating the collinearly improved BK kernel into the impact parameter dependent evolution [104] finds a good description of HERA data.

In conclusion, saturation effects have been captured by varied approaches which are able to describe inclusive deep inelastic scattering data at small-x. Recent developments have explored two important areas: running coupling BK evolution and its resummation corrections are central in precision theory calculations, whereas the impact parameter dependence in other approaches is obligatory for the description of exclusive diffractive processes. Impact parameter dependence is needed for exclusive processes since the total momentum transfer with the target is measured, and it is the Fourier conjugate of the impact parameter. This makes the process sensitive to the transverse structure of the target. The recent developments on the impact parameter dependent BK–JIMWLK evolution have promise to bring precision calculations to exclusive processes, and on the other hand target transverse profile sensitivity to inclusive precision calculations.

3.3 DIS in the dipole picture at next-to-leading order

At next-to-leading order (NLO) in the dipole picture, a gluon contributes to the virtual photon wavefunction in addition to the quark-antiquark dipole. The gluon is emitted by either the quark or the antiquark, and then can participate in the scattering from the target shockwave with the dipole, or it can be reabsorbed by one of the quarks. Contributions of the former type are tree-level at NLO, and the latter are loop contributions — Fig. 3.4 shows an instance for either type of contribution. In addition to this normal emission of the gluon, a transversely polarized photon can instantaneously split into a quark-antiquark-gluon tripole, which introduces additional tree-level and loop diagrams at NLO [1, 2, 86].

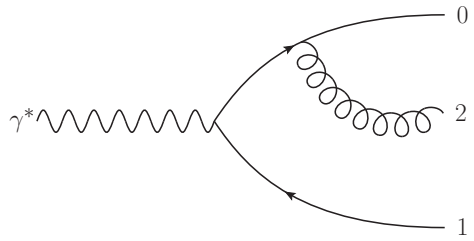

(a) Example of a tree-level diagram: a quark emits a gluon.

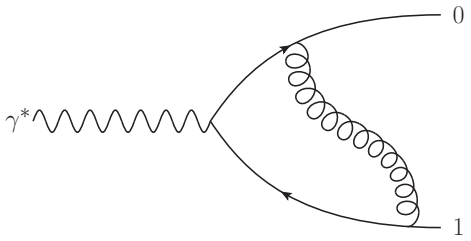

(b) Example of a loop diagram: a gluon is emitted and reabsorbed.

Figure 3.4: Two general types of diagrams contribute to the photon wavefunction at next-to-leading order: tree-level and loop diagrams.

The first calculations of the photon impact factors, i.e. the photon splitting wavefunctions squared and summed over relevant particle helicities, were performed at NLO in momentum space and in a BFKL evolution context [105–108]. Another computation of the impact factors that includes saturation effects has been done in full coordinate space [109], however the results were not presented in the dipole factorized form which complicates their use in phenomenology. They were rewritten in NLO photon impact factor form after a linearization [110], making them compatible with BFKL evolution, but not the gluon saturation regime.

In this section we will discuss the recent derivation of the NLO photon impact factors done in mixed phase space [1, 2, 86], which incorporates gluon saturation effects, and where the results are written in a more suitable form for phenomenological studies. These impact factors were independently derived and verified in [**II**].

3.3.1 Inclusive deep inelastic scattering cross section at next-to-leading order

The calculation of the next-to-leading order DIS cross sections proceeds analogously to the LO derivation discussed in the previous section. One first derives from light-front perturbation theory the NLO corrections to the virtual photon Fock state — normal and instantaneous gluon emissions and loop contributions to the quark-antiquark state. Together these give the virtual photon splitting wavefunctions for the transverse and longitudinal polarizations to NLO accuracy. With these, the optical theorem is used to get the total inclusive DIS cross section from the forward elastic scattering amplitude, like at leading order. Both the tree-level and loop contributions are separately UV-divergent at NLO and must be regulated: conventional dimensional regularization was used to derive

the loop corrections to the photon Fock state in [1], which were combined with the tree-level contributions in [2] for the final result, and the UV divergences canceled in the end. The total NLO cross sections were found to be

$$\sigma_{L,T}^{\mathrm{NLO}} = \sigma_{L,T}^{\mathrm{IC}} + \sigma_{L,T}^{\mathrm{dip}} + \sigma_{L,T}^{qg}. \tag{3.15}$$

The first term is a lowest order contribution — in a strict perturbative expansion sense — to the cross section, where the dipole amplitude is evaluated at the initial scale of the evolution:

$$\sigma_{L,T}^{\mathrm{IC}}(Y_0, Q^2) = 4N_{\mathrm{c}}\alpha_{\mathrm{em}}\frac{\alpha_{\mathrm{s}}C_{\mathrm{F}}}{\pi}\sum_f e_f^2 \int_0^1 \mathrm{d}z_1 \int_{\mathbf{x}_0,\mathbf{x}_1} \mathcal{H}_{L,T}^{\mathrm{LO}}(z_1, \mathbf{x}_0, \mathbf{x}_1) \times \left(1 - \langle S(\mathbf{x}_{01})\rangle_{Y_0}\right), \tag{3.16}$$

where the polarization specific kernels are

$$\mathcal{H}_L^{\mathrm{LO}}(z_1, \mathbf{x}_0, \mathbf{x}_1) = 4Q^2 z_1^2 (1-z_1)^2 \mathrm{K}_0^2(QX_2), \tag{3.17}$$

$$\mathcal{H}_T^{\mathrm{LO}}(z_1, \mathbf{x}_0, \mathbf{x}_1) = Q^2 z_1(1-z_1)\left(z_1^2 + (1-z_1)^2\right)\mathrm{K}_1^2(QX_2), \tag{3.18}$$

with $X_2 \coloneqq z_1(1-z_1)\mathbf{x}_{01}^2$, $\mathbf{x}_{ij} \coloneqq \mathbf{x}_i - \mathbf{x}_j$, and $S(\mathbf{x}_{ij}) = S(\mathbf{x}_{ij}, \mathbf{b})$, and the shorthand $\int_{\mathbf{x}_i} \coloneqq \int \frac{\mathrm{d}^2\mathbf{x}_i}{2\pi}$ was defined. The variables $\mathbf{x}_0, \mathbf{x}_1$ are the transverse coordinates of the quark and antiquark, and z_1 the momentum fraction of the antiquark. Even though (3.17) and (3.18) are the squared LO wavefunctions, i.e. the same as the Eqs. (3.11) and (3.12) but with massless quarks, this is not the full leading order cross section (3.13) since the dipole amplitudes are not evolved[6]. This ties into a discussion about soft gluons that we will look at in a moment. As for the NLO contributions, the 'dipole' term is:

$$\sigma_{L,T}^{\mathrm{dip}} = 4N_{\mathrm{c}}\alpha_{\mathrm{em}}\frac{\alpha_{\mathrm{s}}C_{\mathrm{F}}}{\pi}\sum_f e_f^2 \int_0^1 \mathrm{d}z_1 \int_{\mathbf{x}_0,\mathbf{x}_1} \mathcal{H}_{L,T}^{\mathrm{LO}}(z_1, \mathbf{x}_0, \mathbf{x}_1) \times \left(1 - \langle S(\mathbf{x}_{01})\rangle_Y\right)\left[\frac{1}{2}\ln^2\left(\frac{z_1}{1-z_1}\right) - \frac{\pi^2}{6} + \frac{5}{2}\right], \tag{3.19}$$

and the 'qg' term is:

$$\sigma_{L,T}^{qg} = 8N_{\mathrm{c}}\alpha_{\mathrm{em}}\frac{\alpha_{\mathrm{s}}C_{\mathrm{F}}}{\pi}\sum_f e_f^2 \int_0^1 \mathrm{d}z_1 \int_{z_{2,\min}}^{1-z_1} \frac{\mathrm{d}z_2}{z_2} \times \int_{\mathbf{x}_0,\mathbf{x}_1,\mathbf{x}_2} \mathcal{H}_{L,T}^{\mathrm{NLO}}(z_1, z_2, \mathbf{x}_0, \mathbf{x}_1, \mathbf{x}_2, Y). \tag{3.20}$$

[6] In a strict perturbative expansion sense, σ^{IC} is the leading contribution in α_{s}. However, the BK evolution produces a contribution of the order $\alpha_{\mathrm{s}} \ln \frac{1}{x_{\mathrm{Bj}}} \sim 1$, which is conventionally included in the leading order cross section, upgrading it technically to leading logarithm precision.

The expressions for $\sigma_{L,T}^{\mathrm{dip}}$ or $\sigma_{L,T}^{qg}$ above are not unique, but their sum is. This is due to the UV divergences that the respective contributions contain originally, and which are canceled between the two contributions [1, 2]. The NLO kernels present in the qg contribution are:

$$\begin{aligned}
&\mathcal{K}_L^{\mathrm{NLO}}(z_1, z_2, \mathbf{x}_0, \mathbf{x}_1, \mathbf{x}_2, Y) = 4Q^2 z_1^2 (1-z_1)^2 \\
&\quad \times \Bigg\{ P\left(\frac{z_2}{1-z_1}\right) \frac{\mathbf{x}_{20}}{\mathbf{x}_{20}^2} \cdot \left(\frac{\mathbf{x}_{20}}{\mathbf{x}_{20}^2} - \frac{\mathbf{x}_{21}}{\mathbf{x}_{21}^2}\right) \left[\mathrm{K}_0^2(QX_3)\left(1 - \langle S_{012}\rangle_Y\right) - (\mathbf{x}_2 \to \mathbf{x}_0)\right] \\
&\qquad + \left(\frac{z_2}{1-z_1}\right)^2 \frac{\mathbf{x}_{20}\cdot\mathbf{x}_{21}}{\mathbf{x}_{20}^2\mathbf{x}_{21}^2} \mathrm{K}_0^2(QX_3)\left(1 - \langle S_{012}\rangle_Y\right) \Bigg\},
\end{aligned} \tag{3.21}$$

$$\begin{aligned}
&\mathcal{K}_T^{\mathrm{NLO}}(z_1, z_2, \mathbf{x}_0, \mathbf{x}_1, \mathbf{x}_2, Y) = Q^2 z_1 (1-z_1) \\
&\quad \times \Bigg\{ P\left(\frac{z_2}{1-z_1}\right) \left(z_1^2 + (1-z_1)^2\right) \frac{\mathbf{x}_{20}}{\mathbf{x}_{20}^2} \cdot \left(\frac{\mathbf{x}_{20}}{\mathbf{x}_{20}^2} - \frac{\mathbf{x}_{21}}{\mathbf{x}_{21}^2}\right) \\
&\qquad \times \left[\mathrm{K}_1^2(QX_3)\left(1 - \langle S_{012}\rangle_Y\right) - (\mathbf{x}_2 \to \mathbf{x}_0)\right] \\
&\qquad + \left(\frac{z_2}{1-z_1}\right)^2 \left[\left(z_1^2 + (1-z_1)^2\right) \frac{\mathbf{x}_{20}\cdot\mathbf{x}_{21}}{\mathbf{x}_{20}^2\mathbf{x}_{21}^2} + 2z_0 z_1 \frac{\mathbf{x}_{20}\cdot\mathbf{x}_{21}}{\mathbf{x}_{20}^2 X_3^2} - \frac{z_0(z_1+z_2)}{X_3^2}\right] \\
&\qquad \times \mathrm{K}_1^2(QX_3)\left(1 - \langle S_{012}\rangle_Y\right) \Bigg\}.
\end{aligned} \tag{3.22}$$

Here $\mathbf{x}_0, \mathbf{x}_1, \mathbf{x}_2$, and z_0, z_1, z_2 are the transverse positions and longitudinal momentum fractions of the quark, antiquark and gluon; the indexing is illustrated in Fig 3.4a. The fractions satisfy $\sum_i z_i = 1$. The definitions $X_3^2 := z_0 z_1 \mathbf{x}_{01}^2 + z_0 z_2 \mathbf{x}_{02}^2 + z_2 z_1 \mathbf{x}_{21}^2$ and $P(z) := 1 + (1-z)^2$ are made. The arrow notation denotes that the corresponding limit is to be taken of the preceding term: $f(a, b, c \to a) = f(a, b, a)$. The $q\bar{q}g$ state-target scattering Wilson line operator is [II, 2]

$$\begin{aligned}
S_{012} &:= \frac{1}{N_{\mathrm{c}} C_{\mathrm{F}}} \mathrm{tr}\left(t^b U_F(\mathbf{x}_0) t^a U_F^\dagger(\mathbf{x}_1)\right) U_A(\mathbf{x}_2)_{ba} \\
&= \frac{1}{2N_{\mathrm{c}} C_{\mathrm{F}}} \Big[\mathrm{tr}\left(U_F(\mathbf{x}_0) U_F^\dagger(\mathbf{x}_2)\right) \mathrm{tr}\left(U_F(\mathbf{x}_2) U_F^\dagger(\mathbf{x}_1)\right) \\
&\qquad\qquad - \frac{1}{N_{\mathrm{c}}} \mathrm{tr}\left(U_F(\mathbf{x}_0) U_F^\dagger(\mathbf{x}_1)\right)\Big] \\
&\equiv \frac{N_{\mathrm{c}}}{2C_{\mathrm{F}}} \left(S(\mathbf{x}_{02}) S(\mathbf{x}_{21}) - \frac{1}{{N_{\mathrm{c}}}^2} S(\mathbf{x}_{01})\right),
\end{aligned} \tag{3.23}$$

where in the first step the identity [111] used is:

$$t_{ij}^a t_{kl}^a = \frac{1}{2}\left(\delta_{il}\delta_{jk} - \frac{1}{N_{\mathrm{c}}}\delta_{ij}\delta_{kl}\right). \tag{3.24}$$

Two details are yet to be determined: the rapidity scales Y related to the dipole and qg contributions — since they are not provided by the perturbation theory calculation — and the lower limit $z_{2,\min}$ of the gluon momentum fraction integration that regulates the logarithmically divergent integral. These turn out to be connected, and are the topic of the work done for Article [I], which will be discussed in the next section.

3.3.2 Summary of Article [I]: factorization of the soft gluon large logarithm

The crux to be resolved by Article [I] was the negativity problem of NLO cross sections calculated in the Color Glass Condensate formalism, which was expected to afflict the NLO DIS cross sections as well. For context, in the case of single inclusive forward hadron production in $p+A$ it had been found that the NLO cross sections would become negative when the produced hadron would have a transverse momentum of the order of a few GeV [112]. A resolution to this issue for single inclusive hadron production was proposed [113], which was demonstrated to be effective [114]. The topic of Article [I] was the first numerical computation of the NLO DIS cross sections, whereby we demonstrated the presence of the negativity problem, and the application of the aforementioned solution to correct it. Resolving the negativity problem for the NLO DIS cross sections would bring the perturbative expansion under control, and make precision comparisons between theory and data possible in the future.

The root cause of this problem is the handling of the large logarithm induced by the z_2-integration in the qg contribution (3.20) discussed in the previous section. Qualitatively, it needs to be factorized and absorbed into the BK renormalization group evolution. In practice, this means that the large logarithm that arises from the qg contribution provides the rapidity evolution for the unevolved lowest order cross section (3.16), upgrading it from LO to the full LL (leading log) cross section. If this factorization is done inaccurately, the negative qg contribution has a leftover large logarithm, that can make the NLO cross sections negative. The development of an accurate subtraction scheme for NLO DIS cross sections was the principal goal of Article [I]. Once this was under control, we were able to quantify the importance of the NLO corrections.

This issue would be corrected by accurately connecting the lower limit $z_{2,\min}$, and the rapidity scale of the Wilson-line operators in the qg term, which were discussed in the previous section. It was understood that at NLO the qg contribution drives the exact amount of evolution through $z_{2,\min}$. In connection to this, the qg term dipole amplitudes must be evaluated at a rapidity scale that depends on the longitudinal momentum fraction of the gluon z_2: the evolution

rapidity in this context is defined as $Y \coloneqq \ln z_2$. We derive in [I] that the qg term rapidity scale should be

$$Y_{qg} = \ln \frac{z_2}{z_{2,\min}} = \ln \frac{x_0}{X(z_2)} = \ln \frac{z_2 x_0 Q^2}{x_{\mathrm{Bj}} Q_0^2} \approx \ln \frac{z_2 x_0}{x_{\mathrm{Bj}}}, \tag{3.25}$$

where x_0 is the initial scale of the evolution, and Q_0^2 is some hadronic low transverse momentum scale. The last approximation was done since the Q^2-dependence introduces some complexity, since it affects the subtraction of the soft gluon large logarithm. The quantity $X(z_2)$ is a target momentum fraction scale similarly to x_0 and x_{Bj}. We showed that by using the relation (3.25) instead of the simple $Y = \ln x_0/x_{\mathrm{Bj}}$ the negativity problem is resolved.

The above procedure also naturally regulates the soft gluon large logarithm correctly, leading to the subtraction scheme dubbed 'unsub' scheme:

$$\sigma_{L,T}^{\mathrm{NLO}} = \sigma_{L,T}^{\mathrm{IC}} + \sigma_{L,T}^{\mathrm{dip}} + \sigma_{L,T}^{qg,\mathrm{unsub.}}, \tag{3.26}$$

where the first term is (3.16), the NLO dipole contribution $\sigma_{L,T}^{\mathrm{dip}}$ is (3.19) for which the rapidity scale is chosen to be the same as in the LL cross sections $Y = \ln x_0/x_{\mathrm{Bj}}$, and the qg term is

$$\begin{aligned}\sigma_{L,T}^{qg,\mathrm{unsub,\,approx.}} = 8N_{\mathrm{c}}\alpha_{\mathrm{em}}\frac{\alpha_{\mathrm{s}}C_{\mathrm{F}}}{\pi}\sum_f e_f^2 \int_0^1 \mathrm{d}z_1 \int_{\frac{x_{\mathrm{Bj}}}{x_0}}^{1-z_1} \frac{\mathrm{d}z_2}{z_2} \\ \times \int_{\mathbf{x}_0,\mathbf{x}_1,\mathbf{x}_2} \mathcal{K}_{L,T}^{\mathrm{NLO}}(z_1, z_2, \mathbf{x}_0, \mathbf{x}_1, \mathbf{x}_2, \ln \frac{z_2 x_0}{x_{\mathrm{Bj}}}).\end{aligned} \tag{3.27}$$

This formulation was found to yield physical cross sections. Without the approximation the qg contribution writes

$$\begin{aligned}\sigma_{L,T}^{qg,\mathrm{unsub.}} = 8N_{\mathrm{c}}\alpha_{\mathrm{em}}\frac{\alpha_{\mathrm{s}}C_{\mathrm{F}}}{\pi}\sum_f e_f^2 \int_0^1 \mathrm{d}z_1 \int_{z_{2,\min}}^{1-z_1} \frac{\mathrm{d}z_2}{z_2} \\ \times \int_{\mathbf{x}_0,\mathbf{x}_1,\mathbf{x}_2} \mathcal{K}_{L,T}^{\mathrm{NLO}}(z_1, z_2, \mathbf{x}_0, \mathbf{x}_1, \mathbf{x}_2, Y_{qg}),\end{aligned} \tag{3.28}$$

which is the form that was used in Article [III], with the reparametrization $x_0 \equiv e^{-Y_{0,\mathrm{if}}}$. More details, and a discussion of how an explicit subtraction scheme for the soft gluon large logarithm is derived are found in Article [I]. The factorization of the large logarithm is done with an extra term that subtracts the large log from the qg-term, and resums it into the BK evolution of the σ^{IC} term, upgrading it to the LL accuracy cross section σ^{LO}. This subtraction was called the 'sub' scheme, and it writes

$$\sigma_{L,T}^{\mathrm{NLO}} = \sigma_{L,T}^{\mathrm{LO}} + \sigma_{L,T}^{\mathrm{dip}} + \sigma_{L,T}^{qg,\mathrm{sub.}}, \tag{3.29}$$

where the LL rapidity scale is $Y = \ln x_0/x_{\mathrm{Bj}}$, and

$$\sigma_{L,T}^{qg,\mathrm{sub,\,approx.}} = 8N_{\mathrm{c}}\alpha_{\mathrm{em}}\frac{\alpha_{\mathrm{s}}C_{\mathrm{F}}}{\pi}\sum_f e_f^2\int_0^1 \mathrm{d}z_1 \int_{\frac{x_{\mathrm{Bj}}}{x_0}}^1 \frac{\mathrm{d}z_2}{z_2} \times \int_{\mathbf{x}_0,\mathbf{x}_1,\mathbf{x}_2} \left[\theta(1-z_1-z_2)\mathcal{K}_{L,T}^{\mathrm{NLO}}\left(z_1,z_2,\mathbf{x}_0,\mathbf{x}_1,\mathbf{x}_2,\ln\frac{z_2x_0}{x_{\mathrm{Bj}}}\right) - \mathcal{K}_{L,T}^{\mathrm{NLO}}\left(z_1,0,\mathbf{x}_0,\mathbf{x}_1,\mathbf{x}_2,\ln\frac{z_2x_0}{x_{\mathrm{Bj}}}\right)\right]. \quad (3.30)$$

One relevant detail about the 'unsub' and 'sub' schemes, that is not discussed in [I], is that the equivalence of the two subtraction schemes is broken once a beyond-LO BK evolution is introduced. This creates a finite difference between the schemes of the order of NNLO. Relatedly, selecting between two different beyond-LO BK equations with the same subtraction scheme also introduces a finite difference of the order of NNLO. Sec. 4.3 discusses the estimation of the significance of these effects, and a similar effect concerning the running coupling is discussed in Sec. 4.4.

Analogous subtraction schemes for DIS are put forth in Ref. [2], with some minor differences. In the unsubtracted scheme, the dipole amplitude in the NLO dipole term $\sigma_{L,T}^{\mathrm{dip}}$ is left unevolved like the lowest order contribution. This is valid at this precision of the calculation, since input for the correct scale should arise only at NNLO precision of the cross sections. In Article [I] our preference would have been to evaluate the NLO dipole term $\sigma_{L,T}^{\mathrm{dip}}$ at the same rapidity as the qg-term, i.e. at Y_{qg} in Eq. (3.25), but this was not possible since the integration over the loop momentum fraction z_2 has been performed analytically in Eq. (3.19). The next section discusses the reversion of this integration.

3.3.3 Undoing the loop integration of $\sigma_{L,T}^{\mathrm{dip}}$

As is discussed in [I], the most natural thing to do is to evaluate both $\sigma_{L,T}^{\mathrm{dip}}$ and $\sigma_{L,T}^{qg}$ at the same rapidity scale. However, this was not possible in [I] since the loop momentum integration was performed analytically in [1], and the available results were independent of the gluon longitudinal momentum fraction z_2. In this section we propose a form for $\sigma_{L,T}^{\mathrm{dip}}$, where this integration has been undone, and discuss its features. The derivation here uses the conventions and intermediate results of Ref. [1].

To begin the undoing of the z_2-integrations done in the derivation of (3.19), let us first revert some manipulations:

$$\frac{1}{2}\log^2\left(\frac{z_1}{1-z_1}\right) - \frac{\pi^2}{6} + \frac{5}{2} = -\mathrm{Li}_2\left(-\frac{z_1}{1-z_1}\right) - \mathrm{Li}_2\left(-\frac{1-z_1}{z_1}\right) - \frac{\pi^2}{3} + \frac{5}{2}, \quad (3.31)$$

where the relation used is

$$\mathrm{Li}_2\left(z\right)+\mathrm{Li}_2\left(\frac{1}{z}\right)=-\frac{1}{2}\log^2(z)-\frac{\pi^2}{6}. \tag{3.32}$$

The result is the sum of contributions symmetric in the exchange of the quark and antiquark, so in fact we are looking for one of these halves, which is

$$-\mathrm{Li}_2\left(-\frac{1-z_1}{z_1}\right)-\frac{\pi^2}{6}+\frac{5}{4}+\frac{1}{2}\frac{1}{2}, \tag{3.33}$$

where the last $\frac{1}{4}$ is a half of the UV scheme dependent finite leftover, that will cancel in the full NLO cross section. This contribution arises in a different way for T and L polarizations.

In the case of the longitudinal photon, using the notations and definitions of Ref. [1], these terms are found in the following sum of contributions [1]:

$$\mathcal{V}_A^L+\mathcal{V}_1^L+\mathcal{V}_{3a}^L=\cdots-\mathrm{Li}_2\left(-\frac{k_0^+}{k_1^+}\right)-\frac{\pi^2}{6}+\frac{3}{2}+\cdots, \tag{3.34}$$

where the unrelated terms have been omitted. To discover the unintegrated form, we need to look closely at the integral forms of these contributions. To this end, it is useful to be aware of the following integral relations [1]:

$$\int_0^1\frac{\mathrm{d}\xi}{\xi}\log(1+R\xi)=-\mathrm{Li}_2\left(-R\right), \tag{3.35}$$

$$\int_0^1\frac{\mathrm{d}\xi}{\xi}\log(1-\xi)=-\frac{\pi^2}{6}. \tag{3.36}$$

The integral forms of $\mathcal{V}_A^L$ and $\mathcal{V}_1^L+\mathcal{V}_{3a}^L$ are:

$$\begin{aligned}
\mathcal{V}_A^L=\mathcal{V}_A^T \;=\; & -\int_0^{k_0^+}\frac{\mathrm{d}k_2^+}{k_0^+}\left\{2\left(\frac{k_0^+-k_2^+}{k_2^+}\right)+\frac{k_2^+}{k_0^+}\right\}\left\{\Gamma\left(2-\frac{D}{2}\right)\left[\frac{-2\,k_0^+(ED_{\mathrm{LO}})}{4\pi\,\mu^2}\right]^{\frac{D}{2}-2}\right. \\
& \left.-\log\left(\frac{k_2^+}{k_0^+}\right)-\log\left(\frac{k_0^+-k_2^+}{k_0^+}\right)\right\} \\
& +\int_0^{k_0^+}\frac{\mathrm{d}k_2^+}{k_0^+}\left(\frac{k_2^+}{k_0^+}\right)\;+O\left(D-4\right) \\
= \; & 2\left[\log\left(\frac{k_{\mathrm{min}}^+}{k_0^+}\right)+\frac{3}{4}\right]\Gamma\left(2-\frac{D}{2}\right)\left[\frac{-2\,k_0^+(ED_{\mathrm{LO}})}{4\pi\,\mu^2}\right]^{\frac{D}{2}-2} \\
& -\left[\log\left(\frac{k_{\mathrm{min}}^+}{k_0^+}\right)\right]^2-\frac{\pi^2}{3}+3+\frac{1}{2}+O\left(D-4\right).
\end{aligned} \tag{3.37}$$

and

$$
\begin{aligned}
\mathcal{V}_1^L + \mathcal{V}_{3a}^L \;=\; & \int_0^{k_0^+} \frac{\mathrm{d}k_2^+}{k_0^+} \left\{ \left(\frac{k_0^+}{k_2^+} \right) - \frac{k_1^+}{q^+} - \frac{k_2^+}{q^+} \right\} \\
& \times \left\{ \Gamma\!\left(2 - \frac{D}{2}\right) \left(\frac{\overline{Q}^2}{4\pi\,\mu^2} \right)^{\frac{D}{2}-2} - \log\left(\frac{k_1^+ + k_2^+}{k_1^+} \right) - \log\left(\frac{k_0^+ - k_2^+}{k_0^+} \right) \right\} \\
& + \int_0^{k_0^+} \frac{\mathrm{d}k_2^+}{k_0^+} \left\{ \frac{2k_0^+}{k_2^+} + \left(\frac{k_0^+ - k_1^+}{k_1^+} \right) - \frac{k_2^+}{k_1^+} \right\} \\
& \times \left\{ -\log\left(\frac{k_2^+}{k_0^+} \right) + \log\left(\frac{k_1^+ + k_2^+}{k_1^+} \right) - \log\left(\frac{q^+}{k_1^+} \right) \right\} \\
& - \int_0^{k_0^+} \frac{\mathrm{d}k_2^+}{k_0^+} \left(\frac{k_0^+ - k_2^+}{q^+} \right) + O\,(D-4) \\
= \; & - \left[\log\left(\frac{k_{\mathrm{min}}^+}{k_0^+} \right) + \frac{1}{2} + \frac{k_1^+}{2q^+} \right] \Gamma\!\left(2 - \frac{D}{2}\right) \left(\frac{\overline{Q}^2}{4\pi\,\mu^2} \right)^{\frac{D}{2}-2} \\
& + \left[2\log\left(\frac{k_{\mathrm{min}}^+}{k_0^+} \right) + \frac{3}{2} \right] \log\left(\frac{q^+}{k_1^+} \right) \\
& + \left[\log\left(\frac{k_{\mathrm{min}}^+}{k_0^+} \right) \right]^2 + \frac{\pi^2}{6} - \mathrm{Li}_2\left(-\frac{k_0^+}{k_1^+} \right) - 2 + \frac{k_0^+}{2q^+} \\
& - \frac{k_0^+}{2q^+} + O\,(D-4)\;, \qquad (3.38)
\end{aligned}
$$

where the terms contributing to $\frac{\pi^2}{6}$ and Li_2 have been highlighted in gold and orange, respectively, and the two-colored factor contributes to both. Now we may collect from (3.37) and (3.38) the terms contributing to the polylogarithm and $\frac{\pi^2}{6}$ terms in (3.33):

$$
-\mathrm{Li}_2\left(-\frac{1-z_1}{z_1} \right) = -\mathrm{Li}_2\left(-\frac{k_0^+}{k_1^+} \right) = \int_0^{k_0^+} \frac{\mathrm{d}k_2^+}{k_2^+} \log\left(\frac{k_1^+ + k_2^+}{k_1^+} \right), \qquad (3.39)
$$

$$
-\frac{\pi^2}{6} = \int_0^{k_0^+} \frac{\mathrm{d}k_2^+}{k_2^+} \log\left(\frac{k_0^+ - k_2^+}{k_0^+} \right), \qquad (3.40)
$$

where the temporary variable $\xi := \frac{k_2^+}{k_0^+}$ is used in (3.35), (3.36). Then, adding

this together with the quark-antiquark exchange terms, we can write:

$$\begin{aligned}
\frac{1}{2}\log^2\left(\frac{z_1}{1-z_1}\right) - \frac{\pi^2}{6} &= \left(\mathcal{V}_A^L + \mathcal{V}_1^L + \mathcal{V}_{3a}^L\right)\Big|_{-\mathrm{Li}_2-\frac{\pi^2}{6}} + \left(k_0^+ \leftrightarrow k_1^+\right) \\
&= \int_0^{k_0^+} \frac{\mathrm{d}k_2^+}{k_2^+}\left\{\log\left(\frac{k_1^+ + k_2^+}{k_1^+}\right) + \log\left(\frac{k_0^+ - k_2^+}{k_0^+}\right)\right\} + \left(k_0^+ \leftrightarrow k_1^+\right) \\
&= \int_0^{1-z_1} \mathrm{d}z_2 \left[\frac{1}{z_2}\left(\log\left(1+\frac{z_2}{z_1}\right) + \log\left(1-\frac{z_2}{1-z_1}\right)\right)\right] \\
&\quad + \int_0^{z_1} \mathrm{d}z_2 \left[\frac{1}{z_2}\left(\log\left(1+\frac{z_2}{1-z_1}\right) + \log\left(1-\frac{z_2}{z_1}\right)\right)\right], \qquad (3.41)
\end{aligned}$$

where the vertical bar notation refers to picking only the relevant terms, and in the last equality the change of variables $z_i \coloneqq \frac{k_i^+}{q^+}$ was used together with the identity[7] $z_0 + z_1 = 1$.

The derivation of the respective result for a transverse photon proceeds in an analogous way, however now the contributions come from the diagrams $\mathcal{V}_A^T + \mathcal{V}_1^T + \left(k_0^+ \leftrightarrow k_1^+\right)$. The integral form (3.41) found for the longitudinal photon is found for the transverse polarization as well.

Now, we are left with the constant $\frac{5}{2}$ that has been excluded in the previous discussion, since its derivation is different in a few key ways. First, even though the constant is the same for both transverse and longitudinal photons, it arises from different contributions. While the polylogarithm and π^2 terms were completely UV regularization scheme independent, the $3 = \frac{5}{2} + \frac{1}{2}$ constant seen in the result of the loop contribution receives UV scheme dependent contributions from the quark and antiquark self-energy and total vertex corrections. These will cancel with the UV scheme dependent terms from the $q\bar{q}g$-contribution [2]. In addition to these scheme dependent contributions, the constant receives contributions from a large number of integrals, some of which are IR divergent, and many of which have substantial cancellations at the integrated level. The IR divergences are regulated with an IR cut-off, and the cut-off dependent terms cancel out completely [1]. This means that some of the integrals that contribute to the $\frac{5}{2}$ we are interested in would need to be IR regulated, which could make them precarious for numerical evaluation and the cancellation of the divergences. Lastly, while a half of the constant arises from both of the quark-antiquark symmetric partitions independently for the longitudinal photon, this is not the case for the transverse photon, and it would be necessary to have all the integrals from $\mathcal{V}_A^T + \mathcal{V}_1^T + \left(k_0^+ \leftrightarrow k_1^+\right)$ separately in order to get the correct cancellations.

[7] The loop momentum fraction z_2 is not constrained by the plus-momentum conservation, unlike in the case of the tree-level $q\bar{q}g$ contributions discussed in Sec. 3.3.1.

Due to these complications we chose to keep the final UV scheme independent constant at the integral level as well, as an averaged effect for these contributions.

Now with (3.41) and including the $\frac{5}{4}$ as discussed above, we may rewrite (3.19) back into an integral form:

$$\begin{aligned}
\sigma_{L,T}^{\mathrm{dip},z_2} =& 4N_\mathrm{c}\alpha_\mathrm{em}\frac{\alpha_\mathrm{s}C_\mathrm{F}}{\pi}\sum_f e_f^2\int_{z_{2,\min}}^{1-z_{2,\min}}\mathrm{d}z_1\int_{\mathbf{x}_0,\mathbf{x}_1}\mathscr{K}_{L,T}^{\mathrm{LO}}(z_1,\mathbf{x}_0,\mathbf{x}_1)\\
&\times\left\{\int_{z_{2,\min}}^{z_1}\mathrm{d}z_2\left[\frac{1}{z_2}\left(\log\left(1+\frac{z_2}{1-z_1}\right)+\log\left(1-\frac{z_2}{z_1}\right)\right)+\frac{1}{z_1}\frac{5}{4}\right]\right.\\
&\quad\left.\times\left[1-\langle S_{01}\rangle_{Y_2^+}\right]\right.\\
&+\int_{z_{2,\min}}^{1-z_1}\mathrm{d}z_2\left[\frac{1}{z_2}\left(\log\left(1+\frac{z_2}{z_1}\right)+\log\left(1-\frac{z_2}{1-z_1}\right)\right)+\frac{1}{1-z_1}\frac{5}{4}\right]\\
&\quad\left.\times\left[1-\langle S_{01}\rangle_{Y_2^+}\right]\right\}\\
=& 8N_\mathrm{c}\alpha_\mathrm{em}\frac{\alpha_\mathrm{s}C_\mathrm{F}}{\pi}\sum_f e_f^2\int_{z_{2,\min}}^{1-z_{2,\min}}\mathrm{d}z_1\int_{\mathbf{x}_0,\mathbf{x}_1}\mathscr{K}_{L,T}^{\mathrm{LO}}(z_1,\mathbf{x}_0,\mathbf{x}_1)\\
&\times\int_{z_{2,\min}}^{z_1}\mathrm{d}z_2\left[\frac{1}{z_2}\left(\log\left(1+\frac{z_2}{1-z_1}\right)+\log\left(1-\frac{z_2}{z_1}\right)\right)+\frac{1}{z_1}\frac{5}{4}\right]\\
&\quad\times\left[1-\langle S_{01}\rangle_{Y_2^+}\right],
\end{aligned}\tag{3.42}$$

where in the second equality the two terms symmetric in the quark-antiquark exchange are combined. When the lower limit $z_{2,\min}$ is introduced for z_2 in a subtraction scheme, the phase space of the z_1-integration must be consistently limited as well. The upper limits z_1 or $1-z_1$ cannot become smaller than $z_{2,\min}$. As we wish to give the dipole amplitude a z_2 dependent rapidity scale, we move the dipole amplitude inside the integral make the replacement of the evaluation scale

$$\left[1-\langle S_{01}\rangle_{Y_f^+}\right]\to\left[1-\langle S_{01}\rangle_{Y_2^+}\right],$$

where Y_f^+ is the rapidity scale of the LO+LL DIS cross sections [2], and the new rapidity scale is

$$Y_2^+ := \log\left(\frac{z_2}{z_{2,\min}}\right)=\log\left(z_2\frac{x_0Q^2}{x_\mathrm{Bj}Q_0^2}\right),\tag{3.43}$$

which is the same as was used for the qg contribution in [III], and in the approximation $Q^2/Q_0^2\sim 1$ the same as was used in [I].

In conclusion, we have derived an alternative, and previously unpublished, form (3.42) for the NLO dipole contribution Eq. (3.19). The new form has been rewritten back into a loop-integral form, which permits the consistent usage of the same z_2-dependent rapidity scale (3.43) in both the $q\bar{q}g$ term (3.20) and the

new NLO dipole term (3.42). This would have been the preferred rapidity scale for the NLO dipole term in the works [I, III].

3.3.4 Summary of Article [II]: NLO DIS cross sections in the four-dimensional helicity scheme

The principal purpose of the Article [II] is to develop new methodology for light-front perturbation theory loop calculations, where the key feature is that the elementary vertices are written in a helicity basis. Specifically, in this article the calculation rules originally introduced in [115] are reformulated in a better way, and a correction to the scheme is made. A key point in the new scheme is the proper handling of the Kronecker-deltas of different dimensionalities. As a demonstration, this calculation scheme is then used to derive the virtual photon splitting wavefunctions at next-to-leading order in the dipole picture. These photon wavefunctions are then used to write the NLO DIS cross sections, which are then compared with — and found equivalent to — the ones derived in Refs. [1, 2].

The usage of the explicit helicity basis for the quarks and gluons is naturally combined with the regularization of the UV divergences in the four-dimensional helicity (FDH) scheme. As opposed to the conventional dimensional regularization (CDR) used in Refs. [1, 2] — where all vectors and momenta are continued to d dimensions — the FDH scheme keeps all observed particles in four dimensions and continues unobserved particle momenta to $d > 4$ dimensions, and spins/polarizations of unobserved internal states are $d_s > d$ dimensional.

This new calculation of the NLO DIS cross sections provides a verification of the UV regularization scheme independence of the results in Ref. [2], since while the intermediate steps differ in FDH from CDR, the final results were shown to agree both analytically and numerically. Specifically, the numerical test verifies that the different functional form used for the UV subtraction produces equivalent results with the one used in Ref. [2].

Chapter 4

Next-to-Leading Order DIS fits to HERA data

4.1 Fundamentals

This section briefly describes the steps needed to go from the NLO cross sections Eqs. (3.19), (3.20) to their numerical evaluation and comparison to data. Section 4.1.1 discusses the solution of the BK equation to get the dipole amplitude functional form over a range of rapidity, and the numerical evaluation of the NLO DIS cross sections, including their dimensional reduction for numerical evaluation, and Sec. 4.1.2 covers the basics of the fitting methodology, along with few remaining pieces of the computation needed to be able to make comparisons to data.

4.1.1 Numerical evaluation of the NLO DIS cross sections

Here we discuss the steps that are taken in order to evaluate the NLO DIS cross sections (3.19), (3.28) numerically, and efficiently, leading to the results first presented in Article [I]. The discussion uses the notations and conventions from Sec. 3.3.

The first object we need to understand in our implementation is the scattering amplitude of the dipole, $\langle S_{01} \rangle$. After the BK evolution described in Sec. 2.4 that started from a given initial functional form, and assuming that it is not dependent on the impact parameter or the orientation of the $q\bar{q}$ dipole, it is a scalar function of two parameters: $\langle S_{01} \rangle_Y \equiv S(|\mathbf{x}_{01}|, Y)$. Once we have a numerical solution for S_{01} from the BK equation that is interpolatable both in $|\mathbf{x}_{01}|$ and Y, over both of which we will need to integrate, we may begin calculating the cross sections.

Looking at the expressions (3.19), (3.28), we see that the former has similar structure to the LO cross section (3.16), and the same dimensionality of integration phase space. The latter, on the other hand, has a larger phase space to integrate over. In order to improve the efficiency of the numerical implementation, we wish to reduce the dimension of the integration phase space as far as possible, which uses the assumed symmetry properties of S_{01} discussed above. Secondly it would be ideal to write the vector dot products in terms of scalar quantities in order to have a scalar numerical implementation.

Let us first go through the dimensional reduction that takes place for the leading order contribution, and therefore for the loop contribution as well. Originally the transverse structure of the impact factors comprises of the transverse positions of the quark and antiquark, and after a change of variables, the dipole size $\mathbf{r} \coloneqq \mathbf{x}_0 - \mathbf{x}_1$ and the impact parameter $\mathbf{b} \coloneqq (\mathbf{x}_0 + \mathbf{x}_1)/2$, which is a four-dimensional phase space. Now, since the photon splitting wavefunctions (3.16), and S_{01} are independent of the impact parameter it can be integrated over the target shape profile yielding the target size, which we take to be a constant factor $\sigma_0/2$. Furthermore, since the dipole amplitude was assumed to be agnostic of the quark-antiquark dipole orientation, the cross sections are independent of the angle of $\mathbf{r}$, which can be also integrated analytically. This means that of the transverse integrations, only the integral over $|\mathbf{r}|$ remains — the transverse phase space has been reduced from four to one dimension.

Now we want to apply similar simplifications to the qg contribution (3.28), to apply the same symmetry assumptions, and to achieve a similar reduction in the dimensionality, since this term will absolutely need it in terms of the integration efficiency. Out of the box the qg-term transverse phase space is six dimensional: integrations take place over the quark-antiquark-gluon transverse positions $\mathbf{x}_0, \mathbf{x}_1, \mathbf{x}_2$. A similar reparametrization to impact factor variables, with the addition $\mathbf{z} = \mathbf{x}_2 - \mathbf{b}$, is one way to extract an independent transverse integral that can be recognized as the target size. The scalar parametrization used in this work uses the lengths x_{01}, x_{02}, and the angle $\angle(\mathbf{x}_{01}, \mathbf{x}_{02}) =: \phi$ — with these the third dipole size is $x_{21}^2 = x_{01}^2 + x_{02}^2 - 2x_{01}x_{02}\cos\phi$. With these scalar quantities the qg impact factors are sufficiently parametrized. This leaves one free angular and one transverse planar integral that can be done analytically, given the above assumptions about the dipole amplitude. The latter yields again the target size $\sigma_0/2$. This leaves us with a scalar form of the qg contribution with a three-dimensional transverse phase space.

With the above considerations we are at the stage to implement the remaining integrations numerically. In the work for [I, II, III], this was done in C++ using the Cuba library for multidimensional numerical integration [116, 117]. Specifically Cuba provides powerful methods for Monte Carlo integration, which becomes more efficient in higher phase space dimensions than deterministic in-

tegration, as is the case with the qg contribution. The Monte Carlo methods implemented by Cuba use importance sampling and globally adaptive subdivision, which substantially improve the efficiency of the evaluation of complex high-dimensional integrals. Even with all the possible simplifications done the qg contribution is the hardest by far to compute, especially so for the transversely polarized photon, which is possibly caused by the behavior of the integrands in the aligned jet limit $z_0 \to 0, 1$.

4.1.2 Extraction of the BK evolution initial amplitude shape from data

Based on the previous section we know how to numerically compute the NLO DIS cross sections and structure functions. This can be used to extract the initial condition for the BK evolution given an ansatz functional form for the amplitude. This is done by fitting the initial condition for the BK evolution through the comparison of the calculated cross sections to experimental data. DIS total cross section measurements are typically reported either for the structure functions, or for the reduced cross section, which is defined as

$$\sigma_r(x_{\mathrm{Bj}}, Q^2, y) = F_2(x_{\mathrm{Bj}}, Q^2) - \frac{y^2}{1+(1-y)^2} F_L(x_{\mathrm{Bj}}, Q^2). \tag{4.1}$$

Here y is the so-called inelasticity of the scattering, which is fraction of energy in target rest frame the photon gains from the electron.

Now to fit the initial condition of the BK evolution to data, an ansatz for the functional form is needed, and some initial guess for its parameters. A widely used form is the McLerran-Venugopalan model for the dipole amplitude [36]:

$$S(\mathbf{x}_{ij}, Y = Y_{0,\mathrm{BK}}) = \exp\left[-\frac{\mathbf{x}_{ij}^2 Q_{s,0}^2}{4} \ln\left(\frac{1}{|\mathbf{x}_{ij}|\Lambda_{\mathrm{QCD}}} + e\right)\right], \tag{4.2}$$

where there is only one free shape parameter, $Q_{s,0}$, which is the saturation scale at the earliest rapidity to be considered in the analysis. A modified version of the McLerran-Venugopalan model is the MV-γ model, which writes

$$S(\mathbf{x}_{ij}, Y = Y_{0,\mathrm{BK}}) = \exp\left[-\frac{\left(\mathbf{x}_{ij}^2 Q_{s,0}^2\right)^\gamma}{4} \ln\left(\frac{1}{|\mathbf{x}_{ij}|\Lambda_{\mathrm{QCD}}} + e\right)\right], \tag{4.3}$$

where the new parameter γ controls the steepness of the amplitude tail at small dipole sizes. The MV-γ model has been used in leading order DIS fits [94, 95, 97], and so was chosen as the initial shape for the fits done in [**III**].

On top of the two free parameters discussed above, the running coupling scheme used in [III] introduces a third parameter — the used strong coupling constant in coordinate space is

$$\alpha_{\mathrm{s}}(\mathbf{x}_{ij}^2) = \frac{4\pi}{\beta_0 \ln\left[\left(\frac{\mu_0^2}{\Lambda_{\mathrm{QCD}}^2}\right)^{1/c} + \left(\frac{4C^2}{\mathbf{x}_{ij}^2\Lambda_{\mathrm{QCD}}^2}\right)^{1/c}\right]^c}, \tag{4.4}$$

with $\beta = (11N_{\mathrm{c}} - 2N_{\mathrm{F}})/3$ and $N_{\mathrm{F}} = 3$, $\Lambda_{\mathrm{QCD}} = 0.241$ GeV. The parameter C^2 sets the scaling of the running coupling in coordinate space, i.e. it is the scale in the connection $\alpha_{\mathrm{s}}(k^2) \sim \alpha_{\mathrm{s}}(C^2/r^2)$. Theory calculations give it the value $C^2 = e^{-2\gamma_E}$ [96, 118], however it can be used as free parameter to absorb theoretical uncertainty related to non-perturbative or higher-order contributions. In [III] we use it as a fit parameter in this functionality, as has been done in previous LO DIS analyses [95, 97]. The remaining fixed parameters c and μ_0 control the infrared freezing of the coupling, see [III] for more details.

Two schemes of selecting the dipole size going into the running coupling (4.4) were used in the analysis. First, the simple one, is the parent dipole running coupling where the coupling strength is always set by the quark-antiquark dipole size $\mathbf{r} = \mathbf{x}_{01} = \mathbf{x}_0 - \mathbf{x}_1$, i.e. $\alpha_{\mathrm{s}} = \alpha_{\mathrm{s}}(\mathbf{r}^2)$. The second coupling uses the Balitsky prescription [51] in the LO BK kernel, and the smallest dipole prescription in the resummation kernels and DIS impact factors. In the smallest dipole scheme the smallest daughter dipole sets the coupling strength

$$\alpha_{\mathrm{s,sd}}\left(\mathbf{x}_{01}^2, \mathbf{x}_{02}^2, \mathbf{x}_{21}^2\right) = \alpha_{\mathrm{s}}\left(\min\left\{\mathbf{x}_{01}^2, \mathbf{x}_{02}^2, \mathbf{x}_{21}^2\right\}\right). \tag{4.5}$$

This is motivated by the observation that the typical scale that sets the coupling strength is the largest momentum scale, which in position space corresponds to the smallest length scale. One important feature of the second scheme is that the Balitsky coupling reduces to the smallest dipole coupling in the limit that one of the daughter dipoles is much smaller than the others.

With the initial condition and running coupling schemes determined, we may proceed to make comparisons between theory calculations and data. In the process of fitting a quality function for the agreement of the theory calculation and data is needed, for which then a global minimum or maximum is searched, which ever is the extremum corresponding to the best fit. One such quality function is the χ^2, which is

$$\chi^2 = \sum_{\text{data points } i} \left(\frac{\sigma_{\mathrm{th}}(i) - \sigma_{\mathrm{exp}}(i)}{\epsilon_{\mathrm{exp}}(i)}\right)^2, \tag{4.6}$$

where the measured data set is indexed with i, $\sigma_{\mathrm{exp}}(i)$ is the measurement for the datapoint, $\sigma_{\mathrm{th}}(i)$ the theoretical calculation at the datapoint, and $\epsilon_{\mathrm{exp}}(i)$ the

total error of the measurement for datapoint i. Perfect agreement between the theory and data would give $\chi^2 = 0$, and the larger χ^2 is the worse the fit quality is. Due to the random nature of experimental errors, theory cannot account for them point by point, and so $\chi^2 = 0$ is not actually a good fit. Typically in a well predicted region the difference between the theory calculation and the measurement should be of the order of the experimental error, which gives $\chi^2 \sim N$, or as is typically reported $\chi^2/N \sim 1$, where N is the number of datapoints considered in the analysis. Then in the fitting process inputs are parametrizations of the initial condition and outputs are values of χ^2/N, for which a global minimum is found. This gives the initial condition preferred by the data. One final note is that a more sophisticated analysis could take into account the correlations of experimental errors. These are available [74] for the combined HERA data, but they were not included in the analysis done in [III].

Now that we have gone through the procedure of computing cross sections from the theory and comparing them to data, we can move on to summarize the work and results of Article [III].

4.2 Summary of Article [III]: Fitting NLO DIS cross sections to HERA data

The work done in Article [III] brings together the state-of-the-art dipole picture calculation of the next-to-leading order DIS cross sections [1, 2], and the soft gluon large logarithm resummation work done for NLO DIS in [I], covered in the Sections 3.3.1 and 3.3.2, respectively. Together these works provide a scheme for a stable perturbative expansion of the DIS cross section in the dipole picture up to next-to-leading order, which makes NLO precision comparisons to data possible for the first time. The work done in [III] uses these theory results to determine the initial condition to the BK evolution using NLO accuracy fits to the combined HERA data [74]. The theoretical uncertainty of the calculation is gauged by running fits using alternative prescriptions for the initial condition, BK evolution, and running coupling.

The fit setups are as follows. For the BK evolution we compare the enhanced BK equations: ResumBK, KCBK, and TBK, which are described in Sec. 2.4. These were used instead of the full NLO BK since it is numerically very demanding, though solvable in principle [56, 60]. For the running coupling we use a combination of Balitsky and smallest dipole prescription as the 'realistic' coupling, and compare this to the simple parent dipole coupling. We found that upgrading the simplistic lower limit $z_{2,\min} = x_{\mathrm{Bj}}/x_0$ used in [I], to $z_{2,\min} = (x_{\mathrm{Bj}}Q_0^2)/(x_0Q^2)$ was necessary in order to get a good agreement with

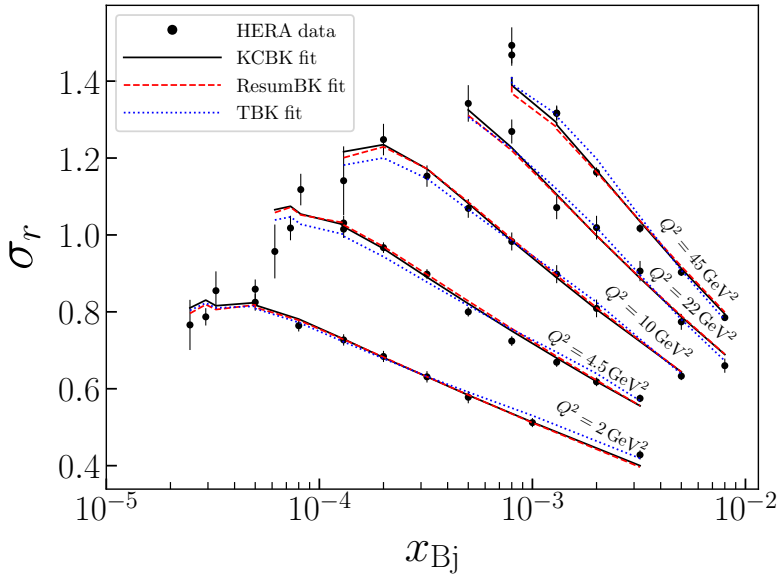

Figure 4.1: HERA data compared to reduced cross section calculated based on three fits, one with each of the enhanced BK evolutions. Balitsky + smallest dipole running coupling and $Y_{0,\mathrm{BK}} = \ln \frac{1}{0.01}$ initial scale were used. From [III].

the data. This more accurate lower limit is discussed in [I, 2, 53]. Lastly, two options for the shape of the BK evolution initial condition were considered. The key difference between the two initial condition schemes is the starting rapidity scale of the BK evolution. In the first setup we take as the initial scale a rapidity corresponding to a reasonably small x_{Bj} to begin the evolution, and in the second we take the rapidity scales of the BK evolution and the impact factors to be the same. Both schemes have their merits, details are found in [III].

The datasets used in this analysis are the combined HERA data of the H1 and ZEUS experiments for the reduced cross section [74], and the charm and bottom quark contributions to the inclusive cross sections [76, 77]. While a newer combined dataset including the data from the HERA-II run would have been available [75], the two datasets result in very comparable fits [93] at low x and moderate Q^2. We verified this with our fit setup as well, where with the fit parametrization using the KCBK equation, Bal+SD coupling, and $Y_{0,\mathrm{BK}} = \ln 1/0.01$ we found that the fit quality receives a minor change from $\chi^2/N = 1.89$ to $\chi^2/N = 1.60$.

The heavy quark dataset is used to generate a light-quark-only dataset by subtracting the charm and bottom contributions from the inclusive reduced cross section, see Sec. 4.3 for details. The motivation for this is the fact that the theory calculation was done for massless quarks, and the heavy quark contributions

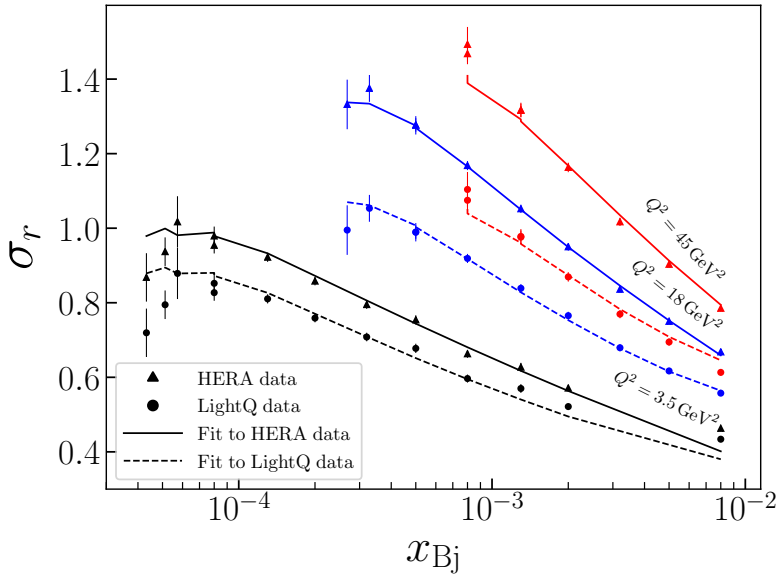

Figure 4.2: Inclusive and light-quark-only reduced cross sections calculated based on KCBK fits to the corresponding dataset compared to their respective datasets. Balitsky + smallest dipole running coupling and $Y_{0,\mathrm{BK}} = \ln \frac{1}{0.01}$ initial scale were used. From [III].

in the inclusive data are non-negligible. The generated light-quark-only reduced cross section data is then used in fits in order to gain insight into the compatibility of the massless quark cross sections and the available data.

As for the results, we find that the NLO cross sections are able to describe the HERA data very well, one comparison is shown in Fig. 4.1. Even the combined HERA data cannot properly differentiate between the enhanced BK equations or running coupling schemes: all setups describe the data comparably. Though we did see that the setups using Bal+SD running coupling on average performed slightly worse in terms of χ^2/N than those using the parent dipole coupling. Description of the light-quark-only data is found to be good as well. The Figure 4.2 shows a fit to the light-quark-only data, and a fit with the same BK equation and α_{s} prescription to the HERA data. We see that the same setup can fit both of the datasets separately, and that the fit parametrizations receive some systematic changes — this allows us to infer some general features of the data by comparing the initial amplitude shapes. Specifically, we find that the light quark data needs a slower BK evolution and a larger target size. We interpret this as the presence of a substantial non-perturbative hadronic contribution in the light-quark-only data.

To summarize, we performed the first NLO accuracy DIS fits to HERA data

to determine the initial condition for the BK evolution. We found a good agreement with the theory and data for both the HERA and light-quark-only datasets. To assess the theoretical uncertainty, we used alternative prescriptions of key pieces of the computation and found the fit results to be quite robust. Thanks to the universality of the dipole amplitude, discussed in Sec. 2.3, the dipole amplitudes determined in these fits can be used in other phenomenological calculations at NLO accuracy, as has already been done for exclusive heavy vector meson production [119].

4.3 Assessing the theory uncertainty

Any theory calculation of an observable has an intrinsic theoretical uncertainty — perfect information of the physical system cannot be had, and various assumptions or approximations are made to make theory calculations possible. In the case of the NLO DIS cross sections evaluated in this work, some of this uncertainty arises due to choices in modeling that cause finite differences that are of higher order in the perturbative expansion. Examples of effects like these are the differences between the running coupling prescriptions and the differences between the resummation techniques of the enhanced BK equations. There is also uncertainty whether the BK evolution prescription should be done in the probe or target rapidity. While the latter seems to be a more natural prescription of the evolution one still has to perform a translation between the evolution prescriptions when computing the DIS impact factors that are derived in the probe rapidity prescription. Lastly, selecting the functional form and rapidity scale for the initial condition of the BK evolution introduces uncertainty.

To gauge the magnitude of these effects we performed the data comparisons with a number of prescription combinations. The fits done in [III] compare BK resummation prescriptions, running coupling schemes, BK initial condition rapidity scales, and HERA and light-quark-only datasets. As discussed above, the BK equation and running coupling prescription effects should be somewhat small, and in [III] we demonstrated that all the used BK equation and running coupling choices were able to describe the data well.

We ran two series of fits to test the sensitivity of the cross sections to the BK evolution initial rapidity scale. In the first set the initial scale was set to $Y_{0,\mathrm{BK}} = \ln 1/0.01$, which has traditionally been considered as reasonably small x to begin the evolution. However, in the cross section computation one needs to evaluate the dipole amplitude in the range $[0, Y_{0,\mathrm{BK}}]$, which is before the evolution begins. We chose to freeze the dipole amplitudes at the initial scale in this region. In the second set the scale was taken to be $Y_{0,\mathrm{BK}} = Y_{0,\mathrm{if}} = 0$, which forgoes the need for freezing, but now the initial scale of the evolution is

at unnaturally large x. We interpret this as the usage a dipole amplitude initial form which is that of an evolved dipole amplitude of $\ln 1/0.01$ units of rapidity evolution. More details and discussion about the results are found in [III].

Lastly, some uncertainty is introduced by the fact that we are making comparisons between inclusive cross sections for massless quarks and HERA data that has notable contributions from charm and bottom quarks especially at $Q^2 \gg m_c^2$. To address this we generated a light-quark-only reduced cross section dataset from HERA data by subtracting the charm and bottom contributions manually. Since the original inclusive and heavy quark datasets are not binned in the same way, we had to perform interpolation using a separate leading order IPsat parametrized fit [93]. The experimental uncertainties of the original HERA data were left unchanged, since the proper calculation of the uncertainties would need to be done by the experimentalists. We expect that this mostly affects the χ^2/N values of the light-quark-only data fits, and not the fit parametrizations that are found which are the key interest in this analysis. The NLO cross sections were found to describe both datasets well, which was briefly discussed in the previous section, and at more detail in [III].

Effects that we could not look into extensively include the functional form of the BK initial condition, the choice of rapidity scale in the NLO dipole contribution, the mismatch between Balitsky and smallest dipole running couplings to be discussed in Sec. 4.4, and the choice of the $Y_{0,\text{if}}$ scale in the impact factors (3.28), which in principle could be taken as a fit parameter.

4.3.1 Assessing the impact of the NLO BK equation

Table 4.1: NLO cross section comparisons to HERA data using NLO BK evolution starting from the initial conditions determined in [III]. The change in χ^2/N is a measure of the difference between the NLO BK and the enhanced BK equations used in the fits. The notation (acc.↓) refers to the relaxed numerical accuracy of the calculation done here, that matches the accuracy of the numerical NLO BK evolution. These lower accuracy values are provided as a reference to gauge the magnitude of the numerical uncertainty of the NLO BK evolution.

Fit BK	α_s	$Y_{0,\text{BK}}$	χ^2/N([III])	χ^2/N (acc.↓)	χ^2/N (NLO BK)
ResumBK	parent	$\ln\frac{1}{0.01}$	2.24	2.3	2.9
KCBK	parent	$\ln\frac{1}{0.01}$	1.85	1.9	4.0
TBK	parent	$\ln\frac{1}{0.01}$	2.76	2.8	2.9
ResumBK	parent	0	1.12	1.2	1.4
KCBK	parent	0	1.24	1.3	5.5
TBK	parent	0	1.03	1.1	1.4

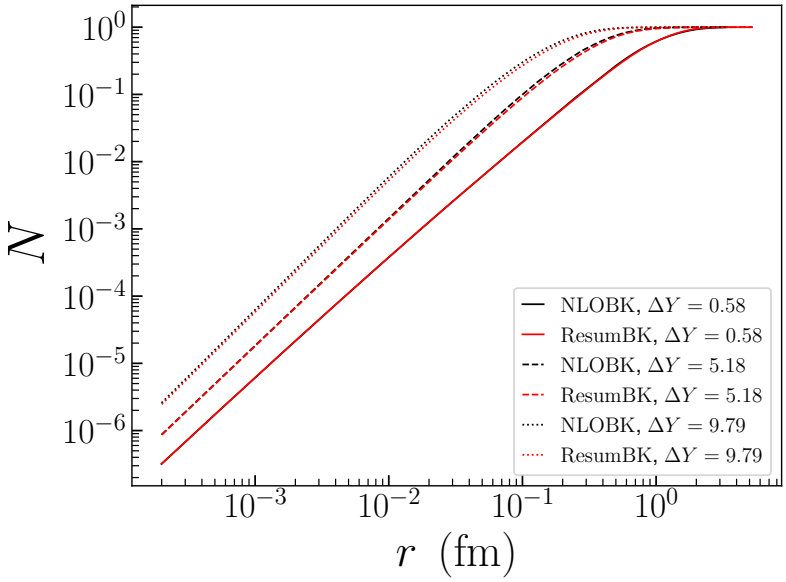

Figure 4.3: The same initial amplitude shape evolved using the ResumBK and NLO BK equations. The initial condition is from the ResumBK, parent dipole, $Y_{0,\mathrm{BK}} = \ln \frac{1}{0.01}$ fit shown in Table 4.1, determined in [III].

Aside from the above discussion is the question of how big an impact will the full next-to-leading order BK evolution [56, 58–60] have. Inclusion the full NLO BK would push the accuracy of the calculation to NLO+NLL order. To assess this, new comparisons between the used enhanced BK equations and the NLO BK including resummations [56, 60] were done for this thesis. Some of the initial shapes of the dipole amplitudes determined in [III] were evolved using the full NLO BK equation [56] and then used for computation of the cross sections for data comparison. Even though the different BK equations used in [III] are quite different[1] theoretically, they take the same functional shape as the initial condition. Thus this comparison gauges the importance of α_s^2 contributions in the NLO BK equation that are not enhanced by large transverse logarithms based on how suitable the initial conditions determined in the fits are for the NLO BK evolution. This suitability is quantified by the change in the goodness of the fit χ^2/N.

As is shown in Table 4.1, the full NLO BK equation causes a fairly small changes in the χ^2/N values of the fits. The smallest changes are seen with the

[1]ResumBK equation resums both single and double large transverse logs, KCBK equation resums double logs, and TBK equation resums the double logs, and it is formulated in the target momentum fraction picture instead of the projectile mom. fraction picture. See Article [III] and references therein for more details.

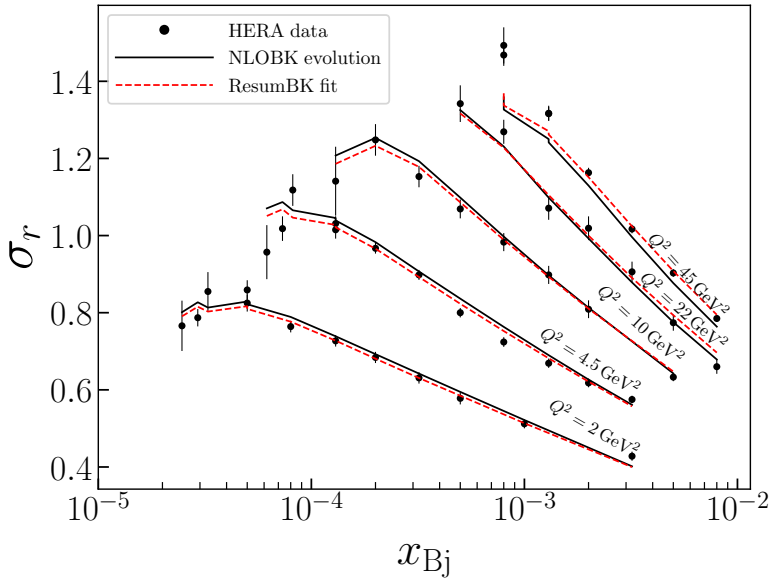

Figure 4.4: Reduced cross section computed using the NLO BK evolved dipole amplitude compared to HERA data. The initial shape is from the fit using the ResumBK equation, $Y_{0,\mathrm{BK}} = \ln \frac{1}{0.01}$ shown in Table 4.1, from [III].

initial conditions of the ResumBK and TBK equations, whereas the KCBK fit initial conditions see slightly larger changes. The ResumBK evolution is expected to approximate the NLO BK evolution the closest since it resums single transverse logs as well as the double logs resummed by the other two prescriptions. In addition to this, the specific prescription of the ResumBK equation used is numerically optimized to match the NLO BK equation with resummations as well as it can [56]. On the other hand, there is little reason to expect that the TBK evolution initial conditions would be good for this formulation of the NLO BK evolution. The TBK evolution is derived in the target momentum fraction picture, whereas the NLO BK evolution is based on the projectile momentum fraction picture. Furthermore, the TBK equation used only resums the large transverse double logs, whereas the NLO BK resums the single transverse logs as well. Thus without further study, we can only conclude that the small changes seen with the TBK equation initial conditions are unexpected.

In Fig. 4.3 is shown the same initial condition evolved using the ResumBK and NLO BK equations, and the close approximation of the NLO BK result by ResumBK is evident. We see that the NLO BK evolution is slightly faster than the ResumBK evolution, as has been seen previously [56].

This NLO BK evolved dipole amplitude is used to compute reduced cross sections for data comparison, which is shown in Fig. 4.4, together with the Re-

sumBK evolved dipole amplitude that was fitted to the data. We see that the difference between the evolution equations is larger both at larger Q^2 and at smaller x, both of which correspond to a later stage in the evolution. This difference seen between the NLO BK and ResumBK results is of the same magnitude as between the enhanced BK equations found in [III]. It is unclear if the available data would discern between the NLO BK and the enhanced BK equations.

The interpretation of this simple comparison is unfortunately muddled by the fact that the unsub scheme used in the computation cannot be consistently upgraded to NLL accuracy with a simple replacement of the evolution equation [2]. The issue is that when one replaces a LL evolved scattering amplitude with an NLL evolved amplitude in the unsub form of the cross section, one is introducing next-to-next-to-leading order (NNLO) corrections together with the NLL contribution from the NLO BK. In the sub scheme these NNLO corrections are canceled between the qg contribution and the subtraction term, producing a strict NLO result. Whereas in unsub scheme the NNLO contribution persists without further work. We note however that while this use of unsub scheme with NLO BK goes beyond strict next-to-leading order, it is the natural result of applying perturbative QCD. To elaborate, calculating all the relevant Feynman diagrams at this order produces this subset of NNLO corrections due to the nested nature of the problem [113] — both the BK evolution and the DIS impact factors get separate $O(\alpha_s)$ contributions which compound naturally, and this higher order contribution would need to be removed manually. In principle it is possible to amend unsub scheme to strict NLO+NLL order by extracting the NNLO contribution with an additional term accounting for the mismatch between the LL evolution contribution contained in the unsub qg term, and the NLL contribution arising from the NLO BK evolution. All this means that the calculations shown in Table 4.1 cannot claim strict NLO+NLL accuracy.

4.4 An outlook for theory improvements to the fits

During the work on Article [III] some theory improvement opportunities for the fits were recognized, however they were out of scope for the project. This section discusses these improvements.

- **Quark and anti-quark momentum fraction constraint**.

  In the expressions (3.19), (3.28) the quark and antiquark momentum fractions z_0 and z_1 can attain all values in their defined regime $[0, 1]$. This

implies that the invariant masses of the included $q\bar{q}$ and $q\bar{q}g$ states can become arbitrarily large:

$$M^2_{q\bar{q}} = (k_0 + k_1)^2 = \frac{\mathbf{k}_0^2}{z_0} + \frac{\mathbf{k}_1^2}{z_1} = \frac{\mathbf{k}_1^2}{z_1(1-z_1)},$$
$$M^2_{q\bar{q}g} = (k_0 + k_1 + k_2)^2 = \frac{\mathbf{k}_0^2}{z_0} + \frac{\mathbf{k}_1^2}{z_1} + \frac{\mathbf{k}_2^2}{z_2},$$

where k_0, k_1, k_2 are the four-momenta of the quark, antiquark and gluon, and z_i are their respective longitudinal momentum fractions. This means that the limits $z_i \to 0$ are problematic. The production of $q\bar{q}$ and $q\bar{q}g$ states with an invariant mass larger than the c.m.s. energy of the scattering is forbidden, so a limit of the type:

$$\frac{\mathbf{k}_1^2}{z_1(1-z_1)} < W^2$$

is needed in the case of $q\bar{q}$ production. However, the consistent implementation of a limit of this type in mixed space of transverse positions and longitudinal momentum fractions is non-trivial and left for further work. Similar analysis needs to be done for the $q\bar{q}g$ contribution as well. Some suggestions for how to do this are outlined in [2]. Traditionally cut-offs like this are not done for regular non-divergent integrals. Such a cut-off for the longitudinal momenta $k^+ > k^+_{min}$ creates effects that are power suppressed in $\frac{k^+_{min}}{W}$ [2]. These effects are in principle beyond the precision of the calculation.

- **NLO dipole term rapidity scale**.

  As is discussed in [I] and Sec. 3.3.3, at NLO the calculation of the photon splitting wavefunctions do not give guidance on what should be the rapidity scale of the dipole amplitude in the loop corrections to the $q\bar{q}$-amplitude. The most natural thing to do would be to take both the loop and the tree-level NLO corrections at the same rapidity scale, which needs to depend on the momentum fraction of the gluon, as discussed in Sec. 3.3. However, this was not possible in [I, III], since the NLO dipole contribution (3.19) had been integrated over the gluon momentum fraction [1]. In Sec. 3.3.3 a form is derived for the NLO dipole contribution, Eq. (3.42), where the momentum fraction integration has been undone and the usage of a consistent rapidity scale with the qg-contribution is possible.

- **Exact running coupling matching in the BK and impact factors**.

  With the Balitsky + smallest dipole running coupling prescription used in [III], there is a subtle mismatch between the evolution equation and the

NLO impact factor. Since this prescription uses the Balitsky coupling in the leading order BK kernel, and the smallest dipole in the BK resummation kernel and DIS impact factors, a sub-optimal finite leftover of order NNLO is produced in the factorization of the soft gluon large logarithm. Note, however, that the Balitsky prescription reduces to the smallest dipole coupling in the limit that one of the dipoles is much smaller than others, which suggests that the finite leftover is not quite as large as one would get without this limit-agreement of the couplings.

As an NNLO effect beyond our precision, the importance of this mismatch is largely unknown. Some light could be shone on this by a comparison to fits using only the smallest dipole coupling. The proposed improvement here is to perform fits using some other realistic running coupling prescriptions that can be implemented consistently in both the BK equation and the impact factors, such as the one proposed in [2]. See also Ref. [120], where an improved running coupling is developed for NLO calculations of forward hadron production in pA-collisions. However, this prescription might only be optimal for observables computed in momentum space.

- **Quark masses**.

  A substantial improvement to the theory would be the inclusion of the quark masses in the calculation of the impact factors. Recently the NLO DIS impact factor with massive quarks for the longitudinal photon has been made available [121].

  The inclusion of the quark masses has the largest effect on the impact factors at small Q^2. A comparison between LO cross sections with massive and massless quarks has been done where the effect was largest at $Q^2 \lesssim 1$ GeV^2 [29]. In this region we are not fitting extensively; the lower limit in our fits was $Q^2 \geq 0.75$ GeV^2 [**III**]. Based on this, it would seem feasible that the fit qualities of the inclusive data fits are mostly affected at small Q^2. However, the fit regime in Q contains the mass scales of the charm and bottom quarks, and especially the contribution of the charm quark to the total cross sections is considerable [76] up to the upper limit of the fit regime in Q. This suggests that there is notable uncertainty regarding the magnitude of the change to the inclusive data fits brought on by the inclusion of the quark masses in the calculation.

  In contrast, a novel possibility with the massive quark impact factors is the ability to fit heavy quark cross sections separately. In [**III**] we found evidence that the inclusive DIS cross sections contain a substantial non-perturbative contribution from the light quarks. This suggests that the

charm and bottom quark cross sections should be better perturbative quantities. The inclusion of heavy quarks in the theory calculations is an important improvement, and will hopefully shed light on the tension between the inclusive and heavy quark data fits seen at leading order [101].

- **Next-to-Leading Order BK evolution**.

  The remaining improvement for the cross section calculation to reach full NLO+NLL accuracy is to use the NLO BK equation [56, 58–60]. This, however, is a non-trivial undertaking due to the computational cost of the NLO BK equation. Even with relaxed numerical precision, the evaluation of the NLO BK evolution is slower by more than two orders of magnitude in comparison to the implementation of the ResumBK equation, which is caused by the larger phase space of the NLO BK equation. This means that a fit is mostly feasible in a small region. It might be possible to use the resummed BK equations as guidance in the determination of the fitting region, as they approximate the NLO BK fairly well [56], which was also verified with some of the fits in Sec. 4.3.

Chapter 5

Diffractive Deep Inelastic Scattering

5.1 Diffraction in particle collisions

In the 1990s, a striking discovery was made when the high-energy electron-proton collisions began at DESY-HERA. As the electrons struck the target protons with immense energy, in roughly 1 in 10 collisions the proton remained intact [18], and instead the virtual photon emitted by the electron would create a shower of hadrons. These hadron showers were seen to be separated by a substantial angle from the beam axis. Diffractive events had been seen in the deep inelastic scattering (DIS) experiment.

The observations of the diffractive DIS (DDIS) events at HERA are nigh on tantalizing for two features. First, it was surprising to see such a large proportion of large angular separation — or large rapidity[1] gap — events. The simple expectation from QCD is that such large rapidity gap events would be exponentially suppressed [122]. The second interesting feature of the HERA data is that the ratio of the diffractive to all events ($\sigma^{\text{diff}}/\sigma^{\text{tot}}$) is almost constant with varying center-of-mass energy of the virtual photon-proton system, W^2 [17]. Here the expectation was that the ratio would grow rapidly with increasing energy, which was not seen in the experiment [17].

For theoretical calculations of high-energy diffractive scattering, it is useful to state an equivalent definition of diffraction [84, 122]: a scattering at *high-energy* in which no quantum numbers are exchanged between the colliding particles is a diffractive scattering. The requirement on high-energy is due to the existence of the exponentially suppressed non-diffractive reactions, which asymptotically

[1] Pseudorapidity is used to parameterize the angle away from the beam axis: $\eta := -\ln\left[\tan\left(\frac{\theta}{2}\right)\right]$. A gap in pseudorapidity is equivalent with a gap in the angular distribution.

become negligible at high-energy. In practice this means that after the virtual photon scatters off the proton, both the target and the parton shower produced by the photon must be in color-singlet states. If they had net color-charge after the scattering, the rapidity gap would be filled by the gluon-bremsstrahlung as the target and produced system would color neutralize during hadronization.

A number of theoretical mechanisms have been constructed for the color-neutral formation of the target and produced system. They can roughly be grouped in three categories: pomeron exchange models, soft color interaction models, and dipole models. For reviews on the topic see Refs. [35, 123], and for a more pedagogical discussion Ref. [84] — note however that these do not cover some of the important saturation framework prescriptions of DDIS, which are covered in some detail in Refs. [17, 18].

The first theoretical description of diffractive DIS was postulated by Ingelman and Schlein (IS) [124] already before it was observed in experiment. In the IS model the target wavefunction contains a hadronic color-singlet component, a so-called pomeron, whose parton structure the virtual photon would probe. This picture would imply that the pomeron structure functions would be universal, which however was falsified by $p\bar{p}$ collision experiments, where hard-diffractive jet pair events were found to only constitute $1-2\%$ of all jet events, in contrast with the 10% of the events in DDIS [125]. Later pomeron exchange models consider the pomeron as a dynamically emergent object in DDIS, which carries the quantum numbers of the vacuum, and has an internal structure of quarks and gluons [84, 126].

In the soft color interaction (SCI) framework [127–129], the view is that the hard part of the process — the virtual photon scattering off a parton — is the same between DIS and DDIS. The color-neutralization then takes place via soft gluon interactions between the target remnants and the scattered off system. While SCI is considered phenomenologically successful, it has also been seen to be limited due to the ad hoc nature of the color exchange and not accounting for perturbative effects like color transparency [84]. Later work has connected the SCI model with a similar soft interaction framework, providing it with a theoretical basis that includes rescattering effects [125].

The dipole model family of DDIS descriptions has two principal branches that have connections to present day CGC framework saturation phenomenology. One is the semiclassical approach to DIS and DDIS by Hebecker et al. [33, 35], which can be considered an early precursor of the CGC framework. As such, the physical picture of the scattering from the semiclassical color-fields of the target is the same as in the case of dipole picture DIS, discussed in Sec. 2.3. Diffraction is introduced by projecting the scattered state into a color-singlet state. In the dipole picture a Fock state with a soft gluon becomes important when the final state has large invariant mass, and a leading twist approximation

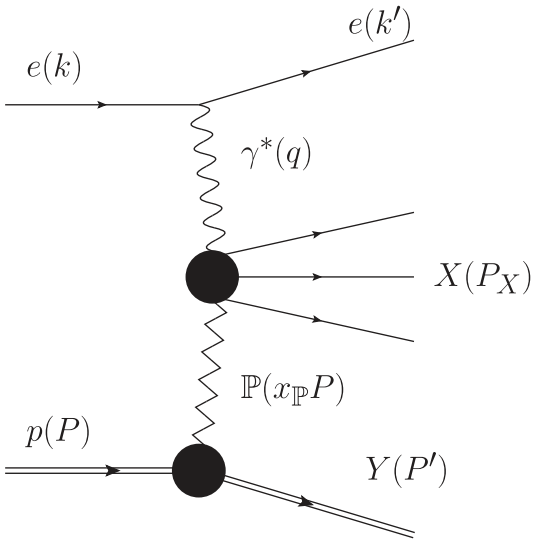

Figure 5.1: Diffractive electron-proton deep inelastic scattering. The proton can either stay intact and $Y = p$ or it can dissociate into the forward direction.

for this — power counting-wise NLO — contribution is derived in Ref. [33]. A missing piece from the framework in comparison to present day CGC is the unitarization of the dipole model, which introduces the non-linear effects that lead to saturation.

The second branch is the two-gluon exchange approximation of DDIS by Wusthoff et al. [130–133]. In this model the diffractive scattering proceeds by the virtual photon fluctuating into a $q\bar{q}$ or $q\bar{q}g$ dipole, which then scatters off the target by the exchange of two soft gluons. The $q\bar{q}g$-contribution to the cross sections is derived in a leading twist, i.e. high-Q^2, approximation. This model was combined with a phenomenological description of saturation, which described the HERA data well [30]. Another early approximative saturation approach was calculated by Munier and Shoshi [134] in the limit that the invariant mass of the diffractive system is large. The Wusthoff and Munier–Shoshi approaches were later connected by Marquet [135] in a work that gave the first CGC framework description of diffraction that builds on the virtual photon wavefunction derived by Wusthoff et al [30, 131, 132]. A good description of HERA data was found using the CGC prescription [136]. In Sec. 5.3 the $q\bar{q}g$-contribution to the diffractive structure functions is calculated in full NLO accuracy without kinematic approximations in the CGC framework for the first time for both longitudinal and transverse virtual photons.

To discuss the general kinematics of diffractive DIS, let us consider diffraction to take place as a pomeron exchange without reference to any specific mechanism

discussed above. In Fig. 5.1 is depicted a general diffractive scattering mediated by the virtual photon scattering off the pomeron, which produces the diffractive color-singlet system X, and the target evolves into the color-singlet system Y. In elastic diffraction the target proton remains intact, or in the inelastic case it dissociates into a hadron shower into the forward direction, either vanishing into the beam pipe or showing up in a forward detector. Analogously to the inclusive DIS discussed in Sec. 3.1, diffractive DIS of a virtual photon off a proton is parametrized by four quantities. We need Q^2 and x_{Bj} like with inclusive DIS, the invariant momentum transfer t, and the invariant mass of the diffractive system M_X:

$$t := -(P - P')^2 \tag{5.1}$$

$$M_X^2 := P_X^2 \tag{5.2}$$

$$x_{\mathbb{P}} := \frac{(P - P') \cdot q}{P \cdot q} = \frac{M_X^2 + Q^2 - t}{W^2 + Q^2 - M^2} \approx \frac{M_X^2 + Q^2}{W^2 + Q^2} \tag{5.3}$$

$$\beta := \frac{Q^2}{2q \cdot (P - P')} \equiv \frac{x_{\mathrm{Bj}}}{x_{\mathbb{P}}} = \frac{Q^2}{Q^2 + M_X^2 - t} \approx \frac{Q^2}{Q^2 + M_X^2}, \tag{5.4}$$

where $x_{\mathbb{P}}$ and β are alternative ways to parameterize the M_X dependence, and the momenta are as shown in Fig. 5.1. They can be given interpretation in the IS model: $x_{\mathbb{P}}$ is the fraction of proton longitudinal momentum the pomeron carries, and β is the fraction of the pomeron momentum the parton struck by the photon carries. The mass of the proton is M and $W^2 = (P + q)^2$ is the energy of the $\gamma^* p$ system.

Due to the distinct physics in the diffractive scattering, specific structure functions are defined for DDIS by writing the total diffractive cross section as [84]:

$$\sigma_{\mathrm{tot}}^{D(4)} = \frac{(2\pi)^2 \alpha_{\mathrm{em}}}{Q^2} F_2^{D(4)}(x_{\mathrm{Bj}}, Q^2, M_X, t) \tag{5.5}$$

$$= \frac{(2\pi)^2 \alpha_{\mathrm{em}}}{Q^2} \left(F_T^{D(4)}(x_{\mathrm{Bj}}, Q^2, M_X, t) + F_L^{D(4)}(x_{\mathrm{Bj}}, Q^2, M_X, t) \right), \tag{5.6}$$

where the superscript (4) refers to the dependence of the diffractive structure functions on four kinematic parameters. As experimental quantities the diffractive structure functions are t-integrated in HERA data[2], and in this case the t-independent structure functions are defined as $F_{2,L,T}^{D(3)} := F_{2,L,T}^{D(3)}(x_{\mathrm{Bj}}, Q^2, M_X)$, or using equivalent parameter choices such as $F_{2,L,T}^{D(3)}(x_{\mathbb{P}}, Q^2, \beta)$.

[2]The Electron-Ion Collider experiment [22–24] is considering measuring $|t|$-differential cross sections, which could be made possible thanks to the higher luminosity of the experiment, in comparison to HERA.

The study of diffraction in high-energy collisions gives us invaluable information on the hadronic structure of the proton or nucleus. As discussed above, there is still much to learn about the mechanism that is taking place, and about the relation between the pomeron exchange and the saturation pictures. Understanding of these details gives insight into the appropriate high-energy degrees-of-freedom of QCD. Diffraction is more sensitive to the non-linear effects of saturation than fully inclusive DIS [30, 135], which is seen explicitly at the cross section level as the dependence on the dipole amplitude squared $\sigma^{\text{diff}} \sim (1-S)^2$ in comparison to the inclusive case $\sigma^{\text{tot}} \sim \text{Re}(1-S)$. This makes diffraction an invaluable tool in the study of the Color Glass Condensate framework.

5.2 DDIS in the dipole picture at leading order

At leading order in the dipole picture the process of diffractive scattering is remarkably similar to the one of the fully inclusive deep inelastic scattering discussed in Sec. 3.2. The incoming virtual photon fluctuates into the $q\bar{q}$ dipole that then scatters eikonally from the target. Diffraction is introduced into the process by requiring that in the dipole-target scattering outgoing $q\bar{q}$-state is a color-singlet. Early LO calculations of DDIS in the dipole picture were done by Ryskin [137], and Nikolaev and Zakharov [138, 139]. It however turns out, that the LO $q\bar{q}$ contribution alone was utterly incapable of describing the diffraction observations seen at HERA — the contribution vanishes when the invariant mass of the produced system M_X is large, or equivalently when $\beta \ll 1$. This is seen in Fig. 5.2 where the $q\bar{q}$ contributions substantially fall short of the data.

The question then is, how are large invariant mass systems created in the dipole picture. To see this, we write the invariant masses of the leading $q_0\bar{q}_1$, and the next-to-leading $q_0\bar{q}_1 g_2$ Fock states:

$$M^2_{q\bar{q}} = (k_0 + k_1)^2 = \frac{\mathbf{k}_0^2}{z_0} + \frac{\mathbf{k}_1^2}{z_1},$$
$$M^2_{q\bar{q}g} = (k_0 + k_1 + k_2)^2 = \frac{\mathbf{k}_0^2}{z_0} + \frac{\mathbf{k}_1^2}{z_1} + \frac{\mathbf{k}_2^2}{z_2},$$

where the indices $0, 1, 2$ refer to the quark, antiquark and gluon, and the frame is set so that the transverse momentum of the photon is zero: $\mathbf{q} = 0$. We see that large M_X arises either if some of the partons have large transverse momentum, or if they have a low longitudinal momentum fraction $z_i \coloneqq k^+/q^+$. In fact, the production of soft gluons is enhanced over the production of soft quarks. This is seen by looking at the schematic k_i^+-dependence of the dipole formation vertex

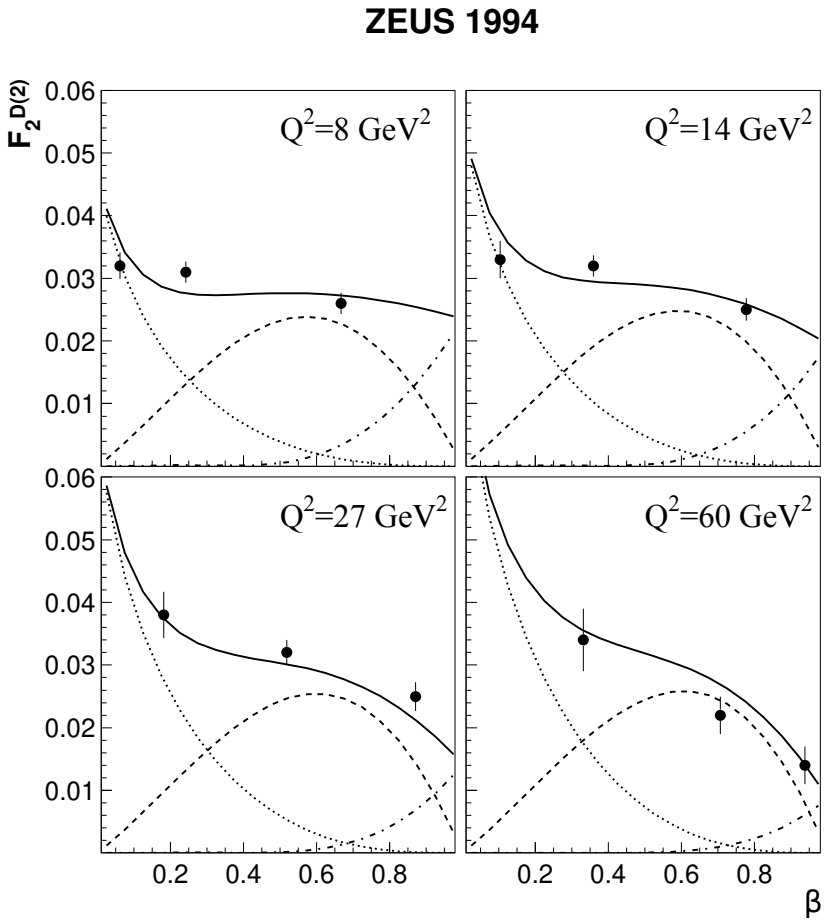

Figure 5.2: The leading contributions to the diffractive structure function F_2^D compared to HERA data [30]. **Dashed** line: $q\bar{q}$ contribution to F_T^D **dot-dashed** line: $q\bar{q}$ contribution to F_L^D **dotted** line: $q\bar{q}g$ contribution to F_T^D. Here it is explicitly seen that the power counting-wise strictly LO $q\bar{q}$-contribution completely fails to describe the data at small-β, or equivalently large-M_X. In this regime the formally NLO $q\bar{q}g$-contribution is enhanced by a large logarithm $\log(Q^2)$ or $\log(1/\beta)$, and so becomes of order $\alpha_s \log(Q^2) \sim 1$ and the main contribution to the structure function at small-β. Reprinted figure with permission from K. Golec-Biernat, and M. Wusthoff, Phys. Rev. D, 60, 114023, 1999. Copyright (1999) by the American Physical Society.

for a transversely polarized photon [86]:

$$\mathcal{V}_{\gamma_T^*(q^+,\mathbf{q})\to q(k_0^+,\mathbf{k}_0)\bar{q}(k_1^+,\mathbf{k}_1)} \sim \sqrt{k_0^+ k_1^+}\,\varepsilon_\lambda \cdot \left[\frac{\mathbf{k}_0+\mathbf{k}_1}{k_0^++k_1^+} - \frac{1-2h_0\lambda}{2}\frac{\mathbf{k}_0}{k_0^+} - \frac{1+2h_0\lambda}{2}\frac{\mathbf{k}_1}{k_1^+}\right]$$

and the gluon emission from a quark vertex [86]:

$$\mathcal{V}_{q(k_0^++k_2^+)\to q(k_0^+,\mathbf{k}_0)g(k_2^+,\mathbf{k}_2)} \sim \sqrt{(k_0^++k_2^+)k_0^+}\,\varepsilon_\lambda^* \cdot \left[\frac{\mathbf{k}_2}{k_2^+} - \frac{1+2h_0\lambda}{2}\frac{\mathbf{k}_0}{k_0^+} - \frac{1-2h_0\lambda}{2}\frac{\mathbf{k}_0+\mathbf{k}_2}{k_0^++k_2^+}\right],$$

where h_0 is the helicity of the quark, and λ that of the photon or gluon. Out of the two vertices above, we see that the gluon emission grows the fastest as $k_i^+ \to 0$. This suggests that the leading process that produces large-M_X diffractive systems is the emission of a gluon from the $q\bar{q}$ Fock state, a formally NLO contribution.

Early attempts to calculate the $q\bar{q}g$ contribution to DDIS were done by Mueller, Ryskin, and Nikolaev&Zakharov [137–140]. A breakthrough was the calculation of the $q\bar{q}g$ contribution at large-Q^2 by Wusthoff et al. [130–133, 141]. In the large-Q^2 regime the contribution is enhanced by a large logarithm $\log(Q^2)$, making the contribution formally of the order $\alpha_s \log(Q^2) \sim 1$, i.e. perturbatively leading order. Specifically, the calculation exclusively considers the contributions where the transverse virtual photon fluctuates into a quark-antiquark pair, after which a gluon is emitted. The $q\bar{q}g$-state then scatters from the proton as an effective gg-dipole by the exchange of two gluons, allowing the diffractive system and proton remnant remain color-neutral. The contribution from the longitudinal photon is not included since it is higher-twist, i.e. suppressed by one power in the Q^2-expansion [132]. This result together with a phenomenological model — the GBW model — was used with tremendous success to describe HERA data [30]. The analysis used the dipole amplitude as determined from inclusive DIS fit [29] to HERA data, which is seen as the success of saturation phenomenology.

A full NLO accuracy calculation without approximations of the $q\bar{q}g$-contribution has not been performed before, let alone the implied loop contributions. These will be discussed in more detail in Sec. 5.3. Due to this, the large-Q^2 $q\bar{q}g$-contribution derived by Wusthoff has remained among the most accurate descriptions[3] of the $q\bar{q}g$-contribution, one other being the small-β leading $\log(1/\beta)$ contribution [134]. The latter being less general, since the structure function result is to be taken at the limit $\beta \equiv 0$. In the following section we will discuss the analysis of Marquet and Kowalski et al. [135, 136], who combined the large-Q^2 and small-β results to have the most accurate dipole picture prescription of DDIS and HERA data to date.

[3]Other studies of the $q\bar{q}g$ contribution include the calculation by Hebecker et al. [33, 34], and in the small-β approximation the analyses [142–146].

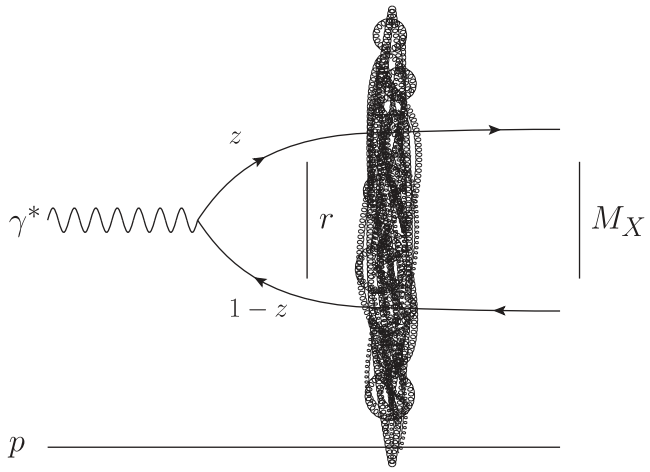

Figure 5.3: Diffractive $\gamma^* p \to Xp$ deep inelastic scattering at leading order in the dipole picture. The diffractive system with invariant mass M_X is formed by the $q\bar{q}$ dipole in the color-singlet state. The figure depicts the scattering amplitude for the process.

5.2.1 Leading contributions to the diffractive structure functions in the dipole picture

The leading order contributions of the $q\bar{q}$ dipole, depicted in Fig. 5.3, to the diffractive structure functions are [135, 136]:

$$x_{\mathbb{P}} F^D_{T,q\bar{q}}(x_{\mathbb{P}}, \beta, Q^2) = \frac{N_c Q^4}{16\pi^3 \beta} \sum_f e_f^2 \int_{z_{\min}}^{\frac{1}{2}} \mathrm{d}z\, z(1-z) \times \left[\varepsilon^2 \left(z^2 + (1-z)^2\right) \mathcal{J}_1 + m_f^2 \mathcal{J}_0\right], \tag{5.7}$$

$$x_{\mathbb{P}} F^D_{L,q\bar{q}}(x_{\mathbb{P}}, \beta, Q^2) = \frac{N_c Q^6}{4\pi^3 \beta} \sum_f e_f^2 \int_{z_{\min}}^{\frac{1}{2}} \mathrm{d}z\, z^3(1-z)^3 \mathcal{J}_0, \tag{5.8}$$

where the auxiliary function is defined as

$$\mathcal{J}_n \coloneqq \int \mathrm{d}^2\mathbf{b} \left[\int_0^\infty dr r \mathrm{K}_n(\varepsilon r) \mathrm{J}_n(\kappa r) \left(2\mathcal{N}(\mathbf{b}, r, x_{\mathbb{P}})\right)\right]^2, \tag{5.9}$$

and $\varepsilon^2 \coloneqq z(1-z)Q^2 + m_f^2$, $\kappa^2 \coloneqq z(1-z)M_X^2 - m_f^2$, $z_{\min} \coloneqq \left(1 - \sqrt{1 - 4m_f^2/M_X^2}\right)/2$. The notation was altered from the one in [135, 136] intentionally to clarify two details. First, the name of κ was changed to distinguish it from the variable k present in the $q\bar{q}g$ contribution to be discussed next, since they are not the same. Second, the substitution $\frac{\mathrm{d}\sigma_{\mathrm{dip}}}{d^2\mathbf{b}}(\mathbf{b}, r, x_{\mathbb{P}}) \equiv 2\mathcal{N}(\mathbf{b}, r, x_{\mathbb{P}})$ was made to make explicit the normalization used for the dipole amplitude.

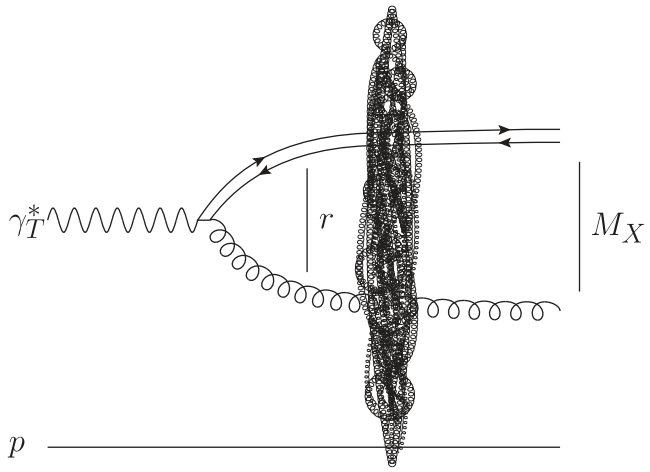

Figure 5.4: Schematic depiction of the leading logarithm large-Q^2 contribution of the transverse virtual photon splitting function to the diffractive $q\bar{q}g$ production. This becomes dominant over the LO $q\bar{q}$ production at small but finite β, or equivalently at large M_X.

Some assumptions or approximations have been made in the expressions (5.7) and (5.8). First, it has been assumed that the dipole amplitude $\mathcal{N}(\mathbf{b}, \mathbf{r}, x_{\mathbb{P}})$ does not depend on the angle $\angle(\mathbf{b}, \mathbf{r})$, which frees one to perform the angular integration of $\mathbf{r}$ in the direct and complex conjugate amplitudes. This leads to the polarization dependent forms with Bessel functions J_0 and J_1. Secondly, the t-integration has been performed under the assumption that a term in the final state transverse momentum integration can be neglected. Specifically, if one assumes that $\exp(i\boldsymbol{\Delta} \cdot (\bar{\mathbf{r}} - \mathbf{r})) \sim 1$, one gets the identity:

$$\int_{-\infty}^{0} \mathrm{d}t \int \frac{\mathrm{d}^2\boldsymbol{\Delta}}{(2\pi)^2} \delta(\boldsymbol{\Delta}^2 - |t|) e^{i\boldsymbol{\Delta}\cdot(\bar{\mathbf{b}}-\mathbf{b})} = \delta^{(2)}\left(\bar{\mathbf{b}} - \mathbf{b}\right), \tag{5.10}$$

where $\boldsymbol{\Delta} \coloneqq \mathbf{p}_0 + \mathbf{p}_1 - \mathbf{q}$ is the momentum transfer in the scattering. This assumption has been justified by stating $|\mathbf{r}| \approx 1/Q$, which is taken to be small. This leads to the elimination of one of the two impact parameter integrals over $\mathbf{b}$ and $\bar{\mathbf{b}}$ that are associated with the calculation of the squared scattering amplitude, which explains how the diffractive structure functions (5.7) and (5.8) have two dipole size $\mathbf{r}$ integrations, but only one impact parameter integral.

Moving onto the leading $\log(Q^2)$ description of the $q\bar{q}g$-contribution, illustrated schematically in Fig. 5.4. It is at leading order only relevant for the transverse structure function, as discussed in the previous section. The original $q\bar{q}g$-contribution in question [30, 132] was written in the following form in

Refs. [135, 136]:

$$x_{\mathbb{P}}F_{T,q\bar{q}g}^{D\ (\mathrm{GBW})}(x_{\mathbb{P}},\beta,Q^2) = \frac{\alpha_{\mathrm{s}}\beta}{8\pi^4}\sum_f e_f^2\int \mathrm{d}^2\mathbf{b}\int_0^{Q^2}\mathrm{d}k^2\int_\beta^1\mathrm{d}z\Bigg\{k^4\ln\frac{Q^2}{k^2}\left[\left(1-\frac{\beta}{z}\right)^2+\left(\frac{\beta}{z}\right)^2\right] \times\left[\int_0^\infty \mathrm{d}r r\mathrm{K}_2\left(\sqrt{z}kr\right)\mathrm{J}_2\left(\sqrt{1-z}kr\right)\left(2\tilde{\mathcal{N}}(\mathbf{b},r,x_{\mathbb{P}})\right)\right]^2\Bigg\} \quad (5.11)$$

where r is the size of the effective gg-dipole, k^2 is the virtuality of the final state gluon, and z is the minus-momentum fraction of the t-channel gluon with respect to the incoming gluon. The t-channel gluon is present in the two-gluon exchange and it is exchanged between the $q\bar{q}$ dipole and gluon coming from the target, which is not shown in Fig. 5.4. In this large-Q^2 leading logarithm approximation the scattering $q\bar{q}g$ state is an adjoint representation gg dipole, and so the dipole amplitude $\tilde{\mathcal{N}}(\mathbf{b},r,x_{\mathbb{P}})$ in the adjoint representation is to be used, which in the large-N_{c} limit can be written as:

$$\tilde{\mathcal{N}}(\mathbf{b},r,x_{\mathbb{P}}) = 1-\left(1-\mathcal{N}(\mathbf{b},r,x_{\mathbb{P}})\right)^2. \quad (5.12)$$

The leading $\log(1/\beta)$ $q\bar{q}g$-contribution to the structure function [134] is written as [135, 136]:

$$x_{\mathbb{P}}F_{T,q\bar{q}g}^{D\ (\mathrm{MS})}(x_{\mathbb{P}},\beta\equiv 0,Q^2) = \frac{C_{\mathrm{F}}\alpha_{\mathrm{s}}Q^2}{4\pi^4\alpha_{\mathrm{em}}}\int \mathrm{d}^2\mathbf{r}\int_0^1\mathrm{d}z\frac{1}{4\pi}\left|\Psi_{\gamma_T^*\to q\bar{q}}\right|^2\int \mathrm{d}^2\mathbf{b}A(\mathbf{r},x_{\mathbb{P}},\mathbf{b}), \quad (5.13)$$

where the wavefunction is the same as for the inclusive LO DIS (3.11), with the normalization $1/4\pi$ added to account for the different normalization used in Eq. (3.11) and Refs. [135, 136]. In this limit the dipole amplitude of the $q\bar{q}g$ tripole $\mathcal{N}^{(2)}$ factorizes into the dipole amplitudes of two dipoles of sizes $\mathbf{r}'$ and $\mathbf{r}-\mathbf{r}'$ and so the amplitude used is in the auxiliary function:

$$A(\mathbf{r},x_{\mathbb{P}},\mathbf{b}) = \int \mathrm{d}^2\mathbf{r}'\frac{\mathbf{r}^2}{\mathbf{r}'^2(\mathbf{r}-\mathbf{r}')^2}\Big[\mathcal{N}(\mathbf{r}')+\mathcal{N}(\mathbf{r}-\mathbf{r}') - \mathcal{N}(\mathbf{r})-\mathcal{N}(\mathbf{r}')\mathcal{N}(\mathbf{r}-\mathbf{r}')\Big]^2. \quad (5.14)$$

It was shown in Ref. [135] that the large-Q^2 result (5.11) does not correctly coincide with the small-β result (5.13) in the limit $\beta\to 0$ at moderate Q^2, where the small-β result is correct by definition. However, the results were shown to

agree in the validity regime $Q^2 \gg Q_s^2$ of the leading $\log(Q^2)$ result Eq. (5.11). To remedy this incompatibility, an interpolation model for $F^D_{T,q\bar{q}g}$ was constructed:

$$x_{\mathbb{P}} F^{D\ (\text{interp})}_{T,q\bar{q}g}(x_{\mathbb{P}}, \beta, Q^2) = \frac{x_{\mathbb{P}} F^{D\ (\text{GBW})}_{T,q\bar{q}}(x_{\mathbb{P}}, \beta, Q^2) \times x_{\mathbb{P}} F^{D\ (\text{MS})}_{T,q\bar{q}}(x_{\mathbb{P}}, Q^2)}{x_{\mathbb{P}} F^{D\ (\text{GBW})}_{T,q\bar{q}}(x_{\mathbb{P}}, \beta = 0, Q^2)}, \quad (5.15)$$

which leverages both results to get a better description of $F^D_{T,q\bar{q}g}$ at moderate Q^2 and small β. With this the complete model for F_2^D is

$$x_{\mathbb{P}} F^D_{2,\ \text{LO+LL}(Q^2)+\text{LL}(1/\beta)}(x_{\mathbb{P}}, \beta, Q^2) = x_{\mathbb{P}} F^D_{L,q\bar{q}}(x_{\mathbb{P}}, \beta, Q^2) + x_{\mathbb{P}} F^D_{T,q\bar{q}}(x_{\mathbb{P}}, \beta, Q^2) + x_{\mathbb{P}} F^{D\ (\text{interp})}_{T,q\bar{q}g}(x_{\mathbb{P}}, \beta, Q^2). \quad (5.16)$$

This formulation has been the most precise description of DDIS in the dipole picture, and was used to describe HERA data very well [136]. After a brief aside in the next section, in Sec. 5.3 we will discuss how this is superseded by NLO calculations.

5.2.2 Impact parameter dependence of the $q\bar{q}g$-contribution in the large-Q^2 limit

Some work is needed to get the form of the GBW structure function (5.11) starting from the original result in Ref. [30]. The intermediate steps of this calculation are not shown in the literature, which is amended here with a calculation connecting the two results.

Our starting point is the $q\bar{q}g$ contribution to F_T^D from Ref. [30][4]:

$$\begin{aligned} x_{\mathbb{P}} F^{D\ (\text{GBW})}_{T,q\bar{q}g} = {} & \frac{81\beta}{512\pi^5 B_D} \sum_f e_f^2 \frac{\alpha_s}{2\pi} \int_\beta^1 \frac{\mathrm{d}z}{z} \left[\left(1 - \frac{\beta}{z}\right)^2 + \left(\frac{\beta}{z}\right)^2 \right] \frac{z}{(1-z)^3} \\ & \times \int \frac{\mathrm{d}^2\mathbf{k}_t}{(2\pi)^2} \mathbf{k}_t^4 \ln\left(\frac{(1-z)Q^2}{\mathbf{k}_t^2}\right) \Theta((1-z)Q^2 - \mathbf{k}_t^2) \\ & \times \int \mathrm{d}^2\mathbf{r} \int \mathrm{d}^2\mathbf{r}' e^{i\mathbf{k}_t\cdot(\mathbf{r}-\mathbf{r}')} \hat{\sigma}(r, x_{\mathbb{P}}) \hat{\sigma}(r', x_{\mathbb{P}}) \left(\delta^{mn} - 2\frac{\mathbf{r}^m \mathbf{r}^n}{r^2}\right) \\ & \times \left(\delta^{mn} - 2\frac{\mathbf{r}'^m \mathbf{r}'^n}{r'^2}\right) \mathrm{K}_2\left(\sqrt{\frac{z}{1-z}} \mathbf{k}_t^2 r^2\right) \mathrm{K}_2\left(\sqrt{\frac{z}{1-z}} \mathbf{k}_t^2 r'^2\right). \end{aligned} \quad (5.17)$$

The angular integrals in the coordinate space can be performed, so we separate

[4] Italicized variables r, r', k_t are the lengths of corresponding vector quantities.

the terms with angular dependence:

$$\begin{aligned}\mathscr{I} &\coloneqq \int \mathrm{d}^2\mathbf{r} \int \mathrm{d}^2\mathbf{r}' e^{i\mathbf{k}_t\cdot(\mathbf{r}-\mathbf{r}')} \left(\delta^{mn} - 2\frac{\mathbf{r}^m\mathbf{r}^n}{r^2}\right)\left(\delta^{mn} - 2\frac{\mathbf{r}'^m\mathbf{r}'^n}{r'^2}\right) \\ &= \int \mathrm{d}^2\mathbf{r} \int \mathrm{d}^2\mathbf{r}' e^{i\mathbf{k}_t\cdot(\mathbf{r}-\mathbf{r}')} \left[4\frac{(\mathbf{r}\cdot\mathbf{r}')^2}{r^2r'^2} - 2\right] \\ &=: 2\mathscr{I}_1 - 2\mathscr{I}_2. \end{aligned} \tag{5.18}$$

We will need the identity

$$\mathrm{J}_n(z) = \frac{1}{2\pi i^n}\int_0^{2\pi} \mathrm{d}\theta \cos(n\theta) e^{iz\cos\theta}. \tag{5.19}$$

The second integral simply yields

$$\mathscr{I}_2 = (2\pi)^2 \int r\,\mathrm{d}r \mathrm{J}_0(k_t r) \int r'\,\mathrm{d}r' \mathrm{J}_0(k_t r'). \tag{5.20}$$

For $\mathscr{I}_1$ we write, parameterizing the angles as $\angle(\mathbf{r},\mathbf{k}_t) =: \theta$, $\angle(\mathbf{r}',\mathbf{k}_t) =: \phi$:

$$\mathbf{r}\cdot\mathbf{r}' = rr'\cos(\phi-\theta) = rr'(\cos\phi\cos\theta + \sin\phi\sin\theta). \tag{5.21}$$

This can be simplified with some trigonometric algebra:

$$\begin{aligned}(\cos\phi\cos\theta + \sin\phi\sin\theta)^2 &= \cos^2\phi\cos^2\theta + \sin^2\phi\sin^2\theta \\ &\quad + 2\cos\phi\cos\theta\cancelto{0}{\sin\phi\sin\theta} \\ &= \frac{1}{2}(\cos 2\theta\cos 2\phi + 1),\end{aligned}$$

where the cross-term linear in $\sin\phi$ vanishes in the integration. Finally computing the first integral, we find

$$\begin{aligned}\mathscr{I}_1 &= \int r\,\mathrm{d}r\,\mathrm{d}\theta \int r'\,\mathrm{d}r'\,\mathrm{d}\phi\, e^{ik_t r\cos\theta} e^{-ik_t r'\cos\phi} 2\frac{(\mathbf{r}\cdot\mathbf{r}')^2}{r^2r'^2} \\ &= \int r\,\mathrm{d}r\,\mathrm{d}\theta \int r'\,\mathrm{d}r'\,\mathrm{d}\phi\, e^{ik_t r\cos\theta} e^{-ik_t r'\cos\phi}(\cos 2\theta\cos 2\phi + 1) \\ &= (2\pi)^2 \int r\,\mathrm{d}r \mathrm{J}_2(k_t r) \int r'\,\mathrm{d}r' \mathrm{J}_2(k_t r') + \mathscr{I}_2. \end{aligned} \tag{5.22}$$

Thus we have found

$$\mathscr{I} = 2(2\pi)^2 \int r\,\mathrm{d}r \mathrm{J}_2(k_t r) \int r'\,\mathrm{d}r' \mathrm{J}_2(k_t r'). \tag{5.23}$$

Integrating over the angle of $\mathbf{k}_t$ and imposing[5] $k_t^2 \equiv (1-z)k^2$, we can write the GBW result (5.17) in the form:

$$x_{\mathbb{P}} F_{T,q\bar{q}g}^{D\ (\mathrm{GBW})} = \frac{81\alpha_s\beta}{512\pi^5 B_D} \sum_f e_f^2 \int_\beta^1 dz \left[\left(1-\frac{\beta}{z}\right)^2 + \left(\frac{\beta}{z}\right)^2 \right] \times \int_0^\infty \mathrm{d}k^2 k^4 \ln\left(\frac{Q^2}{k^2}\right) \Theta(Q^2-k^2) \times \left[\int r\,\mathrm{d}r \hat{\sigma}(r, x_{\mathbb{P}}) \mathrm{K}_2\left(\sqrt{z}kr\right) \mathrm{J}_2\left(\sqrt{1-z}kr\right) \right]^2 . \quad (5.24)$$

It remains to upgrade the model for the adjoint dipole amplitude to be impact parameter dependent. This begins by recognizing that in [30] the model used is [135]:

$$\tilde{\sigma}(r, x_{\mathbb{P}}) \approx \frac{N_c}{C_F} \hat{\sigma}(r, x_{\mathbb{P}}) = \frac{9}{4} \hat{\sigma}(r, x_{\mathbb{P}}), \quad (5.25)$$

where $\tilde{\sigma}$ is the adjoint amplitude of the gg dipole. In the large-Q^2 limit the $q\bar{q}$ dipole size is much smaller than the quark-gluon distance, and so the $q\bar{q}g$-tripole scattering is represented as an effective gg-dipole scattering [30]. Secondly, based on the correct replacement of the diffractive slope model introduced in [135], a factor of $1/(4\pi B_D)$ must be absorbed into the normalization of the dipole amplitudes. This is seen explicitly by assuming that the impact parameter dependence factorizes from the dipole amplitude and taking the normalized Gaussian proton impact parameter profile used in [136] $T_p(\mathbf{b}) \coloneqq \frac{1}{2\pi B_D} \exp\left(-\frac{\mathbf{b}^2}{2B_D}\right)$ and integrating:

$$\int \mathrm{d}\mathbf{b}^2 \left(T_p(\mathbf{b})\right)^2 = \int \mathrm{d}\mathbf{b}^2 \frac{1}{(2\pi B_D)^2} \exp\left(-\frac{\mathbf{b}^2}{B_D}\right) = \frac{1}{4\pi B_D}, \quad (5.26)$$

where the fact is used that the t-integration done in [136] over the full range $[-\infty, 0]$ has forced the impact parameters in the direct and conjugate amplitude to be the same $\mathbf{b}' \equiv \mathbf{b}$. Thus we essentially undo the impact parameter integration to incorporate the impact parameter dependence back into the dipole amplitude, and make the replacement

$$\frac{81}{16} \frac{\hat{\sigma}(r, x_{\mathbb{P}}) \hat{\sigma}(r', x_{\mathbb{P}})}{4\pi B_D} = \frac{\tilde{\sigma}(r, x_{\mathbb{P}}) \tilde{\sigma}(r', x_{\mathbb{P}})}{4\pi B_D} = \int \mathrm{d}^2\mathbf{b} \frac{\mathrm{d}\tilde{\sigma}}{\mathrm{d}^2\mathbf{b}}(\mathbf{b}, \mathbf{r}, x_{\mathbb{P}}) \frac{\mathrm{d}\tilde{\sigma}}{\mathrm{d}^2\mathbf{b}}(\mathbf{b}, \mathbf{r}', x_{\mathbb{P}}). \quad (5.27)$$

[5] The variable k^2 is the mean virtuality of the exchanged t-channel gluon [30, 132], defined as $k^2 \coloneqq \frac{\mathbf{k}_t^2}{1-z}$.

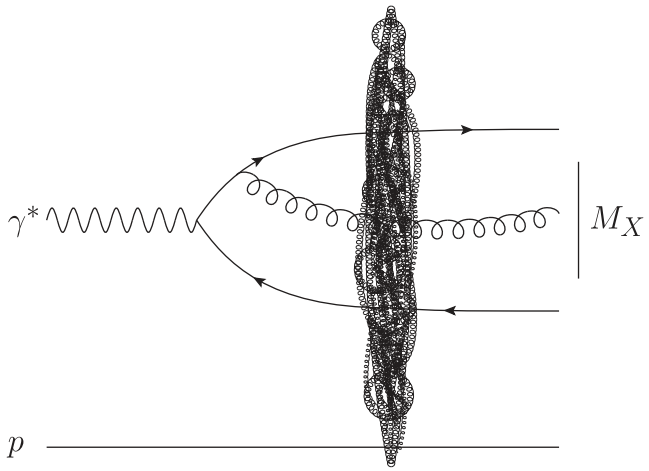

Figure 5.5: An example of a tree-level NLO diagram that contributes to the $q\bar{q}g$-contribution to F_T^D and F_L^D. A gluon is emitted before the scattering by one of the quarks, and all three partons scatter from the color-field of the target into the diffractive color-singlet final state.

With this we finally have

$$x_{\mathbb{P}} F_{T,q\bar{q}g}^{D\ (\mathrm{GBW})} = \frac{\alpha_{\mathrm{s}}\beta}{8\pi^4} \sum_f e_f^2 \int_\beta^1 dz \left[\left(1 - \frac{\beta}{z}\right)^2 + \left(\frac{\beta}{z}\right)^2 \right] \int_0^{Q^2} \mathrm{d}k^2 k^4 \ln\left(\frac{Q^2}{k^2}\right) \times \int \mathrm{d}^2\mathbf{b} \left[\int r\,\mathrm{d}r \frac{\mathrm{d}\tilde{\sigma}}{\mathrm{d}^2\mathbf{b}}(\mathbf{b}, \mathbf{r}', x_{x_{\mathbb{P}}}) \mathrm{K}_2\left(\sqrt{z}kr\right) \mathrm{J}_2\left(\sqrt{1-z}kr\right) \right]^2, \quad (5.28)$$

which is the result derived in [136] and shown in Eq. (5.11).

5.3 DDIS in the dipole picture at next-to-leading order

The next-to-leading order diffractive cross sections receive numerous contributions from both tree-level and loop diagrams, some of which are novel in comparison to NLO DIS [2]. The large-Q^2 limit $q\bar{q}g$-contribution discussed in Sec. 5.2 includes a subset of the NLO tree-level $q\bar{q}g$-contributions under the assumption of strongly ordered kinematics illustrated in Fig. 5.4. In contrast to this, in Fig. 5.5 is shown the corresponding $q\bar{q}g$-contribution in general kinematics at NLO, where there is no strong ordering of the dipole sizes. At full NLO accuracy both the transverse and longitudinal virtual photon contribute to the

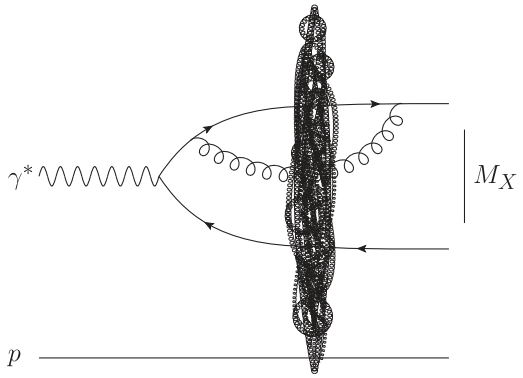

(a) Propagator loop, gluon scatters

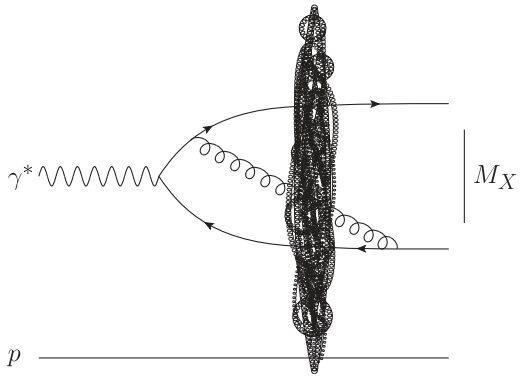

(b) Vertex loop, gluon scatters

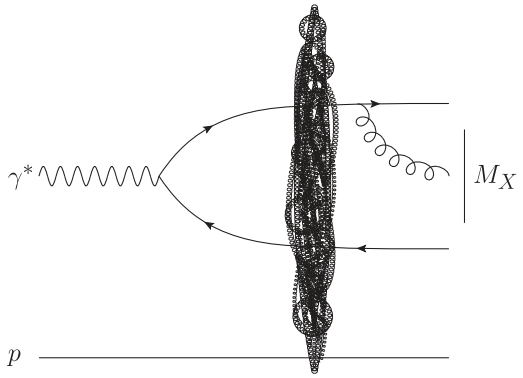

(c) Final state emission

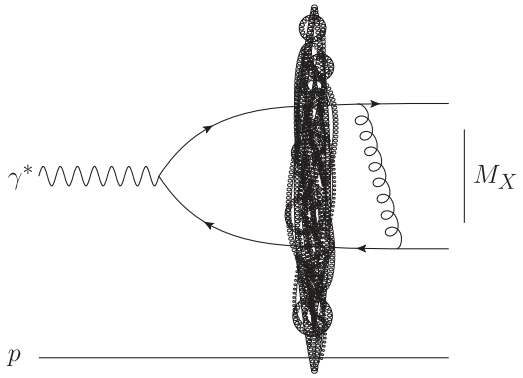

(d) Final state interaction

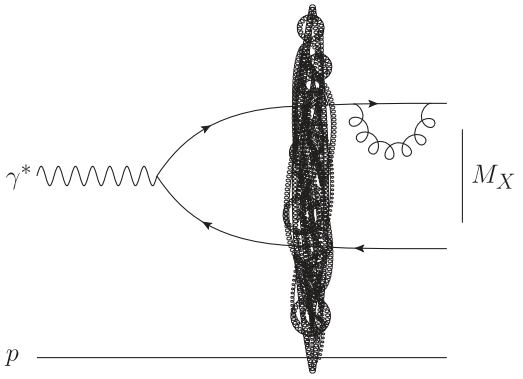

(e) Final state propagator loop

Figure 5.6: Five types of NLO corrections to DDIS that are novel in comparison to NLO DIS [1, 2]. This is not an exhaustive presentation of relevant diagrams, only one out of multiple diagrams is shown for each type.

$q\bar{q}g$-production, and additionally the transversely polarized photon can instantaneously fluctuate into the $q\bar{q}g$ Fock state, introducing new diagrams shown in Fig. 5.7. Then in the CGC framework the formed $q\bar{q}g$-state scatters eikonally from the color-field of the target so that the scattered state is a color-singlet. At NLO the emission of a gluon in the final state is possible, shown in Fig. 5.6c, but these contributions are not included in the large-Q^2 calculation [131, 132]. The full NLO dipole picture result corresponding to the large-Q^2 diffractive $q\bar{q}g$-structure function Eq. (5.11) is discussed in more detail and calculated in the next section.

On top of these tree-level contributions, the diffractive cross sections receive contributions from a variety of loop diagrams. Completely analogously to NLO DIS [1], gluon loop corrections to the quark and antiquark propagators before the scattering contribute, as well as gluon loop corrections to the $\gamma^*_{T,L}q\bar{q}$- and $\gamma^*_T q\bar{q}g$-vertices. These contributions to the virtual photon LFWFs have been calculated in Ref. [1] and should be usable as-is for the calculation of the respective corrections to the diffractive cross sections.

NLO DDIS however receives new types of loop contributions as well, shown in Fig. 5.6. These include propagator and vertex loops where the emission happens before and the absorption after the scattering from the target, shown in Figs. 5.6a and 5.6b respectively. Completely new type of contributions come from the final state, where the quark and antiquark can: emit a gluon, interact by a gluon exchange, or either can receive a propagator loop correction, shown in Figs. 5.6c, 5.6d and 5.6e. These types of diagrams, and their interferences with the above tree-level and loop diagrams familiar from NLO DIS, are novel and will need to be calculated from scratch. These contributions will also include UV divergences which must be regularized and canceled out between the diagrams. The standard method is to use dimensional regularization, which means all tree-level and loop contributions will need to be consistently calculated in D-dimensions, analogously to NLO DIS [1, 2].

5.3.1 The $q\bar{q}g$-contribution to the DDIS structure functions at NLO

As discussed above, the final state emissions are not included in the original large-Q^2 limit calculation of the $q\bar{q}g$-contribution [131, 132]. This means that the derivation of the corresponding full NLO accuracy result without approximations is fairly straightforward: only the tree-level NLO diagrams where the emitted gluon crosses both the shockwaves — in the direct and complex conjugate amplitude — and the cut contribute. An example diagram is shown in Fig. 5.5, and all at the stage of the transverse photon splitting are shown in

Fig. 5.7. For a longitudinal photon only the diagrams (a) and (b) are relevant. A further simplification is that since the final state has a definite invariant mass M_X, all of the relevant contributions — which are tree-level, and as such have no loops — become UV finite and the calculation may simply be done in $D = 4$.

In this section this calculation is done for both the longitudinally and transversely polarized virtual photon, taking advantage of the NLO virtual photon splitting functions calculated in Ref. [2]. The calculation is structured as follows. First we write down the relevant definitions to calculate the diffractive cross section for the $\gamma^* p$ scattering, after which the photon splitting wavefunction contributions are calculated in the case of DDIS. Finally we write the results for F_L^D and F_T^D in NLO accuracy, in somewhat preliminary form.

5.3.2 Definitions: the $q\bar{q}g$ diffractive cross section

The differential cross section for the virtual photon-proton scattering via the $q\bar{q}g$ Fock state is defined as:

$$\begin{aligned}\mathrm{d}\sigma^{\mathrm{NLO}}_{\gamma^*_\lambda \to q\bar{q}g \text{ singlet}} \coloneqq{}& (2q^+)2\pi\delta(p_0^+ + p_1^+ + p_2^+ - q^+) \\ &\times \frac{\mathrm{d}^3\underline{p_0}}{(2\pi)^3}\frac{\theta(p_0^+)}{2p_0^+}\frac{\mathrm{d}^3\underline{p_1}}{(2\pi)^3}\frac{\theta(p_1^+)}{2p_1^+}\frac{\mathrm{d}^3\underline{p_2}}{(2\pi)^3}\frac{\theta(p_2^+)}{2p_2^+}\sum_{q_0\bar{q}_1 g_2 \text{ F. states}}\left|\mathscr{M}^{\mathrm{NLO}}_{\gamma^*\to q\bar{q}g \text{ singlet}}\right|^2, \quad (5.29)\end{aligned}$$

where the scattering amplitude is defined with the relation:

$$\begin{aligned}\left\langle (g_2\bar{q}_1 q_0)_H\right|\left(\hat{S}_E - \mathbf{1}\right)\left|\gamma^*_\lambda(q^+,\mathbf{q};Q^2)_H\right\rangle& \\ = (2q^+)2\pi\delta(p_0^+ + p_1^+ + p_2^+ - q^+) i\mathscr{M}^{\mathrm{NLO}}_{\gamma^*\to q\bar{q}g}&, \quad (5.30)\end{aligned}$$

where H subscript refers to the Heisenberg picture dressed states [1]. The outgoing state is

$$\begin{aligned}\langle (g_2\bar{q}_1 q_0)_H| &= \sqrt{Z_g}\sqrt{Z_q}^2\left\{\langle 0|\, a(p_2^+,\mathbf{p}_2)d(p_1^+,\mathbf{p}_1)b(p_0^+,\mathbf{p}_0) + \dots\right\} \\ &= \sqrt{Z_g}\sqrt{Z_q}^2\Bigg\{\int \mathrm{d}^2\mathbf{x}_0\,\mathrm{d}^2\mathbf{x}_1\,\mathrm{d}^2\mathbf{x}_2 e^{-i\mathbf{p}_0\cdot\mathbf{x}_0}e^{-i\mathbf{p}_1\cdot\mathbf{x}_1}e^{-i\mathbf{p}_2\cdot\mathbf{x}_2} \\ &\qquad \times \langle 0|\,\tilde{a}(p_2^+,\mathbf{x}_2)\tilde{d}(p_1^+,\mathbf{x}_1)\tilde{b}(p_0^+,\mathbf{x}_0) + \dots\Bigg\}, \quad (5.31)\end{aligned}$$

where the normalization is of the order $Z_g Z_q^2 = 1 + \mathcal{O}(\alpha_\mathrm{s})$, and the correction is related to the self-energy loop corrections of the $q\bar{q}$ final state, which do not contribute to the tree-level $q\bar{q}g$-contribution and thus can be dropped in what follows. Using this, the expression (2.2) for the dressed photon wavefunction

and the commutation (2.8)–(2.10) and eikonal scattering operator (2.15)–(2.14) relations from Sec. 2.2 we find for the overlap

$$\begin{aligned}
&\langle 0|\, a(p_2^+,\cdot)d(p_1^+,\cdot)b(p_0^+,\cdot)(\hat{S}_E-\mathbf{1})b^\dagger(k_0'^+,\cdot)d^\dagger(k_1'^+,\cdot)a^\dagger(k_2'^+,\cdot)\,|0\rangle \\
&\quad=(2p_0^+)(2\pi)(2p_1^+)(2\pi)(2p_2^+)(2\pi)\delta(k_0'^+-p_0^+)\delta(k_1'^+-p_1^+)\delta(k_2'^+-p_2^+) \\
&\qquad\times\delta^{(2)}(\mathbf{x}_0'-\mathbf{x}_0)\delta^{(2)}(\mathbf{x}_1'-\mathbf{x}_1)\delta^{(2)}(\mathbf{x}_2'-\mathbf{x}_2)\delta_{h_0',h_0}\delta_{h_1',h_1}\delta_{\lambda_2',\lambda_2} \\
&\times\Big[U_F(\mathbf{x}_0')_{\beta_0'\alpha_0'}U_F^\dagger(\mathbf{x}_1')_{\alpha_1'\beta_1'}U_A(\mathbf{x}_2')_{b'a'}\delta_{\alpha_0,\beta_0'}\delta_{\alpha_1,\beta_1'}\delta_{a,b'}-\delta_{\alpha_0,\alpha_0'}\delta_{\alpha_1,\alpha_1'}\delta_{a,a'}\Big]\,, \qquad (5.32)
\end{aligned}$$

where the shorthand is defined as $b^\dagger(k_0'^+,\cdot)\coloneqq b^\dagger(k_0'^+,\mathbf{x}_0',h_0',\alpha_0')$ in the ket-state and $b(p_0^+,\cdot)\coloneqq b(p_0^+,\mathbf{x}_0,h_0,\alpha_0)$ in the bra-state. Analogously for the antiquark operators with subscript 1. For the gluon they are $a^\dagger(k_2'^+,\cdot)\coloneqq a^\dagger(k_2'^+,\mathbf{x}_2',\lambda_2',a_0')$ and $a(p_2^+,\cdot)\coloneqq a(p_2^+,\mathbf{x}_2,\lambda_2,a_0)$. With this we find for the scattering amplitude

$$\begin{aligned}
&(2q^+)2\pi\delta(p_0^+ + p_1^+ + p_2^+ - q^+)i\mathcal{M}^{\text{tree}}_{\gamma^*\to q\bar{q}g} \\
&\quad=\int \mathrm{d}^2\mathbf{x}_0\int \mathrm{d}^2\mathbf{x}_1\int \mathrm{d}^2\mathbf{x}_2\int \mathrm{d}^2\mathbf{x}_0'\int \mathrm{d}^2\mathbf{x}_1'\int \mathrm{d}^2\mathbf{x}_2' \\
&\qquad\int\frac{\mathrm{d}k_0'^+}{(2\pi)2k_0'^+}\int\frac{\mathrm{d}k_1'^+}{(2\pi)2k_1'^+}\int\frac{\mathrm{d}k_2'^+}{(2\pi)2k_2'^+}e^{-i(\mathbf{p}_0\cdot\mathbf{x}_0+\mathbf{p}_1\cdot\mathbf{x}_1+\mathbf{p}_2\cdot\mathbf{x}_2)} \\
&\qquad\times(2q^+)2\pi\delta(k_0'^+ + k_1'^+ + k_2'^+ - q^+)e^{i\frac{\mathbf{q}}{q^+}\cdot(k_0'^+\mathbf{x}_0'+k_1'^+\mathbf{x}_1'+k_2'^+\mathbf{x}_2')}t^{a_2}_{\alpha_0\alpha_1}\widetilde{\psi}_{\gamma_\lambda^*\to q_0\bar{q}_1g_2} \\
&\qquad\times\langle 0|\, a(p_2^+,\cdot)d(p_1^+,\cdot)b(p_0^+,\cdot)(\hat{S}_E-\mathbf{1})b^\dagger(k_0'^+,\cdot)d^\dagger(k_1'^+,\cdot)a^\dagger(k_2'^+,\cdot)\,|0\rangle \\
&\quad=(2q^+)2\pi\delta(p_0^+ + p_1^+ + p_2^+ - q^+)\int \mathrm{d}^2\mathbf{x}_0\int \mathrm{d}^2\mathbf{x}_1\int \mathrm{d}^2\mathbf{x}_2 \\
&\qquad e^{-i(\mathbf{p}_0\cdot\mathbf{x}_0+\mathbf{p}_1\cdot\mathbf{x}_1+\mathbf{p}_2\cdot\mathbf{x}_2)}e^{i\frac{\mathbf{q}}{q^+}\cdot(p_0^+\mathbf{x}_0+p_1^+\mathbf{x}_1+p_2^+\mathbf{x}_2)} \\
&\qquad\times\widetilde{\psi}_{\gamma_\lambda^*\to q_0\bar{q}_1g_2}\Big[U_F(\mathbf{x}_0)_{\alpha_0\alpha_0'}t^{a'}_{\alpha_0'\alpha_1'}U_F^\dagger(\mathbf{x}_1)_{\alpha_1'\alpha_1}U_A(\mathbf{x}_2)_{aa'}-t^a_{\alpha_0\alpha_1}\Big]\,, \qquad (5.33)
\end{aligned}$$

The diffractive system must be in a color-singlet state, which is enforced with a color projection operator:

$$P^{\text{singlet}}_{q\bar{q}g}\coloneqq\frac{\left(t^{a'}\right)_{\alpha_1'\alpha_0'}\left(t^a\right)_{\alpha_0\alpha_1}}{d(F)C_F}, \qquad (5.34)$$

where $d(F)\equiv N_\mathrm{c}$. The singlet projection acts on the color factor seen above as

$$\begin{aligned}
&\frac{(t^a)_{\alpha_1\alpha_0}\left(t^b\right)_{\beta_0\beta_1}}{d(F)C_F}\Big[U_F(\mathbf{x}_0)_{\alpha_0\alpha_0'}t^{a'}_{\alpha_0'\alpha_1'}U_F^\dagger(\mathbf{x}_1)_{\alpha_1'\alpha_1}U_A(\mathbf{x}_2)_{aa'}-t^a_{\alpha_0\alpha_1}\Big] \\
&\qquad=\left(t^b\right)_{\beta_0\beta_1}\left[\frac{1}{N_cC_F}\,\mathrm{tr}\left[U_F(\mathbf{x}_0)t^{a'}U_F^\dagger(\mathbf{x}_1)t^a\right]U_A(\mathbf{x}_2)_{aa'}-1\right] \\
&\qquad\qquad=\left(t^b\right)_{\beta_0\beta_1}\left[S^{(3)}_{012}-1\right], \qquad (5.35)
\end{aligned}$$

where the tripole scattering amplitude is defined

$$S_{012}^{(3)} \coloneqq \frac{1}{N_c C_F} \operatorname{tr}\left(t^a U_F(\mathbf{x}_0) t^{a'} U_F^\dagger(\mathbf{x}_1)\right) U_A(\mathbf{x}_2)_{aa'}. \tag{5.36}$$

Thus the squared amplitude of the $q\bar{q}g$ singlet production is

$$\begin{aligned}
&\sum_{q_0\bar{q}_1 g_2 \text{ F. states}} \left|\mathscr{M}^{\text{tree}}_{\gamma^*\to q\bar{q}g \text{ singlet}}\right|^2 \\
&\quad = N_c C_F \int \mathrm{d}^2\mathbf{x}_0 \int \mathrm{d}^2\mathbf{x}_1 \int \mathrm{d}^2\mathbf{x}_2 \int \mathrm{d}^2\overline{\mathbf{x}}_0 \int \mathrm{d}^2\overline{\mathbf{x}}_1 \int \mathrm{d}^2\overline{\mathbf{x}}_2 \\
&\qquad \times e^{i\mathbf{x}_{\overline{0}\,0}\left(\mathbf{p}_0 - \frac{p_0^+}{q^+}\mathbf{q}\right)} e^{i\mathbf{x}_{\overline{1}\,1}\left(\mathbf{p}_1 - \frac{p_1^+}{q^+}\mathbf{q}\right)} e^{i\mathbf{x}_{\overline{2}\,2}\left(\mathbf{p}_2 - \frac{p_2^+}{q^+}\mathbf{q}\right)} \\
&\qquad \times \sum_{h_0,h_1,\lambda_2} \left(\tilde{\psi}_{\gamma_\lambda^*\to q_{\overline{0}}\bar{q}_{\overline{1}} g_{\overline{2}}}\right)^\dagger \left(\tilde{\psi}_{\gamma_\lambda^*\to q_0\bar{q}_1 g_2}\right) \left[1 - S^{(3)\dagger}_{\overline{0}\,\overline{1}\,\overline{2}}\right] \left[1 - S^{(3)}_{012}\right],
\end{aligned} \tag{5.37}$$

where we used $\left(\left(t^b\right)_{\beta_0\beta_1}\right)^\dagger \left(t^b\right)_{\beta_0\beta_1} = \operatorname{tr}\left(t^b t^b\right) = N_c C_F$, and the imaginary part of $\mathscr{M}$ was chosen to have a positive sign, i.e. $-(S-1) = (1-S)$.

In order to specify the invariant mass M_X of the diffractive system and the invariant momentum transfer t in the scattering, it will be convenient to define a change of variables to the final state transverse momenta:

$$\mathbf{P}_i \coloneqq \mathbf{p}_i - z_i \mathbf{q}. \tag{5.38}$$

Defining $M_X^2 \coloneqq (p_0 + p_1 + p_2)^2$ and $\boldsymbol{\Delta} \coloneqq \mathbf{p}_0 + \mathbf{p}_1 + \mathbf{p}_2 - \mathbf{q}$, the shifted momenta satisfy the relations

$$\boldsymbol{\Delta} = \mathbf{P}_0 + \mathbf{P}_1 + \mathbf{P}_2, \tag{5.39}$$

$$M_X^2 = \frac{\mathbf{P}_0^2}{z_0} + \frac{\mathbf{P}_1^2}{z_1} + \frac{\mathbf{P}_2^2}{z_2} - \boldsymbol{\Delta}^2. \tag{5.40}$$

Now we are able to write the cross sections for the $q\bar{q}g$ contribution to the diffractive $\gamma^* p$ scattering, where the gluon is emitted before the interaction:

$$\begin{aligned}
\frac{\mathrm{d}\sigma_\lambda^{\text{diff } q\bar{q}g}}{\mathrm{d}M_X^2\,\mathrm{d}|t|} =& \frac{N_c C_F}{(4\pi)^2} \int \frac{\mathrm{d}^2\mathbf{P}_0}{(2\pi)^2} \int \frac{\mathrm{d}^2\mathbf{P}_1}{(2\pi)^2} \int \frac{\mathrm{d}^2\mathbf{P}_2}{(2\pi)^2} \int_0^1 \frac{\mathrm{d}z_0}{z_0} \int_0^1 \frac{\mathrm{d}z_1}{z_1} \int_0^1 \frac{\mathrm{d}z_2}{z_2} \\
&\times \delta(z_0+z_1+z_2-1)\delta(\boldsymbol{\Delta}^2 - |t|)\delta\left(\frac{\mathbf{P}_0^2}{z_0} + \frac{\mathbf{P}_1^2}{z_1} + \frac{\mathbf{P}_2^2}{z_2} - \boldsymbol{\Delta}^2 - M_X^2\right) \\
&\times \int_{\mathbf{x}_0} \int_{\mathbf{x}_1} \int_{\mathbf{x}_2} \int_{\overline{\mathbf{x}}_0} \int_{\overline{\mathbf{x}}_1} \int_{\overline{\mathbf{x}}_2} (2\pi)^6 e^{i\mathbf{x}_{\overline{0}\,0}\mathbf{P}_0} e^{i\mathbf{x}_{\overline{1}\,1}\mathbf{P}_1} e^{i\mathbf{x}_{\overline{2}\,2}\mathbf{P}_2} \\
&\times \sum_{h_0,h_1,\lambda_2} \left(\tilde{\psi}_{\gamma_\lambda^*\to q_{\overline{0}}\bar{q}_{\overline{1}} g_{\overline{2}}}\right)^\dagger \left(\tilde{\psi}_{\gamma_\lambda^*\to q_0\bar{q}_1 g_2}\right) \left[1 - S^{(3)\dagger}_{\overline{0}\,\overline{1}\,\overline{2}}\right] \left[1 - S^{(3)}_{012}\right],
\end{aligned} \tag{5.41}$$

where the shorthand $\int_{\mathbf{x}} \coloneqq \int \frac{\mathrm{d}^2\mathbf{x}}{2\pi}$ was introduced. The last big missing pieces are the squared wavefunctions.

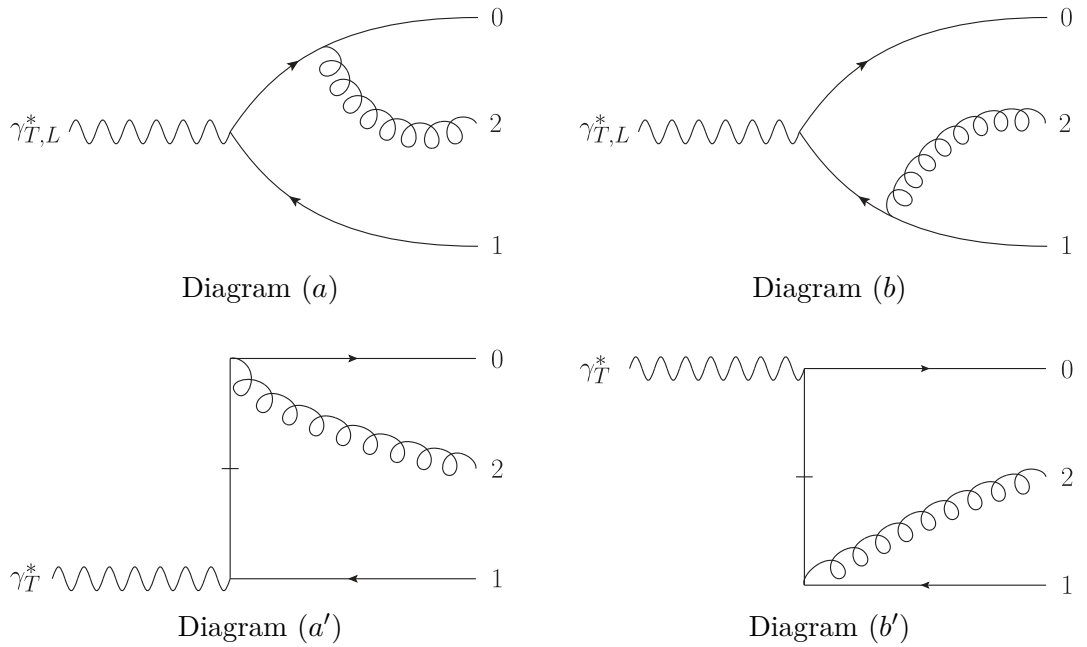

Figure 5.7: The tree-level gluon emission diagrams that contribute at NLO to the $\gamma^* \to q\bar{q}g$ wavefunction (5.43). Diagram labels follow the convention of Ref. [2].

5.3.3 Squaring the wavefunctions

The $q\bar{q}g$-contribution to the NLO DDIS cross sections we are after only gets a contribution from the $q\bar{q}g$ Fock state of the virtual photon. This means that it is relatively straightforward to derive this contribution from the virtual photon light-front wavefunctions for the $q\bar{q}g$ splitting derived in Ref. [2]. In this section the calculation of the DDIS impact factor that goes into the cross sections is shown.

We begin by writing the $D = 4$ wavefunctions for the $\gamma^* \to q\bar{q}g$ splitting [2] in the normalization scheme for the reduced wavefunctions (2.7) introduced in Sec. 2.2. For the longitudinal photon the LFWF becomes

$$\widetilde{\psi}^{\text{Tree}}_{\gamma^*_L \to q_0\bar{q}_1 g_2} = e\, e_f\, g\, \frac{i}{(2\pi)^2} \varepsilon^{j*}_{\lambda_2}\, 2Q\, \mathrm{K}_0(QX_{012})\, \sqrt{z_0}\, \sqrt{z_1}\, \delta_{h_1,-h_0}$$
$$\times \left\{ z_1 \Big[(2z_0+z_2)\delta^{jm} - i(2h_0)\, z_2\, \epsilon^{jm} \Big] \left(\frac{\mathbf{x}^m_{20}}{\mathbf{x}^2_{20}} \right) \right.$$
$$\left. - z_0 \Big[(2z_1+z_2)\delta^{jm} + i(2h_0)\, z_2\, \epsilon^{jm} \Big] \left(\frac{\mathbf{x}^m_{21}}{\mathbf{x}^2_{21}} \right) \right\}, \quad (5.42)$$

and for the transverse photon:

$$\widetilde{\psi}^{\rm Tree}_{\gamma^*_\lambda\to q_0\bar{q}_1 g_2} = \frac{e\,e_f\,g}{(2\pi)^2}\,\varepsilon^i_\lambda\,\varepsilon^{j*}_{\lambda_2}\,\sqrt{z_0}\,\sqrt{z_1}\,\delta_{h_1,-h_0}\,\frac{Q}{X_{012}}\,{\rm K}_1(QX_{012})$$
$$\times\Bigg\{z_1\Big[(2z_0{+}z_2)\delta^{jm}-i\,(2h_0)\,z_2\,\epsilon^{jm}\Big]\Big[(2z_1{-}1)\delta^{il}-i\,(2h_0)\,\epsilon^{il}\Big]\,\mathbf{x}^l_{0+2;1}\begin{pmatrix}\mathbf{x}^m_{20}\\ \mathbf{x}^2_{20}\end{pmatrix}$$
$$+\,z_0\Big[(2z_1{+}z_2)\delta^{jm}+i(2h_0)\,z_2\,\epsilon^{jm}\Big]\Big[(2z_0{-}1)\delta^{il}+i\,(2h_0)\,\epsilon^{il}\Big]\,\mathbf{x}^l_{0;1+2}\begin{pmatrix}\mathbf{x}^m_{21}\\ \mathbf{x}^2_{21}\end{pmatrix}$$
$$-\,\frac{z_0z_1z_2}{z_0{+}z_2}\Big[\delta^{ij}-i\,(2h_0)\,\epsilon^{ij}\Big]+\frac{z_0z_1z_2}{z_1{+}z_2}\Big[\delta^{ij}+i\,(2h_0)\,\epsilon^{ij}\Big]\Bigg\}, \tag{5.43}$$

where X_{012}, $\mathbf{x}_{0+2;1}$ and $\mathbf{x}_{0;1+2}$ are defined

$$X^2_{012} \coloneqq z_0z_1\mathbf{x}^2_{01}+z_0z_2\mathbf{x}^2_{02}+z_1z_2\mathbf{x}^2_{12} \tag{5.44}$$
$$\mathbf{x}_{0+2;1} \coloneqq -\frac{z_0}{z_0+z_2}\mathbf{x}_{20}+\mathbf{x}_{21}=\mathbf{x}_{01}+\frac{z_2}{z_0+z_2}\mathbf{x}_{20} \tag{5.45}$$
$$\mathbf{x}_{0;1+2} \coloneqq -\mathbf{x}_{20}+\frac{z_1}{z_1+z_2}\mathbf{x}_{21}=\mathbf{x}_{01}-\frac{z_2}{z_1+z_2}\mathbf{x}_{21}\,. \tag{5.46}$$

Following the convention of Ref. [2], in the discussion that follows the contributions of the four terms in the curly braces of Eq. (5.43) are denoted by (a), (b), (a') and (b') — visualized in Fig. 5.7.

The DDIS cross sections (5.41) depend on the squares of the above wavefunctions summed over the quantum numbers of the quark, antiquark and gluon. Specifically, the momentum fractions of the partons are conserved and therefore the same in the direct and complex conjugate amplitude, but the transverse coordinates of the particles are different: $\mathbf{x}_0,\mathbf{x}_1,\mathbf{x}_2$ in the direct amplitude, and $\overline{\mathbf{x}}_0,\overline{\mathbf{x}}_1,\overline{\mathbf{x}}_2$ in the c.c. amplitude, respectively for the quark, antiquark and gluon. Squaring the longitudinal splitting wavefunction is a straightforward affair:

$$\sum_{h_0,h_1,\lambda_2}\Big(\widetilde{\psi}^{\rm Tree}_{\gamma^*_L\to q_{\overline{0}}\bar{q}_{\overline{1}}g_{\overline{2}}}\Big)^*\,\widetilde{\psi}^{\rm Tree}_{\gamma^*_L\to q_0\bar{q}_1g_2}=$$
$$\frac{e^2e_f^2g^2}{(2\pi)^4}\left(\sum_{\lambda_2}\varepsilon^{j'}_{\lambda_2}\varepsilon^{j*}_{\lambda_2}\right)4z_0z_1Q^2{\rm K}_0\left(QX_{012}\right){\rm K}_0\left(QX_{\overline{0}\,\overline{1}\,\overline{2}}\right)\sum_{h_0,h_1}\delta_{h_1,-h_0}$$
$$\times\Bigg\{z_1\Big[(2z_0{+}z_2)\delta^{j'm'}{+}i(2h_0)z_2\epsilon^{j'm'}\Big]\begin{pmatrix}\mathbf{x}^{m'}_{2\,\overline{0}}\\ \mathbf{x}^2_{2\,\overline{0}}\end{pmatrix}-z_0\Big[(2z_1{+}z_2)\delta^{j'm'}{-}i(2h_0)z_2\epsilon^{j'm'}\Big]\begin{pmatrix}\mathbf{x}^{m'}_{2\,\overline{1}}\\ \mathbf{x}^2_{2\,\overline{1}}\end{pmatrix}\Bigg\}$$
$$\times\Bigg\{z_1\Big[(2z_0{+}z_2)\delta^{jm}-i(2h_0)z_2\epsilon^{jm}\Big]\begin{pmatrix}\mathbf{x}^m_{20}\\ \mathbf{x}^2_{20}\end{pmatrix}-z_0\Big[(2z_1{+}z_2)\delta^{jm}+i(2h_0)z_2\epsilon^{jm}\Big]\begin{pmatrix}\mathbf{x}^m_{21}\\ \mathbf{x}^2_{21}\end{pmatrix}\Bigg\}$$

$$
\begin{aligned}
&= 2\frac{\alpha_{\mathrm{em}}\alpha_{\mathrm{s}}e_f^2}{\pi^2}4z_0z_1Q^2\mathrm{K}_0\left(QX_{012}\right)\mathrm{K}_0\left(QX_{\overline{0}\,\overline{1}\,\overline{2}}\right)\Bigg\{2z_1^2\left(2z_0(z_0+z_2)+z_2^2\right)\frac{\mathbf{x}_{\overline{2}\,\overline{0}}\cdot\mathbf{x}_{20}}{\mathbf{x}_{\overline{2}\,\overline{0}}^2\mathbf{x}_{20}^2}\\
&\qquad - z_0z_1\left(2z_0(z_1+z_2)+2z_1(z_0+z_2)\right)\left(\frac{\mathbf{x}_{\overline{2}\,\overline{0}}\cdot\mathbf{x}_{21}}{\mathbf{x}_{\overline{2}\,\overline{0}}^2\mathbf{x}_{21}^2}+\frac{\mathbf{x}_{20}\cdot\mathbf{x}_{\overline{2}\,\overline{1}}}{\mathbf{x}_{20}^2\mathbf{x}_{\overline{2}\,\overline{1}}^2}\right)\\
&\qquad + 2z_0^2\left(2z_1(z_1+z_2)+z_2^2\right)\frac{\mathbf{x}_{\overline{2}\,\overline{1}}\cdot\mathbf{x}_{21}}{\mathbf{x}_{\overline{2}\,\overline{1}}^2\mathbf{x}_{21}^2}\Bigg\}\\
&= 4\frac{\alpha_{\mathrm{em}}\alpha_{\mathrm{s}}e_f^2}{\pi^2}4z_0z_1Q^2\mathrm{K}_0\left(QX_{012}\right)\mathrm{K}_0\left(QX_{\overline{0}\,\overline{1}\,\overline{2}}\right)\Bigg\{\\
&\quad z_1^2\Bigg[\left(2z_0(z_0+z_2)+z_2^2\right)\left(\frac{\mathbf{x}_{20}}{\mathbf{x}_{20}^2}\cdot\left(\frac{\mathbf{x}_{\overline{2}\,\overline{0}}}{\mathbf{x}_{\overline{2}\,\overline{0}}^2}-\frac{1}{2}\frac{\mathbf{x}_{\overline{2}\,\overline{1}}}{\mathbf{x}_{\overline{2}\,\overline{1}}^2}\right)-\frac{1}{2}\frac{\mathbf{x}_{\overline{2}\,\overline{0}}\cdot\mathbf{x}_{21}}{\mathbf{x}_{\overline{2}\,\overline{0}}^2\mathbf{x}_{21}^2}\right)\\
&\qquad + \frac{z_2^2}{2}\left(\frac{\mathbf{x}_{\overline{2}\,\overline{0}}\cdot\mathbf{x}_{21}}{\mathbf{x}_{\overline{2}\,\overline{0}}^2\mathbf{x}_{21}^2}+\frac{\mathbf{x}_{20}\cdot\mathbf{x}_{\overline{2}\,\overline{1}}}{\mathbf{x}_{20}^2\mathbf{x}_{\overline{2}\,\overline{1}}^2}\right)\Bigg]\\
&\quad + z_0^2\Bigg[\left(2z_1(z_1+z_2)+z_2^2\right)\left(\frac{\mathbf{x}_{21}}{\mathbf{x}_{21}^2}\cdot\left(\frac{\mathbf{x}_{\overline{2}\,\overline{1}}}{\mathbf{x}_{\overline{2}\,\overline{1}}^2}-\frac{1}{2}\frac{\mathbf{x}_{\overline{2}\,\overline{0}}}{\mathbf{x}_{\overline{2}\,\overline{0}}^2}\right)-\frac{1}{2}\frac{\mathbf{x}_{20}\cdot\mathbf{x}_{\overline{2}\,\overline{1}}}{\mathbf{x}_{20}^2\mathbf{x}_{\overline{2}\,\overline{1}}^2}\right)\\
&\qquad + \frac{z_2^2}{2}\left(\frac{\mathbf{x}_{\overline{2}\,\overline{0}}\cdot\mathbf{x}_{21}}{\mathbf{x}_{\overline{2}\,\overline{0}}^2\mathbf{x}_{21}^2}+\frac{\mathbf{x}_{20}\cdot\mathbf{x}_{\overline{2}\,\overline{1}}}{\mathbf{x}_{20}^2\mathbf{x}_{\overline{2}\,\overline{1}}^2}\right)\Bigg]\Bigg\}. \qquad (5.47)
\end{aligned}
$$

In the second equality — analogously to Ref. [2] — the result is rearranged to be symmetric in the exchanges of the quark and antiquark: $(z_0,\mathbf{x}_0)\leftrightarrow(z_1,\mathbf{x}_1)$ and $(z_0,\overline{\mathbf{x}}_0)\leftrightarrow(z_1,\overline{\mathbf{x}}_1)$. In the limit $\overline{\mathbf{x}}_i\to\mathbf{x}_i$, the first and second term match the corresponding results in Eqs. (84) and (85) of the NLO DIS calculation [2]. However, the same simplifications as in Ref. [2] are not seen since the particle coordinates are not the same in the direct and c.c. amplitude.

The calculation is more involved for the transversely polarized virtual photon. To begin the discussion, let us write down the different terms to be considered by referring to them by their respective diagrams (a), (b), (a') and (b') and coordinates. Specifically, let $\overline{(a)}$ denote the contribution of the first term in the complex conjugate of the wavefunction (5.43), which implies the usage of the transverse coordinates $\overline{\mathbf{x}}_i$ of the complex conjugate. Thus the square consists of the terms:

$$
\begin{aligned}
\left(\widetilde{\psi}^{\mathrm{Tree}}_{\gamma_\lambda^*\to q_{\overline{0}}\bar{q}_{\overline{1}}g_{\overline{2}}}\right)^*\widetilde{\psi}^{\mathrm{Tree}}_{\gamma_\lambda^*\to q_0\bar{q}_1g_2} &= \overline{(a)}(a)+\overline{(b)}(b)+\overline{(a)}(b)+\overline{(b)}(a)\\
&\quad+\overline{(a')}(a')+\overline{(a')}(a)+\overline{(a)}(a')+\overline{(a')}(b)+\overline{(b)}(a')\\
&\quad+\overline{(b')}(b')+\overline{(b')}(a)+\overline{(a)}(b')+\overline{(b')}(b)+\overline{(b)}(b')\\
&\quad+\overline{(a')}(b')+\overline{(b')}(a').
\end{aligned}
$$

The interference terms of the instantaneous contributions $\overline{(a')}(b')$ and $\overline{(b')}(a')$ vanish exactly since both are proportional to $\delta^{ij}\delta^{ij} - \epsilon^{ij}\epsilon^{ij} \equiv 0$, similarly as happens in the case of NLO DIS [2]. Terms containing either instantaneous contribution could have feasibly been read from the intermediate results of Ref. [2] and then replacing $\mathbf{x}_i \to \overline{\mathbf{x}}_i$ as would be appropriate. However this could not have been done for the contributions of the regular emissions (a) and (b), where the transverse structures interact non-trivially. Furthermore the squared contributions $\overline{(a)}(a)$, $\overline{(b)}(b)$ are not computed in $D = 4$ at all due to the UV regularization that is required [2]. As stated previously, UV regularization is not necessary for the real 3-parton contribution to DDIS in question here, since the invariant mass constraint does it for us.

Beginning with the contributions of the regular emissions, we have for $(a)^2$:

$$\sum_{T\,\mathrm{pol.}\,\lambda,\lambda_2}\sum_{h_0,h_1}\left(\widetilde{\psi}^{(a)}_{\gamma^*_\lambda\to q_{\overline{0}}\bar{q}_{\overline{1}}g_{\overline{2}}}\right)^*\widetilde{\psi}^{(a)}_{\gamma^*_\lambda\to q_0\bar{q}_1g_2} = \frac{e^2g^2e_f^2}{(2\pi)^4}\frac{z_0z_1Q^2}{X_{012}X_{\overline{0}\,\overline{1}\,\overline{2}}}\mathrm{K}_1(QX_{012})\mathrm{K}_1(QX_{\overline{0}\,\overline{1}\,\overline{2}})$$
$$\times z_1^2\Bigg[(4z_0(z_0+z_2)+2z_2^2)(2-4z_1(1-z_1))\left(\mathbf{x}_{\overline{0}+\overline{2};\overline{1}}\cdot\mathbf{x}_{0+2;1}\right)\frac{(\mathbf{x}_{\overline{2}\,\overline{0}}\cdot\mathbf{x}_{20})}{\mathbf{x}^2_{\overline{2}\,\overline{0}}\mathbf{x}^2_{20}}$$
$$-4z_2(2z_0+z_2)(2z_1-1)\left(\mathbf{x}_{\overline{0}+\overline{2};\overline{1}}\wedge\mathbf{x}_{0+2;1}\right)\frac{(\mathbf{x}_{\overline{2}\,\overline{0}}\wedge\mathbf{x}_{20})}{\mathbf{x}^2_{\overline{2}\,\overline{0}}\mathbf{x}^2_{20}}\Bigg], \quad (5.48)$$

and for $(b)^2$:

$$\sum_{T\,\mathrm{pol.}\,\lambda,\lambda_2}\sum_{h_0,h_1}\left(\widetilde{\psi}^{(b)}_{\gamma^*_\lambda\to q_{\overline{0}}\bar{q}_{\overline{1}}g_{\overline{2}}}\right)^*\widetilde{\psi}^{(b)}_{\gamma^*_\lambda\to q_0\bar{q}_1g_2} = \frac{e^2g^2e_f^2}{(2\pi)^4}\frac{z_0z_1Q^2}{X_{012}X_{\overline{0}\,\overline{1}\,\overline{2}}}\mathrm{K}_1(QX_{012})\mathrm{K}_1(QX_{\overline{0}\,\overline{1}\,\overline{2}})$$
$$\times z_0^2\Bigg[(4z_1(z_1+z_2)+2z_2^2)(2-4z_0(1-z_0))\left(\mathbf{x}_{\overline{0};\overline{1}+\overline{2}}\cdot\mathbf{x}_{0;1+2}\right)\frac{(\mathbf{x}_{\overline{2}\,\overline{1}}\cdot\mathbf{x}_{21})}{\mathbf{x}^2_{\overline{2}\,\overline{1}}\mathbf{x}^2_{21}}$$
$$-4z_2(2z_1+z_2)(2z_0-1)\left(\mathbf{x}_{\overline{0};\overline{1}+\overline{2}}\wedge\mathbf{x}_{0;1+2}\right)\frac{(\mathbf{x}_{\overline{2}\,\overline{1}}\wedge\mathbf{x}_{21})}{\mathbf{x}^2_{\overline{2}\,\overline{1}}\mathbf{x}^2_{21}}\Bigg], \quad (5.49)$$

and for the interference of (a) and (b):

$$\sum_{T\,\mathrm{pol.}\,\lambda,\lambda_2}\sum_{h_0,h_1}\left\{\left(\widetilde{\psi}^{(a)}_{\gamma^*_\lambda\to q_{\overline{0}}\bar{q}_{\overline{1}}g_{\overline{2}}}\right)^*\widetilde{\psi}^{(b)}_{\gamma^*_\lambda\to q_0\bar{q}_1g_2} + \left(\widetilde{\psi}^{(b)}_{\gamma^*_\lambda\to q_{\overline{0}}\bar{q}_{\overline{1}}g_{\overline{2}}}\right)^*\widetilde{\psi}^{(a)}_{\gamma^*_\lambda\to q_0\bar{q}_1g_2}\right\}$$
$$= \frac{e^2g^2e_f^2}{(2\pi)^4}\frac{z_0z_1Q^2}{X_{012}X_{\overline{0}\,\overline{1}\,\overline{2}}}\mathrm{K}_1(QX_{012})\mathrm{K}_1(QX_{\overline{0}\,\overline{1}\,\overline{2}})$$
$$\times\Bigg\{-z_0z_1\left[2z_1(z_0+z_2)+2z_0(z_1+z_2)\right]\left[2z_0(z_0+z_2)+2z_1(z_1+z_2)\right]$$

$$\times\Bigg[\Big(\mathbf{x}_{\overline{0}+\overline{2};\overline{1}}\cdot\mathbf{x}_{0;1+2}\Big)\,\frac{(\mathbf{x}_{\overline{2}\,\overline{0}}\cdot\mathbf{x}_{21})}{\mathbf{x}^2_{\overline{2}\,\overline{0}}\mathbf{x}^2_{21}}+\Big(\mathbf{x}_{\overline{0};\overline{1}+\overline{2}}\cdot\mathbf{x}_{0+2;1}\Big)\,\frac{(\mathbf{x}_{\overline{2}\,\overline{1}}\cdot\mathbf{x}_{20})}{\mathbf{x}^2_{\overline{2}\,\overline{1}}\mathbf{x}^2_{20}}\Bigg]+4z_0z_1z_2(z_0-z_1)^2$$
$$\times\Bigg[\Big(\mathbf{x}_{\overline{0}+\overline{2};\overline{1}}\wedge\mathbf{x}_{0;1+2}\Big)\frac{(\mathbf{x}_{\overline{2}\,\overline{0}}\wedge\mathbf{x}_{21})}{\mathbf{x}^2_{\overline{2}\,\overline{0}}\mathbf{x}^2_{21}}+\Big(\mathbf{x}_{\overline{0};\overline{1}+\overline{2}}\wedge\mathbf{x}_{0+2;1}\Big)\frac{(\mathbf{x}_{\overline{2}\,\overline{1}}\wedge\mathbf{x}_{20})}{\mathbf{x}^2_{\overline{2}\,\overline{1}}\mathbf{x}^2_{20}}\Bigg]\Bigg\}. \quad (5.50)$$

Next, the contributions involving instantaneous diagram (a') are

$$\sum_{T\,\mathrm{pol.}\,\lambda,\lambda_2}\sum_{h_0,h_1}\Bigg\{\Big(\widetilde{\psi}^{(a')}_{\gamma^*_\lambda\to q_{\overline{0}}\bar{q}_{\overline{1}}g_{\overline{2}}}\Big)^*\widetilde{\psi}^{(a')}_{\gamma^*_\lambda\to q_0\bar{q}_1g_2}+\Big(\widetilde{\psi}^{(a')}_{\gamma^*_\lambda\to q_{\overline{0}}\bar{q}_{\overline{1}}g_{\overline{2}}}\Big)^*\widetilde{\psi}^{(a)}_{\gamma^*_\lambda\to q_0\bar{q}_1g_2}$$
$$+\Big(\widetilde{\psi}^{(a)}_{\gamma^*_\lambda\to q_{\overline{0}}\bar{q}_{\overline{1}}g_{\overline{2}}}\Big)^*\widetilde{\psi}^{(a')}_{\gamma^*_\lambda\to q_0\bar{q}_1g_2}+\Big(\widetilde{\psi}^{(a')}_{\gamma^*_\lambda\to q_{\overline{0}}\bar{q}_{\overline{1}}g_{\overline{2}}}\Big)^*\widetilde{\psi}^{(b)}_{\gamma^*_\lambda\to q_0\bar{q}_1g_2}+\Big(\widetilde{\psi}^{(b)}_{\gamma^*_\lambda\to q_{\overline{0}}\bar{q}_{\overline{1}}g_{\overline{2}}}\Big)^*\widetilde{\psi}^{(a')}_{\gamma^*_\lambda\to q_0\bar{q}_1g_2}\Bigg\}$$
$$=\frac{e^2g^2e_f^2}{(2\pi)^4}\frac{z_0z_1Q^2}{X_{012}X_{\overline{0}\,\overline{1}\,\overline{2}}}\mathrm{K}_1(QX_{012})\mathrm{K}_1(QX_{\overline{0}\,\overline{1}\,\overline{2}})\Bigg\{4\frac{z_0^2z_1^2z_2^2}{(z_0+z_2)^2}$$
$$-4\frac{z_0^2z_1^3z_2}{z_0+z_2}\left(\frac{\mathbf{x}_{0+2;1}\cdot\mathbf{x}_{20}}{\mathbf{x}^2_{20}}+\frac{\mathbf{x}_{\overline{0}+\overline{2};\overline{1}}\cdot\mathbf{x}_{\overline{2}\,\overline{0}}}{\mathbf{x}^2_{\overline{2}\,\overline{0}}}\right)$$
$$+4\frac{z_0^2z_1(z_1+z_2)^2z_2}{z_0+z_2}\left(\frac{\mathbf{x}_{0;1+2}\cdot\mathbf{x}_{21}}{\mathbf{x}^2_{21}}+\frac{\mathbf{x}_{\overline{0};\overline{1}+\overline{2}}\cdot\mathbf{x}_{\overline{2}\,\overline{1}}}{\mathbf{x}^2_{\overline{2}\,\overline{1}}}\right)\Bigg\}. \quad (5.51)$$

The contributions involving (b') are

$$\sum_{T\,\mathrm{pol.}\,\lambda,\lambda_2}\sum_{h_0,h_1}\Bigg\{\Big(\widetilde{\psi}^{(b')}_{\gamma^*_\lambda\to q_{\overline{0}}\bar{q}_{\overline{1}}g_{\overline{2}}}\Big)^*\widetilde{\psi}^{(b')}_{\gamma^*_\lambda\to q_0\bar{q}_1g_2}+\Big(\widetilde{\psi}^{(b')}_{\gamma^*_\lambda\to q_{\overline{0}}\bar{q}_{\overline{1}}g_{\overline{2}}}\Big)^*\widetilde{\psi}^{(a)}_{\gamma^*_\lambda\to q_0\bar{q}_1g_2}$$
$$+\Big(\widetilde{\psi}^{(a)}_{\gamma^*_\lambda\to q_{\overline{0}}\bar{q}_{\overline{1}}g_{\overline{2}}}\Big)^*\widetilde{\psi}^{(b')}_{\gamma^*_\lambda\to q_0\bar{q}_1g_2}+\Big(\widetilde{\psi}^{(b')}_{\gamma^*_\lambda\to q_{\overline{0}}\bar{q}_{\overline{1}}g_{\overline{2}}}\Big)^*\widetilde{\psi}^{(b)}_{\gamma^*_\lambda\to q_0\bar{q}_1g_2}+\Big(\widetilde{\psi}^{(b)}_{\gamma^*_\lambda\to q_{\overline{0}}\bar{q}_{\overline{1}}g_{\overline{2}}}\Big)^*\widetilde{\psi}^{(b')}_{\gamma^*_\lambda\to q_0\bar{q}_1g_2}\Bigg\}$$
$$=\frac{e^2g^2e_f^2}{(2\pi)^4}\frac{z_0z_1Q^2}{X_{012}X_{\overline{0}\,\overline{1}\,\overline{2}}}\mathrm{K}_1(QX_{012})\mathrm{K}_1(QX_{\overline{0}\,\overline{1}\,\overline{2}})\Bigg\{4\frac{z_0^2z_1^2z_2^2}{(z_1+z_2)^2}$$
$$-4\frac{z_0z_1^2(z_0+z_2)^2z_2}{z_1+z_2}\left(\frac{\mathbf{x}_{0+2;1}\cdot\mathbf{x}_{20}}{\mathbf{x}^2_{20}}+\frac{\mathbf{x}_{\overline{0}+\overline{2};\overline{1}}\cdot\mathbf{x}_{\overline{2}\,\overline{0}}}{\mathbf{x}^2_{\overline{2}\,\overline{0}}}\right)$$
$$+4\frac{z_0^3z_1^2z_2}{z_1+z_2}\left(\frac{\mathbf{x}_{0;1+2}\cdot\mathbf{x}_{21}}{\mathbf{x}^2_{21}}+\frac{\mathbf{x}_{\overline{0};\overline{1}+\overline{2}}\cdot\mathbf{x}_{\overline{2}\,\overline{1}}}{\mathbf{x}^2_{\overline{2}\,\overline{1}}}\right)\Bigg\}. \quad (5.52)$$

In the above expressions, the exterior products are defined as

$$\mathbf{x}\wedge\mathbf{y}\coloneqq\epsilon^{ij}\mathbf{x}^i\mathbf{y}^j. \quad (5.53)$$

The products of two exterior products can be simplified with the identity[6] for

[6]The determinant form can be used as a mnemonic since in that case the indices have a row-column pattern. The identity generalizes to higher dimensions.

the product of two Levi-Civita symbols:

$$\epsilon^{ij}\epsilon^{mn} = \begin{vmatrix} \delta^{im} & \delta^{in} \\ \delta^{jm} & \delta^{jn} \end{vmatrix} = \delta^{im}\delta^{jn} - \delta^{in}\delta^{jm}. \tag{5.54}$$

Collecting the results, the squared splitting function for the transverse photon becomes

$$\begin{aligned} \frac{1}{2} \sum_{T\,\text{pol.}} \sum_{\lambda,\lambda_2} \sum_{h_0,h_1} & \left(\widetilde{\psi}^{\text{Tree}}_{\gamma^*_\lambda \to q_{\overline{0}} \bar{q}_{\overline{1}} g_{\overline{2}}}\right)^* \widetilde{\psi}^{\text{Tree}}_{\gamma^*_\lambda \to q_0 \bar{q}_1 g_2} \\ &= \frac{1}{2} \frac{\alpha_{\text{em}} \alpha_{\text{s}} e_f^2}{\pi^2} z_0 z_1 \frac{Q^2}{X_{012} X_{\overline{0}\,\overline{1}\,\overline{2}}} \mathrm{K}_1\left(QX_{012}\right) \mathrm{K}_1\left(QX_{\overline{0}\,\overline{1}\,\overline{2}}\right) \\ &\qquad \times 4\left\{\Upsilon^{(|a|^2)}_{\text{reg.}} + \Upsilon^{(|b|^2)}_{\text{reg.}} + \Upsilon^{(a')}_{\text{inst.}} + \Upsilon^{(b')}_{\text{inst.}} + \Upsilon^{(ab)}_{\text{interf.}}\right\}, \end{aligned} \tag{5.55}$$

where

$$\begin{aligned} \Upsilon^{(|a|^2)}_{\text{reg.}} =& z_1^2 \Bigg[(2z_0(z_0+z_2) + z_2^2)(1 - 2z_1(1-z_1)) \left(\mathbf{x}_{\overline{0}+\overline{2};\overline{1}} \cdot \mathbf{x}_{0+2;1}\right) \frac{\left(\mathbf{x}_{\overline{2}\,\overline{0}} \cdot \mathbf{x}_{20}\right)}{\mathbf{x}^2_{\overline{2}\,\overline{0}} \mathbf{x}^2_{20}} \\ &- z_2(2z_0+z_2)(2z_1-1) \left(\mathbf{x}_{\overline{0}+\overline{2};\overline{1}} \wedge \mathbf{x}_{0+2;1}\right) \frac{\left(\mathbf{x}_{\overline{2}\,\overline{0}} \wedge \mathbf{x}_{20}\right)}{\mathbf{x}^2_{\overline{2}\,\overline{0}} \mathbf{x}^2_{20}} \Bigg] \end{aligned} \tag{5.56}$$

$$\begin{aligned} \Upsilon^{(|b|^2)}_{\text{reg.}} =& z_0^2 \Bigg[(2z_1(z_1+z_2) + z_2^2)(1 - 2z_0(1-z_0)) \left(\mathbf{x}_{\overline{0};\overline{1}+\overline{2}} \cdot \mathbf{x}_{0;1+2}\right) \frac{\left(\mathbf{x}_{\overline{2}\,\overline{1}} \cdot \mathbf{x}_{21}\right)}{\mathbf{x}^2_{\overline{2}\,\overline{1}} \mathbf{x}^2_{21}} \\ &- z_2(2z_1+z_2)(2z_0-1) \left(\mathbf{x}_{\overline{0};\overline{1}+\overline{2}} \wedge \mathbf{x}_{0;1+2}\right) \frac{\left(\mathbf{x}_{\overline{2}\,\overline{1}} \wedge \mathbf{x}_{21}\right)}{\mathbf{x}^2_{\overline{2}\,\overline{1}} \mathbf{x}^2_{21}} \Bigg] \end{aligned} \tag{5.57}$$

$$\begin{aligned} \Upsilon^{(a')}_{\text{inst.}} =& \frac{z_0^2 z_1^2 z_2^2}{(z_0+z_2)^2} - \frac{z_0^2 z_1^3 z_2}{z_0+z_2} \left(\frac{\mathbf{x}_{0+2;1} \cdot \mathbf{x}_{20}}{\mathbf{x}^2_{20}} + \frac{\mathbf{x}_{\overline{0}+\overline{2};\overline{1}} \cdot \mathbf{x}_{\overline{2}\,\overline{0}}}{\mathbf{x}^2_{\overline{2}\,\overline{0}}}\right) \\ &+ \frac{z_0^2 z_1 (z_1+z_2)^2 z_2}{z_0+z_2} \left(\frac{\mathbf{x}_{0;1+2} \cdot \mathbf{x}_{21}}{\mathbf{x}^2_{21}} + \frac{\mathbf{x}_{\overline{0};\overline{1}+\overline{2}} \cdot \mathbf{x}_{\overline{2}\,\overline{1}}}{\mathbf{x}^2_{\overline{2}\,\overline{1}}}\right) \end{aligned} \tag{5.58}$$

$$\begin{aligned} \Upsilon^{(b')}_{\text{inst.}} =& \frac{z_0^2 z_1^2 z_2^2}{(z_1+z_2)^2} - \frac{z_0 z_1^2 (z_0+z_2)^2 z_2}{z_1+z_2} \left(\frac{\mathbf{x}_{0+2;1} \cdot \mathbf{x}_{20}}{\mathbf{x}^2_{20}} + \frac{\mathbf{x}_{\overline{0}+\overline{2};\overline{1}} \cdot \mathbf{x}_{\overline{2}\,\overline{0}}}{\mathbf{x}^2_{\overline{2}\,\overline{0}}}\right) \\ &+ \frac{z_0^3 z_1^2 z_2}{z_1+z_2} \left(\frac{\mathbf{x}_{0;1+2} \cdot \mathbf{x}_{21}}{\mathbf{x}^2_{21}} + \frac{\mathbf{x}_{\overline{0};\overline{1}+\overline{2}} \cdot \mathbf{x}_{\overline{2}\,\overline{1}}}{\mathbf{x}^2_{\overline{2}\,\overline{1}}}\right) \end{aligned} \tag{5.59}$$

$$\begin{aligned} \Upsilon^{(ab)}_{\text{interf.}} =& - z_0 z_1 \left[z_1(z_0+z_2) + z_0(z_1+z_2)\right] \left[z_0(z_0+z_2) + z_1(z_1+z_2)\right] \\ &\times \left[\left(\mathbf{x}_{\overline{0}+\overline{2};\overline{1}} \cdot \mathbf{x}_{0;1+2}\right) \frac{\left(\mathbf{x}_{\overline{2}\,\overline{0}} \cdot \mathbf{x}_{21}\right)}{\mathbf{x}^2_{\overline{2}\,\overline{0}} \mathbf{x}^2_{21}} + \left(\mathbf{x}_{\overline{0};\overline{1}+\overline{2}} \cdot \mathbf{x}_{0+2;1}\right) \frac{\left(\mathbf{x}_{\overline{2}\,\overline{1}} \cdot \mathbf{x}_{20}\right)}{\mathbf{x}^2_{\overline{2}\,\overline{1}} \mathbf{x}^2_{20}}\right] \\ &+ z_0 z_1 z_2 (z_0 - z_1)^2 \end{aligned}$$

$$\times \left[\left(\mathbf{x}_{\overline{0}+\overline{2};\overline{1}} \wedge \mathbf{x}_{0;1+2} \right) \frac{(\mathbf{x}_{\overline{2}\,\overline{0}} \wedge \mathbf{x}_{21})}{\mathbf{x}^2_{\overline{2}\,\overline{0}} \mathbf{x}^2_{21}} + \left(\mathbf{x}_{\overline{0};\overline{1}+\overline{2}} \wedge \mathbf{x}_{0+2;1} \right) \frac{(\mathbf{x}_{\overline{2}\,\overline{1}} \wedge \mathbf{x}_{20})}{\mathbf{x}^2_{\overline{2}\,\overline{1}} \mathbf{x}^2_{20}} \right]. \quad (5.60)$$

The wedge products in the interference contribution can be expanded as

$$\begin{aligned}
&\left(\mathbf{x}_{\overline{0}+\overline{2};\overline{1}} \wedge \mathbf{x}_{0;1+2} \right) \frac{(\mathbf{x}_{\overline{2}\,\overline{0}} \wedge \mathbf{x}_{21})}{\mathbf{x}^2_{\overline{2}\,\overline{0}} \mathbf{x}^2_{21}} + \left(\mathbf{x}_{\overline{0};\overline{1}+\overline{2}} \wedge \mathbf{x}_{0+2;1} \right) \frac{(\mathbf{x}_{\overline{2}\,\overline{1}} \wedge \mathbf{x}_{20})}{\mathbf{x}^2_{\overline{2}\,\overline{1}} \mathbf{x}^2_{20}} \\
&\quad = \left(\frac{z_0}{z_0+z_2} \mathbf{x}_{\overline{2}\,\overline{0}} \wedge \mathbf{x}_{20} + \frac{z_1}{z_1+z_2} \mathbf{x}_{\overline{2}\,\overline{1}} \wedge \mathbf{x}_{21} \right) \left(\frac{(\mathbf{x}_{\overline{2}\,\overline{0}} \wedge \mathbf{x}_{21})}{\mathbf{x}^2_{\overline{2}\,\overline{0}} \mathbf{x}^2_{21}} + \frac{(\mathbf{x}_{\overline{2}\,\overline{1}} \wedge \mathbf{x}_{20})}{\mathbf{x}^2_{\overline{2}\,\overline{1}} \mathbf{x}^2_{20}} \right) \\
&\qquad - \left(\frac{z_0 z_1}{(z_0+z_2)(z_1+z_2)} (\mathbf{x}_{\overline{2}\,\overline{0}} \wedge \mathbf{x}_{21}) + (\mathbf{x}_{\overline{2}\,\overline{1}} \wedge \mathbf{x}_{20}) \right) \frac{(\mathbf{x}_{\overline{2}\,\overline{0}} \wedge \mathbf{x}_{21})}{\mathbf{x}^2_{\overline{2}\,\overline{0}} \mathbf{x}^2_{21}} \\
&\qquad - \left(\frac{z_0 z_1}{(z_0+z_2)(z_1+z_2)} (\mathbf{x}_{\overline{2}\,\overline{1}} \wedge \mathbf{x}_{20}) + (\mathbf{x}_{\overline{2}\,\overline{0}} \wedge \mathbf{x}_{21}) \right) \frac{(\mathbf{x}_{\overline{2}\,\overline{1}} \wedge \mathbf{x}_{20})}{\mathbf{x}^2_{\overline{2}\,\overline{1}} \mathbf{x}^2_{20}} \qquad (5.61) \\
&\quad \xrightarrow{\overline{0},\overline{1},\overline{2} \to 0,1,2} \frac{2z_2}{(z_0+z_2)(z_1+z_2)} \frac{(\mathbf{x}_{20} \wedge \mathbf{x}_{21})^2}{\mathbf{x}^2_{20} \mathbf{x}^2_{21}}, \qquad (5.62)
\end{aligned}$$

where the correct correspondence to Ref. [2] is seen in the DIS limit $\mathbf{x}_{\overline{0}} \to \mathbf{x}_0, \mathbf{x}_{\overline{1}} \to \mathbf{x}_1, \mathbf{x}_{\overline{2}} \to \mathbf{x}_2$.

5.3.4 The $q\bar{q}g$ diffractive structure functions at next-to-leading order

Now we have the key pieces to write the $q\bar{q}g$ structure functions at NLO accuracy. Let us first define an auxiliary integral to encapsulate the integrations over the final state momenta:

$$\begin{aligned}
\mathcal{I}_{\text{F.S.}}(M_X, t) \coloneqq \int \frac{\mathrm{d}^2\mathbf{P}_0}{(2\pi)^2} \int \frac{\mathrm{d}^2\mathbf{P}_1}{(2\pi)^2} \int \frac{\mathrm{d}^2\mathbf{P}_2}{(2\pi)^2} e^{i\mathbf{x}_{\overline{0}\,0}\mathbf{P}_0} e^{i\mathbf{x}_{\overline{1}\,1}\mathbf{P}_1} e^{i\mathbf{x}_{\overline{2}\,2}\mathbf{P}_2} \\
\times \delta(\boldsymbol{\Delta}^2 - |t|) \delta \left(\frac{\mathbf{P}_0^2}{z_0} + \frac{\mathbf{P}_1^2}{z_1} + \frac{\mathbf{P}_2^2}{z_2} - \boldsymbol{\Delta}^2 - M_X^2 \right). \qquad (5.63)
\end{aligned}$$

With this and the squared wavefunctions (5.47), (5.55) we may write the NLO cross section (5.41) into diffractive structure functions F_L^D and F_T^D (5.6):

$$\begin{aligned}
F^{D(4)\,\text{NLO}}_{L,\,q\bar{q}g}(x_{\text{Bj}}, Q^2, M_X, t) = 4N_\text{c} Q^2 \alpha_\text{s} C_\text{F} \sum_f e_f^2 \int_0^1 \frac{\mathrm{d}z_0}{z_0} \int_0^1 \frac{\mathrm{d}z_1}{z_1} \int_0^1 \frac{\mathrm{d}z_2}{z_2} \\
\times \delta(z_0+z_1+z_2-1) \int_{\mathbf{x}_0} \int_{\mathbf{x}_1} \int_{\mathbf{x}_2} \int_{\overline{\mathbf{x}}_0} \int_{\overline{\mathbf{x}}_1} \int_{\overline{\mathbf{x}}_2} \mathcal{I}_{\text{F.S.}}(M_X, t) \\
\times 4 z_0 z_1 Q^2 \mathrm{K}_0 \left(Q X_{012} \right) \mathrm{K}_0 \left(Q X_{\overline{0}\,\overline{1}\,\overline{2}} \right) \Bigg\{
\end{aligned}$$

$$
\begin{aligned}
&z_1^2\Bigg[\left(2z_0(z_0+z_2)+z_2^2\right)\left(\frac{\mathbf{x}_{20}}{\mathbf{x}_{20}^2}\cdot\left(\frac{\mathbf{x}_{\bar{2}\bar{0}}}{\mathbf{x}_{\bar{2}\bar{0}}^2}-\frac{1}{2}\frac{\mathbf{x}_{\bar{2}\bar{1}}}{\mathbf{x}_{\bar{2}\bar{1}}^2}\right)-\frac{1}{2}\frac{\mathbf{x}_{\bar{2}\bar{0}}\cdot\mathbf{x}_{21}}{\mathbf{x}_{\bar{2}\bar{0}}^2\mathbf{x}_{21}^2}\right)\\
&\qquad+\frac{z_2^2}{2}\left(\frac{\mathbf{x}_{\bar{2}\bar{0}}\cdot\mathbf{x}_{21}}{\mathbf{x}_{\bar{2}\bar{0}}^2\mathbf{x}_{21}^2}+\frac{\mathbf{x}_{20}\cdot\mathbf{x}_{\bar{2}\bar{1}}}{\mathbf{x}_{20}^2\mathbf{x}_{\bar{2}\bar{1}}^2}\right)\Bigg]\\
&+z_0^2\Bigg[\left(2z_1(z_1+z_2)+z_2^2\right)\left(\frac{\mathbf{x}_{21}}{\mathbf{x}_{21}^2}\cdot\left(\frac{\mathbf{x}_{\bar{2}\bar{1}}}{\mathbf{x}_{\bar{2}\bar{1}}^2}-\frac{1}{2}\frac{\mathbf{x}_{\bar{2}\bar{0}}}{\mathbf{x}_{\bar{2}\bar{0}}^2}\right)-\frac{1}{2}\frac{\mathbf{x}_{20}\cdot\mathbf{x}_{\bar{2}\bar{1}}}{\mathbf{x}_{20}^2\mathbf{x}_{\bar{2}\bar{1}}^2}\right)\\
&\qquad+\frac{z_2^2}{2}\left(\frac{\mathbf{x}_{\bar{2}\bar{0}}\cdot\mathbf{x}_{21}}{\mathbf{x}_{\bar{2}\bar{0}}^2\mathbf{x}_{21}^2}+\frac{\mathbf{x}_{20}\cdot\mathbf{x}_{\bar{2}\bar{1}}}{\mathbf{x}_{20}^2\mathbf{x}_{\bar{2}\bar{1}}^2}\right)\Bigg]\Bigg\}\left[1-S^{(3)\dagger}_{\bar{0}\bar{1}\bar{2}}\right]\left[1-S^{(3)}_{012}\right]
\end{aligned}
\tag{5.64}
$$

for the longitudinal, and

$$
\begin{aligned}
F^{D(4)\,\mathrm{NLO}}_{T,\,q\bar{q}g}(x_{\mathrm{Bj}},Q^2,M_X,t) &= 2N_{\mathrm{c}}Q^2\alpha_{\mathrm{s}}C_{\mathrm{F}}\sum_f e_f^2\int_0^1\frac{\mathrm{d}z_0}{z_0}\int_0^1\frac{\mathrm{d}z_1}{z_1}\int_0^1\frac{\mathrm{d}z_2}{z_2}\\
&\times\delta(z_0+z_1+z_2-1)\int_{\mathbf{x}_0}\int_{\mathbf{x}_1}\int_{\mathbf{x}_2}\int_{\overline{\mathbf{x}}_0}\int_{\overline{\mathbf{x}}_1}\int_{\overline{\mathbf{x}}_2}\mathscr{J}_{\mathrm{F.S.}}(M_X,t)\\
&\times z_0z_1\frac{Q^2}{X_{012}X_{\bar{0}\bar{1}\bar{2}}}\mathrm{K}_1\left(QX_{012}\right)\mathrm{K}_1\left(QX_{\bar{0}\bar{1}\bar{2}}\right)\\
&\times\left\{\Upsilon^{(|a|^2)}_{\mathrm{reg.}}+\Upsilon^{(|b|^2)}_{\mathrm{reg.}}+\Upsilon^{(a')}_{\mathrm{inst.}}+\Upsilon^{(b')}_{\mathrm{inst.}}+\Upsilon^{(ab)}_{\mathrm{interf.}}\right\}\left[1-S^{(3)\dagger}_{\bar{0}\bar{1}\bar{2}}\right]\left[1-S^{(3)}_{012}\right]
\end{aligned}
\tag{5.65}
$$

for the transverse polarization, where the Υ terms are defined in Eqs. (5.56)–(5.60). The dipole scattering amplitudes are understood to be evaluated at the rapidity:

$$
S^{(3)}_{012}\equiv\left\langle S^{(3)}_{012}\right\rangle_{Y_2^+},
\tag{5.66}
$$

$$
Y_2^+=\log\left(z_2\frac{x_0Q^2}{x_{\mathrm{Bj}}Q_0^2}\right)
\tag{5.67}
$$

analogously to NLO DIS [III, 2]. Both NLO accuracy $q\bar{q}g$ contributions (5.64), (5.65) to the structure functions in the form presented here are new and previously unpublished. Contrasting to the previous results known in the literature, $F^D_{L,\,q\bar{q}g}$ has not been known in any approximation, and the $F^D_{T,\,q\bar{q}g}$ calculated above supersedes the large-Q^2 limit approximation Eq. (5.11). Some analytical work is left to be done in future work however: the final state integrals (5.63) need to be performed, and ideally the transverse squared wavefunction (5.55) would be symmetrized in the quark-antiquark exchange, as was done for NLO DIS in Ref. [2]. Though we do note that the symmetrization of (5.64) is done and the two terms in the curly braces could be combined using the symmetry of the phase space, which would combine the terms into one and produce an overall factor of two. Further work is also to see how the result Eq. (5.65) reduces to the large-Q^2 limit result Eq. (5.11), and how the adjoint dipole structure emerges.

Chapter 6

Conclusions and outlook

The work presented in this thesis builds on a decade of next-to-leading order Color Glass Condensate theory progress. It culminates in the state-of-the-art accuracy theory calculation and data comparison of the deep inelastic scattering cross sections from the CGC effective field theory. This paves the way towards accurate understanding of gluon saturation in QCD, and high accuracy theory calculations will be needed in the forthcoming precision small-x era to be kicked off by the Electron-Ion Collider in early 2030s.

In Article [II], new light-front perturbation theory tools are developed to facilitate the calculations of loop contributions which are present at next-to-leading order and beyond in the perturbation theory. The developed formalism is built on the four-dimensional helicity scheme of dimensional regularization, and the resulting calculation rules should be automatable for computational analytic calculation of observables at NLO accuracy and beyond. These tools are used to calculate the next-to-leading order DIS cross sections in the CGC formalism, which were verified to agree with the known results from the literature [1, 2].

The Articles [I] and [III] work towards the first numerical evaluation and data comparison of the next-to-leading order DIS cross sections to HERA data. First in Article [I] we show that at NLO the kinematics of the scattering are intimately related to the factorization of the large soft gluon logarithm into the Balitsky-Kovchegov renormalization group evolution. This brought the perturbative calculation of the cross sections under control and reasonable NLO corrections were seen, which would make comparisons between theory and data possible in the future.

Article [III] proceeds to combine the NLO DIS impact factors evaluated in the first article with enhanced BK equations known in the literature, which include in their prescriptions some of the most important beyond leading order corrections to the BK equation. Together these yield the state-of-the-art theory accuracy evaluation of the DIS cross sections calculated in the CGC formalism.

We fit the initial shape of the dipole amplitudes using these NLO cross sections to the combined HERA data and found excellent description of the data. We found that the three different resummation approaches to the BK evolution described the available data comparably, and that new data from future experiments might be able to discern between the prescriptions. The determined dipole amplitudes can be used to calculate predictions of other observables, the data are available at [147]. As the first application, the dipole amplitudes have been used as an ingredient to calculate exclusive production of longitudinally polarized heavy vector mesons in next-to-leading order accuracy [119]. The results of Article [**III**] are discussed in more detail in Sec. 4.2, and the theoretical uncertainties of the results are discussed in Sec. 4.3.

Some new and unpublished results are presented in this thesis as well. We derive a new form for the NLO DIS loop contribution in Sec. 3.3.3, which makes it possible to evaluate the dipole amplitudes of the NLO contributions at the same consistent rapidity scale, which was not possible previously as discussed in [**I**, **III**]. While this distinction is a beyond NLO effect, it could be numerically important for phenomenology.

In Sec. 4.3.1 we estimate the impact of the NLO BK evolution on the fits of Article [**III**] by computing NLO BK evolved dipole amplitudes using the initial conditions determined in [**III**]. These NLO BK evolved dipole amplitudes are used to compute reduced cross sections which are compared to HERA data. The enhanced BK equations are found to approximate the NLO BK equation reasonably well in this simple data comparison, which is promising for the prospect of a full NLO+NLL accuracy fit.

Lastly, we calculate analytically for the first time the tree-level NLO contribution to the diffractive DIS structure functions for both longitudinally and transversely polarized virtual photon in Sec. 5.3. However, final state emissions of gluons were not included and some finalization work is left to be done, as discussed in Sec. 5.3.1. This $q\bar{q}g$ contribution has previously been known only for the transversely polarized photon and in leading $\log(Q^2)$ accuracy valid at large Q^2 — this is discussed in Ch. 5. Once the full NLO accuracy diffractive DIS cross sections become available, they will provide a key opportunity to study saturation and test the universality of the dipole amplitude.

The CGC theory field is progressing with strides towards next-to-leading order accuracy in multiple fronts. NLO accuracy calculations of scattering processes are becoming available, with the longitudinal NLO DIS cross section for massive quarks being available [121], and the calculation of the transverse case is ongoing. Other processes are advancing to NLO as well: the single inclusive hadron production [113, 114, 120, 148–156], exclusive light [157] and heavy vector meson production [119], dijets in pA collisions [158] and dijets in DIS [159, 160]. Improvements to the description of the scattering process off the color-field

are being studied as well. The NLO BK equation has been derived in the target momentum fraction prescription [52], the behavior of which will be important to compare to the projectile momentum fraction picture equation [58]. Finite-N_c corrections to the NLO BK equation have been calculated [59], and corrections to the eikonal approximation are being calculated for the gluon and quark propagators in next-to-eikonal accuracy [161–164]. The NLO DIS cross sections for massive quarks will be of great interest from the perspective of this thesis, since they will make possible to account for the contribution of the charm quark in the HERA data, which will improve the accuracy of the analysis. Overall, the general progress of the field towards NLO calculations of observables is bringing about the era of precision saturation phenomenology.

References

[1] G. Beuf, Dipole factorization for DIS at NLO: Loop correction to the $\gamma^*_{T,L} \to q\bar{q}$ light-front wave functions, Phys. Rev. D **94**.5 (2016) 054016, arXiv: 1606.00777 [hep-ph].

[2] G. Beuf, Dipole factorization for DIS at NLO: Combining the $q\bar{q}$ and $q\bar{q}g$ contributions, Phys. Rev. D **96**.7 (2017) 074033, arXiv: 1708.06557 [hep-ph].

[3] P.A. Zyla et al. (Particle Data Group), Review of particle physics, Prog. Theor. Exp. Phys. **2020**.8 (2020) 083C01.

[4] E. Rutherford, LIV. Collision of α particles with light atoms. IV. An anomalous effect in nitrogen, The London, Edinburgh, and Dublin Philosophical Magazine and Journal of Science **37**.222 (1919) 581–587.

[5] A. Romer, Proton or prouton?: Rutherford and the depths of the atom, American Journal of Physics **65**.8 (1997) 707–716.

[6] A. Walker-Loud, Dissecting the mass of the proton, APS Physics **11** (2018) 118.

[7] X.-D. Ji, A QCD analysis of the mass structure of the nucleon, Phys. Rev. Lett. **74** (1995) 1071–1074, arXiv: hep-ph/9410274.

[8] Y.-B. Yang et al., Proton mass decomposition from the QCD energy momentum tensor, Phys. Rev. Lett. **121**.21 (2018) 212001, arXiv: 1808.08677 [hep-lat].

[9] J. C. Bernauer, The proton radius puzzle – 9 years later, EPJ Web Conf. **234** (2020) 01001.

[10] E. C. Aschenauer et al., The RHIC Spin Program: achievements and future opportunities, (Mar. 2013), arXiv: 1304.0079 [nucl-ex].

[11] E.-C. Aschenauer et al., The RHIC SPIN Program: achievements and future opportunities, (Jan. 2015), arXiv: 1501.01220 [nucl-ex].

[12] Y. V. Kovchegov, A. Tarasov and Y. Tawabutr, Helicity evolution at small x: the single-logarithmic contribution, (Apr. 2021), arXiv: 2104.11765 [hep-ph].

[13] E. Leader and C. Lorcé, The angular momentum controversy: What's it all about and does it matter?, Phys. Rept. **541**.3 (2014) 163–248, arXiv: 1309.4235 [hep-ph].

[14] Y. V. Kovchegov and M. D. Sievert, Small-x helicity evolution: an operator treatment, Phys. Rev. D **99**.5 (2019) 054032, arXiv: 1808.09010 [hep-ph].

[15] E. Iancu and R. Venugopalan, The Color Glass Condensate and high-energy scattering in QCD, *Quark-gluon plasma 4*, Mar. 2003, arXiv: hep-ph/0303204.

[16] H. Weigert, Evolution at small x_{Bj}: the Color Glass Condensate, Prog. Part. Nucl. Phys. **55** (2005) 461–565, arXiv: hep-ph/0501087.

[17] F. Gelis, E. Iancu, J. Jalilian-Marian and R. Venugopalan, The Color Glass Condensate, Ann. Rev. Nucl. Part. Sci. **60** (2010) 463–489, arXiv: 1002.0333 [hep-ph].

[18] J. L. Albacete and C. Marquet, Gluon saturation and initial conditions for relativistic heavy ion collisions, Prog. Part. Nucl. Phys. **76** (2014) 1–42, arXiv: 1401.4866 [hep-ph].

[19] J.-P. Blaizot, High gluon densities in heavy ion collisions, Rept. Prog. Phys. **80**.3 (2017) 032301, arXiv: 1607.04448 [hep-ph].

[20] A. Morreale and F. Salazar, Mining for gluon saturation at colliders, Universe **7**.8 (2021) 312, arXiv: 2108.08254 [hep-ph].

[21] G. Dvali and R. Venugopalan, Classicalization and unitarization of wee partons in QCD and Gravity: The CGC-Black Hole correspondence, (June 2021), arXiv: 2106.11989 [hep-th].

[22] A. Accardi et al., Electron Ion Collider: The Next QCD Frontier: Understanding the glue that binds us all, Eur. Phys. J. A **52**.9 (2016) 268, arXiv: 1212.1701 [nucl-ex].

[23] E. C. Aschenauer et al., The electron–ion collider: assessing the energy dependence of key measurements, Rept. Prog. Phys. **82**.2 (2019) 024301, arXiv: 1708.01527 [nucl-ex].

[24] R. Abdul Khalek et al., Science requirements and detector concepts for the Electron-Ion Collider: EIC yellow report, (Mar. 2021), arXiv: 2103.05419 [physics.ins-det].

[25] A. H. Mueller, Parton saturation: An Overview, *Cargese Summer School on QCD Perspectives on Hot and Dense Matter*, arXiv: hep-ph/0111244.

[26] J. D. Bjorken, J. B. Kogut and D. E. Soper, Quantum electrodynamics at infinite momentum: scattering from an external field, Phys. Rev. D **3** (1971) 1382.

[27] S. J. Brodsky, H.-C. Pauli and S. S. Pinsky, Quantum chromodynamics and other field theories on the light cone, Phys. Rept. **301** (1998) 299–486, arXiv: hep-ph/9705477.

[28] Y. V. Kovchegov and E. Levin, Quantum chromodynamics at high energy, Camb. Monogr. Part. Phys. Nucl. Phys. Cosmol. **33** (2012) 1–350.

[29] K. J. Golec-Biernat and M. Wusthoff, Saturation effects in deep inelastic scattering at low Q^2 and its implications on diffraction, Phys. Rev. D **59** (1998) 014017, arXiv: hep-ph/9807513.

[30] K. J. Golec-Biernat and M. Wusthoff, Saturation in diffractive deep inelastic scattering, Phys. Rev. D **60** (1999) 114023, arXiv: hep-ph/9903358.

[31] W. Buchmuller and A. Hebecker, Semiclassical approach to structure functions at small x, Nucl. Phys. B **476** (1996) 203–224, arXiv: hep-ph/9512329.

[32] W. Buchmuller, M. F. McDermott and A. Hebecker, Gluon radiation in diffractive electroproduction, Nucl. Phys. B **487** (1997), [Erratum: Nucl.Phys.B 500, 621–622 (1997)] 283–310, arXiv: hep-ph/9607290.

[33] A. Hebecker, Diffractive parton distributions in the semiclassical approach, Nucl. Phys. B **505** (1997) 349–365, arXiv: hep-ph/9702373.

[34] W. Buchmuller, T. Gehrmann and A. Hebecker, Inclusive and diffractive structure functions at small x, Nucl. Phys. B **537** (1999) 477–500, arXiv: hep-ph/9808454.

[35] A. Hebecker, Diffraction in deep inelastic scattering, Phys. Rept. **331** (2000) 1–115, arXiv: hep-ph/9905226.

[36] L. D. McLerran and R. Venugopalan, Computing quark and gluon distribution functions for very large nuclei, Phys. Rev. D **49** (1994) 2233–2241, arXiv: hep-ph/9309289.

[37] L. D. McLerran and R. Venugopalan, Gluon distribution functions for very large nuclei at small transverse momentum, Phys. Rev. D **49** (1994) 3352–3355, arXiv: hep-ph/9311205.

[38] L. D. McLerran and R. Venugopalan, Green's functions in the color field of a large nucleus, Phys. Rev. D **50** (1994) 2225–2233, arXiv: hep-ph/9402335.

[39] J. Jalilian-Marian, A. Kovner, L. D. McLerran and H. Weigert, The Intrinsic glue distribution at very small x, Phys. Rev. D **55** (1997) 5414–5428, arXiv: hep-ph/9606337.

[40] J. Jalilian-Marian, A. Kovner, A. Leonidov and H. Weigert, The BFKL equation from the Wilson renormalization group, Nucl. Phys. B **504** (1997) 415–431, arXiv: hep-ph/9701284.

[41] J. Jalilian-Marian, A. Kovner, A. Leonidov and H. Weigert, The Wilson renormalization group for low x physics: Towards the high density regime, Phys. Rev. D **59** (1998) 014014, arXiv: hep-ph/9706377.

[42] J. Jalilian-Marian, A. Kovner and H. Weigert, The Wilson renormalization group for low x physics: Gluon evolution at finite parton density, Phys. Rev. D **59** (1998) 014015, arXiv: hep-ph/9709432.

[43] I. Balitsky, Operator expansion for high-energy scattering, Nucl. Phys. **B463** (1996) 99–160, arXiv: hep-ph/9509348 [hep-ph].

[44] Y. V. Kovchegov, Small x F_2 structure function of a nucleus including multiple pomeron exchanges, Phys. Rev. **D60** (1999) 034008, arXiv: hep-ph/9901281 [hep-ph].

[45] Y. V. Kovchegov, Unitarization of the BFKL pomeron on a nucleus, Phys. Rev. D **61** (2000) 074018, arXiv: hep-ph/9905214.

[46] E. Iancu, A. Leonidov and L. D. McLerran, Nonlinear gluon evolution in the Color Glass Condensate. 1., Nucl. Phys. A **692** (2001) 583–645, arXiv: hep-ph/0011241.

[47] E. Iancu and L. D. McLerran, Saturation and universality in QCD at small x, Phys. Lett. B **510** (2001) 145–154, arXiv: hep-ph/0103032.

[48] E. Iancu, A. Leonidov and L. D. McLerran, The Renormalization group equation for the Color Glass Condensate, Phys. Lett. B **510** (2001) 133–144, arXiv: hep-ph/0102009.

[49] E. Ferreiro, E. Iancu, A. Leonidov and L. McLerran, Nonlinear gluon evolution in the Color Glass Condensate. 2., Nucl. Phys. A **703** (2002) 489–538, arXiv: hep-ph/0109115.

[50] R. Venugopalan, Classical methods in DIS and nuclear scattering at small x, Acta Phys. Polon. B **30** (1999) 3731–3761, arXiv: hep-ph/9911371.

[51] I. Balitsky, Quark contribution to the small-x evolution of color dipole, Phys. Rev. D **75** (2007) 014001, arXiv: hep-ph/0609105.

[52] B. Ducloué, E. Iancu, A. H. Mueller, G. Soyez and D. N. Triantafyllopoulos, Non-linear evolution in QCD at high-energy beyond leading order, JHEP **04** (2019) 081, arXiv: 1902.06637 [hep-ph].

[53] G. Beuf, Improving the kinematics for low-x QCD evolution equations in coordinate space, Phys. Rev. D **89**.7 (2014) 074039, arXiv: 1401.0313 [hep-ph].

[54] E. Iancu, J. D. Madrigal, A. H. Mueller, G. Soyez and D. N. Triantafyllopoulos, Resumming double logarithms in the QCD evolution of color dipoles, Phys. Lett. B **744** (2015) 293–302, arXiv: 1502.05642 [hep-ph].

[55] E. Iancu, J. D. Madrigal, A. H. Mueller, G. Soyez and D. N. Triantafyllopoulos, Collinearly-improved BK evolution meets the HERA data, Phys. Lett. B **750** (2015) 643–652, arXiv: 1507.03651 [hep-ph].

[56] T. Lappi and H. Mäntysaari, Next-to-leading order Balitsky-Kovchegov equation with resummation, Phys. Rev. D **93**.9 (2016) 094004, arXiv: 1601.06598 [hep-ph].

[57] J. L. Albacete, Resummation of double collinear logs in BK evolution versus HERA data, Nucl. Phys. A **957** (2017) 71–84, arXiv: 1507.07120 [hep-ph].

[58] I. Balitsky and G. A. Chirilli, Next-to-leading order evolution of color dipoles, Phys. Rev. D **77** (2008) 014019, arXiv: 0710.4330 [hep-ph].

[59] T. Lappi, H. Mäntysaari and A. Ramnath, Next-to-leading order Balitsky-Kovchegov equation beyond large N_c, Phys. Rev. D **102**.7 (2020) 074027, arXiv: 2007.00751 [hep-ph].

[60] T. Lappi and H. Mäntysaari, Direct numerical solution of the coordinate space Balitsky-Kovchegov equation at next to leading order, Phys. Rev. D **91**.7 (2015) 074016, arXiv: 1502.02400 [hep-ph].

[61] I. Balitsky and G. A. Chirilli, Rapidity evolution of Wilson lines at the next-to-leading order, Phys. Rev. D **88** (2013) 111501, arXiv: 1309.7644 [hep-ph].

[62] A. Kovner, M. Lublinsky and Y. Mulian, Jalilian-Marian, Iancu, McLerran, Weigert, Leonidov, Kovner evolution at next to leading order, Phys. Rev. D **89**.6 (2014) 061704, arXiv: 1310.0378 [hep-ph].

[63] Y. Hatta and E. Iancu, Collinearly improved JIMWLK evolution in Langevin form, JHEP **08** (2016) 083, arXiv: 1606.03269 [hep-ph].

[64] S. Cali et al., On systematic effects in the numerical solutions of the JIMWLK equation, Eur. Phys. J. C **81**.663 (2021), arXiv: 2104.14254 [hep-ph].

[65] E. D. Bloom et al., High-energy inelastic ep scattering at 6-degrees and 10-degrees, Phys. Rev. Lett. **23** (1969) 930–934.

[66] M. Breidenbach et al., Observed behavior of highly inelastic electron-proton scattering, Phys. Rev. Lett. **23** (1969) 935–939.

[67] C. Adloff et al., A Measurement of the proton structure function $F_2(x, Q^2)$ at low x and low Q^2 at HERA, Nucl. Phys. B **497** (1997) 3–30, arXiv: hep-ex/9703012.

[68] S. Aid et al., A Measurement and QCD analysis of the proton structure function $F_2(x, Q^2)$ at HERA, Nucl. Phys. B **470** (1996) 3–40, arXiv: hep-ex/9603004.

[69] J. Breitweg et al., Measurement of the proton structure function F_2 and $\sigma_{tot}^{\gamma^* p}$ at low Q^2 and very low x at HERA, Phys. Lett. B **407** (1997) 432–448, arXiv: hep-ex/9707025.

[70] M. Derrick et al., Measurement of the proton structure function F_2 at low x and low Q^2 at HERA, Z. Phys. C **69** (1996) 607–620, arXiv: hep-ex/9510009.

[71] J. Breitweg et al., Measurement of the proton structure function F_2 at very low Q^2 at HERA, Phys. Lett. B **487** (2000) 53–73, arXiv: hep-ex/0005018.

[72] S. Chekanov et al., Measurement of the neutral current cross-section and F_2 structure function for deep inelastic e^+p scattering at HERA, Eur. Phys. J. C **21** (2001) 443–471, arXiv: hep-ex/0105090.

[73] C. Adloff et al., Deep inelastic inclusive ep scattering at low x and a determination of α_s, Eur. Phys. J. C **21** (2001) 33–61, arXiv: hep-ex/0012053.

[74] F. D. Aaron et al., Combined measurement and QCD analysis of the inclusive $e^\pm p$ scattering cross sections at HERA, JHEP **01** (2010) 109, arXiv: 0911.0884 [hep-ex].

[75] H. Abramowicz et al., Combination of measurements of inclusive deep inelastic $e^\pm p$ scattering cross sections and QCD analysis of HERA data, Eur. Phys. J. **C75**.12 (2015) 580, arXiv: 1506.06042 [hep-ex].

[76] H. Abramowicz et al., Combination and QCD analysis of charm and beauty production cross-section measurements in deep inelastic ep scattering at HERA, Eur. Phys. J. **C78**.6 (2018) 473, arXiv: 1804.01019 [hep-ex].

[77] H. Abramowicz et al., Combination and QCD analysis of charm production cross section measurements in deep-inelastic ep scattering at HERA, Eur. Phys. J. **C73**.2 (2013) 2311, arXiv: 1211.1182 [hep-ex].

[78] V. Andreev et al., Measurement of inclusive ep cross sections at high Q^2 at $\sqrt{s} = 225$ and 252 GeV and of the longitudinal proton structure function F_L at HERA, Eur. Phys. J. C **74**.4 (2014) 2814, arXiv: 1312.4821 [hep-ex].

[79] H. Abramowicz et al., Deep inelastic cross-section measurements at large y with the ZEUS detector at HERA, Phys. Rev. D **90**.7 (2014) 072002, arXiv: 1404.6376 [hep-ex].

[80] P. Taels, Quantum Chromodynamics at small Bjorken-x, PhD thesis, Antwerp U., 2017, arXiv: 1711.03928 [hep-ph].

[81] N. N. Nikolaev and B. G. Zakharov, Color transparency and scaling properties of nuclear shadowing in deep inelastic scattering, Z. Phys. C **49** (1991) 607–618.

[82] H. G. Dosch, T. Gousset, G. Kulzinger and H. J. Pirner, Vector meson leptoproduction and nonperturbative gluon fluctuations in QCD, Phys. Rev. D **55** (1997) 2602–2615, arXiv: hep-ph/9608203.

[83] A. M. Stasto, K. J. Golec-Biernat and J. Kwiecinski, Geometric scaling for the total $\gamma^* p$ cross-section in the low x region, Phys. Rev. Lett. **86** (2001) 596–599, arXiv: hep-ph/0007192.

[84] V. Barone and E. Predazzi, *High-energy particle diffraction*, vol. 565, Texts and Monographs in Physics, Berlin Heidelberg: Springer-Verlag, 2002, ISBN: 978-3-540-42107-8.

[85] E. Iancu, K. Itakura and L. McLerran, A Gaussian effective theory for gluon saturation, Nucl. Phys. A **724** (2003) 181–222, arXiv: hep-ph/0212123.

[86] G. Beuf, NLO corrections for the dipole factorization of DIS structure functions at low x, Phys. Rev. D **85** (2012) 034039, arXiv: 1112.4501 [hep-ph].

[87] H. Kowalski, L. Motyka and G. Watt, Exclusive diffractive processes at HERA within the dipole picture, Phys. Rev. D **74** (2006) 074016, arXiv: hep-ph/0606272.

[88] J. Bartels, K. J. Golec-Biernat and H. Kowalski, A modification of the saturation model: DGLAP evolution, Phys. Rev. D **66** (2002) 014001, arXiv: hep-ph/0203258.

[89] E. Iancu, K. Itakura and S. Munier, Saturation and BFKL dynamics in the HERA data at small x, Phys. Lett. B **590** (2004) 199–208, arXiv: hep-ph/0310338.

[90] G. Watt and H. Kowalski, Impact parameter dependent colour glass condensate dipole model, Phys. Rev. D **78** (2008) 014016, arXiv: 0712.2670 [hep-ph].

[91] H. Kowalski and D. Teaney, An Impact parameter dipole saturation model, Phys. Rev. D **68** (2003) 114005, arXiv: hep-ph/0304189.

[92] A. H. Rezaeian, M. Siddikov, M. Van de Klundert and R. Venugopalan, Analysis of combined HERA data in the Impact-Parameter dependent Saturation model, Phys. Rev. D **87**.3 (2013) 034002, arXiv: 1212.2974 [hep-ph].

[93] H. Mäntysaari and P. Zurita, In depth analysis of the combined HERA data in the dipole models with and without saturation, Phys. Rev. D **98** (2018) 036002, arXiv: 1804.05311 [hep-ph].

[94] J. L. Albacete, N. Armesto, J. G. Milhano and C. A. Salgado, Non-linear QCD meets data: A Global analysis of lepton-proton scattering with running coupling BK evolution, Phys. Rev. D **80** (2009) 034031, arXiv: 0902.1112 [hep-ph].

[95] J. L. Albacete, N. Armesto, J. G. Milhano, P. Quiroga-Arias and C. A. Salgado, AAMQS: A non-linear QCD analysis of new HERA data at small-x including heavy quarks, Eur. Phys. J. C **71** (2011) 1705, arXiv: 1012.4408 [hep-ph].

[96] Y. V. Kovchegov and H. Weigert, Triumvirate of running couplings in small-x evolution, Nucl. Phys. A **784** (2007) 188–226, arXiv: hep-ph/0609090.

[97] T. Lappi and H. Mäntysaari, Single inclusive particle production at high energy from HERA data to proton-nucleus collisions, Phys. Rev. D **88** (2013) 114020, arXiv: 1309.6963 [hep-ph].

[98] J. Kuokkanen, K. Rummukainen and H. Weigert, HERA-data in the light of small x evolution with state of the art NLO input, Nucl. Phys. A **875** (2012) 29–93, arXiv: 1108.1867 [hep-ph].

[99] J. Kwiecinski, A. D. Martin and A. M. Stasto, A Unified BFKL and GLAP description of F_2 data, Phys. Rev. D **56** (1997) 3991–4006, arXiv: hep-ph/9703445.

[100] K. Kutak and S. Sapeta, Gluon saturation in dijet production in p-Pb collisions at Large Hadron Collider, Phys. Rev. D **86** (2012) 094043, arXiv: 1205.5035 [hep-ph].

[101] B. Ducloué, E. Iancu, G. Soyez and D. N. Triantafyllopoulos, HERA data and collinearly-improved BK dynamics, Phys. Lett. B **803** (2020) 135305, arXiv: 1912.09196 [hep-ph].

[102] J. Berger and A. M. Stasto, Small x nonlinear evolution with impact parameter and the structure function data, Phys. Rev. D **84** (2011) 094022, arXiv: 1106.5740 [hep-ph].

[103] H. Mäntysaari and B. Schenke, Confronting impact parameter dependent JIMWLK evolution with HERA data, Phys. Rev. D **98**.3 (2018) 034013, arXiv: 1806.06783 [hep-ph].

[104] D. Bendova, J. Cepila, J. G. Contreras and M. Matas, Solution to the Balitsky-Kovchegov equation with the collinearly improved kernel including impact-parameter dependence, Phys. Rev. D **100**.5 (2019) 054015, arXiv: 1907.12123 [hep-ph].

[105] J. Bartels, S. Gieseke and C. F. Qiao, The $(\gamma^* \to q\bar{q})$ – Reggeon vertex in next-to-leading order QCD, Phys. Rev. D **63** (2001), [Erratum: Phys.Rev.D 65, 079902 (2002)] 056014, arXiv: hep-ph/0009102.

[106] J. Bartels, S. Gieseke and A. Kyrieleis, The Process $\gamma_L^* + q \to (q\bar{q}g) + q$: Real corrections to the virtual photon impact factor, Phys. Rev. D **65** (2002) 014006, arXiv: hep-ph/0107152.

[107] J. Bartels, D. Colferai, S. Gieseke and A. Kyrieleis, NLO corrections to the photon impact factor: Combining real and virtual corrections, Phys. Rev. D **66** (2002) 094017, arXiv: hep-ph/0208130.

[108] J. Bartels and A. Kyrieleis, NLO corrections to the γ^* impact factor: First numerical results for the real corrections to γ_L^*, Phys. Rev. D **70** (2004) 114003, arXiv: hep-ph/0407051.

[109] I. Balitsky and G. A. Chirilli, Photon impact factor in the next-to-leading order, Phys. Rev. D **83** (2011) 031502, arXiv: 1009.4729 [hep-ph].

[110] I. Balitsky and G. A. Chirilli, Photon impact factor and k_T-factorization for DIS in the next-to-leading order, Phys. Rev. D **87**.1 (2013) 014013, arXiv: 1207.3844 [hep-ph].

[111] R. D. Field, *Applications of perturbative QCD*, vol. 77, Frontiers in physics, Addison-Wesley, 1989, ISBN: 978-0201483628.

[112] A. M. Stasto, B.-W. Xiao and D. Zaslavsky, Towards the test of saturation physics beyond leading logarithm, Phys. Rev. Lett. **112**.1 (2014) 012302, arXiv: 1307.4057 [hep-ph].

[113] E. Iancu, A. H. Mueller and D. N. Triantafyllopoulos, CGC factorization for forward particle production in proton-nucleus collisions at next-to-leading order, JHEP **12** (2016) 041, arXiv: 1608.05293 [hep-ph].

[114] B. Ducloué, T. Lappi and Y. Zhu, Implementation of NLO high energy factorization in single inclusive forward hadron production, Phys. Rev. D **95**.11 (2017) 114007, arXiv: 1703.04962 [hep-ph].

[115] T. Lappi and R. Paatelainen, The one loop gluon emission light cone wave function, Annals Phys. **379** (2017) 34–66, arXiv: 1611.00497 [hep-ph].

[116] T. Hahn, CUBA: A Library for multidimensional numerical integration, Comput. Phys. Commun. **168** (2005) 78–95, arXiv: hep-ph/0404043.

[117] T. Hahn, Concurrent Cuba, J. Phys. Conf. Ser. **608**.1 (2015) 012066, arXiv: 1408.6373 [physics.comp-ph].

[118] T. Lappi and H. Mäntysaari, On the running coupling in the JIMWLK equation, Eur. Phys. J. C **73**.2 (2013) 2307, arXiv: 1212.4825 [hep-ph].

[119] H. Mäntysaari and J. Penttala, Exclusive heavy vector meson production at next-to-leading order in the dipole picture, (Apr. 2021), arXiv: 2104.02349 [hep-ph].

[120] B. Ducloué et al., Use of a running coupling in the NLO calculation of forward hadron production, Phys. Rev. D **97**.5 (2018) 054020, arXiv: 1712.07480 [hep-ph].

[121] G. Beuf, T. Lappi and R. Paatelainen, Massive quarks in NLO dipole factorization for DIS: longitudinal photon, (Mar. 2021), arXiv: 2103.14549 [hep-ph].

[122] J. D. Bjorken, Rapidity gaps and jets as a new physics signature in very high-energy hadron hadron collisions, Phys. Rev. D **47** (1993) 101–113.

[123] M. Boonekamp, F. Chevallier, C. Royon and L. Schoeffel, Understanding the structure of the proton: From HERA and Tevatron to LHC, Acta Phys. Polon. B **40** (2009) 2239–2321, arXiv: 0902.1678 [hep-ph].

[124] G. Ingelman and P. E. Schlein, Jet structure in high mass diffractive scattering, Phys. Lett. B **152** (1985) 256–260.

[125] S. J. Brodsky, R. Enberg, P. Hoyer and G. Ingelman, Hard diffraction from parton rescattering in QCD, Phys. Rev. D **71** (2005) 074020, arXiv: hep-ph/0409119.

[126] A. D. Martin, M. G. Ryskin and G. Watt, A QCD analysis of diffractive deep-inelastic scattering data, Eur. Phys. J. C **37** (2004) 285–292, arXiv: hep-ph/0406224.

[127] A. Edin, G. Ingelman and J. Rathsman, Soft color interactions as the origin of rapidity gaps in DIS, Phys. Lett. B **366** (1996) 371–378, arXiv: hep-ph/9508386.

[128] A. Edin, G. Ingelman and J. Rathsman, Unified description of rapidity gaps and energy flows in DIS final states, Z. Phys. C **75** (1997) 57–70, arXiv: hep-ph/9605281.

[129] G. Ingelman, A. Edin and J. Rathsman, LEPTO 6.5: A Monte Carlo generator for deep inelastic lepton - nucleon scattering, Comput. Phys. Commun. **101** (1997) 108–134, arXiv: hep-ph/9605286.

[130] J. Bartels and M. Wusthoff, The Triple Regge limit of diffractive dissociation in deep inelastic scattering, Z. Phys. C **66** (1995) 157–180.

[131] M. Wusthoff, Photon diffractive dissociation in deep inelastic scattering, DESY-95-166, PhD thesis, Sept. 1995.

[132] M. Wusthoff, Large rapidity gap events in deep inelastic scattering, Phys. Rev. D **56** (1997) 4311–4321, arXiv: hep-ph/9702201.

[133] M. Wusthoff and A. D. Martin, The QCD description of diffractive processes, J. Phys. G **25** (1999) R309–R344, arXiv: hep-ph/9909362.

[134] S. Munier and A. Shoshi, Diffractive photon dissociation in the saturation regime from the Good and Walker picture, Phys. Rev. D **69** (2004) 074022, arXiv: hep-ph/0312022.

[135] C. Marquet, A Unified description of diffractive deep inelastic scattering with saturation, Phys. Rev. D **76** (2007) 094017, arXiv: 0706.2682 [hep-ph].

[136] H. Kowalski, T. Lappi, C. Marquet and R. Venugopalan, Nuclear enhancement and suppression of diffractive structure functions at high energies, Phys. Rev. C **78** (2008) 045201, arXiv: 0805.4071 [hep-ph].

[137] M. G. Ryskin, Photon diffractive dissociation in deep inelastic scattering, Sov. J. Nucl. Phys. **52** (1990) 529–535.

[138] N. Nikolaev and B. G. Zakharov, Pomeron structure function and diffraction dissociation of virtual photons in perturbative QCD, Z. Phys. C **53** (1992) 331–346.

[139] N. N. Nikolaev and B. G. Zakharov, The Triple pomeron regime and the structure function of the pomeron in the diffractive deep inelastic scattering at very small x, Z. Phys. C **64** (1994) 631–652, arXiv: hep-ph/9306230.

[140] A. H. Mueller, Small x behavior and parton saturation: a QCD model, Nucl. Phys. B **335** (1990) 115–137.

[141] E. Levin and M. Wusthoff, Photon diffractive dissociation in deep inelastic scattering, Phys. Rev. D **50** (1994) 4306–4327.

[142] B. Z. Kopeliovich, A. Schafer and A. V. Tarasov, Nonperturbative effects in gluon radiation and photoproduction of quark pairs, Phys. Rev. D **62** (2000) 054022, arXiv: hep-ph/9908245.

[143] J. Bartels, H. Jung and M. Wusthoff, Quark - anti-quark gluon jets in DIS diffractive dissociation, Eur. Phys. J. C **11** (1999) 111–125, arXiv: hep-ph/9903265.

[144] Y. V. Kovchegov, Diffractive gluon production in proton nucleus collisions and in DIS, Phys. Rev. D **64** (2001), [Erratum: Phys.Rev.D 68, 039901 (2003)] 114016, arXiv: hep-ph/0107256.

[145] C. Marquet, A QCD dipole formalism for forward-gluon production, Nucl. Phys. B **705** (2005) 319–338, arXiv: hep-ph/0409023.

[146] K. J. Golec-Biernat and C. Marquet, Testing saturation with diffractive jet production in deep inelastic scattering, Phys. Rev. D **71** (2005) 114005, arXiv: hep-ph/0504214.

[147] G. Beuf, H. Hänninen, T. Lappi and H. Mäntysaari, Color Glass Condensate at next-to-leading order meets HERA data (software), URL: https://doi.org/10.5281/zenodo.4229269.

[148] B. Ducloué, T. Lappi and Y. Zhu, Single inclusive forward hadron production at next-to-leading order, Phys. Rev. D **93**.11 (2016) 114016, arXiv: 1604.00225 [hep-ph].

[149] H.-Y. Liu, Y.-Q. Ma and K.-T. Chao, Improvement for Color Glass Condensate factorization: single hadron production in pA collisions at next-to-leading order, Phys. Rev. D **100**.7 (2019) 071503, arXiv: 1909.02370 [nucl-th].

[150] H.-Y. Liu, Z.-B. Kang and X. Liu, Threshold resummation for hadron production in the small-x region, Phys. Rev. D **102**.5 (2020) 051502, arXiv: 2004.11990 [hep-ph].

[151] G. A. Chirilli, B.-W. Xiao and F. Yuan, One-loop factorization for inclusive hadron production in pA collisions in the saturation formalism, Phys. Rev. Lett. **108** (2012) 122301, arXiv: 1112.1061 [hep-ph].

[152] G. A. Chirilli, B.-W. Xiao and F. Yuan, Inclusive hadron productions in pA collisions, Phys. Rev. D **86** (2012) 054005, arXiv: 1203.6139 [hep-ph].

[153] T. Altinoluk, N. Armesto, G. Beuf, A. Kovner and M. Lublinsky, Single-inclusive particle production in proton-nucleus collisions at next-to-leading order in the hybrid formalism, Phys. Rev. D **91**.9 (2015) 094016, arXiv: 1411.2869 [hep-ph].

[154] K. Watanabe, B.-W. Xiao, F. Yuan and D. Zaslavsky, Implementing the exact kinematical constraint in the saturation formalism, Phys. Rev. D **92**.3 (2015) 034026, arXiv: 1505.05183 [hep-ph].

[155] A. M. Staśto, B.-W. Xiao, F. Yuan and D. Zaslavsky, Matching collinear and small x factorization calculations for inclusive hadron production in pA collisions, Phys. Rev. D **90**.1 (2014) 014047, arXiv: 1405.6311 [hep-ph].

[156] Z.-B. Kang, I. Vitev and H. Xing, Next-to-leading order forward hadron production in the small-x regime: rapidity factorization, Phys. Rev. Lett. **113** (2014) 062002, arXiv: 1403.5221 [hep-ph].

[157] R. Boussarie, A. V. Grabovsky, D. Y. Ivanov, L. Szymanowski and S. Wallon, Next-to-leading order computation of exclusive diffractive light vector meson production in a saturation framework, Phys. Rev. Lett. **119**.7 (2017) 072002, arXiv: 1612.08026 [hep-ph].

[158] E. Iancu and Y. Mulian, Forward dijets in proton-nucleus collisions at next-to-leading order: the real corrections, JHEP **03** (2021) 005, arXiv: 2009.11930 [hep-ph].

[159] K. Roy and R. Venugopalan, NLO impact factor for inclusive photon+dijet production in $e + A$ DIS at small x, Phys. Rev. D **101**.3 (2020) 034028, arXiv: 1911.04530 [hep-ph].

[160] P. Caucal, F. Salazar and R. Venugopalan, Dijet impact factor in DIS at next-to-leading order in the Color Glass Condensate, (Aug. 2021), arXiv: 2108.06347 [hep-ph].

[161] T. Altinoluk, N. Armesto, G. Beuf, M. Martínez and C. A. Salgado, Next-to-eikonal corrections in the CGC: gluon production and spin asymmetries in pA collisions, JHEP **07** (2014) 068, arXiv: 1404.2219 [hep-ph].

[162] T. Altinoluk, N. Armesto, G. Beuf and A. Moscoso, Next-to-next-to-eikonal corrections in the CGC, JHEP **01** (2016) 114, arXiv: 1505.01400 [hep-ph].

[163] T. Altinoluk, G. Beuf, A. Czajka and A. Tymowska, Quarks at next-to-eikonal accuracy in the CGC: Forward quark-nucleus scattering, Phys. Rev. D **104**.1 (2021) 014019, arXiv: 2012.03886 [hep-ph].

[164] T. Altinoluk and G. Beuf, Quark and scalar propagators at next-to-eikonal accuracy in the CGC through a dynamical background gluon field, (Sept. 2021), arXiv: 2109.01620 [hep-ph].

ORIGINAL PAPERS

I

DEEP INELASTIC SCATTERING IN THE DIPOLE PICTURE AT NEXT-TO-LEADING ORDER

by

B. Ducloué, H. Hänninen, T. Lappi and Y. Zhu 2017

Physical Review D 96.9, 094017

DOI: 10.1103/PhysRevD.96.094017

PHYSICAL REVIEW D **96,** 094017 (2017)

Deep inelastic scattering in the dipole picture at next-to-leading order

B. Ducloué,[1,2] H. Hänninen,[1] T. Lappi,[1,2] and Y. Zhu[1,2]

[1]*Department of Physics, P.O. Box 35, 40014 University of Jyväskylä, Finland*
[2]*Helsinki Institute of Physics, P.O. Box 64, 00014 University of Helsinki, Finland*

(Received 7 September 2017; published 20 November 2017)

We study quantitatively the importance of the recently derived next-to-leading-order corrections to the deep inelastic scattering structure functions at small x in the dipole formalism. We show that these corrections can be significant and depend on the factorization scheme used to resum large logarithms of energy into renormalization group evolution with the Balitsky-Kovchegov equation. This feature is similar to what has recently been observed for single inclusive forward hadron production. Using a factorization scheme consistent with the one recently proposed for the single inclusive cross section, we show that it is possible to obtain meaningful results for the deep inelastic scattering cross sections.

DOI: 10.1103/PhysRevD.96.094017

I. INTRODUCTION

At high energy (or equivalently small values of the longitudinal momentum fraction x), the gluon density in hadrons can become nonperturbatively large; this is the regime of gluon saturation. However, the evolution of this gluon density as a function of the momentum fraction x can still be computed using weak coupling techniques, leading to the Balitsky-Kovchegov (BK) evolution equation [1,2]. Knowing the initial gluon density at a given $x = x_0$, one can thus evolve it perturbatively to any $x < x_0$. This initial condition involves nonperturbative dynamics and needs to be extracted from data, but the evolution equation then gives a first principles prediction for smaller x.

The cleanest process to study the partonic structure of hadrons is provided by deep inelastic scattering (DIS). At small x, this process is most conveniently understood in the dipole picture, where the scattering is factorized into a QED splitting of the virtual photon into a quark-antiquark dipole and the subsequent QCD interaction of this dipole with the target. Here, the BK equation describes the dependence of the dipole-target scattering amplitude on the collision energy. Several groups have been able to obtain satisfactory fits to HERA DIS data in the leading-order dipole picture, using the BK equation with running coupling corrections (see for example Refs. [3,4]). To advance the saturation formalism to next-to-leading order (NLO), two key ingredients are needed: the NLO BK equation and the process-dependent NLO impact factors. In addition to many recent methodological developments for these higher-order calculations (see e.g. Refs. [5,6]), progress has been made in both of these directions. The NLO corrections to the BK equation have been computed in Ref. [7] and evaluated numerically in Ref. [8], where it was shown that they can lead to unphysical results. This problem has been subsequently solved by resumming classes of large logarithms [9–11], indeed leading to reasonable results [12].

Concerning impact factors, most of the recent work has concentrated on the NLO corrections to single inclusive forward hadron production. The impact factor for this process has been known for some time [13,14], but the first numerical implementation of these expressions showed that they can make the cross section negative when the transverse momentum of the produced hadron is of the order of a few GeV [15]. Several works have been devoted to solving this issue [16–20], and recently a new proposed formulation of the NLO cross section [21] was shown to lead to physical results [22], albeit with a remaining issue concerning the best way to implement a running QCD coupling constant.

Also, the impact factor for DIS in the dipole picture has been studied in several papers [23–26]. However, the full expressions in the mixed space representation (longitudinal momentum, but transverse coordinate) that are most naturally combined with BK evolution have only become available more recently [27,28]. For a practical implementation of these results, it is essential to match the impact factor calculation with the evolution equation in the correct way, i.e. to factorize the leading high energy logarithms into the high energy evolution. As we shall discuss below, the situation here is very analogous to that of single inclusive particle production.

The main purpose of this paper is twofold. We first want to study the importance of the NLO corrections to have a first estimate of the stability of the perturbative expansion for this quantity. Second, we want to develop a good factorization procedure for matching the renormalization group evolution with the previous calculation of the impact factor. Both of these are prerequisites for a description of experimental data, which will be pursued in a continuation of this work. Our focus in this paper is to demonstrate the feasibility of the factorization scheme and study the general characteristics of the NLO corrections to the cross sections. A full NLO calculation will additionally require including an NLO evolution equation. In this paper, we shall first, in Sec. II, briefly present the NLO impact factor as calculated in Refs. [27,28]. We shall then, in Sec. III, quantify the

effects of the NLO corrections for the Q^2- and x_{Bj}-dependence of the transverse and longitudinal DIS cross sections.

II. IMPACT FACTOR

In the dipole framework, the interaction of a virtual photon with the proton in DIS is factorized as the scattering of a quark-antiquark dipole with the proton. At leading order, the expressions for the cross sections of transversally or longitudinally polarized virtual photons $\sigma_{L,T}$ read

$$\sigma_{L,T}^{\mathrm{LO}}(x_{Bj},Q^2)=4N_{\mathrm{c}}\alpha_{em}\sum_f e_f^2\int_0^1 \mathrm{d}z_1 \times\int_{\mathbf{x}_0,\mathbf{x}_1}\mathcal{K}_{L,T}^{\mathrm{LO}}(z_1,\mathbf{x}_0,\mathbf{x}_1,x_{Bj}), \quad (1)$$

with the shorthand $\int_{\mathbf{x}_0}=\int\frac{\mathrm{d}^2\mathbf{x}_0}{2\pi}$. The integrands are given by the squares of the light cone wave functions for the $\gamma^*\to q\bar{q}$ splitting and the scattering amplitudes for the $q\bar{q}$ dipole to scatter off the target

$$\mathcal{K}_L^{\mathrm{LO}}(z_1,\mathbf{x}_0,\mathbf{x}_1,X)=4Q^2z_1^2(1-z_1)^2 \times K_0^2(QX_2)(1-S_{01}(X)), \quad (2)$$

$$\mathcal{K}_T^{\mathrm{LO}}(z_1,\mathbf{x}_0,\mathbf{x}_1,X)=Q^2z_1(1-z_1)(z_1^2+(1-z_1)^2) \times K_1^2(QX_2)(1-S_{01}(X)), \quad (3)$$

for the longitudinal (L) and transverse (T) polarized virtual photons respectively. Here, the argument of the Bessel functions, related to the lifetime of the $q\bar{q}$-fluctuation, is $X_2^2=z_1(1-z_1)\mathbf{x}_{01}^2$. The scattering amplitude of the dipole is given, in the Color Glass Condensate picture, by the two point function of a correlator of Wilson lines, namely

$$S_{01}(X)\equiv S(\mathbf{x}_{01}=\mathbf{x}_0-\mathbf{x}_1,X) =\left\langle\frac{1}{N_{\mathrm{c}}}\mathrm{Tr}U(\mathbf{x}_0)U^\dagger(\mathbf{x}_1)\right\rangle_X, \quad (4)$$

where we denote by X the momentum fraction (corresponding to the evolution variable in the BK equation $y=\ln 1/X$) at which the Wilson line correlator is to be evaluated.

The NLO corrections to these expressions have been computed in Refs. [27,28]. They involve two kinds of terms: the one loop corrections to the $q\bar{q}$-state and a new $q\bar{q}g$-component in the γ^* Fock state. Following the general idea exposed in Ref. [21] for single inclusive hadron production, we write the (unsubtracted) NLO cross sections as

$$\sigma_{L,T}^{\mathrm{NLO}}=\sigma_{L,T}^{(0)}+\sigma_{L,T}^{qg}+\sigma_{L,T}^{\mathrm{dip}}. \quad (5)$$

In this expression, the first term corresponds to the lowest-order contribution with an unevolved target (i.e. evaluated at the rapidity $X=x_0$). The terms proportional to α_{s} have been organized into two parts. First, the gluon contribution $\sigma_{L,T}^{qg}$ includes all the real contributions (with a gluon emitted into the final state) and a subset of the virtual corrections that need to be combined with the real corrections to cancel any ultraviolet or collinear divergences. The dipole contribution $\sigma_{L,T}^{\mathrm{dip}}$ contains the rest of the virtual corrections. The separation between these two terms is not unique, but the sum of the two is fully determined by the NLO calculation. The expressions for these terms can be written as

$$\sigma_{L,T}^{qg}=8N_{\mathrm{c}}\alpha_{em}\frac{\alpha_sC_{\mathrm{F}}}{\pi}\sum_f e_f^2\int_0^1\mathrm{d}z_1\int^{1-z_1}\frac{\mathrm{d}z_2}{z_2} \times\int_{\mathbf{x}_0,\mathbf{x}_1,\mathbf{x}_2}\mathcal{K}_{L,T}^{\mathrm{NLO}}(z_1,z_2,\mathbf{x}_0,\mathbf{x}_1,\mathbf{x}_2,X(z_2)), \quad (6)$$

$$\sigma_{L,T}^{\mathrm{dip}}=4N_{\mathrm{c}}\alpha_{em}\frac{\alpha_sC_{\mathrm{F}}}{\pi}\sum_f e_f^2\int_0^1\mathrm{d}z_1 \times\int_{\mathbf{x}_0,\mathbf{x}_1}\mathcal{K}_{L,T}^{\mathrm{LO}}(z_1,\mathbf{x}_0,\mathbf{x}_1,X^{\mathrm{dip}}) \times\left[\frac{1}{2}\ln^2\left(\frac{z_1}{1-z_1}\right)-\frac{\pi^2}{6}+\frac{5}{2}\right], \quad (7)$$

with

$$\mathcal{K}_L^{\mathrm{NLO}}(z_1,z_2,\mathbf{x}_0,\mathbf{x}_1,\mathbf{x}_2,X)=4Q^2z_1^2(1-z_1)^2 \times\left\{P\left(\frac{z_2}{1-z_1}\right)\frac{\mathbf{x}_{20}}{\mathbf{x}_{20}^2}\cdot\left(\frac{\mathbf{x}_{20}}{\mathbf{x}_{20}^2}-\frac{\mathbf{x}_{21}}{\mathbf{x}_{21}^2}\right) \times[K_0^2(QX_3)(1-S_{012}(X))-(\mathbf{x}_2\to\mathbf{x}_0)] +\left(\frac{z_2}{1-z_1}\right)^2\frac{\mathbf{x}_{20}\cdot\mathbf{x}_{21}}{\mathbf{x}_{20}^2\mathbf{x}_{21}^2}K_0^2(QX_3)(1-S_{012}(X))\right\}, \quad (8)$$

$$\mathcal{K}_T^{\mathrm{NLO}}(z_1,z_2,\mathbf{x}_0,\mathbf{x}_1,\mathbf{x}_2,X)=Q^2z_1(1-z_1) \times\left\{P\left(\frac{z_2}{1-z_1}\right)(z_1^2+(1-z_1)^2)\frac{\mathbf{x}_{20}}{\mathbf{x}_{20}^2} \cdot\left(\frac{\mathbf{x}_{20}}{\mathbf{x}_{20}^2}-\frac{\mathbf{x}_{21}}{\mathbf{x}_{21}^2}\right)[K_1^2(QX_3)(1-S_{012}(X))-(\mathbf{x}_2\to\mathbf{x}_0)] +\left(\frac{z_2}{1-z_1}\right)^2\left[(z_1^2+(1-z_1)^2)\frac{\mathbf{x}_{20}\cdot\mathbf{x}_{21}}{\mathbf{x}_{20}^2\mathbf{x}_{21}^2} +2z_0z_1\frac{\mathbf{x}_{20}\cdot\mathbf{x}_{21}}{\mathbf{x}_{20}^2X_3^2}-\frac{z_0(z_1+z_2)}{X_3^2}\right]K_1^2(QX_3)(1-S_{012}(X))\right\}. \quad (9)$$

Here, the longitudinal momentum fractions of the quark, antiquark, and gluon are denoted as z_0, z_1, z_2 with

$z_0 + z_1 + z_2 = 1$. The argument of the Bessel functions, related to the lifetime of the $q\bar{q}g$-fluctuation, is $X_3^2 = z_0 z_1 \mathbf{x}_{01}^2 + z_0 z_2 \mathbf{x}_{20}^2 + z_2 z_1 \mathbf{x}_{21}^2$, $P(z) = 1 + (1-z)^2$, and the Wilson line operator corresponding to the scattering of the $q\bar{q}g$-state is

$$S_{012}(X) = \frac{N_c}{2C_F}\left(S_{02}(X)S_{21}(X) - \frac{1}{N_c{}^2}S_{01}(X)\right). \quad (10)$$

It is important to note that, because the functions $\mathcal{K}_{L,T}^{\mathrm{NLO}}(z_1, z_2, \mathbf{x}_0, \mathbf{x}_1, \mathbf{x}_2, X)$ approach a nonzero value when $z_2 \to 0$ at fixed X, the integral over z_2 in $\sigma_{L,T}^{qg}$ produces a large logarithm which should be resummed in the BK evolution of the target. We will do this using the same procedure introduced in Refs. [9,21] and demonstrated in Ref. [22] for the case of single inclusive particle production in forward proton-nucleus collisions. Note that, similarly to the "C_F-term" in the case of the single inclusive cross section, the "dipole" term does not generate such a large logarithmic contribution and therefore does not contribute to the BK evolution.

The starting point of the BK-factorization procedure is to identify the first term in Eq. (5) as the initial condition for the BK evolution with the longitudinal momentum fraction $x_0 \sim 0.01$, i.e.

$$\sigma_{L,T}^{\mathrm{IC}} = 4N_c\alpha_{em}\sum_f e_f^2 \int_0^1 \mathrm{d}z_1 \int_{\mathbf{x}_0,\mathbf{x}_1} \mathcal{K}_{L,T}^{\mathrm{LO}}(z_1, \mathbf{x}_0, \mathbf{x}_1, x_0). \quad (11)$$

As discussed in great detail in Refs. [9,21], the essential feature required for a stable perturbative expansion is that the dipole correlators in $\sigma_{L,T}^{qg}$ must be evaluated at a rapidity scale that depends on the longitudinal momentum of the emitted gluon, i.e. z_2. Here, there are several different possibilities, which are all equivalent at the leading logarithmic level. At NLO accuracy, the different schemes lead to different expressions which are in principle equivalent, but more naturally lend themselves to different approximations.

The choice advocated in Ref. [9] is to consistently use the probe longitudinal momentum k^+ as the evolution variable, sometimes referred to as "probe evolution." In this case, the evolution rapidity is by definition $y = \ln 1/z_2 + y_0$ with some constant y_0 used to make $y = 0$ correspond to the initial condition for the evolution. To determine the lower integration limit for z_2 in this scheme, we have to compare the longitudinal momentum of the emitted soft gluon $z_2 q^+$ to momentum scales in the target. The typical target hadronic momentum scale is given by $P^+ = Q_0^2/(2P^-)$, where Q_0 is some hadronic low transverse momentum scale and the total target light cone energy P^- is obtained from the total center-of-mass energy of the γ^*-target system by $W^2 = 2q^+P^-$. For the eikonal approximation to be valid, we require that the probe gluon momentum is larger than the target momentum scale by a large factor $1/x_0$, i.e. $z_2 q^+ > (1/x_0)P^+$. This translates, using $x_{Bj} \approx Q^2/W^2$, into an integration limit, $z_2 > (x_{Bj}/x_0)(Q_0^2/Q^2)$. If now the soft gluon has a transverse momentum $k_\perp$, the light cone energy required from the target to put the $q\bar{q}g$-state on shell is $\Delta k^- \gtrsim k_\perp^2/(2z_2 q^+)$. The limit on z_2 means that we allow the γ^* system to take a fraction $\Delta k^-/P^- \lesssim x_0(k_\perp^2/Q_0^2)$ of the target light cone energy. If the typical gluon $k_\perp$ is at the hadronic scale Q_0, this is indeed the limit $\Delta k^-/P^- < x_0$ that we would want for the fraction of the target light cone energy. However, the contribution from $k_\perp^2 \sim Q^2 \gg Q_0^2$ goes to larger values of the target momentum fraction $\Delta k^-/P^-$ than we would want. This can generally be expected to be a problem that must be corrected by imposing an additional "kinematical constraint" on the evolution equation [9,29] and on the impact factor [17,19,20].

The other option to probe evolution is to take the view that the evolution variable should always be the target momentum fraction, i.e. the fraction of the target light cone energy $X = \Delta k^-/P^-$. Keeping this momentum fraction small, $X < x_0$, removes the need for an additional kinematical constraint, significantly simplifying the evolution equation. On the other hand, using $\Delta k^-/P^-$ as the evolution variable adds the significant complication that this momentum fraction depends on the transverse momentum of the gluon, $X(z_2) \approx k_\perp^2/(z_2 W^2)$, and when z_2 is not very small also on the momenta of the quark and antiquark. This makes it difficult to implement a light cone energy factorization scale or evolution variable exactly. Parametrically, the transverse momentum $k_\perp$ can range from a hadronic scale Q_0 to the hard scale Q. If one estimates the typical target momentum fraction Δk^- assuming that the typical gluon transverse momentum is at the hadronic scale $k_\perp^2 \sim Q_0^2$, one recovers the same limit $z_2 > (x_{Bj}/x_0)(Q_0^2/Q^2)$ as argued from using k^+ as the factorization variable. In contrast, the argument used in the recent work on single inclusive particle production in proton-nucleus collisions [21,22] was that, at least in that case, the typical transverse momentum of the gluon in the impact factor is in fact the hard scale of the process $k_\perp \sim Q$. Assuming that this is the case also for DIS means that one should restrict the integrals to a smaller phase space $z_2 > (x_{Bj}/x_0)$. The latter is the limit that we will use in this work. In terms of the k^+-momentum, this limit corresponds to the emitted gluon having longitudinal momentum $z_2 q^+ \gtrsim (Q^2/Q_0^2)(1/x_0)P^+$ instead of the $z_2 q^+ > (1/x_0)P^+$ that one would use in the factorization scheme with k^+. This approximation leads to a rather simple formulation for the cross section. Improving the accuracy would require including the additional phase space $(x_{Bj}/x_0)(Q_0^2/Q^2) < z_2 < (x_{Bj}/x_0)$ in the cross section on one hand but cutting out the large logarithmic increase from this region by using a kinematical constraint

in the evolution equation, as advocated e.g. in Refs. [9,27,28]. Due to the considerably increased complication of this formulation, we will defer studying this alternative to future work.

To summarize, in this paper, we will follow the choice made for single inclusive particle production in proton-nucleus collisions in Refs. [21,22] and choose the target momentum fraction as the evolution variable, supplemented with the assumption that all transverse momenta are of the order Q. Thus, we take $X(z_2) = x_{Bj}/z_2$ and set the kinematical limit by requiring $X(z_2) < x_0$, i.e. $z_2 > x_{Bj}/x_0$. Implementing this limit, we can now complete the "unsubtracted" form of the cross section (5) with the lower integration limit in z_2 as

$$\sigma_{L,T}^{\mathrm{NLO}} = \sigma_{L,T}^{\mathrm{IC}} + \sigma_{L,T}^{qg,\mathrm{unsub}} + \sigma_{L,T}^{\mathrm{dip}}, \tag{12}$$

with

$$\sigma_{L,T}^{qg,\mathrm{unsub}} = 8N_c\alpha_{em}\frac{\alpha_s C_F}{\pi}\sum_f e_f^2\int_0^1 \mathrm{d}z_1\int_{x_{Bj}/x_0}^{1-z_1}\frac{\mathrm{d}z_2}{z_2} \times \int_{\mathbf{x}_0,\mathbf{x}_1,\mathbf{x}_2} \mathcal{K}_{L,T}^{\mathrm{NLO}}(z_1,z_2,\mathbf{x}_0,\mathbf{x}_1,\mathbf{x}_2,X(z_2)). \tag{13}$$

We then note that taking $z_2 = 0$ as the explicit z_2-argument in $\mathcal{K}_{L,T}^{\mathrm{NLO}}$ [but not in the implicit dependence through $X(z_2)$] leads to an integral version of the BK equation. Using this, we can also rewrite Eq. (12) in a form that involves the leading-order cross sections with BK-evolved dipole operators evaluated at the scale x_{Bj} instead of x_0. The result is a strictly equivalent "subtracted" form of the cross section

$$\sigma_{L,T}^{\mathrm{NLO}} = \sigma_{L,T}^{\mathrm{LO}} + \sigma_{L,T}^{qg,\mathrm{sub}} + \sigma_{L,T}^{\mathrm{dip}}, \tag{14}$$

where $\sigma_{L,T}^{\mathrm{LO}}$ is the well-known leading-order expression (1) and

$$\sigma_{L,T}^{qg,\mathrm{sub}} = 8N_c\alpha_{em}\frac{\alpha_s C_F}{\pi}\sum_f e_f^2\int_0^1 \mathrm{d}z_1\int_{x_{Bj}/x_0}^{1}\frac{\mathrm{d}z_2}{z_2} \times \int_{\mathbf{x}_0,\mathbf{x}_1,\mathbf{x}_2} [\theta(1-z_1-z_2) \times \mathcal{K}_{L,T}^{\mathrm{NLO}}(z_1,z_2,\mathbf{x}_0,\mathbf{x}_1,\mathbf{x}_2,X(z_2)) - \mathcal{K}_{L,T}^{\mathrm{NLO}}(z_1,0,\mathbf{x}_0,\mathbf{x}_1,\mathbf{x}_2,X(z_2))]. \tag{15}$$

Contrary to $\sigma_{L,T}^{qg}$, the dipole term $\sigma_{L,T}^{\mathrm{dip}}$ is not associated with the rapidity evolution of the target, and thus the rapidity scale of the dipole operators in this term is left unspecified. As presented in Refs. [27,28], this term is already integrated over z_2. Therefore, it is not possible to evaluate the dipole operators in this term at the same scale $X(z_2) = x_{Bj}/z_2$ as in $\sigma_{L,T}^{qg}$, which would arguably be the most natural thing to do. Here, we will evaluate this term at $X^{\mathrm{dip}} = x_{Bj}$ since the integrand vanishes when $z_2 \to 0$, and therefore one can expect the integral to be dominated by the region where z_2 is close to 1. Note, however, that the difference between $X = x_{Bj}/z_2$ and $X = x_{Bj}$, while formally subleading for the dipole term, could be numerically important, as is the case for the analogous C_F-terms in single inclusive particle production [22].

To obtain the previous expressions, we followed closely the original idea of Ref. [21], which was shown in Ref. [22] to lead to reasonable numerical results for single inclusive particle production at all transverse momenta. Bear in mind that the two expressions in Eqs. (12) and (14) are completely equivalent and are related through the BK evolution equation. In the following, it will also be interesting to compare the results obtained in this formulation with what we denote here as the "x_{Bj}-subtraction" scheme, which is expressed as

$$\sigma_{L,T}^{\mathrm{NLO},x_{Bj}-\mathrm{sub}} = \sigma_{L,T}^{\mathrm{LO}} + \sigma_{L,T}^{qg,\mathrm{sub}^*} + \sigma_{L,T}^{\mathrm{dip}}, \tag{16}$$

where $\sigma_{L,T}^{qg,\mathrm{sub}^*}$ is an approximation of Eq. (15) by using $X(z_2) = x_{Bj}$ and taking the limit $x_{Bj}/x_0 \to 0$ in the lower limit of the integral over z_2. This is the analog of what was denoted in Refs. [20,22] as the "CXY" subtraction scheme after the authors of [13,14] for the case of single inclusive particle production, which is formally equivalent at this order of perturbation theory, but leads to problematic results for high momentum scales.

III. NUMERICAL RESULTS

Since we do not consider a possible impact parameter dependence of the dipole correlators, one of the coordinate integrals in the expressions shown in the previous section is trivial and leads to a factor corresponding to the target transverse area, denoted as $\sigma_0/2$. This quantity is usually determined by a fit to data, such as in Refs. [3,4]. Performing such a fit goes well beyond the scope of the present work; therefore, for simplicity, we leave out this overall normalization factor and present results for $F_{L,T}/\frac{\sigma_0}{2}$, where the structure functions $F_{L,T}$ are defined as

$$F_{L,T}(x_{Bj},Q^2) = \frac{Q^2}{4\pi^2\alpha_{\mathrm{em}}}\sigma_{L,T}(x_{Bj},Q^2). \tag{17}$$

We first focus on the fixed coupling case, using $\alpha_s = 0.2$ both when evaluating the NLO cross section and when solving the leading-order Balitsky-Kovchegov equation. Note that for the factorization scheme to be consistent both the cross section calculation and the BK equation need to have the same coupling constant. For the BK equation, we use a McLerran-Venugopalan initial condition [30]

$$S(\mathbf{r},x_0) = \exp\left[-\frac{\mathbf{r}^2Q_{s,0}^2}{4}\ln\left(\frac{1}{|\mathbf{r}|\Lambda_{\mathrm{QCD}}}+e\right)\right], \tag{18}$$

where we take $Q_{s,0}^2 = 0.2\ \mathrm{GeV}^2$ and $\Lambda_{\mathrm{QCD}} = 0.241\ \mathrm{GeV}$.

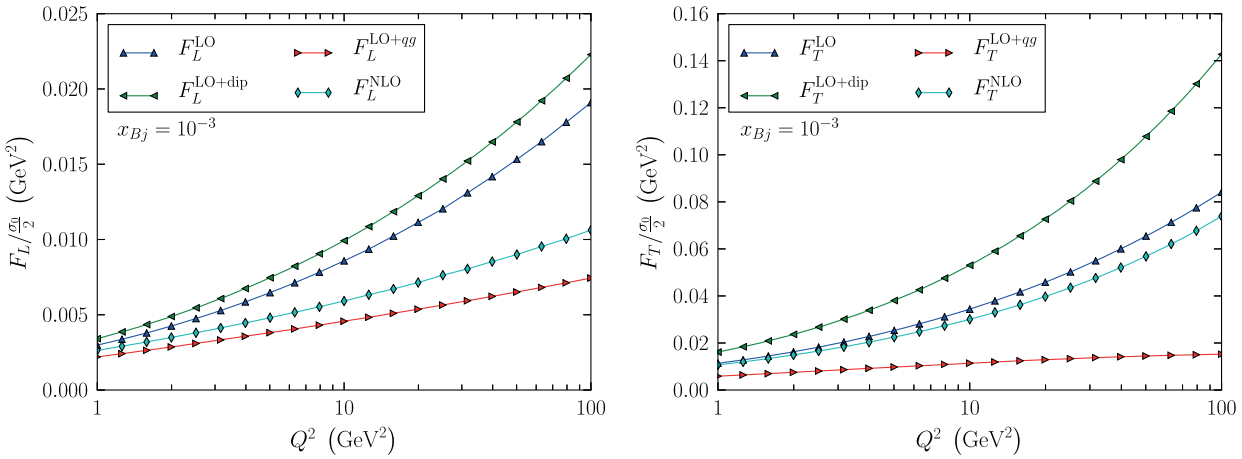

FIG. 1. LO and NLO contributions to F_L (left) and F_T (right) as a function of Q^2 at $x_{Bj} = 10^{-3}$ with $\alpha_s = 0.2$.

In Fig. 1, we show the importance of the NLO corrections σ^{dip} and σ^{qg} to F_L and F_T as a function of Q^2 at $x_{Bj} = 10^{-3}$. In both the longitudinal and transverse cases, the sign of these corrections is the same: the dipole contribution is positive, which can be understood from Eq. (7), while the qg contribution is negative. Because the second correction is larger in magnitude than the first one, the total NLO cross section is smaller than the leading-order (LO) one.

In Fig. 2, we show how these results change if we use the approximate x_{Bj}-subtraction in Eq. (16) for the qg-term. This term is still negative and has a larger magnitude, especially at large Q, which makes the whole NLO cross section negative for $Q^2 \gtrsim 10$ GeV^2, both in the longitudinal and transverse cases. Therefore, approximating Eq. (14) by Eq. (16), while in principle justified in a weak coupling sense, has in fact a large effect in this region and can lead to unphysical results. A similar behavior was observed in single inclusive particle production at large transverse momenta [22]. This shows that to get meaningful results one should really use the factorization procedure in Eq. (12) or equivalently Eq. (14), which we will do for the rest of this paper.

We also show in Figs. 3 and 4 the x_{Bj}-dependence of the different NLO contributions to F_L and F_T for fixed $Q^2 = 1$ and 50 GeV^2. These plots show a change of behavior: at small x_{Bj}, the NLO cross section is smaller than the LO one, while it becomes larger when x_{Bj} approaches x_0. The reason is the following: as explained previously, the dipole NLO correction is always positive. In addition, as can be seen from Eq. (13), the qg-part is 0 at $x_{Bj} = x_0$ since the z_2-integration range vanishes. Therefore, the NLO cross section is the sum of the leading-order one and a positive correction, i.e. always larger than the leading-order one. This is related to the reason why, as explained in the previous section, we would prefer to use an expression of

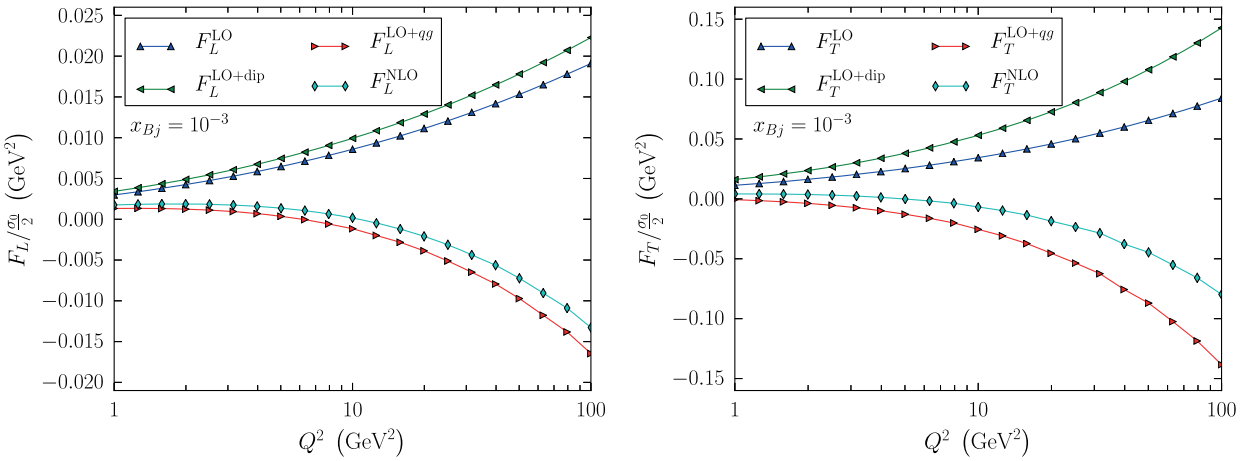

FIG. 2. LO and NLO contributions to F_L (left) and F_T (right) as a function of Q^2 at $x_{Bj} = 10^{-3}$ with $\alpha_s = 0.2$ and using the x_{Bj}-subtraction procedure.

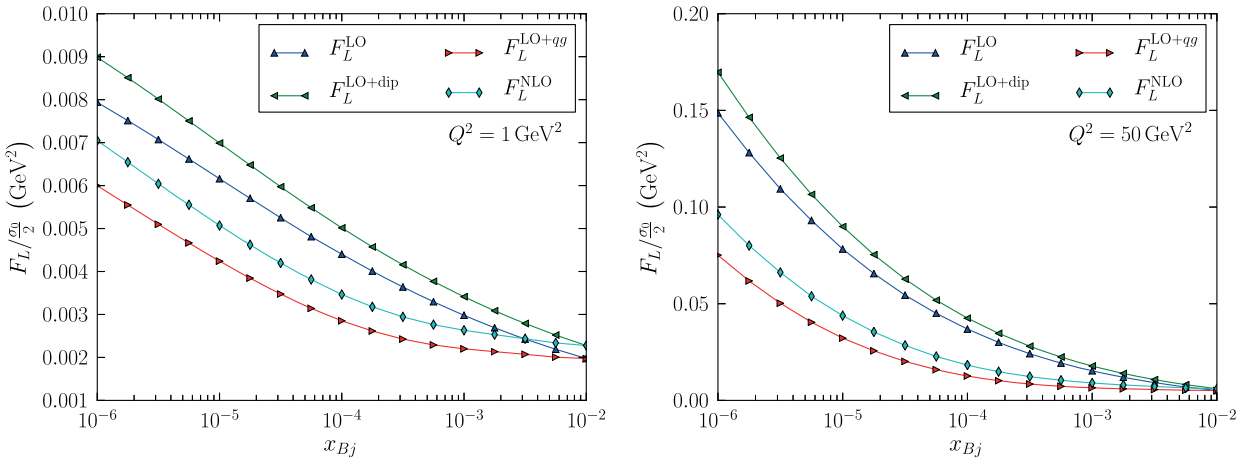

FIG. 3. LO and NLO contributions to F_L as a function of x_{Bj} at $Q^2 = 1$ GeV^2 (left) and $Q^2 = 50$ GeV^2 (right) with $\alpha_s = 0.2$.

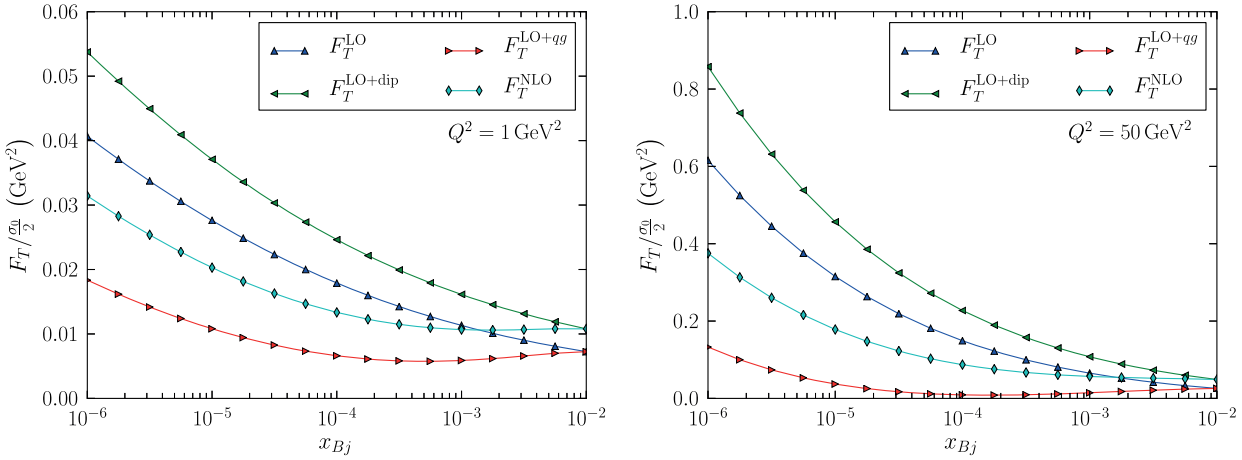

FIG. 4. LO and NLO contributions to F_T as a function of x_{Bj} at $Q^2 = 1$ GeV^2 (left) and $Q^2 = 50$ GeV^2 (right) with $\alpha_s = 0.2$.

the dipole part which has an explicit integration over z_2. This would allow one to use, also in the dipole term, Wilson line operators at a rapidity scale which depends on the gluon momentum fraction, i.e. the invariant mass of the $q\bar{q}g$-state, in a way that is more consistent with the qg-part. The expressions we currently use restrict the kinematics to the regime of validity of the dipole picture $X < x_0$ for the qg-part but not for the dipole part. This leads to a sign change of the total NLO contribution as a function of x_{Bj} near x_0.

While the running of the strong coupling α_s is in principle a subleading effect in a leading-order calculation, this effect has to be taken into account at next-to-leading order. To evaluate its importance here, we use the simple parent dipole prescription in which the coupling is given by

$$\alpha_s(\mathbf{x}_{01}^2) = \frac{4\pi}{\beta_0 \ln\left(\frac{4C^2}{\mathbf{x}_{01}^2 \Lambda_{\mathrm{QCD}}^2}\right)}, \tag{19}$$

with $\beta_0 = (11N_c - 2n_f)/3$. The scaling parameter C^2 is taken to be $C^2 = e^{-2\gamma_e}$, as suggested in Refs. [31,32], and the coupling is frozen at the value 0.7 at large dipole sizes. When fitting the initial condition of the BK equation to data at leading order (see e.g. Refs. [3,4]), one usually uses instead the Balitsky prescription [33] for the running coupling and additionally takes C^2 as a fit parameter in order to obtain a slow enough evolution. However, in principle, the choice of the running coupling prescription is a higher-order effect, and thus the parent dipole prescription is equally well justified in a weak coupling sense. Also, on the phenomenological level, it has been shown [8,10–12] that the NLO corrections to the BK kernel slow down the evolution, and thus it is not *a priori* obvious which prescription will yield a good description of experimental data at the NLO level.

As stated before, our purpose here is not to achieve a fit to DIS data but to quantify the effect of the NLO corrections to the impact factor compared to previous

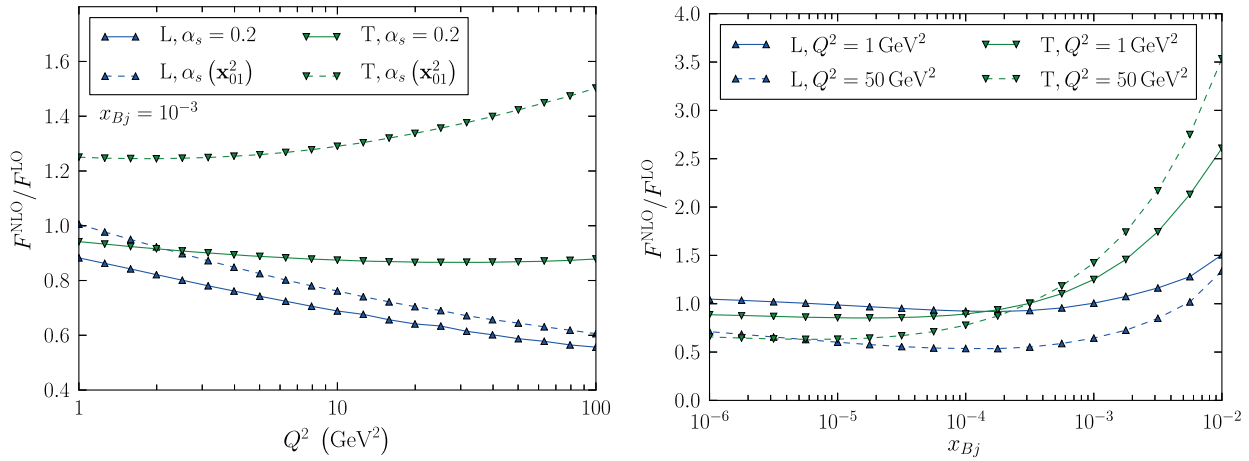

FIG. 5. Left: NLO/leading-order ratio for F_L and F_T as a function of Q^2 at $x_{Bj} = 10^{-3}$ with fixed (solid) and running (dashed) coupling. Right: NLO/leading-order ratio for F_L and F_T as a function of x_{Bj} at $Q^2 = 1$ GeV^2 (solid) and $Q^2 = 50$ GeV^2 (dashed) with running coupling.

LO calculations. Therefore, we show, in the left panel of Fig. 5, the NLO/LO ratio for F_L and F_T as a function of Q^2 at $x_{Bj} = 10^{-3}$ with fixed and running coupling. In the right panel, we show the same ratio as a function of x_{Bj} at $Q^2 = 1$ and 50 GeV^2 with running coupling. We see that for fixed coupling the net effect of the NLO corrections is to decrease the cross section. However, especially for a running coupling, this feature is reversed close to the initial rapidity scale $x_{Bj} \approx x_0$. As discussed above, this is related to the fact that the negative NLO corrections related to BK evolution vanish in this limit while the positive ones in the dipole term do not, indicating a strong dependence on the details of the factorization scheme. While this is a transient effect that does not alter the asymptotic high energy behavior, treating it carefully will be important for an attempt to describe experimental data.

IV. OUTLOOK

In conclusion, we have in this paper evaluated, for the first time, the total DIS cross section in the dipole picture with an impact factor derived at NLO accuracy. We developed a factorization procedure to resum the leading high energy logarithms into a BK renormalization group evolution of the target, in line with recent developments for single inclusive cross sections. We showed that this procedure leads to physical, well-behaved expressions for the cross sections with, however, large transient effects in the region close to the limit of validity of the eikonal approximation. With the caveat of understanding these transient effects, there is a good perspective for a comparison with experimental data. In order to achieve this at consistent NLO accuracy, the impact factors studied here must be combined with a solution of the NLO BK equation [12] or at least a collinearly resummed version of the LO equation [10,11]. A major missing theoretical ingredient that is needed for a more detailed comparison with data is to work out the corresponding impact factor for massive quarks. This should in principle be a straightforward, if laborious, extension of the existing calculation for massless quarks.

ACKNOWLEDGMENTS

We thank G. Beuf for sharing and discussing the results of Ref. [28] before publication, R. Paatelainen for discussions, and H. Mäntysaari for sharing his BK evolution code. This work has been supported by the Academy of Finland, Projects No. 273464 and No. 303756 and by the European Research Council, Grant No. ERC-2015-CoG-681707.

[1] I. Balitsky, Operator expansion for high-energy scattering, Nucl. Phys. **B463**, 99 (1996).

[2] Y. V. Kovchegov, Small-x F2 structure function of a nucleus including multiple pomeron exchanges, Phys. Rev. D **60**, 034008 (1999).

[3] J. L. Albacete, N. Armesto, J. G. Milhano, P. Quiroga-Arias, and C. A. Salgado, AAMQS: A non-linear QCD analysis of new HERA data at small-x including heavy quarks, Eur. Phys. J. C **71**, 1705 (2011).

[4] T. Lappi and H. Mäntysaari, Single inclusive particle production at high energy from HERA data to proton-nucleus collisions, Phys. Rev. D **88**, 114020 (2013).
[5] T. Lappi and R. Paatelainen, The one loop gluon emission light cone wave function, Ann. Phys. (Amsterdam) **379**, 34 (2017).
[6] A. Ayala, M. Hentschinski, J. Jalilian-Marian, and M. E. Tejeda-Yeomans, Spinor helicity methods in high-energy factorization: Efficient momentum-space calculations in the color glass condensate formalism, Nucl. Phys. **B920**, 232 (2017).
[7] I. Balitsky and G. A. Chirilli, Next-to-leading order evolution of color dipoles, Phys. Rev. D **77**, 014019 (2008).
[8] T. Lappi and H. Mäntysaari, Direct numerical solution of the coordinate space Balitsky-Kovchegov equation at next to leading order, Phys. Rev. D **91**, 074016 (2015).
[9] G. Beuf, Improving the kinematics for low-x QCD evolution equations in coordinate space, Phys. Rev. D **89**, 074039 (2014).
[10] E. Iancu, J. D. Madrigal, A. H. Mueller, G. Soyez, and D. N. Triantafyllopoulos, Resumming double logarithms in the QCD evolution of color dipoles, Phys. Lett. B **744**, 293 (2015).
[11] E. Iancu, J. D. Madrigal, A. H. Mueller, G. Soyez, and D. N. Triantafyllopoulos, Collinearly-improved BK evolution meets the HERA data, Phys. Lett. B **750**, 643 (2015).
[12] T. Lappi and H. Mäntysaari, Next-to-leading order Balitsky-Kovchegov equation with resummation, Phys. Rev. D **93**, 094004 (2016).
[13] G. A. Chirilli, B.-W. Xiao, and F. Yuan, One-Loop Factorization for Inclusive Hadron Production in pA Collisions in the Saturation Formalism, Phys. Rev. Lett. **108**, 122301 (2012).
[14] G. A. Chirilli, B.-W. Xiao, and F. Yuan, Inclusive hadron productions in pA collisions, Phys. Rev. D **86**, 054005 (2012).
[15] A. M. Stasto, B.-W. Xiao, and D. Zaslavsky, Towards the Test of Saturation Physics beyond Leading Logarithm, Phys. Rev. Lett. **112**, 012302 (2014).
[16] Z.-B. Kang, I. Vitev, and H. Xing, Next-to-Leading Order Forward Hadron Production in the Small-x Regime: Rapidity Factorization, Phys. Rev. Lett. **113**, 062002 (2014).
[17] A. M. Staśto, B.-W. Xiao, F. Yuan, and D. Zaslavsky, Matching collinear and small x factorization calculations for inclusive hadron production in pA collisions, Phys. Rev. D **90**, 014047 (2014).
[18] T. Altinoluk, N. Armesto, G. Beuf, A. Kovner, and M. Lublinsky, Single-inclusive particle production in proton-nucleus collisions at next-to-leading order in the hybrid formalism, Phys. Rev. D **91**, 094016 (2015).
[19] K. Watanabe, B.-W. Xiao, F. Yuan, and D. Zaslavsky, Implementing the exact kinematical constraint in the saturation formalism, Phys. Rev. D **92**, 034026 (2015).
[20] B. Ducloué, T. Lappi, and Y. Zhu, Single inclusive forward hadron production at next-to-leading order, Phys. Rev. D **93**, 114016 (2016).
[21] E. Iancu, A. H. Mueller, and D. N. Triantafyllopoulos, CGC factorization for forward particle production in proton-nucleus collisions at next-to-leading order, J. High Energy Phys. 12 (2016) 041.
[22] B. Ducloué, T. Lappi, and Y. Zhu, Implementation of NLO high energy factorization in single inclusive forward hadron production, Phys. Rev. D **95**, 114007 (2017).
[23] I. Balitsky and G. A. Chirilli, Photon impact factor in the next-to-leading order, Phys. Rev. D **83**, 031502 (2011).
[24] G. Beuf, NLO corrections for the dipole factorization of DIS structure functions at low x, Phys. Rev. D **85**, 034039 (2012).
[25] R. Boussarie, A. V. Grabovsky, L. Szymanowski, and S. Wallon, Impact factor for high-energy two and three jets diffractive production, J. High Energy Phys. 09 (2014) 026.
[26] R. Boussarie, A. V. Grabovsky, L. Szymanowski, and S. Wallon, On the one loop $\gamma^{(*)} \to q\bar{q}$ impact factor and the exclusive diffractive cross sections for the production of two or three jets, J. High Energy Phys. 11 (2016) 149.
[27] G. Beuf, Dipole factorization for DIS at NLO: Loop correction to the photon to quark-antiquark light-front wave-functions, Phys. Rev. D **94**, 054016 (2016).
[28] G. Beuf, Dipole factorization for DIS at NLO: Combining the $q\bar{q}$ and $q\bar{q}g$ contributions, Phys. Rev. D **96**, 074033 (2017).
[29] L. Motyka and A. M. Stasto, Exact kinematics in the small x evolution of the color dipole and gluon cascade, Phys. Rev. D **79**, 085016 (2009).
[30] L. D. McLerran and R. Venugopalan, Computing quark and gluon distribution functions for very large nuclei, Phys. Rev. D **49**, 2233 (1994).
[31] Y. V. Kovchegov and H. Weigert, Triumvirate of running couplings in small-x evolution, Nucl. Phys. **A784**, 188 (2007).
[32] T. Lappi and H. Mäntysaari, On the running coupling in the JIMWLK equation, Eur. Phys. J. C **73**, 2307 (2013).
[33] I. Balitsky, Quark contribution to the small-x evolution of color dipole, Phys. Rev. D **75**, 014001 (2007).

II

ONE-LOOP CORRECTIONS TO LIGHT CONE WAVE FUNCTIONS: THE DIPOLE PICTURE DIS CROSS SECTION

by

H. Hänninen, T. Lappi and R. Paatelainen 2018

Annals of Physics 393, 358–412

DOI: 10.1016/j.aop.2018.04.015

Annals of Physics 393 (2018) 358–412

Contents lists available at ScienceDirect

Annals of Physics

journal homepage: www.elsevier.com/locate/aop

One-loop corrections to light cone wave functions: The dipole picture DIS cross section

H. Hänninen [a], T. Lappi [a,b], R. Paatelainen [c,b,a,*]

[a] Department of Physics, P.O. Box 35, 40014 University of Jyväskylä, Finland
[b] Helsinki Institute of Physics, P.O. Box 64, 00014 University of Helsinki, Finland
[c] Department of Physics, P.O. Box 64, 00014 University of Helsinki, Finland

ARTICLE INFO

Article history:
Received 5 February 2018
Accepted 11 April 2018
Available online 22 April 2018

Keywords:
Light-cone perturbation theory
QCD
Small-x
DIS
Color glass Condensate

ABSTRACT

We develop methods to perform loop calculations in light cone perturbation theory using a helicity basis, refining the method introduced in our earlier work. In particular this includes implementing a consistent way to contract the four-dimensional tensor structures from the helicity vectors with d-dimensional tensors arising from loop integrals, in a way that can be fully automatized. We demonstrate this explicitly by calculating the one-loop correction to the virtual photon to quark–antiquark dipole light cone wave function. This allows us to calculate the deep inelastic scattering cross section in the dipole formalism to next-to-leading order accuracy. Our results, obtained using the four dimensional helicity scheme, agree with the recent calculation by Beuf using conventional dimensional regularization, confirming the regularization scheme independence of this cross section.

1. Introduction

Light cone perturbation theory (LCPT), the Hamiltonian formulation of field theory on the light front [1–4] is a widely used calculational tool in particle and hadronic physics. Its added calculational complexity compared to covariant perturbation theory is balanced by several advantages in the description of bound states or other multiparton systems. The light cone wave functions (LCWF's) and operators have a simpler behavior under transverse Lorentz boosts than covariant ones. The perturbative expansion is organized in terms of a Fock state expansions involving only physical

* Corresponding author at: Helsinki Institute of Physics, P.O. Box 64, 00014 University of Helsinki, Finland.
E-mail address: risto.paatelainen@jyu.fi (R. Paatelainen).

https://doi.org/10.1016/j.aop.2018.04.015
0003-4916/

degrees of freedom with definite helicities. This gives a natural physical interpretation for the factorization of scattering processes into the properties of the incoming and outgoing hadronic states on one hand, and the short distance partonic scatterings between elementary constituents on the other.

Modern hadronic and nuclear scattering experiments probe QCD with increasing accuracy in the high energy or small-x regime. Here the large available phase space for gluon radiation enables the generation of a dense system of gluons with nonperturbatively large gluon fields. One the other hand, balancing the complication arising from the nonlinear dynamics of the gluons, the high collision energy simplifies the treatment of the scattering by allowing an eikonal approximation for the interactions of individual partons with the color field. Typically this situation is described using the effective theory of QCD known as the Color Glass Condensate (CGC) [5]. In this picture, the scattering of a dilute probe off the dense color field is factorized into the partonic structure of the "simple" probe (virtual photon, or an individual quark or gluon in the case of forward rapidities in proton–nucleus collisions), and the eikonal scattering of the partons of the probe with the target color field. This allows for a treatment that includes nonlinear interactions in the dense target color field to all orders, while the simple probe can be treated exactly. This picture is advantageous in particular for understanding exclusive processes. Light cone perturbation theory is the method of choice for understanding the structure of the probe.

In order to develop a more quantitative description of several scattering processes in the high energy limit, CGC calculations have recently been advancing to next-to-leading order (NLO) accuracy for several different processes. The NLO corrections to the small-x evolution equations (in particular the Balitsky–Kovchegov (BK) equation [6–8]) have been derived and the required resummations of collinear logarithms studied in several papers [9–19]. There have been several calculations of single [20–25] and double [26] inclusive parton production at forward rapidity in high energy proton–nucleus collisions. In the context of deep inelastic scattering, both inclusive [27–31] and exclusive [32–34] processes have been studied at the NLO order.

Our present paper is a follow-up of our recent work [35], where we introduced the idea of performing loop calculations in LCPT using a helicity basis for the elementary vertices. In this paper we will present a better formulation of the calculational scheme introduced in [35], correcting a partially incorrect formulation used in that paper. As a demonstration, we will calculate the one-loop correction to the virtual photon to quark–antiquark dipole light cone wave function. We will then use this to derive the NLO cross section for inclusive DIS in the dipole factorization picture. We perform the calculation using the four-dimensional helicity (FDH) scheme, where polarization sums are calculated in four dimensions, and ultraviolet divergences are regularized by performing momentum integrals in d dimensions. Our results recover the ones obtained in [29,30] after a lengthy manual calculation, in what we would argue to be a more systematical and economical way. Also, although intermediate results are different in the FDH scheme used here and the conventional dimensional regularization (CDR) used in [29,30], we see that these scheme dependent terms cancel in the final result. As a separate small difference to the calculation in [29,30], we implement the cancellation between UV divergences in the real and virtual corrections to the cross section by adding and subtracting a slightly different subtraction term, leading to a numerically smoother expression for the cross section. We verify both analytically and numerically that our results are equivalent to those in [29,30].

The rest of the paper is structured as follows. We will first discuss the technical aspects of the calculation in Section 2, concentrating on the differences compared to our earlier work [35]. We then recall how one calculates cross sections by combining eikonal interactions with a color field target with light cone wave functions in Section 3. After briefly rederiving the leading order virtual photon wave functions in Section 4 we calculate the corresponding one-loop corrections in Section 5. After calculating also the real corrections, i.e. the wave functions for gluon emission from the dipole, in Section 6 we combine our results into the NLO DIS cross section in Section 7, before concluding in Section 8. Technical details of the calculation have been spelled out in the Appendices.

2. Higher order LCPT computations

The purpose of this paper is to develop and demonstrate techniques for the perturbative calculation of *light cone wave functions*. These are formed from interaction vertices, where spatial momentum

($\vec{p} = (p^+, \mathbf{p})$) is conserved but light cone energy p^- is not, and energy denominators which depend on the energy differences between intermediate states. In loop diagrams, the spatial momentum circulating in the loop must be integrated over. In these momentum integrals we encounter $p^+ \to 0$ divergences, $\mathbf{p} \to 0$ divergences and ultraviolet (UV) divergences ($\mathbf{p} \to \infty$). Combinations of the first two divergences encode soft, collinear and spurious gauge divergences. All of these divergences have very different physical interpretations, and it makes therefore sense to regularize them all by different means. In particular we will regularize, if needed, the soft divergence with a cutoff, and regulate the UV divergences by integrating over the transverse momenta in $2 - 2\varepsilon$ dimensions. The basic normalizations, notations etc. are explained in much more detail in Ref. [35], and we will here concentrate only on the differences with respect to the formulation used there. We first discuss the different flavors of dimensional regularization in Section 2.1, and the required modifications to the formulation of the elementary vertices compared to the explicitly 2-dimensional one used in [35] in Section 2.2. We will then, as an explicit demonstration, calculate two helicity sums appearing in the calculation of the NLO DIS impact factor in Section 2.3, and briefly write down the instantaneous vertices needed in our calculation in Section 2.4.

2.1. Dimensional regularization schemes in gauge field theories

In the evaluation of loop and phase space momentum integrals one encounters divergences which have to be properly regularized. In gauge field theories a satisfactory regulator has to respect gauge invariance and unitarity which requires that one treats the momenta and helicities equally. For practical computations, the only choice is a form of dimensional regularization.

For the discussion of different versions of dimensional regularization schemes it is useful to define unobserved and observed particles. Unobserved particles are either virtual ones which circulate in internal loops or particles which are external but soft or collinear with other external particles. All the rest are observed particles. The common feature in all dimensional regularization schemes is the continuation of the momenta of the unobserved particles into $d \neq 4$. Once this is done, there is still some freedom regarding the dimensionality of the momenta of the observed particles as well as the treatment of polarization vectors (or helicities) of the unobserved and observed particles. Thus, one can define a set of different versions of dimensional regularization schemes:

- The conventional dimensional regularization (CDR) scheme [36], in which both observed and unobserved polarization vectors and momenta are continued to d dimension (i.e. all gluons have $d - 2$ helicity states).
- The 't Hooft–Veltman (HV) scheme [37], in which the unobserved particle momenta and polarization vectors are continued to d dimensions (i.e. unobserved gluons have $d - 2$ helicity states), but the momenta and polarization vectors of observed particles are kept in four dimensions (i.e. observed gluons have 2 helicity states)
- The dimensional reduction (DR) scheme [38], in which the momenta of unobserved particles are continued to $d < 4$ dimensions, but polarization vectors of unobserved and observed particles are kept in four dimensions (i.e. all gluons have 2 helicity states).
- The four dimensional helicity (FDH) scheme [39,40], in which the momenta of unobserved particles is continued to $d > 4$ dimensions, and all observed particles are kept in four dimensions (i.e. observed gluons have 2 helicity states). All unobserved internal states are treated as d_s-dimensional, where $d_s > d$ in all intermediate steps. Any factor of dimension arising from the numerator Lorentz and Dirac algebra should be labeled as d_s, and should be distinct from the dimension d. Once the spin and tensor algebra is done one analytically continues the result to $d < 4$ and takes the limit $d_s \to 4$ for the spins of the internal particles.

Typically the dimensionality is parametrized as $d = 4 - 2\varepsilon$. We will also use the notation $d_\perp \equiv d - 2 = 2 - 2\varepsilon$ for the number of transverse dimensions in light cone coordinates. Within the DR and FDH schemes one can still choose the momentum of observed particles to be either d-dimensional or 4-dimensional. At one-loop order, however, these choices lead to difference of $\mathcal{O}(\varepsilon)$ and thus one can set the observed particles momenta to be 4-dimensional.

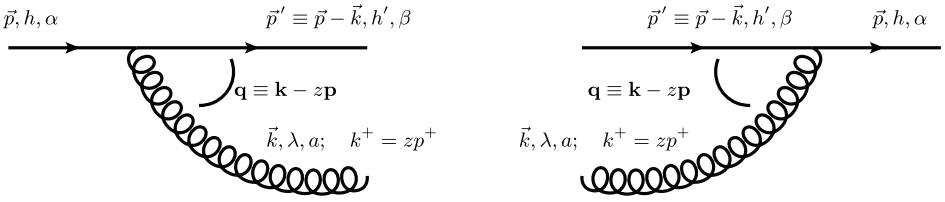

Fig. 1. Left: Gluon emission vertex from a quark $V^{\alpha;\beta,a}_{h;h',\lambda}(\mathbf{q}, z)$ Eq. (6), where α, β are quark colors, h, h' the quark helicities before and after the emission, a the gluon color and λ the gluon helicity. Right: Gluon absorption vertex into quark $V^{\beta,a;\alpha}_{h',\lambda;h}(\mathbf{q}, z)$ Eq. (8).

The question of which regularization scheme is most efficient for a given calculation is of course very subjective. We would like to argue in this paper that for one-loop LCPT calculations the helicity basis supplemented with the FDH regularization scheme is in fact the most efficient one. However, as we will show below, the helicity basis approach can also be combined with other dimensional regularization scheme choices, and in particular with the CDR scheme. Our overall motivation for using the FDH scheme is the following. The one-loop results for physical observables arise from a product of a one-loop tensorial loop integral and another tensor from the spin/helicity structure of the vertices. The resulting contributions can be classified into three kinds of terms. The most divergent part is obtained by taking the divergent $1/\varepsilon$-term from the integral, and evaluating the helicity structure in 4 spacetime dimensions. This part has no scheme dependence. The scheme dependent finite part comes from taking a $\sim \varepsilon$ term from the helicity structure and multiplying it by the $1/\varepsilon$-term from the loop integral. The scheme independent finite part, on the other hand, involves the finite part of the integral and a helicity structure which can, at one-loop accuracy, be evaluated in $d_s = 4$ dimensions. Out of these three, the scheme independent finite part is by far the most complicated one, because in many cases the tensorial structure in the finite part of the loop integral is much more complicated than in the pole part. Thus being able to calculate the finite scheme independent part as efficiently as possible is a priority.

Our strategy is to write the elementary vertices of the theory in a way which, in 4 dimensions, has a very practical structure in terms of the helicities of the particles. These structures are, when the helicities are evaluated in 4 dimensions, written in terms of Levi-Civita tensors in 2 transverse dimensions. This leads to a very easy way to calculate the most complicated scheme independent finite part. The price to pay, however, is that calculating the scheme dependent ε/ε-part becomes more complicated, because to evaluate the helicity sums accurately up to order ε the Levi-Civita structure cannot be used any more. In stead, one must carefully evaluate contractions involving both d_s-dimensional structures from the spin sums and d-dimensional ones from the loop integrals. Here, however, one is dealing with the simpler tensorial structure of the $1/\varepsilon$-part of the loop integral, and this represents a relatively small part of the calculation.

2.2. Decomposition of quark vertices

Let us first consider the simplest light cone vertex shown in Fig. 1 (left), where a gluon with momentum $\vec{k}$ and helicity h is emitted from a quark with momentum $\vec{p}$ and helicity h. For simplicity of notation we denote the two quark spin states with spin $\pm 1/2$ by $h = \pm 1$, i.e. the actual helicity of the quark is $h/2$. As discussed in [35], we denote this vertex[1] as

$$V^{\alpha;\beta,a}_{h;h',\lambda} = -gt^a_{\beta\alpha}\left[\bar{u}_{h'}(p')\not{\epsilon}^*_\lambda(k)u_h(p)\right]. \tag{1}$$

Using the Dirac equation satisfied by the spinors, 3-momentum conservation $\vec{p} = \vec{p}\,' + \vec{k}$ and some Dirac algebra (see Appendix A for the details), the tensorial structure of matrix element in Eq. (1) can

[1] Our sign convention for the covariant derivative is $D_\mu = \partial_\mu - igA_\mu$, which is the opposite to that of Refs. [29,30].

be decomposed to the symmetric and antisymmetric parts as

$$V^{\alpha;\beta,a}_{h;h',\lambda}(\mathbf{q},z)=\frac{-gt^a_{\beta\alpha}}{z(1-z)p^+}\left[\left(1-\frac{z}{2}\right)\delta^{ij}\bar{u}_{h'}(p')\gamma^+u_h(p)-\frac{z}{4}\bar{u}_{h'}(p')\gamma^+[\gamma^i,\gamma^j]u_h(p)\right]\mathbf{q}^i\boldsymbol{\epsilon}^{*j}_\lambda. \tag{2}$$

Here we have expressed the vertex in terms of the momentum fraction $z=k^+/p^+$, $0\le z\le 1$ and the center-of-mass transverse momentum $\mathbf{q}=\mathbf{k}-z\mathbf{p}$. The first matrix element is simple

$$\bar{u}_{h'}(p')\gamma^+u_h(p)=2p^+\sqrt{1-z}\delta_{h,h'}. \tag{3}$$

The antisymmetric matrix element $\bar{u}_{h'}(p')\gamma^+[\gamma^i,\gamma^j]u_h(p)$, on the other hand, can only be calculated simply in exactly four dimensions by relating it to the helicity operator. For the loop computations we also encounter it in situations where the indices i,j have to be contracted with $d_\perp$-dimensional Kronecker deltas arising from $d_\perp$-dimensional tensorial transverse momentum integrals. For performing the numerator algebra in these cases we introduce for it a more general notation

$$\mathcal{V}^{ij}_{h',h}\equiv\frac{\bar{u}_{h'}(p')\gamma^+[\gamma^i,\gamma^j]u_h(p)}{2p^+\sqrt{1-z}}. \tag{4}$$

In exactly $d_\perp=2$ transverse dimensions this simplifies (see Appendix A) to

$$\mathcal{V}^{ij}_{h',h}\underset{d_\perp\to 2}{\to}-2ih\delta_{h,h'}\epsilon^{ij}. \tag{5}$$

However, when the helicity sums (numerators of loop diagrams) are needed to order ϵ we need to remember the full definition (4). A similar procedure can be carried out for the gluon absorption vertex, for antiquarks and for quark–antiquark pair creation and annihilation vertices. Let us simply collect the results here, in every case parametrizing the longitudinal momentum with a splitting momentum fraction $0\le z\le 1$:

- Gluon emission from quark Fig. 1 (left), with momentum conservation $\vec{p}=\vec{p}\,'+\vec{k}$, $z=k^+/p^+$ and $\mathbf{q}=\mathbf{k}-z\mathbf{p}$:

$$\begin{aligned}V^{\alpha;\beta,a}_{h;h',\lambda}(\mathbf{q},z)&=-gt^a_{\beta\alpha}\left[\bar{u}_{h'}(p')\not{\epsilon}^*_\lambda(k)u_h(p)\right]\\&=\frac{-2gt^a_{\beta\alpha}}{z\sqrt{1-z}}\left[\left(1-\frac{z}{2}\right)\delta^{ij}\delta_{h',h}-\frac{z}{4}\mathcal{V}^{ij}_{h',h}\right]\mathbf{q}^i\boldsymbol{\epsilon}^{*j}_\lambda,\end{aligned} \tag{6}$$

  with

$$\mathcal{V}^{ij}_{h',h}\equiv\frac{\bar{u}_{h'}(p')\gamma^+[\gamma^i,\gamma^j]u_h(p)}{2p^+\sqrt{1-z}}\underset{d_\perp\to 2}{\to}-2ih\delta_{h',h}\epsilon^{ij}. \tag{7}$$

- Gluon absorption by quark Fig. 1 (right), with momentum conservation $\vec{p}=\vec{p}\,'+\vec{k}$, $z=k^+/p^+$ and $\mathbf{q}=\mathbf{k}-z\mathbf{p}$:

$$V^{\beta,a;\alpha}_{h',\lambda;h}(\mathbf{q},z)=-gt^a_{\alpha\beta}\left[\bar{u}_h(p)\not{\epsilon}_\lambda(k)u_{h'}(p')\right]=\frac{-2gt^a_{\alpha\beta}}{z\sqrt{1-z}}\left[\left(1-\frac{z}{2}\right)\delta^{ij}\delta_{h,h'}+\frac{z}{4}\mathcal{V}^{ij}_{h,h'}\right]\mathbf{q}^i\boldsymbol{\epsilon}^j_\lambda, \tag{8}$$

  with

$$\mathcal{V}^{ij}_{h,h'}\equiv\frac{\bar{u}_h(p)\gamma^+[\gamma^i,\gamma^j]u_{h'}(p')}{2p^+\sqrt{1-z}}\underset{d_\perp\to 2}{\to}-2ih\delta_{h,h'}\epsilon^{ij}. \tag{9}$$

- Gluon emission from antiquark with momentum $\vec{p}$, with momentum conservation $\vec{p}=\vec{p}\,'+\vec{k}$, $z=k^+/p^+$ and $\mathbf{q}=\mathbf{k}-z\mathbf{p}$:

$$\begin{aligned}\overline{V}^{\alpha;\beta,a}_{h;h',\lambda}(\mathbf{q},z)&=-gt^a_{\alpha\beta}\left[-\bar{v}_h(p)\not{\epsilon}^*_\lambda(k)v_{h'}(p')\right]\\&=\frac{2gt^a_{\alpha\beta}}{z\sqrt{1-z}}\left[\left(1-\frac{z}{2}\right)\delta^{ij}\delta_{h,h'}+\frac{z}{4}\overline{\mathcal{V}}^{ij}_{h,h'}\right]\mathbf{q}^i\boldsymbol{\epsilon}^{*j}_\lambda,\end{aligned} \tag{10}$$

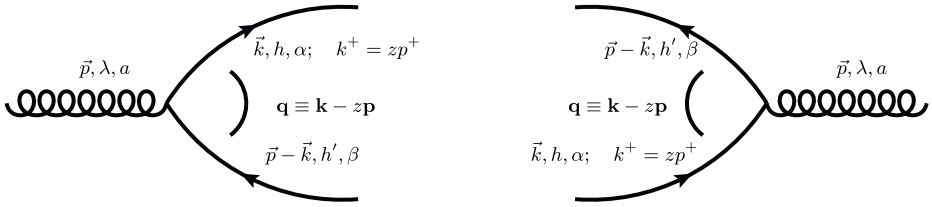

Fig. 2. Left: Gluon splitting vertex into quark–antiquark pair, $A^{a;\beta,\alpha}_{\lambda;h,h'}(\mathbf{q}, z)$ Eq. (14). Right: Quark–antiquark annihilation vertex into gluon $A^{\beta,\alpha;a}_{h',h;\lambda}(\mathbf{q}, z)$ Eq. (16).

with

$$\overline{\mathcal{V}}^{ij}_{h,h'} \equiv \frac{\bar{v}_h(p)\gamma^+[\gamma^i, \gamma^j]v_{h'}(p')}{2p^+\sqrt{1-z}} \underset{d_\perp \to 2}{\to} 2ih\delta_{h,h'}\epsilon^{ij}. \tag{11}$$

- Gluon absorption into antiquark, with momentum conservation $\vec{p} = \vec{p}\,' + \vec{k}$, $z = k^+/p^+$ and $\mathbf{q} = \mathbf{k} - z\mathbf{p}$:

$$\begin{aligned} \overline{V}^{\beta,a;\alpha}_{h',\lambda;h}(\mathbf{q}, z) &= -gt^a_{\beta\alpha}\left[-\bar{v}_{h'}(p')\not{\epsilon}_\lambda(k)v_h(p)\right] \\ &= \frac{2gt^a_{\beta\alpha}}{z\sqrt{1-z}}\left[\left(1-\frac{z}{2}\right)\delta^{ij}\delta_{h',h} - \frac{z}{4}\overline{\mathcal{V}}^{ij}_{h',h}\right]\mathbf{q}^i\boldsymbol{\epsilon}^j_\lambda, \end{aligned} \tag{12}$$

with

$$\overline{\mathcal{V}}^{ij}_{h',h} \equiv \frac{\bar{v}_{h'}(p')\gamma^+[\gamma^i, \gamma^j]v_h(p)}{2p^+\sqrt{1-z}} \underset{d_\perp \to 2}{\to} 2ih\delta_{h',h}\epsilon^{ij}. \tag{13}$$

- Gluon with momentum $\vec{p}$ splitting into quark with momentum $\vec{k}$ and antiquark, Fig. 2, with momentum conservation $\vec{p} = \vec{p}\,' + \vec{k}$, $z = k^+/p^+$ and $\mathbf{q} = \mathbf{k} - z\mathbf{p}$:

$$\begin{aligned} A^{a;\alpha,\beta}_{\lambda;h,h'}(\mathbf{q}, z) &= -gt^a_{\alpha\beta}\left[\bar{u}_h(k)\not{\epsilon}_\lambda(p)v_{h'}(p')\right] \\ &= \frac{-2gt^a_{\alpha\beta}}{\sqrt{z(1-z)}}\left[\left(z-\frac{1}{2}\right)\delta^{ij}\delta_{h,-h'} + \frac{1}{4}\mathcal{A}^{ij}_{h,h'}\right]\mathbf{q}^i\boldsymbol{\epsilon}^j_\lambda, \end{aligned} \tag{14}$$

with

$$\mathcal{A}^{ij}_{h,h'} \equiv \frac{\bar{u}_h(k)\gamma^+[\gamma^i, \gamma^j]v_{h'}(p')}{2p^+\sqrt{z(1-z)}} \underset{d_\perp \to 2}{\to} -2ih\delta_{h,-h'}\epsilon^{ij}. \tag{15}$$

- Quark with momentum $\vec{k}$ and antiquark annihilating to gluon with momentum $\vec{p}$, Fig. 2, with momentum conservation $\vec{p} = \vec{p}\,' + \vec{k}$, $z = k^+/p^+$ and $\mathbf{q} = \mathbf{k} - z\mathbf{p}$:

$$\begin{aligned} \overline{A}^{\alpha,\beta;a}_{h',h;\lambda}(\mathbf{q}, z) &= -gt^a_{\beta\alpha}\left[-\bar{v}_{h'}(p')\not{\epsilon}^*_\lambda(p)u_h(k)\right] \\ &= \frac{2gt^a_{\beta\alpha}}{\sqrt{z(1-z)}}\left[\left(z-\frac{1}{2}\right)\delta^{ij}\delta_{h,-h'} - \frac{1}{4}\overline{\mathcal{A}}^{ij}_{h',h}\right]\mathbf{q}^i\boldsymbol{\epsilon}^{*j}_\lambda, \end{aligned} \tag{16}$$

with

$$\overline{\mathcal{A}}^{ij}_{h',h} \equiv \frac{\bar{v}_{h'}(p')\gamma^+[\gamma^i, \gamma^j]u_h(k)}{2p^+\sqrt{z(1-z)}} \underset{d_\perp \to 2}{\to} -2ih\delta_{h',-h}\epsilon^{ij}. \tag{17}$$

2.3. Evaluating helicity sums

The value of a diagram in the perturbative expansion of light cone wave functions is obtained by multiplying the factors for the vertices, integrating over internal momenta in loops and summing over the helicities of internal particles. Let us demonstrate how this procedure works in terms of the quark vertices introduced above with two concrete examples that will be needed in the calculation of the virtual photon wave function.

First, let us look at a quark propagator correction diagram such as the one shown in Fig. 8. The loop part involves the product of the gluon emission vertex (6) and the absorption of the same gluon (8), summed over the helicities of the quark and gluon inside the loop

$$\sum_{\lambda,h'} V^{\alpha;\beta,a}_{h;h',\lambda}(\mathbf{q},z)V^{\beta,a;\alpha}_{h',\lambda;h}(\mathbf{q},z). \tag{18}$$

The integrand in the transverse momentum integral is proportional to $q^i q^j$, thus the value of the dimensionally regulated integral is proportional to a $(d-2)$-dimensional Kronecker delta $\delta^{ij}_{(d)}$. The vertices are proportional to (d_s-2)-dimensional gluon polarization vectors, and summing over the helicity states of the gluon yields

$$\sum_{\lambda} \boldsymbol{\varepsilon}^{*k}_{\lambda}\boldsymbol{\varepsilon}^{l}_{\lambda} = \delta^{kl}_{(d_s)}. \tag{19}$$

We are then tasked with evaluating the expression

$$\mathrm{num}_1 = \sum_{h'}\left[\left(1-\frac{z}{2}\right)\delta^{ik}\delta_{h',h} - \frac{z}{4}\mathcal{V}^{ik}_{h',h}\right]\left[\left(1-\frac{z}{2}\right)\delta^{jl}\delta_{h,h'} + \frac{z}{4}\mathcal{V}^{jl}_{h,h'}\right]\delta^{ij}_{(d)}\delta^{kl}_{(d_s)}. \tag{20}$$

Now in principle, to correctly evaluate this for arbitrary $d_s > d > 4$, we need to use the definitions (7) and (9) and carefully perform the Dirac matrix algebra. This we will do in detail for the more complicated case of Eq. (26). However, let us here evaluate the sum (20) with a simple, but less general trick that yields the same result.

In this case the most complicated structure appearing is the product of two antisymmetric tensors, not more. In fact, in such a case we can formally express the antisymmetric vertex structure in terms of a "(d_s-2)-dimensional" two-index Levi-Civita tensor $\epsilon^{ij}_{(d_s)}$. In general such an object does of course not exist, but here it can be given an explicit meaning in terms of perfectly well-defined (d_s-2)-dimensional Kronecker deltas using the Fierz identity

$$\epsilon^{ij}_{(d_s)}\epsilon^{kl}_{(d_s)} = \delta^{ik}_{(d_s)}\delta^{jl}_{(d_s)} - \delta^{il}_{(d_s)}\delta^{jk}_{(d_s)}. \tag{21}$$

When there are more than two Levi-Civita tensors, there would be several inequivalent ways to get rid of them using the Fierz identity. Thus the trick we are now describing cannot be used in these more complicated cases.

To now evaluate the helicity sum (20) we first use the fact that for massless quarks helicity is conserved at the emission vertex and thus the sum over the intermediate quark helicity h' is trivial. This gives, promoting the 4-dimensional expressions for the antisymmetric tensors in Eqs. (7) and (9) into d_s-dimensional ones,

$$\mathrm{num}_1 = \left[\left(1-\frac{z}{2}\right)\delta^{ik} + ih\frac{z}{2}\epsilon^{ik}_{(d_s)}\right]\left[\left(1-\frac{z}{2}\right)\delta^{jl} - ih\frac{z}{2}\epsilon^{jl}_{(d_s)}\right]\delta^{ij}_{(d)}\delta^{kl}_{(d_s)}. \tag{22}$$

We then get rid of the Levi-Civita-tensors using the Fierz identity (21) to get

$$\mathrm{num}_1 = \left(1-\frac{z}{2}\right)^2(d-2) + \left(\frac{z}{2}\right)^2(d-2)(d_s-3), \tag{23}$$

where one must remember that $d_s > d$, i.e.

$$\delta^{ij}_{(d_s)}\delta^{ij}_{(d_s)} = d_s-2, \quad \delta^{ij}_{(d)}\delta^{ij}_{(d)} = d-2, \quad \delta^{ij}_{(d_s)}\delta^{ij}_{(d)} = d-2 \tag{24}$$

and that $h^2 = 1$ in our convention. This yields the correct result for both the FDH (taking $d_s = 4$, $d = 4 - 2\varepsilon$) and for the CDR schemes (taking $d_s = d = 4 - 2\varepsilon$). The result (23) appears in perfectly conventional QCD calculations of the $q \to qg$ splitting function in dimensional regularization. One could speculate about a physical interpretation for the two terms, independent of d_s and proportional to $d_s - 3$. The first one results from the part of the vertex that is independent of helicity, and therefore does not depend on the number of helicity states. The second term comes from the antisymmetric part of the vertex where the gluon and quark are constrained to have a different helicity, thus it is proportional not to the total number of gluon helicities $d_s - 2$, but to the number of helicities orthogonal to that of the quark, namely $d_s - 3$.

A more complicated example is provided by vertex correction diagrams, such as the one in Fig. 10. Here (with a trivial simplification of the color structure of the gluon splitting vertex (14) to a virtual photon splitting), one has a structure like

$$\sum_{h',h'',\sigma} V^{\tilde{\alpha},a;\alpha}_{h',\sigma;h}(\mathbf{q}, z_1) A_{\lambda;h',h''}(\mathbf{k}, z_2) \overline{V}^{\tilde{\alpha};\beta,a}_{h'';h''',\sigma}(\mathbf{p}, z_3). \tag{25}$$

Writing this out in terms of the decompositions (8), (14) and (10) of the vertices into symmetric and antisymmetric parts, one encounters a product of three antisymmetric vertex factors. This structure is then multiplied with a $(d_s - 2)$-dimensional Kronecker delta from the sum over the internal gluon helicity σ, but also $(d - 2)$-dimensional ones from the loop integrals. Now there would be three inequivalent ways to use the Fierz identity (21) to remove two of the three Levi-Civita tensors, and thus we cannot get an unambiguous result in the same way as above. Thus we need to use the definitions of the antisymmetric vertex factors, (9), (15) and (11).

In stead of working out the full expression here, let us concentrate on the most difficult part involving a product of three antisymmetric structures in the vertices. We take as an example one of the kind of terms that arise when evaluating the structure (25), and calculate

$$\mathrm{num}_2^{lm} = \sum_{h',h''} \mathcal{V}^{ij}_{h,h'} \mathcal{A}^{kl}_{h',h''} \overline{\mathcal{V}}^{mn}_{h'',h'''} \delta^{ik}_{(d)} \delta^{jn}_{(d_s)}, \tag{26}$$

where we have already performed the sum over the helicity σ, yielding a $(d_s - 2)$-dimensional $\delta^{jn}_{(d_s)}$, and taken one particular term of the $(d - 2)$-dimensional tensor integral with indices ikm. Writing this out in terms of the full definitions of the antisymmetric vertex factors (9), (15) and (11) we have

$$\begin{aligned} \mathrm{num}_2^{lm} = \sum_{h',h''} & \frac{\bar{u}_h(p_1)\gamma^+[\gamma^i, \gamma^j]u_{h'}(p_2)}{2\sqrt{p_1^+ p_2^+}} \frac{\bar{u}_{h'}(p_2)\gamma^+[\gamma^k, \gamma^l]v_{h''}(p_3)}{2\sqrt{p_2^+ p_3^+}} \\ & \times \frac{\bar{v}_{h''}(p_3)\gamma^+[\gamma^m, \gamma^n]v_{h'''}(p_4)}{2\sqrt{p_3^+ p_4^+}} \delta^{ik}_{(d)} \delta^{jn}_{(d_s)}. \end{aligned} \tag{27}$$

In a massless theory helicity is conserved at the vertex, therefore we know that $h = h' = -h'' = -h'''$. However, in order to evaluate this expression we do not use this, but revert to the usual procedure from covariant perturbation theory calculations and transform the sums over intermediate fermion helicities to Dirac matrices. Thus we substitute

$$\sum_h u_h(p)\bar{u}_h(p) = \not{p} \tag{28}$$

to write

$$\mathrm{num}_2^{lm} = \frac{\bar{u}_h(p_1)\gamma^+[\gamma^i, \gamma^j]\not{p}_2\gamma^+[\gamma^k, \gamma^l]\not{p}_3\gamma^+[\gamma^m, \gamma^n]v_{h'''}(p_4)}{2\sqrt{p_1^+ p_2^+}2\sqrt{p_2^+ p_3^+}2\sqrt{p_3^+ p_4^+}} \delta^{ik}_{(d)} \delta^{jn}_{(d_s)}. \tag{29}$$

Now we note that $\gamma^+\gamma^+ = 0$ and γ^+ and γ^- commute with $[\gamma^i, \gamma^j]$. Thus the only nonzero contribution to the matrix element comes from the terms where one takes from every $\not{p}_i$ the term $p_i^+\gamma^-$ in order to kill the corresponding γ^+. Using $\gamma^+\gamma^-\gamma^+ = 2\gamma^+$ it is easy to see that effectively

every factor $\not{p}_i\gamma^+$ is just replaced by $2p_i^+$, canceling the corresponding factor in the denominator. We are then left with

$$\mathrm{num}_2^{lm} = \frac{\bar{u}_h(p_1)\gamma^+[\gamma^i,\gamma^j][\gamma^k,\gamma^l][\gamma^m,\gamma^n]v_{h'''}(p_4)}{2\sqrt{p_1^+p_4^+}}\delta^{ik}_{(d)}\delta^{jn}_{(d_s)}. \tag{30}$$

Now remembering that the external momenta and polarization vectors are 2-dimensional, and $d_s > d > 4$ at this stage, it is a straightforward task to evaluate either manually or, most importantly, using a symbolic calculation program:

$$[\gamma^i,\gamma^j][\gamma^k,\gamma^l][\gamma^m,\gamma^n]\delta^{ik}_{(d)}\delta^{jn}_{(d_s)} = 8(d-3)(d_s-4)\delta^{lm} - 4(19-3d_s-6d+dd_s)[\gamma^l,\gamma^m]. \tag{31}$$

Here we have identified terms of the type $\delta^{mm'}_{(d)}[\gamma^l,\gamma^{m'}]$ with $[\gamma^l,\gamma^m]$ and written both $\delta^{lm}_{(d_s)}$ and $\delta^{mm'}_{(d)}\delta^{lm'}_{(d_s)}$ simply as δ^{lm} knowing that both indices l and m are to be contracted with external vectors. Using this result we can write the result in terms of the symmetric and antisymmetric parts of the leading order vertex structure as

$$\mathrm{num}_2^{lm} = 4(d-3)(d_s-4)\delta^{lm} - 4(19-3d_s-6d+dd_s)\mathcal{A}^{lm}_{hh'''}. \tag{32}$$

Setting $d = d_s$ here one would obtain the CDR result. It is interesting to note that in the FDH scheme $d_s = 4$ the symmetric δ^{lm}-term vanishes; this is an additional simplification that one gains at the expense of evaluating the algebra in d, d_s dimensions. As a consistency check we can go to the limit $d = d_s = 4$:

$$\mathrm{num}_2^{lm} \underset{d=d_s\to 4}{\to} -8ih\delta_{h,-h'''}\epsilon^{lm} = 4\mathcal{A}^{lm}_{h,h'''}. \tag{33}$$

The same result can be obtained directly by taking the terms in (26) in $d = d_s = 4$ dimensions

$$\begin{aligned}\mathrm{num}_2^{lm} &\underset{d=d_s=4}{=} \left[-2ih\delta_{h,h'}\epsilon^{ij}\right]\left[-2ih'\delta_{h',-h''}\epsilon^{kl}\right]\left[2ih''\delta_{h'',h'''}\epsilon^{mn}\right]\delta^{ik}\delta^{jn} \\ &= -8ih\delta_{h,-h'''}\epsilon^{lm} = 4\mathcal{A}^{lm}_{h,h'''}.\end{aligned} \tag{34}$$

Note that as a calculational operation, the introduction and subsequent removal of the $\not{p}$ happens in the same way in all combinations of emission vertices from fermions. In practice one can keep track of the terms of the calculation by writing out the vertices in terms of the $d = 4$ notation involving 2-dimensional Levi-Civita tensors. Then, whenever an ambiguity arises as to the meaning of products of the Levi-Civita-tensors, one replaces ϵ^{ij} by $[\gamma^i,\gamma^j]$, orders the vertices following the fermion line, performs contractions of the γ-matrices with d- and d_s-dimensional external tensors, expresses the result in terms of $[\gamma^i,\gamma^j]$ and δ^{ij} and identifies these in terms of the vertex structure of the leading order diagram. This procedure greatly simplifies the appearance of a factorized form for the loop corrections, which appear as multiplicative corrections to the corresponding leading order wave functions.

Note on [35]

Let us briefly note the difference between the formulation introduced here and the one used in our earlier work [35]. There we first calculated the $(d-2)$-dimensional loop tensorial integrals, which result in a structure that contains $(d-2)$-dimensional Kronecker deltas. These were then contracted with the $(d_s-2=2)$-dimensional gluon polarization vectors as $\delta^{ij}_{(d)}\boldsymbol{\varepsilon}^j_\lambda \to \boldsymbol{\varepsilon}^i_\lambda$. The error in this calculation comes when the resulting polarization vectors were then treated again as (d_s-2)-dimensional ones in order to perform the polarization sums. In fact, contracting with a lower dimensional Kronecker delta projects the polarization vector into a lower dimensional subspace; this was not taken into account in the calculation of [35]. We have checked that with the correct treatment presented in this paper, the power divergences in the longitudinal cutoff α, present in the final result of [35], cancel.

Let us finally point out an essential technical aspect that enables the correct way to calculate the polarization sums. One has to write all 3-particle vertices in a form where the only dependence

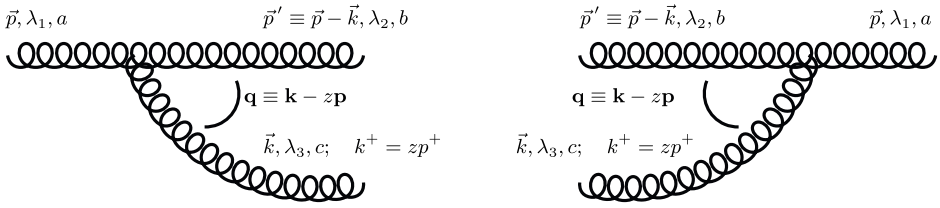

Fig. 3. Left: Gluon splitting vertex $\Gamma^{a;bc}_{\lambda_1;\lambda_2,\lambda_3}(\mathbf{q}, z)$ Eq. (35), where a, b, c are the gluon colors and $\lambda_1, \lambda_2, \lambda_3$ gluon helicities. Right: Gluon merging vertex $\Gamma^{bc;a}_{\lambda_2,\lambda_3;\lambda_1}(\mathbf{q}, z)$ Eq. (36).

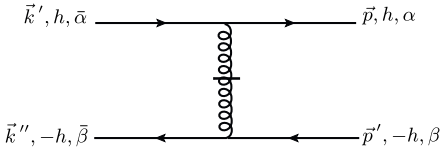

Fig. 4. Time ordered (momenta flows from left to right) instantaneous vertex contributing to the $q\bar{q}$-component of the longitudinal virtual photon wave function at NLO.

on the gluon polarization is in the linear dependence on the polarization vector of each gluon, see e.g. Eq. (6) or Eq. (35). Then the expression for a given diagram becomes quadratic in the internal gluon polarization vectors, and the polarization sum can be evaluated using Eq. (19). The resulting $(d_s - 2)$-dimensional Kronecker delta can then be correctly contracted with both $(d_s - 2)$- and $(d - 2)$-dimensional objects. In contrast, writing the elementary vertex (1) in a form like $\delta_{h,h'}\left(\delta_{\lambda,h} + (1-z)\delta_{\lambda,-h}\right)\boldsymbol{\epsilon}_\lambda \cdot \mathbf{q}$ as in Ref. [35], while correct, has an additional dependence on the polarization λ. This results in expressions where summing over the internal polarizations correctly is difficult.

2.4. Other vertices

In addition, we also have two different type of LC elementary vertices with 3-gluon self interaction: The elementary vertex for $1 \to 2$ gluon splitting shown in Fig. 3 is given by

$$\Gamma^{a;b,c}_{\lambda_1;\lambda_2,\lambda_3}(\mathbf{q}, z) = -2igf^{abc}\left[\frac{\boldsymbol{\epsilon}^{*j}_{\lambda_2}\boldsymbol{\epsilon}^{*k}_{\lambda_3}\boldsymbol{\epsilon}^{l}_{\lambda_1}}{1-z} + \frac{\boldsymbol{\epsilon}^{*j}_{\lambda_3}\boldsymbol{\epsilon}^{*k}_{\lambda_2}\boldsymbol{\epsilon}^{l}_{\lambda_1}}{z} - \boldsymbol{\epsilon}^{j}_{\lambda_1}\boldsymbol{\epsilon}^{*k}_{\lambda_3}\boldsymbol{\epsilon}^{*l}_{\lambda_2}\right]\delta^{ij}\delta^{kl}\mathbf{q}^i. \tag{35}$$

Similarly, the $2 \to 1$ gluon merging vertex is given by

$$\Gamma^{b,c;a}_{\lambda_2,\lambda_3;\lambda_1}(\mathbf{q}, z) = +2igf^{abc}\left[\frac{\boldsymbol{\epsilon}^{j}_{\lambda_2}\boldsymbol{\epsilon}^{k}_{\lambda_3}\boldsymbol{\epsilon}^{*l}_{\lambda_1}}{1-z} + \frac{\boldsymbol{\epsilon}^{j}_{\lambda_3}\boldsymbol{\epsilon}^{k}_{\lambda_2}\boldsymbol{\epsilon}^{*l}_{\lambda_1}}{z} - \boldsymbol{\epsilon}^{*j}_{\lambda_1}\boldsymbol{\epsilon}^{k}_{\lambda_3}\boldsymbol{\epsilon}^{l}_{\lambda_2}\right]\delta^{ij}\delta^{kl}\mathbf{q}^i. \tag{36}$$

As we will discuss in more detail below, the instantaneous interaction diagrams contribute to the one-loop wave functions and to the 3-particle final states. We will not present here the full set of instantaneous vertices (see [4]) but merely the ones needed here, and for the combinations of helicities needed for our calculation. Similarly as above, one can easily derive more general expressions as discussed above, here we present only the ones in $d_s = 4$ dimensions that are needed for our present calculation.

The instantaneous gluon exchange diagram Fig. 4 is given by the following matrix element

$$\mathfrak{I}^{(4)} = -g^2 t^a_{\alpha\bar{\alpha}} t^a_{\beta\bar{\beta}}\left[\bar{u}_h(p)\gamma^+ u_h(k')\right]\frac{1}{(k'^+ - p^+)^2}\left[\bar{v}_{-h}(k'')\gamma^+ v_{-h}(p')\right] \tag{37}$$

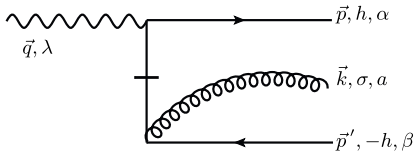

Fig. 5. Time ordered (momenta flows from left to right) instantaneous diagram contributing to the $q\bar{q}g$-component of the transverse virtual photon wave function at NLO.

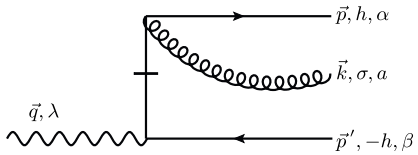

Fig. 6. Time ordered (momenta flows from left to right) instantaneous diagram contributing to the $q\bar{q}g$-component of the transverse virtual photon wave function at NLO.

which simplifies in $d_s = 4$ to

$$\mathfrak{I}^{(4)} = -4g^2 t^a_{\alpha\bar{\alpha}} t^a_{\beta\bar{\beta}} \frac{\sqrt{p^+ p'^+ k'^+ k''^+}}{(k'^+ - p^+)^2}, \tag{38}$$

where the momenta are labeled as in Fig. 4.

The matrix element for $\gamma \to q\bar{q}g$ via the exchange of an instantaneous quark, diagram Fig. 5, is given by

$$\mathfrak{I}^{(5)} = \frac{-ee_f g t^a_{\alpha\beta}}{2} \bar{u}_h(p) \not{\epsilon}_\lambda(q) \frac{\gamma^+}{(p'^+ + k^+)} \not{\epsilon}^*_\sigma(k) v_{-h}(p') \tag{39}$$

which, in $d_s = 4$, can be expressed in the helicity basis as

$$\mathfrak{I}^{(5)} = -ee_f g t^a_{\alpha\beta} \frac{\sqrt{p^+ p'^+}}{(p'^+ + k^+)} \left[\delta^{ij} - ih\epsilon^{ij}\right] \boldsymbol{\epsilon}^{*i}_\sigma \boldsymbol{\epsilon}^j_\lambda. \tag{40}$$

Similarly, the matrix element for the other instantaneous quark $\gamma \to q\bar{q}g$ diagram Fig. 6 is given by

$$\mathfrak{I}^{(6)} = \frac{+ee_f g t^a_{\alpha\beta}}{2} \bar{u}_h(p) \not{\epsilon}^*_\sigma(k) \frac{\gamma^+}{(p^+ + k^+)} \not{\epsilon}_\lambda(q) v_{-h}(p'), \tag{41}$$

which in the helicity basis and $d_s = 4$ reduces to

$$\mathfrak{I}^{(6)} = +ee_f g t^a_{\alpha\beta} \frac{\sqrt{p^+ p'^+}}{(p^+ + k^+)} \left[\delta^{ij} + ih\epsilon^{ij}\right] \boldsymbol{\epsilon}^{*i}_\sigma \boldsymbol{\epsilon}^j_\lambda. \tag{42}$$

3. Calculating the DIS cross section from light cone wave functions

We consider a setup where a relativistic projectile moving in the light-cone x^+ direction scatters on a very dense and highly boosted target moving in the light-cone x^- direction. At high energy the target consists of a gluon field, and the scattering can be evaluated using the eikonal approximation in terms of Wilson lines in this field [2,41]. The total cross section for a virtual photon scattering from a classical gluon field can be obtained by the optical theorem as twice the forward inelastic scattering amplitude. With the appropriate normalization [2] this results in:

$$\sigma^{\gamma^*}[A] = \frac{2}{2q^+(2\pi)\delta(q'^+ - q^+)} \mathrm{Re}\left[{}_{\mathrm{i}}\langle \gamma^*(\vec{q}\,', Q^2, \lambda') | 1 - \hat{S}_E | \gamma^*(\vec{q}, Q^2, \lambda)\rangle_{\mathrm{i}}\right]. \tag{43}$$

The full perturbative Fock state decomposition for the virtual photon in the momentum space with momentum $\vec{q}$, virtuality Q, and helicity λ is given by

$$\begin{aligned}|\gamma^*(\vec{q},Q^2,\lambda)\rangle_{\rm i} =&\sqrt{Z_{\gamma^*}(q^+)}\Bigg[|\gamma(\vec{q},\lambda)\rangle_{\rm b}+\int \widetilde{\rm d}p\widetilde{\rm d}p'(2\pi)^3\delta^{(3)}(\vec{q}-\vec{p}-\vec{p}\,')\psi^{\gamma^*\to q\bar{q}}\\ &\times|q(\vec{p},h,\alpha)\bar{q}(\vec{p}\,',h',\beta)\rangle+\int \widetilde{\rm d}p\widetilde{\rm d}p'\widetilde{\rm d}k(2\pi)^3\delta^{(3)}(\vec{q}-\vec{p}-\vec{p}\,'-\vec{k})\psi^{\gamma^*\to q\bar{q}g}\\ &\times|q(\vec{p},h,\alpha)\bar{q}(\vec{p}\,',h',\beta)g(\vec{k},\sigma,a)\rangle+\cdots\Bigg],\end{aligned}\tag{44}$$

where $|\gamma^*(\vec{q},Q^2,\lambda)\rangle_{\rm i}$ is the physical one particle state in the interaction picture and $|\gamma(\vec{q},\lambda)\rangle_{\rm b}$ the corresponding free bare state. Note that the free bare states are defined by creation operators, depending only on the spatial momentum $\vec{q}$, operating on the vacuum. Thus the bare state $|\gamma(\vec{q},\lambda)\rangle_{\rm b}$ is independent of Q^2 and on shell, as are all LCPT free states. The full interacting theory state $|\gamma^*(\vec{q},Q^2,\lambda)\rangle_{\rm i}$, on the other hand, "knows" that it has a virtuality $-Q^2$. This is reflected in the wave functions $\psi^{\gamma^*\to q\bar{q}}$ etc. via the energy denominators that depend on the light cone energy of the initial state.[2] We have ignored electromagnetic contributions (i.e. $\gamma^*\to\ell\bar{\ell}$ and $\gamma^*\to\ell\bar{\ell}\gamma$, etc.) since we are only interested in the order $\mathcal{O}(\alpha_{\rm e.m.}\alpha_{\rm s})$ NLO correction to the order $\mathcal{O}(\alpha_{\rm e.m.})$ leading order cross section. The Fock states are defined as

$$\begin{aligned}|q(\vec{p},h,\alpha)\bar{q}(\vec{p}\,',h',\beta)\rangle &= b^\dagger(\vec{p},h,\alpha)d^\dagger(\vec{p}\,',h',\beta)|0\rangle\\ |q(\vec{p},h,\alpha)\bar{q}(\vec{p}\,',h',\beta)g(\vec{k},\sigma,a)\rangle &= b^\dagger(\vec{p},h,\alpha)d^\dagger(\vec{p}\,',h',\beta)a^\dagger(\vec{k},\sigma,a)|0\rangle\\ &\cdots\end{aligned}\tag{45}$$

where the operators $b^\dagger$ ($d^\dagger$) create quark q (anti-quark $\bar{q}$) with momentum $\vec{p}$ ($\vec{p}\,'$) and helicity h (h') and the fundamental color index α (β), and similarly $a^\dagger$ create gluon g with momentum $\vec{k}$, helicity σ and adjoint color index a. The normalization of the operators b, d and a is chosen such that commutation and anti-commutation rules in momentum space satisfy

$$\begin{aligned}\{b(\vec{p},h,\alpha),b^\dagger(\vec{q},s,\beta)\}=\{d(\vec{p},h,\alpha),d^\dagger(\vec{q},s,\beta)\}&=2p^+(2\pi)^3\delta^{(3)}(\vec{p}-\vec{q})\delta_{h,s}\delta_{\alpha,\beta}\\ [a(\vec{k},\sigma,a),a^\dagger(\vec{q},s,b)]&=2k^+(2\pi)^3\delta^{(3)}(\vec{k}-\vec{q})\delta_{\sigma,s}\delta_{a,b}.\end{aligned}\tag{46}$$

The renormalization constant $\sqrt{Z_{\gamma^*}}$ can be determined from the normalization requirement

$${}_{\rm int}\langle\gamma^*(\vec{q}\,',Q^2,\lambda')|\gamma^*(\vec{q},Q^2,\lambda)\rangle_{\rm int}=2q^+(2\pi)^3\delta^{(3)}(\vec{q}\,'-\vec{q})\delta_{\lambda',\lambda}.\tag{47}$$

However, since all the corrections to the photon wave function are proportional to the electromagnetic coupling, $Z=1+\mathcal{O}(\alpha_{\rm e.m.})$. Thus working at lowest order in $\alpha_{\rm e.m.}$ we can drop the photon wave function renormalization.

The Fock state representation in momentum space $(k^+,\mathbf{k})$ is switched to the mixed space representation $(k^+,\mathbf{x})$ by the transverse Fourier transform of all the creation operators present in the state, with

$$\begin{aligned}a^\dagger(\vec{k},\sigma,a)&=\int_{\mathbf{x}}e^{i\mathbf{k}\cdot\mathbf{x}}a^\dagger(k^+,\mathbf{x},\sigma,a)\\ b^\dagger(\vec{p},h,\alpha)&=\int_{\mathbf{x}}e^{i\mathbf{p}\cdot\mathbf{x}}b^\dagger(p^+,\mathbf{x},h,\alpha)\\ d^\dagger(\vec{p},h,\alpha)&=\int_{\mathbf{x}}e^{i\mathbf{p}\cdot\mathbf{x}}d^\dagger(p^+,\mathbf{x},h,\alpha),\end{aligned}\tag{48}$$

where

$$\int_{\mathbf{x}}=\int{\rm d}^2\mathbf{x}.\tag{49}$$

[2] We thank G. Beuf for pointing this out to us.

The mixed space operators satisfy

$$\begin{aligned}\{b(p^+,\mathbf{x},h,\alpha),b^\dagger(q^+,\mathbf{y},s,\beta)\}&=\{d(p^+,\mathbf{x},h,\alpha),d^\dagger(q^+,\mathbf{y},s,\beta)\}\\&=2p^+(2\pi)\delta(p^+-q^+)\delta^{(2)}(\mathbf{x}-\mathbf{y})\delta_{h,s}\delta_{\alpha,\beta}\\[a(k^+,\mathbf{x},\sigma,a),a^\dagger(q^+,\mathbf{y},s,b)]&=2k^+(2\pi)\delta(k^+-q^+)\delta^{(2)}(\mathbf{x}-\mathbf{y})\delta_{\sigma,s}\delta_{a,b}.\end{aligned}\tag{50}$$

Since the high energy scattering of the projectile partons off the gluon target is eikonal, the scattering operator $\hat{S}_E$ acts on Fock states by only color rotating each partons by a Wilson line defined along the partons trajectory through the target:

$$\begin{aligned}\hat{S}_E b^\dagger(p^+,\mathbf{x},h,\alpha)d^\dagger(p'^+,\mathbf{y},h',\beta)|0\rangle=\sum_{\bar\alpha,\bar\beta}[U[A](\mathbf{x})]_{\bar\alpha\alpha}[U^\dagger[A](\mathbf{y})]_{\beta\bar\beta}b^\dagger(p^+,\mathbf{x},h,\bar\alpha)d^\dagger\\\times\,(p'^+,\mathbf{y},h',\bar\beta)|0\rangle\end{aligned}\tag{51}$$

and

$$\begin{aligned}\hat{S}_E b^\dagger(p^+,\mathbf{x},h,\alpha)d^\dagger(p'^+,\mathbf{y},h',\beta)a^\dagger(k^+,\mathbf{z},\sigma,a)|0\rangle=\sum_{\bar\alpha,\bar\beta,b}[U[A](\mathbf{x})]_{\bar\alpha\alpha}[U^\dagger[A](\mathbf{y})]_{\beta\bar\beta}[V[A](\mathbf{z})]_{ba}\\\times\,b^\dagger(p^+,\mathbf{x},h,\bar\alpha)d^\dagger(p'^+,\mathbf{y},h',\bar\beta)\\\times\,a^\dagger(k^+,\mathbf{z},\sigma,b)|0\rangle,\end{aligned}\tag{52}$$

where the fundamental and adjoint Wilson line are respectively defined as the path ordered exponential for a classical gluon target A:

$$\begin{aligned}U[A](\mathbf{x})&=\mathcal{P}\exp\left[ig\int \mathrm{d}x^+t^aA_a^-(x^+,0,\mathbf{x})\right]\\V[A](\mathbf{x})&=\mathcal{P}\exp\left[ig\int \mathrm{d}x^+T^aA_a^-(x^+,0,\mathbf{x})\right].\end{aligned}\tag{53}$$

Applying Eq. (48), we can define the amplitudes corresponding to the $q\bar{q}$-component and $q\bar{q}g$-component of the Fock state decomposition in the mixed space:

$$|\gamma^*(q^+,Q^2,\lambda)\rangle_{q\bar q}=\mathcal{PS}^+_{(2)}\int_{\mathbf{xy}}\widetilde{\psi}^{\gamma^*\to q\bar q}|q(p^+,\mathbf{x},h,\alpha)\bar q(p'^+,\mathbf{y},h',\beta)\rangle\tag{54}$$

$$|\gamma^*(q^+,Q^2,\lambda)\rangle_{q\bar qg}=\mathcal{PS}^+_{(3)}\int_{\mathbf{xyz}}\widetilde{\psi}^{\gamma^*\to q\bar qg}|q(p^+,\mathbf{x},h,\alpha)\bar q(p'^+,\mathbf{y},h',\beta)g(k^+,\mathbf{z},\sigma,a)\rangle,\tag{55}$$

where the two and three particle longitudinal phase space factors $\mathcal{PS}^+_{(2)}$ and $\mathcal{PS}^+_{(3)}$, respectively, are defined as

$$\begin{aligned}\mathcal{PS}^+_{(2)}&=\int_0^\infty\frac{\mathrm{d}p^+}{2p^+(2\pi)}\int_0^\infty\frac{\mathrm{d}p'^+}{2p'^+(2\pi)}(2\pi)\delta(q^+-p^+-p'^+)\\\mathcal{PS}^+_{(3)}&=\int_0^\infty\frac{\mathrm{d}p^+}{2p^+(2\pi)}\int_0^\infty\frac{\mathrm{d}p'^+}{2p'^+(2\pi)}\int_0^\infty\frac{\mathrm{d}k^+}{2k^+(2\pi)}(2\pi)\delta(q^+-p^+-p'^+-k^+).\end{aligned}\tag{56}$$

The mixed space wave functions $\widetilde{\psi}$ are transverse Fourier transforms of the LCWF's:

$$\begin{aligned}\widetilde{\psi}^{\gamma^*\to q\bar q}\left(\mathbf{x},p^+,\mathbf{y},p'^+\right)=\int\frac{\mathrm{d}^2\mathbf{p}}{(2\pi)^2}\int\frac{\mathrm{d}^2\mathbf{p}'}{(2\pi)^2}(2\pi)^2\delta^{(2)}(\mathbf{q}-\mathbf{p}-\mathbf{p}')\\\psi^{\gamma^*\to q\bar q}\left(\mathbf{p},p^+,\mathbf{p}',p'^+\right)e^{i\mathbf{p}\cdot\mathbf{x}}e^{i\mathbf{p}'\cdot\mathbf{y}}\end{aligned}\tag{57}$$

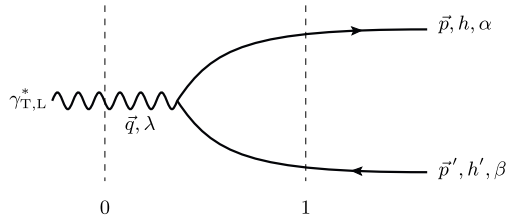

Fig. 7. Time ordered (momenta flows from left to right) diagram contributing to the $q\bar{q}$-component of the transverse and longitudinal virtual photon wave function at leading order with energy denominators and kinematics. Momentum conservation: $\vec{q} = \vec{p} + \vec{p}'$. The longitudinal momentum fractions for quark and anti-quark are parametrized as $p^+ = zq^+$ and $p'^+ = (1-z)q^+$.

and

$$\widetilde{\psi}^{\gamma^*\to q\bar{q}g}\left(\mathbf{x}, p^+, \mathbf{y}, p'^+, \mathbf{z}, k^+\right) = \int \frac{\mathrm{d}^2\mathbf{p}}{(2\pi)^2}\int \frac{\mathrm{d}^2\mathbf{p}'}{(2\pi)^2}\int \frac{\mathrm{d}^2\mathbf{k}}{(2\pi)^2}(2\pi)^2\delta^{(2)}(\mathbf{q}-\mathbf{p}-\mathbf{p}'-\mathbf{k}) \psi^{\gamma^*\to q\bar{q}g}\left(\mathbf{p}, p^+, \mathbf{p}', p'^+, \mathbf{k}, k^+\right) e^{i\mathbf{p}\cdot\mathbf{x}} e^{i\mathbf{p}'\cdot\mathbf{y}} e^{i\mathbf{k}\cdot\mathbf{z}}. \tag{58}$$

Using the shorthand notation for the different Fock state components the virtual photon state (44) is

$$|\gamma^*(q^+, Q^2, \lambda)\rangle_{\mathrm{i}} = |\gamma(q^+, \lambda)\rangle_{\mathrm{b}} + |\gamma^*(q^+, Q^2, \lambda)\rangle_{q\bar{q}} + |\gamma^*(q^+, Q^2, \lambda)\rangle_{q\bar{q}g} + \cdots, \tag{59}$$

with the two last terms on the right-hand side given in mixed space by Eqs. (54) and (55). In this decomposition the photon cross section at NLO accuracy can be written as

$$\sigma^{\gamma^*}[A] = \frac{2}{2q^+(2\pi)\delta(q'^+ - q^+)}\Big\{ {}_{q\bar{q}}\langle\gamma^*(q'^+, Q^2, \lambda')|1-\hat{S}_E|\gamma^*(q^+, Q^2, \lambda)\rangle_{q\bar{q}} + {}_{q\bar{q}g}\langle\gamma^*(q'^+, Q^2, \lambda')|1-\hat{S}_E|\gamma^*(q^+, Q^2, \lambda)\rangle_{q\bar{q}g}\Big\}. \tag{60}$$

Here the $q\bar{q}$-component contains the leading order (LO) contribution and the NLO contribution coming from the one-loop virtual diagrams, and the $q\bar{q}g$-component contains the NLO contribution coming from the radiative correction diagrams.

We shall now set out to calculate the wave function $\widetilde{\psi}^{\gamma^*\to q\bar{q}}$ to one-loop accuracy and $\widetilde{\psi}^{\gamma^*\to q\bar{q}g}$ at tree level, and using these results return to the cross section (60) in Section 7.

4. Leading order wave function

The leading order $\gamma^* \to q\bar{q}$ wave functions shown in Fig. 7 are well known, but we will briefly write them down here to set the normalization in our conventions. Following the diagrammatic rules listed in [35] the light cone wave function contributing to the transverse or longitudinal virtual photon splitting into a quark anti-quark dipole is given by

$$\psi^{\gamma^*_{\mathrm{T/L}}\to q\bar{q}}_{\mathrm{LO}} = \frac{-ee_f\delta_{\alpha\beta}}{\Delta^-_{01}}\left[\bar{u}_h(p)\not{\epsilon}_{\lambda,\mathrm{T/L}}(q)v_{h'}(p')\right], \tag{61}$$

where the LC energy denominator can be cast in the following form

$$\Delta^-_{01} = q^- - (p^- + p'^-) = -\frac{Q^2}{2q^+} - \left(\frac{\mathbf{p}^2}{2p^+} + \frac{\mathbf{p}^2}{2p'^+}\right) = \frac{1}{(-2q^+)z(1-z)}\left[\mathbf{p}^2 + \overline{Q}^2\right] \tag{62}$$

with $\overline{Q}^2 = z(1-z)Q^2$. Note that we are working in a frame where the transverse momentum of the photon is zero and thus $\mathbf{p} = -\mathbf{p}'$; otherwise the transverse momentum argument $\mathbf{p}$ would be replaced by the center of mass momentum $\mathbf{p} - z\mathbf{q}$.

4.1. Transversely polarized virtual photon

In the $\mathbf{q} = 0$ frame the polarization vector for a transversely polarized virtual photon in the LC gauge is given by

$$\varepsilon^{\mu}_{\lambda,\mathrm{T}}(q) = (0, \frac{\mathbf{q}\cdot\boldsymbol{\epsilon}_\lambda}{q^+}, \boldsymbol{\epsilon}_\lambda) = (0, 0, \boldsymbol{\epsilon}_\lambda). \tag{63}$$

Using Eq. (63) the light cone wave function for the transversely polarized virtual photon in Eq. (61) can be expressed in the explicit helicity basis as

$$\psi^{\gamma^*_\mathrm{T}\to q\bar{q}}_{\mathrm{LO}}(\mathbf{p}, z) = \frac{\delta_{\alpha\beta}}{\Delta^-_{01}} A^{\gamma^*_\mathrm{T}}_{\lambda;h,h'}(\mathbf{p}, z) \tag{64}$$

with $A^{\gamma^*_\mathrm{T}}_{\lambda;h,h'}$ defined as for the gluon vertex in (14):

$$A^{\gamma^*_\mathrm{T}}_{\lambda;h,h'}(\mathbf{p}, z) = \frac{-2ee_f}{\sqrt{z(1-z)}}\left[\left(z-\frac{1}{2}\right)\delta^{ij}\delta_{h,-h'} + \frac{1}{4}\mathcal{A}^{ij}_{h,h'}\right]\mathbf{p}^i\boldsymbol{\epsilon}^j_\lambda. \tag{65}$$

Here we have kept the helicity notation as general as possible. However, for a massless quarks the helicity is conserved in the light cone vertices. This implies that for the $\gamma q\bar{q}$-vertex $h = -h'$.

4.2. Longitudinally polarized virtual photon

Strictly speaking there is no such thing as a longitudinal photon in the spectrum of physical states in the theory. In stead, a longitudinal photon in DIS is a part of an instantaneous interaction vertex with the lepton. However, for calculational purposes we will here leave out the lepton and simply define a longitudinal virtual photon polarization vector, treating the longitudinal photon analogously to the transverse one. The polarization vector for a longitudinally polarized virtual photon in the LC gauge can be expressed as

$$\varepsilon^{\mu}_{\lambda,\mathrm{L}}(q) = (0, \frac{\sqrt{Q^2-\mathbf{q}^2}}{q^+}, \frac{\mathbf{q}}{\sqrt{Q^2-\mathbf{q}^2}}) = (0, \frac{Q}{q^+}, \mathbf{0}). \tag{66}$$

Thus the light cone wave function for the longitudinally polarized virtual photon in Eq. (61) can be cast in the following form

$$\psi^{\gamma^*_\mathrm{L}\to q\bar{q}}_{\mathrm{LO}}(Q, z) = \frac{\delta_{\alpha\beta}}{\Delta^-_{01}} A^{\gamma^*_\mathrm{L}}_{\lambda;h,h'}(Q, z), \tag{67}$$

where

$$\begin{aligned} A^{\gamma^*_\mathrm{L}}_{\lambda;h,h'}(Q, z) &= -ee_f\frac{Q}{q^+}\left[\bar{u}_h(p)\gamma^+ v_{h'}(p')\right] = -2ee_f\frac{Q}{q^+}\sqrt{p^+p'^+}\delta_{h,-h'} \\ &= -2ee_f Q\sqrt{z(1-z)}\delta_{h,-h'}. \end{aligned} \tag{68}$$

5. Virtual photon LCWF'S

5.1. Quark self-energy diagrams

The quark self energy diagrams are explicitly proportional to the leading order $\gamma^* \to q\bar{q}$ vertex, so one does not need to calculate them separately for the different virtual photon polarizations. There are two diagrams that contribute, the ones shown in Figs. 8 and 9.

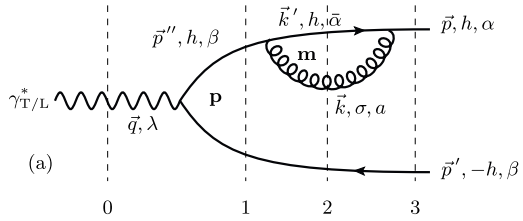

Fig. 8. Quark self-energy diagram (a) contributing to the $q\bar{q}$-component of the transverse virtual photon wave function at NLO with energy denominators and kinematics. Momentum conservation: $\vec{q} = \vec{p} + \vec{p}', \vec{p}'' = \vec{k}' + \vec{k}$ and $\vec{k}' + \vec{k} = \vec{p}$. The longitudinal momentum fractions for quark and anti-quark are parametrized as $p^+ = zq^+$ and $p'^+ = (1-z)q^+$. The momentum fraction of the virtual photon splitting into a $q\bar{q}$ dipole is $p^+/q^+ = z$ and the natural momentum is $\mathbf{p} - z\mathbf{q} = \mathbf{p}$ (note $\mathbf{q} = \mathbf{0}$). The momentum fraction of the gluon emission and absorption is $k^+/p^+ = z'/z$, and the natural momentum in the gluon loop is $\mathbf{m} = \mathbf{k} - (z'/z)\mathbf{p}$.

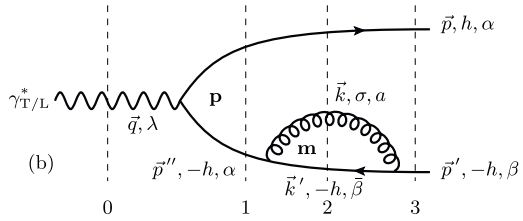

Fig. 9. Antiquark self-energy diagram (b) contributing to the $q\bar{q}$-component of the transverse virtual photon wave function at NLO with energy denominators and kinematics. Momentum conservation: $\vec{q} = \vec{p} + \vec{p}', \vec{p}'' = \vec{k}' + \vec{k}$ and $\vec{k}' + \vec{k} = \vec{p}'$. The longitudinal momentum fractions for quark and anti-quark are parametrized as $p^+ = zq^+$ and $p'^+ = (1-z)q^+$. The momentum fraction of the virtual photon splitting vertex is $p^+/q^+ = z$ and the natural momentum $\mathbf{p} - z\mathbf{q} = \mathbf{p}$ (note $\mathbf{q} = \mathbf{0}$). The momentum fraction of the gluon emission and absorption is $k^+/p'^+ = z'/(1-z)$, and the natural momentum in the gluon loop is $\mathbf{m} = \mathbf{k} - (z'/(1-z))\mathbf{p}$.

The LCWF for quark self-energy diagram (a) shown in Fig. 8 is given by

$$\psi^{\gamma^*_{\mathrm{T/L}} \to q\bar{q}}_{(\mathrm{a})} = \int \widetilde{\mathrm{d}k}\widetilde{\mathrm{d}k}'\widetilde{\mathrm{d}p}''(2\pi)^{d-1}\delta^{(d-1)}(\vec{p}'' - \vec{k}' - \vec{k})(2\pi)^{d-1}\delta^{(d-1)}(\vec{k}' + \vec{k} - \vec{p}) \times \frac{1}{\Delta^-_{01}\Delta^-_{02}\Delta^-_{03}}\mathrm{num}\Big|_{(\mathrm{a})}, \tag{69}$$

where the Lorentz invariant measure in d dimensions is defined as $\widetilde{\mathrm{d}k} \equiv \frac{\mathrm{d}k^+\,\mathrm{d}^{d-2}\mathbf{k}}{2k^+(2\pi)^{d-1}}$, and the numerator for the transversally polarized virtual photon becomes

$$\mathrm{num}\Big|_{(\mathrm{a})} = V^{\bar{\alpha},a;\alpha}_{h,\sigma;h}(\mathbf{m}, z'/z)V^{\beta;\bar{\alpha},a}_{h;h,\sigma}(\mathbf{m}, z'/z)A^{\gamma^*_{\mathrm{T}}}_{\lambda,h,-h}(\mathbf{p}, z). \tag{70}$$

Correspondingly, the numerator for longitudinally polarized virtual photon in Eq. (69) is obtained by the trivial replacement

$$A^{\gamma^*_{\mathrm{T}}}_{\lambda,h,-h}(\mathbf{p}, z) \to A^{\gamma^*_{\mathrm{L}}}_{\lambda,h,-h}(\mathrm{Q}, z). \tag{71}$$

In Eq. (70) the vertex for the virtual photon splitting into a $q\bar{q}$ dipole is given in Eq. (65) or Eq. (68) depending on the polarization and the gluon emission and absorption vertices $V^{\beta;\bar{\alpha},a}_{h;h\sigma}(\mathbf{m}, z'/z)$ and $V^{\bar{\alpha},a;\alpha}_{h\sigma;h}(\mathbf{m}, z'/z)$ are given by Eqs. (6) and (8). The LC energy denominators in Eq. (69) are

$$\Delta^-_{01} = \Delta^-_{03} = \frac{1}{(-2q^+)z(1-z)}\left[\mathbf{p}^2 + \overline{\mathrm{Q}}^2\right] \tag{72}$$

and

$$\Delta_{02}^{-} = \frac{z}{(-2q^+)z'(z-z')}\left[\mathbf{m}^2 + M^{(\mathrm{a})}\right] \quad \text{with} \quad M^{(\mathrm{a})} = \frac{z'(z-z')}{z^2(1-z)}\left(\mathbf{p}^2 + \overline{Q}^2\right). \tag{73}$$

The phase space measure simplifies to

$$\begin{aligned}&\int \widetilde{\mathrm{d}k}\widetilde{\mathrm{d}k}'\widetilde{\mathrm{d}p}(2\pi)^{d-1}\delta^{(d-1)}(\vec{k}\,' - \vec{p} + \vec{k})(2\pi)^{d-1}\delta^{(d-1)}(\vec{p} - \vec{k}\,' - \vec{k})\\ &= \frac{1}{16\pi(q^+)^2}\int \frac{\mathrm{d}z'}{zz'(z-z')}\int \frac{\mathrm{d}^{d-2}\mathbf{m}}{(2\pi)^{d-2}},\end{aligned} \tag{74}$$

where $k^+ > 0$ and $k'^+ > 0$, so that $0 < z' < z$.

Performing the helicity sums as described in Section 2.3, and integrating over the loop transverse momentum (with dimensionally regularized integrals given in Appendix B) and the longitudinal momentum, regulating the soft divergence with $\alpha < z' < z$, we obtain

$$\psi_{(\mathrm{a})}^{\gamma_{\mathrm{T}}^*\to q\bar{q}} = \psi_{\mathrm{LO}}^{\gamma_{\mathrm{T}}^*\to q\bar{q}}(\mathbf{p}, z)\left(\frac{g_r^2 C_{\mathrm{F}}}{8\pi^2}\right)\left\{\left[\frac{3}{2} + 2\log\left(\frac{\alpha}{z}\right)\right]C_{(\mathrm{a})} - \log^2\left(\frac{\alpha}{z}\right) - \frac{\pi^2}{3} + 3\right\} + \mathcal{O}(\varepsilon), \tag{75}$$

where

$$C_{(\mathrm{a})} = \frac{1}{\varepsilon_{\overline{\mathrm{MS}}}} + \log\left(\frac{\mu^2}{\overline{Q}^2}\right) - \log\left(\frac{\mathbf{p}^2 + \overline{Q}^2}{\overline{Q}^2}\right) + \log(1-z), \tag{76}$$

with $\varepsilon_{\overline{\mathrm{MS}}} = 1/\varepsilon - \gamma_{\mathrm{E}} + \ln(4\pi)$. Similarly for the longitudinally polarized virtual photon,

$$\psi_{(\mathrm{a})}^{\gamma_{\mathrm{L}}^*\to q\bar{q}} = \psi_{\mathrm{LO}}^{\gamma_{\mathrm{L}}^*\to q\bar{q}}(Q, z)\left(\frac{g_r^2 C_{\mathrm{F}}}{8\pi^2}\right)\left\{\left[\frac{3}{2} + 2\log\left(\frac{\alpha}{z}\right)\right]C_{(\mathrm{a})} - \log^2\left(\frac{\alpha}{z}\right) - \frac{\pi^2}{3} + 3\right\} + \mathcal{O}(\varepsilon). \tag{77}$$

The LCWF for diagram (b) shown in Fig. 9 can be now easily obtained by using the symmetry between the diagrams (a) and (b) (i.e. by making the substitution $z \leftrightarrow 1-z$ and $\mathbf{p} \to -\mathbf{p}$ simultaneously) as

$$\psi_{(\mathrm{b})}^{\gamma_{\mathrm{T}}^*\to q\bar{q}} = \psi_{\mathrm{LO}}^{\gamma_{\mathrm{T}}^*\to q\bar{q}}(\mathbf{p}, z)\left(\frac{g_r^2 C_{\mathrm{F}}}{8\pi^2}\right)\left\{\left[\frac{3}{2} + 2\log\left(\frac{\alpha}{1-z}\right)\right]C_{(\mathrm{b})} - \log^2\left(\frac{\alpha}{1-z}\right) - \frac{\pi^2}{3} + 3\right\} \tag{78}$$

and

$$\psi_{(\mathrm{b})}^{\gamma_{\mathrm{L}}^*\to q\bar{q}} = \psi_{\mathrm{LO}}^{\gamma_{\mathrm{L}}^*\to q\bar{q}}(Q, z)\left(\frac{g_r^2 C_{\mathrm{F}}}{8\pi^2}\right)\left\{\left[\frac{3}{2} + 2\log\left(\frac{\alpha}{1-z}\right)\right]C_{(\mathrm{b})} - \log^2\left(\frac{\alpha}{1-z}\right) - \frac{\pi^2}{3} + 3\right\} \tag{79}$$

with

$$C_{(\mathrm{b})} = \frac{1}{\varepsilon_{\overline{\mathrm{MS}}}} + \log\left(\frac{\mu^2}{\overline{Q}^2}\right) - \log\left(\frac{\mathbf{p}^2 + \overline{Q}^2}{\overline{Q}^2}\right) + \log(z). \tag{80}$$

5.2. Transverse photons

Next we calculate the LCWFs for diagrams (c) and (d) shown in Figs. 10 and 11. Since there is a lot of symmetry between these it makes sense to present the result for the sum of the two.

For diagram (c), with kinematical variables as in Fig. 10, the LCWF can be cast in the following form

$$\begin{aligned}\psi_{(\mathrm{c})}^{\gamma_{\mathrm{T}}^*\to q\bar{q}} = &\int \widetilde{\mathrm{d}k}\widetilde{\mathrm{d}k}'\widetilde{\mathrm{d}k}''(2\pi)^{d-1}\delta^{(d-1)}(\vec{k}\,' - \vec{p} + \vec{k})(2\pi)^{d-1}\delta^{(d-1)}(\vec{k}\,'' - \vec{k} - \vec{p}\,')\\ &\times \frac{V^{\tilde{\alpha},a;\alpha}_{\sigma,h';h}(\mathbf{m}, \frac{z'}{z})A^{\gamma_{\mathrm{T}}^*}_{\lambda;h',h''}(\mathbf{k}', z-z')\overline{V}^{\tilde{\alpha};\beta,a}_{h'';-h,\sigma}(\mathbf{h}, \frac{z'}{(1-z+z')})}{\Delta_{01}^{-}\Delta_{02}^{-}\Delta_{03}^{-}},\end{aligned} \tag{81}$$

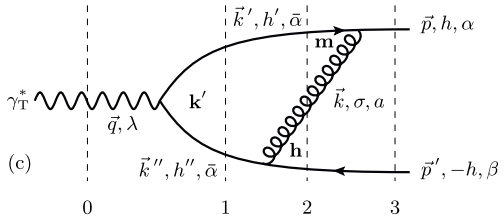

Fig. 10. Vertex diagram (c) contributing to the $q\bar{q}$-component of the transverse virtual photon wave function at NLO with energy denominators and kinematics. Momentum conservation: $\vec{q} = \vec{k}' + \vec{k}'' = \vec{p} + \vec{p}', \vec{k}' = \vec{p} - \vec{k}$ and $\vec{k}'' = \vec{k} + \vec{p}'$. The longitudinal momentum fractions for quark and anti-quark are parametrized as $p^+ = zq^+$ and $p'^+ = (1-z)q^+$, and for the gluon in the loop $k^+ = z'q^+$ with $k'^+ = (z-z')q^+$ and $k''^+ = (1-z+z')q^+$. The longitudinal momentum fraction of the virtual photon splitting into a $q\bar{q}$ dipole is $k'^+/q^+ = z - z'$ and the natural momentum is $\mathbf{k}'$. The momentum fraction of the gluon emission is $k^+/k''^+ = z'/(1-z+z')$ and gluon absorption $k^+/p^+ = z'/z$. The natural momentum for the gluon emission is $\mathbf{h} = \mathbf{k} - (z'/(1-z+z'))\mathbf{k}''$ and for the gluon absorption $\mathbf{m} = \mathbf{k} - (z'/z)\mathbf{p}$. In order to use $\mathbf{m}$ as the integration variable we need to know that $\mathbf{k}' = -\mathbf{m} + ((z-z')/z)\mathbf{p}$ and $\mathbf{h} = ((1-z)/(1-z+z'))(\mathbf{m} + (z'/(z(1-z))\mathbf{p}))$.

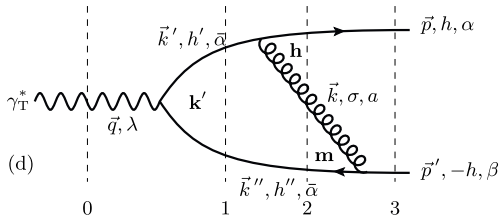

Fig. 11. Diagram (d) contributing to the $q\bar{q}$-component of the transverse virtual photon wave function at NLO with energy denominators and kinematics. Momentum conservation: $\vec{q} = \vec{k}' + \vec{k}'' = \vec{p} + \vec{p}', \vec{k}' = \vec{k} + \vec{p}$ and $\vec{k}'' = \vec{p}' - \vec{k}$. The longitudinal momentum fractions for quark and anti-quark are parametrized as $p^+ = zq^+$ and $p'^+ = (1-z)q^+$, and for the gluon in the loop $k^+ = z'q^+$ with $k'^+ = (z+z')q^+$ and $k''^+ = (1-z-z')q^+$. The longitudinal momentum fraction of the virtual photon splitting into a $q\bar{q}$ dipole is $k'^+/q^+ = z + z'$ and the natural momentum is $\mathbf{k}'$. The momentum fraction of the gluon emission is $k^+/k'^+ = z'/(z+z')$ and gluon absorption $k^+/p'^+ = z'/(1-z)$. The natural momentum for the gluon emission is $\mathbf{h} = \mathbf{k} - (z'/(z+z'))\mathbf{k}'$ and for the gluon absorption $\mathbf{m} = \mathbf{k} + (z'/(1-z))\mathbf{p}$. In order to use $\mathbf{m}$ as the integration variable we need to know that $\mathbf{k}' = \mathbf{m} + ((1-z-z')/(1-z))\mathbf{p}$ and $\mathbf{h} = (z/(z+z'))(\mathbf{m} - (z'/(z(1-z))\mathbf{p}))$.

where the gluon emission and absorption vertices are given by Eqs. (8) and (10) and the photon vertex by Eq. (65). The phase space measure simplifies to

$$\begin{aligned} &\int \widetilde{\mathrm{d}k}\widetilde{\mathrm{d}k}'\widetilde{\mathrm{d}k}''(2\pi)^{d-1}\delta^{(d-1)}(\vec{k}' - \vec{p} + \vec{k})(2\pi)^{d-1}\delta^{(d-1)}(\vec{k}'' - \vec{k} - \vec{p}') \\ &= \frac{1}{16\pi(q^+)^2}\int_0^z \frac{\mathrm{d}z'}{z'(z-z')(1-z+z')}\int \frac{\mathrm{d}^{d-2}\mathbf{m}}{(2\pi)^{d-2}} \end{aligned} \tag{82}$$

The LC energy denominators are given by

$$\begin{aligned} \Delta_{01}^- &= \frac{1}{(-2q^+)(z-z')(1-z+z')}\left[\left(\mathbf{m} - \frac{(z-z')}{z}\mathbf{p}\right)^2 + M_2^{(\mathrm{c})}\right] \\ \Delta_{02}^- &= \frac{z}{(-2q^+)z'(z-z')}\left[\mathbf{m}^2 + M_1^{(\mathrm{c})}\right] \end{aligned} \tag{83}$$

and

$$\Delta_{03}^- = \frac{1}{(-2q^+)z(1-z)}\left[\mathbf{p}^2 + \overline{Q}^2\right], \tag{84}$$

where the coefficients $M_1^{(c)}$ and $M_2^{(c)}$ are given by

$$M_1^{(c)} = \frac{z'(z-z')}{z^2(1-z)}\left(\mathbf{p}^2 + \overline{Q}^2\right) \quad \text{and} \quad M_2^{(c)} = \frac{(z-z')(1-z+z')}{z(1-z)}\overline{Q}^2. \tag{85}$$

For diagram (d), with kinematical variables as in Fig. 11, the LCWF is

$$\begin{aligned}\psi_{(d)}^{\gamma_T^*\to q\bar{q}} = &\int \widetilde{\mathrm{d}k}\widetilde{\mathrm{d}k}'\widetilde{\mathrm{d}k}''(2\pi)^{d-1}\delta^{(d-1)}(\vec{k}\,' - \vec{p} - \vec{k})(2\pi)^{d-1}\delta^{(d-1)}(\vec{k}\,'' - \vec{p}\,' + \vec{k}) \\ &\times \frac{V_{h';\sigma,h}^{\tilde{\alpha};\alpha,a}(\mathbf{h}, \frac{z'}{z+z'})A_{\lambda;h',h''}^{\gamma_T^*}(\mathbf{k}', z+z')\overline{V}_{h'',\sigma;-h}^{\tilde{\alpha},a;\beta}(\mathbf{m}, \frac{z'}{(1-z)})}{\Delta_{01}^- \Delta_{02}^- \Delta_{03}^-}.\end{aligned} \tag{86}$$

The phase space measure simplifies to

$$\begin{aligned}&\int \widetilde{\mathrm{d}k}\widetilde{\mathrm{d}k}'\widetilde{\mathrm{d}k}''(2\pi)^{d-1}\delta^{(d-1)}(\vec{k}\,' - \vec{p} - \vec{k})(2\pi)^{d-1}\delta^{(d-1)}(\vec{k}\,'' - \vec{p}\,' + \vec{k}) \\ &= \frac{1}{16\pi(q^+)^2}\int_0^{1-z}\frac{\mathrm{d}z'}{z'(z+z')(1-z-z')}\int\frac{\mathrm{d}^{d-2}\mathbf{m}}{(2\pi)^{d-2}}\end{aligned} \tag{87}$$

and the LC energy denominators are given by

$$\begin{aligned}\Delta_{01}^- &= \frac{1}{(-2q^+)(z+z')(1-z-z')}\left[\left(\mathbf{m} + \frac{(1-z-z')}{1-z}\mathbf{p}\right)^2 + M_2^{(d)}\right] \\ \Delta_{02}^- &= \frac{1-z}{(-2q^+)z'(1-z-z')}\left[\mathbf{m}^2 + M_1^{(d)}\right]\end{aligned} \tag{88}$$

and

$$\Delta_{03}^- = \frac{1}{(-2q^+)z(1-z)}\left[\mathbf{p}^2 + \overline{Q}^2\right], \tag{89}$$

where the coefficients $M_1^{(d)}$ and $M_2^{(d)}$ are given by

$$M_1^{(d)} = \frac{z'(1-z-z')}{z(1-z)^2}\left(\mathbf{p}^2 + \overline{Q}^2\right) \quad \text{and} \quad M_2^{(d)} = \frac{(z+z')(1-z-z')}{z(1-z)}\overline{Q}^2. \tag{90}$$

Now one first performs the transverse momentum integrals using the results in Appendix B, then performs the numerator helicity sums as described in Section 2.3 and finally integrates over the longitudinal momentum fraction regulating the soft divergences by a cutoff α. The result for the sum of the diagrams (c) and (d) simplifies to

$$\begin{aligned}\psi_{(c)+(d)}^{\gamma_T^*\to q\bar{q}} = &\psi_{LO}^{\gamma_T^*\to q\bar{q}}(\mathbf{p}, z)\left(\frac{g_r^2 C_F}{8\pi^2}\right)\left\{\left[-\frac{3}{2} - \log\left(\frac{\alpha}{z}\right) - \log\left(\frac{\alpha}{1-z}\right)\right]C_{(c)+(d)}^T + \Gamma^T\right\} \\ &+ \mathcal{O}(\varepsilon),\end{aligned} \tag{91}$$

where the coefficients C and Γ are given by

$$C_{(c)+(d)}^T = \frac{1}{\varepsilon_{\overline{MS}}} + \log\left(\frac{\mu^2}{\overline{Q}^2}\right) + \left(\frac{\mathbf{p}^2 + \overline{Q}^2}{\mathbf{p}^2}\right)\log\left(\frac{\mathbf{p}^2 + \overline{Q}^2}{\overline{Q}^2}\right) \tag{92}$$

and

$$\begin{aligned}\Gamma^T = &-\frac{21}{6} + \frac{2\pi^2}{6} - \frac{3}{2}\log(1-z) - \frac{3}{2}\log(z) + 4\log(1-z)\log(z) + \log^2\left(\frac{\alpha}{z}\right) \\ &+ \log^2\left(\frac{\alpha}{1-z}\right) - 2\log(1-z)\log(\alpha) - 2\log(z)\log(\alpha) \\ &- \mathrm{Li}_2\left(-\frac{z}{1-z}\right) - \mathrm{Li}_2\left(-\frac{1-z}{z}\right).\end{aligned} \tag{93}$$

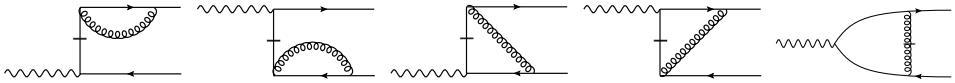

Fig. 12. Instantaneous diagrams for the $q\bar{q}$-component of the virtual photon wave function at NLO, yielding zero in dimensional regularization.

The sum of two dilogarithm functions above can be simplified by applying the identity

$$\mathrm{Li}_2\left(-x\right)+\mathrm{Li}_2\left(-\frac{1}{x}\right)=-\frac{\pi^2}{6}-\frac{1}{2}\log^2(x),\quad x>0. \tag{94}$$

In principle one also has to compute the instantaneous vertex correction diagrams shown in Fig. 12. These however vanish in dimensional regularization. This is easiest to see by taking as the integration variable the natural momentum of the only non-instantaneous vertex in the diagram, in which case this vertex and consequently the whole transverse momentum integrand are linear in the integration variable [35].

Adding the one-loop quark self-energy corrections in Eqs. (75) and (78) together with Eq. (91), we get the expression for the full one-loop corrected LCWF for $\gamma_{\mathrm{T}}^*\to q\bar{q}$ computed in the FDH scheme

$$\begin{aligned}\psi_{\mathrm{NLO}}^{\gamma_{\mathrm{T}}^*\to q\bar{q}}\Big|_{\mathrm{FDH}}&=\psi_{\mathrm{LO}}^{\gamma_{\mathrm{T}}^*\to q\bar{q}}(\mathbf{p},z)\left(\frac{g_r^2C_{\mathrm{F}}}{8\pi^2}\right)\left\{\left[\frac{3}{2}+\log\left(\frac{\alpha}{z}\right)+\log\left(\frac{\alpha}{1-z}\right)\right]C_{\mathrm{full}}^{(\mathrm{T})}\right.\\&\left.+\frac{1}{2}\log^2\left(\frac{z}{1-z}\right)-\frac{\pi^2}{6}+\frac{5}{2}\right\}+\mathcal{O}(\varepsilon),\end{aligned} \tag{95}$$

where

$$C_{\mathrm{full}}^{(\mathrm{T})}=\frac{1}{\varepsilon_{\overline{\mathrm{MS}}}}+\log\left(\frac{\mu^2}{\overline{Q}^2}\right)+\left(\frac{\overline{Q}^2-\mathbf{p}^2}{\mathbf{p}^2}\right)\log\left(\frac{\mathbf{p}^2+\overline{Q}^2}{\overline{Q}^2}\right). \tag{96}$$

For comparison the full result computed in the CDR scheme [29] and [34] is

$$\begin{aligned}\psi_{\mathrm{NLO}}^{\gamma_{\mathrm{T}}^*\to q\bar{q}}\Big|_{\mathrm{CDR}}&=\psi_{\mathrm{LO}}^{\gamma_{\mathrm{T}}^*\to q\bar{q}}(\mathbf{p},z)\left(\frac{g_r^2C_{\mathrm{F}}}{8\pi^2}\right)\left\{\left[\frac{3}{2}+\log\left(\frac{\alpha}{z}\right)+\log\left(\frac{\alpha}{1-z}\right)\right]C_{\mathrm{full}}^{(\mathrm{T})}\right.\\&\left.+\frac{1}{2}\log^2\left(\frac{z}{1-z}\right)-\frac{\pi^2}{6}+\frac{5}{2}+\frac{1}{2}\right\}+\mathcal{O}(\varepsilon),\end{aligned} \tag{97}$$

where the additional factor 1/2 is the scheme dependent part of the CDR scheme calculation.

5.3. Longitudinal photons

For diagram (e), with kinematical variables as in Fig. 13, the LCWF can be cast in the following form

$$\begin{aligned}\psi_{(\mathrm{e})}^{\gamma_{\mathrm{L}}^*\to q\bar{q}}=&\int\mathrm{d}\tilde{k}\mathrm{d}\tilde{k}'\mathrm{d}\tilde{k}''(2\pi)^{d-1}\delta^{(d-1)}(\vec{k}'-\vec{p}+\vec{k})(2\pi)^{d-1}\delta^{(d-1)}(\vec{k}''-\vec{k}-\vec{p}\,')\\&\times\frac{V^{\tilde{\alpha},a;\alpha}_{\sigma,h';h}(\mathbf{m},\frac{z'}{z})A^{\gamma_{\mathrm{L}}^*}_{\lambda,h',h''}(Q,z-z')\overline{V}^{\tilde{\alpha};\beta,a}_{h'';-h,\sigma}(\mathbf{h},\frac{z'}{1-z+z'})}{\Delta_{01}^-\Delta_{02}^-\Delta_{03}^-},\end{aligned} \tag{98}$$

where the gluon emission and absorption vertices are given by Eqs. (8), (10) and the longitudinal photon splitting vertex by (68). The LC energy denominators are the same as in Eq. (83) for diagram (c), as is the phase space measure (82). Adding everything together and summing over the colors we

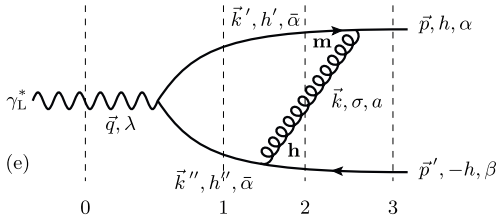

Fig. 13. Vertex diagram (e) contributing to the $q\bar{q}$-component of the longitudinal virtual photon wave function. Momentum conservation: $\vec{q} = \vec{k}' + \vec{k}'' = \vec{p} + \vec{p}'$, $\vec{k}' = \vec{p} - \vec{k}$ and $\vec{k}'' = \vec{k} + \vec{p}'$. The longitudinal momentum fractions for quark and anti-quark are parametrized as $p^+ = zq^+$ and $p'^+ = (1-z)q^+$, and for the gluon in the loop $k^+ = z'q^+$ with $k'^+ = (z-z')q^+$ and $k''^+ = (1-z+z')q^+$. The longitudinal momentum fraction of the virtual photon splitting into a $q\bar{q}$ dipole is $k'^+/q^+ = z-z'$. The momentum fraction of the gluon emission is $k^+/k''^+ = z'/(1-z+z')$ and gluon absorption $k^+/p^+ = z'/z$. The natural momentum for the gluon emission is $\mathbf{h} = \mathbf{k} - (z'/(1-z+z'))\mathbf{k}''$ and for the gluon absorption $\mathbf{m} = \mathbf{k} - (z'/z)\mathbf{p}$. In order to use $\mathbf{m}$ as the integration variable we need to know that $\mathbf{h} = ((1-z)/(1-z+z'))(\mathbf{m} + (z'/(z(1-z))\mathbf{p}))$.

get

$$\psi^{\gamma_T^*\to q\bar{q}}_{(e)} = \psi^{\gamma_L^*\to q\bar{q}}_{LO}(Q,z)\left(\frac{-g^2C_F}{\pi}\right)\int_0^z \frac{dz'(z-z')(1-z+z')}{(z')^2} \times \int \frac{d^{d-2}\mathbf{m}}{(2\pi)^{d-2}} \frac{m^i\left(m+\frac{z'}{z(1-z)}p\right)^n}{\left[\mathbf{m}^2+M_1^{(c)}\right]\left[\left(\mathbf{m}-\frac{(z-z')}{z}\mathbf{p}\right)^2+M_2^{(c)}\right]} \times \text{num}(z,z')\Big|_{(e)}, \tag{99}$$

with the mass scales $M_1^{(c)}$ and $M_2^{(c)}$ from Eq. (85). Because of the simple structure of the longitudinal photon splitting vertex, we can directly evaluate the numerator of (99) in d_s dimensions in terms of Levi-Civita tensors:

$$\text{num}(z,z')\Big|_{(e)} = \left[\left(1-\frac{z'}{2z}\right)\delta^{ij}_{(d_s)} - ih\left(\frac{z'}{2z}\right)\epsilon^{ij}_{(d_s)}\right] \times \left[\left(1-\frac{1}{2}\left(\frac{z'}{1-z+z'}\right)\right)\delta^{nm}_{(d_s)} - ih\frac{1}{2}\left(\frac{z'}{1-z+z'}\right)\epsilon^{nm}_{(d_s)}\right]\delta^{jm}_{(d_s)}. \tag{100}$$

For diagram (f), with kinematical variables as in Fig. 14, the LCWF is

$$\psi^{\gamma_L^*\to q\bar{q}}_{(f)} = \int \tilde{d}k\tilde{d}k'\tilde{d}k''(2\pi)^{d-1}\delta^{(d-1)}(\vec{k}'-\vec{p}-\vec{k})(2\pi)^{d-1}\delta^{(d-1)}(\vec{k}''-\vec{p}'+\vec{k}) \times \frac{V^{\bar{\alpha};\alpha,a}_{h';\sigma,h}(\mathbf{h},\frac{z'}{z+z'})A^{\gamma_L^*}_{\lambda;h',h''}(Q,z+z')\overline{V}^{\bar{\alpha},a;\beta}_{h'',\sigma,-h}(\mathbf{m},\frac{z'}{1-z})}{\Delta^-_{01}\Delta^-_{02}\Delta^-_{03}}, \tag{101}$$

where the phase space measure is the same as in Eq. (87) for diagram (d), as are the energy denominators in Eq. (88). Putting everything together and summing over the colors gives

$$\psi^{\gamma_L^*\to q\bar{q}}_{(f)} = \psi^{\gamma_L^*\to q\bar{q}}_{LO}(Q,z)\left(\frac{-g^2C_F}{\pi}\right)\int_0^{1-z} \frac{dz'(z+z')(1-z-z')}{(z')^2} \times \int \frac{d^{d-2}\mathbf{m}}{(2\pi)^{d-2}} \frac{m^i\left(m-\frac{z'}{z(1-z)}p\right)^n}{\left[\mathbf{m}^2+M_1^{(d)}\right]\left[\left(\mathbf{m}+\frac{(1-z-z')}{1-z}\mathbf{p}\right)^2+M_2^{(d)}\right]} \times \text{num}(z,z')\Big|_{(f)}. \tag{102}$$

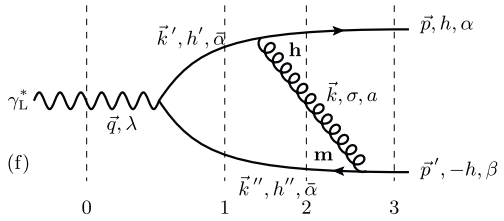

Fig. 14. Vertex correction diagram (f) contributing to the $q\bar{q}$-component of the longitudinal virtual photon wave function at NLO with energy denominators and kinematics. Momentum conservation: $\vec{q} = \vec{k}\,' + \vec{k}\,'' = \vec{p} + \vec{p}\,', \vec{k}\,' = \vec{k} + \vec{p}$ and $\vec{k}\,'' = \vec{p}\,' - \vec{k}$. The longitudinal momentum fractions for quark and anti-quark are parametrized as $p^+ = zq^+$ and $p'^+ = (1-z)q^+$, and for the gluon in the loop $k^+ = z'q^+$ with $k'^+ = (z+z')q^+$ and $k''^+ = (1-z-z')q^+$. The longitudinal momentum fraction of the virtual photon splitting into a $q\bar{q}$ dipole is $k'^+/q^+ = z + z'$. The momentum fraction of the gluon emission is $k^+/k'^+ = z'/(z+z')$ and gluon absorption $k^+/p'^+ = z'/(1-z)$. The natural momentum for the gluon emission is $\mathbf{h} = \mathbf{k} - (z'/(z+z'))\mathbf{k}'$ and for the gluon absorption $\mathbf{m} = \mathbf{k} + (z'/(1-z))\mathbf{p}$. In order to use $\mathbf{m}$ as the integration variable we need to know that $\mathbf{k}' = \mathbf{m} + ((1-z-z')/(1-z))\mathbf{p}$ and $\mathbf{h} = (z/(z+z'))(\mathbf{m} - (z'/(z(1-z))\mathbf{p}))$.

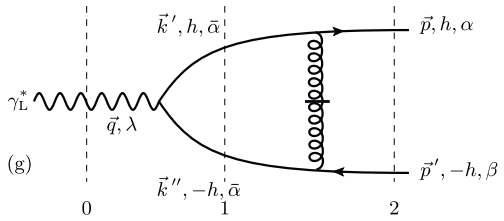

Fig. 15. Instantaneous gluon diagram (g) contributing to the $q\bar{q}$-component of the longitudinal virtual photon wave function at NLO with energy denominators and kinematics. Momentum conservation: $\vec{q} = \vec{k}\,' + \vec{k}\,''$ and $\vec{q} = \vec{p} + \vec{p}\,'$. The longitudinal momentum fractions for quark and anti-quark are parametrized as $p^+ = zq^+$ and $p'^+ = (1-z)q^+$, and $k'^+ = z'q^+$ and $k''^+ = (1-z')q^+$. The longitudinal momentum fraction of the virtual photon splitting into a $q\bar{q}$ dipole is $k'^+/q^+ = z'$.

with $M_1^{(\mathrm{d})}$ and $M_2^{(\mathrm{d})}$ from Eq. (90). Again we can directly use the d_s-dimensional expression for the numerator

$$\begin{aligned}\mathrm{num}(z,z')\Big|_{(\mathrm{f})} = &\left[\left(1 - \frac{z'}{2(1-z)}\right)\delta^{ij}_{(d_s)} + ih\frac{1}{2}\left(\frac{z'}{1-z}\right)\epsilon^{ij}_{(d_s)}\right] \\ &\times \left[\left(1 - \frac{1}{2}\left(\frac{z'}{z+z'}\right)\right)\delta^{nm}_{(d_s)} + ih\frac{1}{2}\left(\frac{z'}{z+z'}\right)\epsilon^{nm}_{(d_s)}\right]\delta^{jm}_{(d_s)}\end{aligned} . \tag{103}$$

For the longitudinal photon there is only one instantaneous diagram, (g) shown in Fig. 15, contributing to the $\gamma_L^* \to q\bar{q}$ LCWF at one-loop level. It is given by

$$\psi^{\gamma_L^* \to q\bar{q}}_{(\mathrm{g})} = \int \mathrm{d}\widetilde{k}'\mathrm{d}\widetilde{k}''(2\pi)^{d-1}\delta^{(d-1)}(\vec{q} - \vec{k}\,' - \vec{k}\,'')\frac{A^{\gamma_L^*}_{\lambda;h,-h}(Q,z')\mathfrak{I}^{(4)}}{\Delta^-_{01}\Delta^-_{02}}, \tag{104}$$

where the instantaneous vertex $\mathfrak{I}^{(4)}$ is given by Eq. (37). The phase space measure simplifies to

$$\begin{aligned}\int \mathrm{d}\widetilde{k}'\mathrm{d}\widetilde{k}''(2\pi)^{d-1}\delta^{(d-1)}(\vec{q} - \vec{k}\,' - \vec{k}\,'') &= \int \frac{\mathrm{d}k'^+}{2k'^+(2\pi)}\int \frac{\mathrm{d}^{d-2}\mathbf{k}'}{(2\pi)^{d-2}}\frac{1}{2k''^+} \\ &= \frac{1}{8\pi q^+}\int_0^1 \frac{\mathrm{d}z'}{z'(1-z')}\int \frac{\mathrm{d}^{d-2}\mathbf{k}'}{(2\pi)^{d-2}}\end{aligned} \tag{105}$$

and the LC energy denominators are

$$\begin{aligned}\Delta_{01}^{-} &= \frac{1}{(-2q^+)z'(1-z')}\left[\mathbf{k}'^2 + M\right] \quad \text{with} \quad M = \frac{z'(1-z')}{z(1-z)}\overline{Q}^2 \\ \Delta_{02}^{-} &= \frac{1}{(-2q^+)z(1-z)}\left[\mathbf{p}^2 + \overline{Q}^2\right].\end{aligned} \tag{106}$$

The instantaneous vertex $\mathfrak{I}^{(4)}$ simplifies to

$$\mathfrak{I}^{(4)} = -4g^2 t^a_{\alpha\bar{\alpha}} t^a_{\bar{\alpha}\beta} \frac{\sqrt{z(1-z)z'(1-z')}}{(z'-z)^2}. \tag{107}$$

Now adding the results from diagrams (e), (f) and (g) together, we get for the full vertex correction

$$\begin{aligned}\psi^{\gamma_L^*\to q\bar{q}}_{(e)+(f)+(g)} = \psi^{\gamma_L^*\to q\bar{q}}_{LO}(Q,z)\left(\frac{g_r^2 C_F}{8\pi^2}\right)\Bigg\{\left[\frac{1}{\varepsilon_{\overline{MS}}} + \log\left(\frac{\mu^2}{\overline{Q}^2}\right)\right] \\ \times\left(-\frac{3}{2} - \log\left(\frac{\alpha}{z}\right) - \log\left(\frac{\alpha}{1-z}\right)\right) + \Gamma^L\Bigg\} + \mathcal{O}(\varepsilon),\end{aligned} \tag{108}$$

where the coefficient Γ^L has the same expression as in Eq. (93). Finally, adding the one-loop quark self energy corrections Eqs. (77) and (79) to (108) we get the full expression for one-loop corrected LCWF for $\gamma_L^* \to q\bar{q}$ in the FDH scheme

$$\begin{aligned}\psi^{\gamma_L^*\to q\bar{q}}_{NLO}\Big|_{FDH} = \psi^{\gamma_L^*\to q\bar{q}}_{LO}(Q,z)\left(\frac{g_r^2 C_F}{8\pi^2}\right)\Bigg\{\left[\frac{3}{2} + \log\left(\frac{\alpha}{z}\right) + \log\left(\frac{\alpha}{1-z}\right)\right]C^{(L)}_{full} \\ + \frac{1}{2}\log^2\left(\frac{z}{1-z}\right) - \frac{\pi^2}{6} + \frac{5}{2}\Bigg\} + \mathcal{O}(\varepsilon),\end{aligned} \tag{109}$$

where

$$C^{(L)}_{full} = \frac{1}{\varepsilon_{\overline{MS}}} + \log\left(\frac{\mu^2}{\overline{Q}^2}\right) - 2\log\left(\frac{\mathbf{p}^2 + \overline{Q}^2}{\overline{Q}^2}\right). \tag{110}$$

Again for comparison the full result computed in CDR scheme [29] and [34] is

$$\begin{aligned}\psi^{\gamma_L^*\to q\bar{q}}_{NLO}\Big|_{CDR} = \psi^{\gamma_L^*\to q\bar{q}}_{LO}(Q,z)\left(\frac{g_r^2 C_F}{8\pi^2}\right)\Bigg\{\left[\frac{3}{2} + \log\left(\frac{\alpha}{z}\right) + \log\left(\frac{\alpha}{1-z}\right)\right]C^{(L)}_{full} \\ + \frac{1}{2}\log^2\left(\frac{z}{1-z}\right) - \frac{\pi^2}{6} + \frac{5}{2} + \frac{1}{2}\Bigg\} + \mathcal{O}(\varepsilon),\end{aligned} \tag{111}$$

where the only difference is the term 1/2, which was identified as a scheme dependent part in the CDR calculation.

6. Wave functions for gluon emission

We then move to the wave functions for quark–antiquark–gluon contributions, needed for real emission contributions to the cross section. Here all the vertices can be, in the FDH scheme, evaluated directly in $d_s = 4$ dimensions.

6.1. Transverse photon

For transverse photons, we need to calculate the diagrams (h)–(k) shown in Figs. 16–19. The LCWF for diagram (h) in Fig. 16 can be written as

$$\psi^{\gamma_T^*\to q\bar{q}g}_{(h)} = \int \bar{d}\tilde{k}'(2\pi)^{d-1}\delta^{(d-1)}(\vec{k}' - \vec{p} - \vec{k})\frac{A^{\gamma_T^*}_{\lambda;h,-h}(\mathbf{k}', z_1+z_2)V^{\beta;\alpha,a}_{h;\sigma,h}(\mathbf{m}, z_2/(z_1+z_2))}{\Delta_{01}^{-}\Delta_{02}^{-}} \tag{112}$$

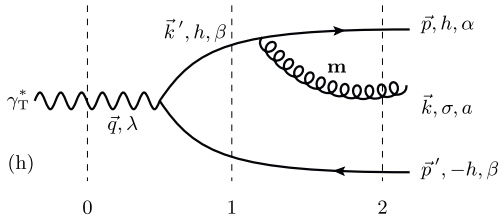

Fig. 16. Diagram (h) contributing to the $q\bar{q}g$-component of the longitudinal virtual photon wave function at NLO with energy denominators and kinematics. Momentum conservation: $\vec{q} = \vec{k}' + \vec{p}'$, $\vec{k}' = \vec{p} + \vec{k}$ and $\vec{q} = \vec{p} + \vec{p}' + \vec{k}$. Momentum fractions are defined by $p^+ = z_1 q^+$, $k^+ = z_2 q^+$, $p'^+ = z_3 q^+$ and $k'^+ = (z_1 + z_2) q^+$. The momentum fraction of the transverse virtual photon splitting into a quark anti-quark dipole is $k'^+/q^+ = z_1 + z_2$, and the natural momentum is $\mathbf{k}' = -\mathbf{p}'$. The momentum fraction of the gluon emission is $k^+/k'^+ = z_2/(z_1 + z_2)$, and the natural momenta for the gluon emission vertex is $\mathbf{m} \equiv \mathbf{k} - (z_2/(z_1 + z_2))\mathbf{k}' = \mathbf{k} + (z_2/(z_1 + z_2))\mathbf{p}'$. Note that the momentum fractions are related to each other via relation $z_1 + z_2 + z_3 = 1$.

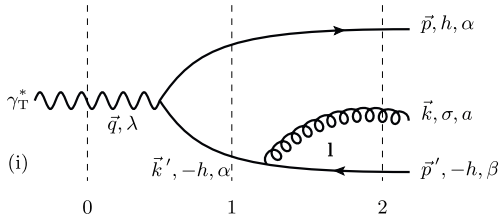

Fig. 17. Diagram (i) contributing to the $q\bar{q}g$-component of the longitudinal virtual photon wave function at NLO with energy denominators and kinematics. Momentum conservation: $\vec{q} = \vec{p} + \vec{k}'$, $\vec{k}' = \vec{k} + \vec{p}'$ and $\vec{q} = \vec{p} + \vec{p}' + \vec{k}$. Momentum fractions are defined by $p^+ = z_1 q^+$, $k^+ = z_2 q^+$, $p'^+ = z_3 q^+$ and $k'^+ = (z_2 + z_3) q^+$. The natural momentum fraction of the transverse virtual photon splitting into a quark anti-quark dipole is $p^+/q^+ = z_1$, and the momentum fraction is $\mathbf{p}$. The momentum fraction of the gluon emission is $k^+/k'^+ = z_2/(z_2 + z_3)$, and the natural momenta for the gluon emission vertex is $\mathbf{l} \equiv \mathbf{k} - (z_2/(z_2 + z_3))\mathbf{k}' = \mathbf{k} + (z_2/(z_2 + z_3))\mathbf{p}$. Note that the momentum fractions are related to each other via relation $z_1 + z_2 + z_3 = 1$.

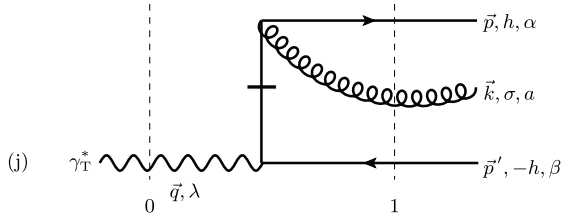

Fig. 18. Diagram (j) contributing to the $q\bar{q}g$-component of the transverse virtual photon wave function at NLO with energy denominators and kinematics. Momentum conservation: $\vec{q} = \vec{p} + \vec{k} + \vec{p}'$. Momentum fractions are defined by $p^+ = z_1 q^+$, $k^+ = z_2 q^+$ and $p'^+ = z_3 q^+$.

where the vertex $A^{\gamma_{\mathrm{T}}^*}_{\lambda;h,-h}(\mathbf{k}', z_1 + z_2)$ for a transverse photon splitting into a quark–antiquark dipole is defined in Eq. (65) and the gluon emission vertex $V^{\beta;\alpha,a}_{h;\sigma,h}(\mathbf{m}, z_2/(z_1 + z_2))$ from a quark is given by Eq. (6). The phase space measure simplifies to

$$\int \mathrm{d}\tilde{k}'(2\pi)^{d-1}\delta^{(d-1)}(\vec{k}' - \vec{p} - \vec{k}) = \frac{1}{2(z_1 + z_2)q^+} \tag{113}$$

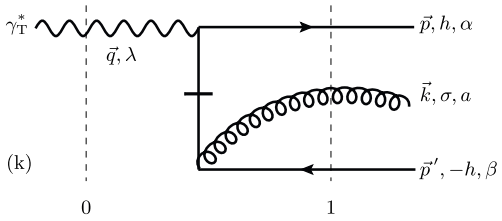

Fig. 19. Diagram (k) contributing to the $q\bar{q}g$-component of the transverse virtual photon wave function at NLO with energy denominators and kinematics. Momentum conservation: $\vec{q} = \vec{p} + \vec{k} + \vec{p}\,'$. Momentum fractions are defined by $p^+ = z_1 q^+$, $k^+ = z_2 q^+$ and $p'^+ = z_3 q^+$.

and the LC energy denominators are given by

$$\begin{aligned} \Delta_{01}^- &= \frac{1}{(-2q^+)z_3(z_1+z_2)}\left[\mathbf{p}'^2 + \overline{Q}_{(\mathrm{h})}^2\right] \\ \Delta_{02}^- &= \frac{z_1+z_2}{(-2q^+)z_1 z_2}\left[\mathbf{m}^2 + \omega_{(\mathrm{h})}\left(\mathbf{p}'^2 + \overline{Q}_{(\mathrm{h})}^2\right)\right], \end{aligned} \tag{114}$$

where

$$\overline{Q}_{(\mathrm{h})}^2 = z_3(z_1+z_2)Q^2, \qquad \omega_{(\mathrm{h})} = \frac{z_1 z_2}{z_3(z_1+z_2)^2}. \tag{115}$$

Using Eqs. (113) and (114) as well as the expression for the vertices, we find

$$\begin{aligned} \psi_{(\mathrm{h})}^{\gamma_T^* \to q\bar{q}g} &= +8q^+ e e_f (g t^a_{\alpha\beta})(z_1 z_3)^{1/2}\left[\left(z_1+z_2-\frac{1}{2}\right)\delta^{ij}_{(d_s)} - ih\frac{1}{2}\epsilon^{ij}_{(d_s)}\right] \\ &\quad\times\left[\left(1-\frac{1}{2}\left(\frac{z_2}{z_1+z_2}\right)\right)\delta^{kl}_{(d_s)} + ih\frac{1}{2}\left(\frac{z_2}{z_1+z_2}\right)\epsilon^{kl}_{(d_s)}\right] \\ &\quad\times\frac{(-\mathbf{p}')^i \mathbf{m}^k \boldsymbol{\varepsilon}_\lambda^j \boldsymbol{\varepsilon}_\sigma^{*l}}{\left[\mathbf{p}'^2 + \overline{Q}_{(\mathrm{h})}^2\right]\left[\mathbf{m}^2 + \omega_{(\mathrm{h})}\left(\mathbf{p}'^2 + \overline{Q}_{(\mathrm{h})}^2\right)\right]}. \end{aligned} \tag{116}$$

Similarly, the LCWF for diagram (i) is given by

$$\psi_{(\mathrm{i})}^{\gamma_T^* \to q\bar{q}g} = \int \widetilde{\mathrm{d}k}'(2\pi)^{d-1}\delta^{(d-1)}(\vec{k}\,' - \vec{k} - \vec{p}\,')\frac{A^{\gamma_T^*}_{\lambda;h,-h}(\mathbf{p}, z_1)\overline{V}^{\alpha;\beta,a}_{-h;,\sigma,-h}(\mathbf{l}, z_2/(z_2+z_3))}{\Delta_{01}^-\Delta_{02}^-} \tag{117}$$

where the gluon emission vertex $\overline{V}^{\alpha;\beta,a}_{-h;\sigma,-h}(\mathbf{l}, z_2/(z_2+z_3))$ from an anti-quark is given by Eq. (10). The phase space measure simplifies to

$$\int \widetilde{\mathrm{d}k}'(2\pi)^{d-1}\delta^{(d-1)}(\vec{k}\,' - \vec{k} - \vec{p}\,') = \frac{1}{2(z_2+z_3)q^+} \tag{118}$$

and the LC energy denominators are given by

$$\begin{aligned} \Delta_{01}^- &= \frac{1}{(-2q^+)z_1(z_2+z_3)}\left[\mathbf{p}^2 + \overline{Q}_{(\mathrm{i})}^2\right] \\ \Delta_{02}^- &= \frac{z_2+z_3}{(-2q^+)z_2 z_3}\left[\mathbf{l}^2 + \omega_{(\mathrm{i})}\left(\mathbf{p}^2 + \overline{Q}_{(\mathrm{i})}^2\right)\right] \end{aligned} \tag{119}$$

with

$$\overline{Q}_{(\mathrm{i})}^2 = z_1(z_2+z_3)Q^2, \qquad \omega_{(\mathrm{i})} = \frac{z_2 z_3}{z_1(z_2+z_3)^2}. \tag{120}$$

Putting everything together we obtain

$$\begin{aligned}\psi^{\gamma_T^*\to q\bar{q}g}_{(\mathrm{i})} &= -8q^+ee_f(gt^a_{\alpha\beta})(z_1z_3)^{1/2}\left[\left(z_1-\frac{1}{2}\right)\delta^{ij}_{(d_s)}-ih\frac{1}{2}\epsilon^{ij}_{(d_s)}\right]\\ &\times\left[\left(1-\frac{1}{2}\left(\frac{z_2}{z_2+z_3}\right)\right)\delta^{kl}_{(d_s)}-ih\frac{1}{2}\left(\frac{z_2}{z_2+z_3}\right)\epsilon^{kl}_{(d_s)}\right]\\ &\times\frac{\mathbf{p}^i\mathbf{l}^k\boldsymbol{\varepsilon}^j_\lambda\boldsymbol{\varepsilon}^{*l}_\sigma}{\left[\mathbf{p}^2+\overline{\mathrm{Q}}^2_{(\mathrm{i})}\right]\left[\mathbf{l}^2+\omega_{(\mathrm{i})}\left(\mathbf{p}^2+\overline{\mathrm{Q}}^2_{(\mathrm{i})}\right)\right]}.\end{aligned} \tag{121}$$

The LCWF for the instantaneous diagram (j) shown in Fig. 18 is given by

$$\psi^{\gamma_T^*\to q\bar{q}g}_{(\mathrm{j})} = -2q^+ee_f(gt^a_{\alpha\beta})\frac{z_1z_2}{(z_1+z_2)^2}(z_1z_3)^{1/2}\left[\delta^{ij}_{(d_s)}+ih\epsilon^{ij}_{(d_s)}\right]\frac{\boldsymbol{\varepsilon}^{*i}_\sigma\boldsymbol{\varepsilon}^j_\lambda}{\left[\mathbf{m}^2+\omega_{(\mathrm{j})}\left(\mathbf{p}'^2+\overline{\mathrm{Q}}^2_{(\mathrm{j})}\right)\right]} \tag{122}$$

where the matrix element for the instantaneous interaction is defined in Eq. (41), and the LC energy denominator is given by Eq. (114) with $\mathbf{m}=\mathbf{k}+(z_2/(z_1+z_2))\mathbf{p}'$ and

$$\overline{\mathrm{Q}}^2_{(\mathrm{j})} = z_3(z_1+z_2)Q^2, \qquad \omega_{(\mathrm{j})} = \frac{z_1z_2}{z_3(z_1+z_2)^2}. \tag{123}$$

Similarly, the LCWF for (k) shown in Fig. 19 is given by

$$\psi^{\gamma_T^*\to q\bar{q}g}_{(\mathrm{k})} = +2q^+ee_f(gt^a_{\alpha\beta})\frac{z_3z_2}{(z_2+z_3)^2}(z_1z_3)^{1/2}\left[\delta^{ij}_{(d_s)}-ih\epsilon^{ij}_{(d_s)}\right]\frac{\boldsymbol{\varepsilon}^{*i}_\sigma\boldsymbol{\varepsilon}^j_\lambda}{\left[\mathbf{l}^2+\omega_{(\mathrm{k})}\left(\mathbf{p}^2+\mathrm{Q}^2_{(\mathrm{k})}\right)\right]} \tag{124}$$

where the matrix element for the instantaneous interaction is defined in Eq. (39), and the LC energy denominator is given by Eq. (119) with $\mathbf{l}=\mathbf{k}+(z_2/(z_2+z_3))\mathbf{p}$ and

$$\mathrm{Q}^2_{(\mathrm{k})} = z_1(z_2+z_3)Q^2, \qquad \omega_{(\mathrm{k})} = \frac{z_2z_3}{z_1(z_2+z_3)^2}. \tag{125}$$

Finally, adding the results in Eqs. (116), (121), (122) and (124) together, we obtain the full tree level contribution to $q\bar{q}g$-component of the transverse virtual photon wave function

$$\begin{aligned}\psi^{\gamma_T^*\to q\bar{q}g}\Big|_{\mathrm{FDH}} &= 8q^+ee_f(gt^a_{\alpha\beta})(z_1z_3)^{1/2}\left\{-\Sigma^{ijkl}_{(\mathrm{h})}\frac{\mathbf{p}'^i\mathbf{m}^k\boldsymbol{\varepsilon}^j_\lambda\boldsymbol{\varepsilon}^{*l}_\sigma}{\left[\mathbf{p}'^2+\overline{\mathrm{Q}}^2_{(\mathrm{h})}\right]\left[\mathbf{m}^2+\omega_{(\mathrm{h})}\left(\mathbf{p}'^2+\overline{\mathrm{Q}}^2_{(\mathrm{h})}\right)\right]}\right.\\ &-\Sigma^{ijkl}_{(\mathrm{i})}\frac{\mathbf{p}^i\mathbf{l}^k\boldsymbol{\varepsilon}^j_\lambda\boldsymbol{\varepsilon}^{*l}_\sigma}{\left[\mathbf{p}^2+\overline{\mathrm{Q}}^2_{(\mathrm{i})}\right]\left[\mathbf{l}^2+\omega_{(\mathrm{i})}\left(\mathbf{p}^2+\overline{\mathrm{Q}}^2_{(\mathrm{i})}\right)\right]}\\ &\left.-\Sigma^{ij}_{(\mathrm{j})}\frac{\boldsymbol{\varepsilon}^{*i}_\sigma\boldsymbol{\varepsilon}^j_\lambda}{\left[\mathbf{m}^2+\omega_{(\mathrm{j})}\left(\mathbf{p}'^2+\overline{\mathrm{Q}}^2_{(\mathrm{j})}\right)\right]}+\Sigma^{ij}_{(\mathrm{k})}\frac{\boldsymbol{\varepsilon}^{*i}_\sigma\boldsymbol{\varepsilon}^j_\lambda}{\left[\mathbf{l}^2+\omega_{(\mathrm{k})}\left(\mathbf{p}^2+\mathrm{Q}^2_{(\mathrm{k})}\right)\right]}\right\},\end{aligned} \tag{126}$$

where we have introduced the following notation:

$$\begin{aligned}\Sigma^{ijkl}_{(\mathrm{h})} &= \left[\left(z_1+z_2-\frac{1}{2}\right)\delta^{ij}_{(d_s)}-ih\frac{1}{2}\epsilon^{ij}_{(d_s)}\right]\left[\left(1-\frac{1}{2}\left(\frac{z_2}{z_1+z_2}\right)\right)\delta^{kl}_{(d_s)}\right.\\ &\left.+ih\frac{1}{2}\left(\frac{z_2}{z_1+z_2}\right)\epsilon^{kl}_{(d_s)}\right]\end{aligned} \tag{127}$$

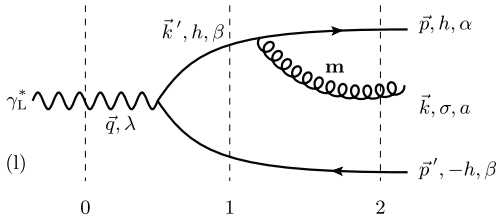

Fig. 20. Diagram (l) contributing to the $q\bar{q}g$-component of the longitudinal virtual photon wave function at NLO with energy denominators and kinematics. Momentum conservation: $\vec{q} = \vec{k}' + \vec{p}', \vec{k}' = \vec{p} + \vec{k}$ and $\vec{q} = \vec{p} + \vec{p}' + \vec{k}$. Momentum fractions are defined by $p^+ = z_1 q^+, k^+ = z_2 q^+, p'^+ = z_3 q^+$ and $k'^+ = (z_1 + z_2) q^+$. The momentum fraction of the virtual photon splitting into a quark anti-quark dipole is $k'^+/q^+ = z_1 + z_2$ and the momentum fraction of the gluon emission is $k^+/k'^+ = z_2/(z_1 + z_2)$. The natural momenta for the gluon emission vertex is $\mathbf{m} \equiv \mathbf{k} - (z_2/(z_1+z_2))\mathbf{k}' = \mathbf{k} + (z_2/(z_1+z_2))\mathbf{p}'$. Note that the momentum fractions are related to each other via relation $z_1 + z_2 + z_3 = 1$.

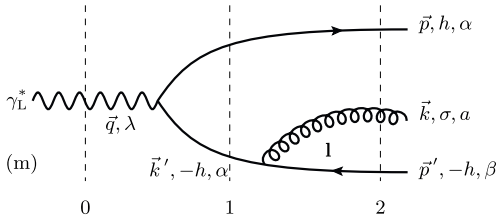

Fig. 21. Diagram (m) contributing to the $q\bar{q}g$-component of the longitudinal virtual photon wave function at NLO with energy denominators and kinematics. Momentum conservation: $\vec{q} = \vec{p} + \vec{k}', \vec{k}' = \vec{k} + \vec{p}'$ and $\vec{q} = \vec{p} + \vec{p}' + \vec{k}$. Momentum fractions are defined by $p^+ = z_1 q^+, k^+ = z_2 q^+, p'^+ = z_3 q^+$ and $k'^+ = (z_2 + z_3) q^+$. The momentum fraction of the virtual photon splitting into a quark anti-quark dipole is $p^+/q^+ = z_1$ and the momentum fraction of the gluon emission is $k^+/k'^+ = z_2/(z_2 + z_3)$. The natural momenta for the gluon emission vertex is $\mathbf{l} \equiv \mathbf{k} - (z_2/(z_2 + z_3))\mathbf{k}' = \mathbf{k} + (z_2/(z_2 + z_3))\mathbf{p}$. Note that the momentum fractions are related to each other via relation $z_1 + z_2 + z_3 = 1$.

$$\Sigma^{ijkl}_{(\mathrm{i})} = \left[\left(z_1 - \frac{1}{2}\right)\delta^{ij}_{(d_s)} - ih\frac{1}{2}\epsilon^{ij}_{(d_s)}\right]\left[\left(1 - \frac{1}{2}\left(\frac{z_2}{z_2+z_3}\right)\right)\delta^{kl}_{(d_s)} - ih\frac{1}{2}\left(\frac{z_2}{z_2+z_3}\right)\epsilon^{kl}_{(d_s)}\right] \tag{128}$$

$$\Sigma^{ij}_{(\mathrm{j})} = \frac{1}{4}\frac{z_1 z_2}{(z_1+z_2)^2}\left[\delta^{ij}_{(d_s)} + ih\epsilon^{ij}_{(d_s)}\right] \tag{129}$$

$$\Sigma^{ij}_{(\mathrm{k})} = \frac{1}{4}\frac{z_3 z_2}{(z_2+z_3)^2}\left[\delta^{ij}_{(d_s)} - ih\epsilon^{ij}_{(d_s)}\right]. \tag{130}$$

6.2. Longitudinal photon

For gluon emission from a longitudinal photon state, we calculate the diagrams (l) and (m) shown in Figs. 20 and 21 contributing to the $q\bar{q}g$-component of the longitudinal virtual photon wave function at NLO. There are no instantaneous diagrams to consider, because strictly speaking the longitudinal photon itself is a part of an instantaneous interaction with the emitting electron.

The LCWF for diagram (l) is given by

$$\psi^{\gamma^*_{\rm L}\to q\bar{q}g}_{(\mathrm{l})} = \int \mathrm{d}\widetilde{k}'(2\pi)^{d-1}\delta^{(d-1)}(\vec{k}' - \vec{p} - \vec{k})\frac{A^{\gamma^*_{\rm L}}_{\lambda;h,-h}(Q, z_1+z_2)V^{\beta;\alpha,a}_{h;\sigma,h}(\mathbf{m}, z_2/(z_1+z_2))}{\Delta^-_{01}\Delta^-_{02}} \tag{131}$$

where the vertex $A^{\gamma_L^*}_{\lambda;h,-h}(Q,z)$ for a longitudinal photon splitting into an quark anti-quark dipole is defined in Eq. (68) and the gluon emission vertex $V^{\beta;\alpha,a}_{h;\sigma,h}$ in Eq. (6). The phase space measure and LC energy denominators are the same as in Eqs. (113) and (114), and thus we get

$$\begin{aligned}\psi^{\gamma_L^*\to q\bar{q}g}_{(\mathrm{l})} &= +8q^+ee_f Q(gt^a_{\alpha\beta})z_1z_3(z_1+z_2)\left(\frac{z_3}{z_1}\right)^{1/2}\left[\left(1-\frac{1}{2}\left(\frac{z_2}{z_1+z_2}\right)\right)\delta^{ij}_{(d_s)}\right.\\ &\left.+ih\frac{1}{2}\left(\frac{z_2}{z_1+z_2}\right)\epsilon^{ij}_{(d_s)}\right]\times\frac{\mathbf{m}^i\boldsymbol{\varepsilon}^{*j}_\sigma}{\left[\mathbf{p}'^2+\overline{Q}^2_{(\mathrm{l})}\right]\left[\mathbf{m}^2+\omega_{(\mathrm{l})}\left(\mathbf{p}'^2+\overline{Q}^2_{(\mathrm{l})}\right)\right]},\end{aligned} \tag{132}$$

where

$$\overline{Q}^2_{(\mathrm{l})}=z_3(z_1+z_2)Q^2,\qquad \omega_{(\mathrm{l})}=\frac{z_1z_2}{(z_1+z_2)^2z_3}. \tag{133}$$

Similarly, the LCWF for diagram (m) can be written as

$$\psi^{\gamma_L^*\to q\bar{q}g}_{(\mathrm{m})}=\int \mathrm{d}\widetilde{k}'(2\pi)^{d-1}\delta^{(d-1)}(\vec{k}'-\vec{k}-\vec{p}\,')\frac{A^{\gamma_L^*}_{\lambda;h,-h}(Q,z_1)\overline{V}^{\alpha;\beta,a}_{-h;\sigma,-h}(\mathbf{l},z_2/(z_2+z_3))}{\Delta^-_{01}\Delta^-_{02}}, \tag{134}$$

where the phase space measure and LC energy denominators are given in Eqs. (118) and (119). Putting everything together we obtain

$$\begin{aligned}\psi^{\gamma_L^*\to q\bar{q}g}_{(\mathrm{m})} &= -8q^+ee_f Q(gt^a_{\alpha\beta})z_1z_3(z_2+z_3)\left(\frac{z_1}{z_3}\right)^{1/2}\\ &\times\left[\left(1-\frac{1}{2}\left(\frac{z_2}{z_2+z_3}\right)\right)\delta^{ij}_{(d_s)}-ih\frac{1}{2}\left(\frac{z_2}{z_2+z_3}\right)\epsilon^{ij}_{(d_s)}\right]\\ &\times\frac{\mathbf{l}^i\boldsymbol{\varepsilon}^{*j}_\sigma}{\left[\mathbf{p}^2+\overline{Q}^2_{(\mathrm{m})}\right]\left[\mathbf{l}^2+\omega_{(\mathrm{m})}\left(\mathbf{p}^2+\overline{Q}^2_{(\mathrm{m})}\right)\right]},\end{aligned} \tag{135}$$

where

$$\overline{Q}^2_{(\mathrm{m})}=z_1(z_2+z_3)Q^2,\qquad \omega_{(\mathrm{m})}=\frac{z_2z_3}{(z_2+z_3)^2z_1}. \tag{136}$$

Finally, summing the contributions in Eqs. (132) and (135) together we get

$$\begin{aligned}\psi^{\gamma_L^*\to q\bar{q}g}\Big|_{\mathrm{FDH}} &= 8q^+ee_f Q(gt^a_{\alpha\beta})z_1z_3\left[\Sigma^{ij}_{(\mathrm{l})}\frac{\mathbf{m}^i}{\left[\mathbf{p}'^2+\overline{Q}^2_{(\mathrm{l})}\right]\left[\mathbf{m}^2+\omega_{(\mathrm{l})}\left(\mathbf{p}'^2+\overline{Q}^2_{(\mathrm{l})}\right)\right]}\right.\\ &\left.-\Sigma^{ij}_{(\mathrm{m})}\frac{\mathbf{l}^i}{\left[\mathbf{p}^2+\overline{Q}^2_{(\mathrm{m})}\right]\left[\mathbf{l}^2+\omega_{(\mathrm{m})}\left(\mathbf{p}^2+\overline{Q}^2_{(\mathrm{m})}\right)\right]}\right]\boldsymbol{\varepsilon}^{*j}_\sigma,\end{aligned} \tag{137}$$

where we have defined

$$\Sigma^{ij}_{(\mathrm{l})}=(z_1+z_2)\left(\frac{z_3}{z_1}\right)^{1/2}\left[\left(1-\frac{1}{2}\left(\frac{z_2}{z_1+z_2}\right)\right)\delta^{ij}_{(d_s)}+ih\frac{1}{2}\left(\frac{z_2}{z_1+z_2}\right)\epsilon^{ij}_{(d_s)}\right] \tag{138}$$

$$\Sigma^{ij}_{(\mathrm{m})}=(z_2+z_3)\left(\frac{z_1}{z_3}\right)^{1/2}\left[\left(1-\frac{1}{2}\left(\frac{z_2}{z_2+z_3}\right)\right)\delta^{ij}_{(d_s)}-ih\frac{1}{2}\left(\frac{z_2}{z_2+z_3}\right)\epsilon^{ij}_{(d_s)}\right]. \tag{139}$$

7. NLO DIS cross section

As explained in Section 3, in order to calculate the DIS cross section we first need to Fourier transform the final momentum space expressions of the transverse and longitudinal virtual photon LCWFs to mixed space. Because of the simple algebraic structure, we will first consider the longitudinal virtual photon case.

7.1. Longitudinal photon

According to Eq. (54), the mixed space expression for the $q\bar{q}$-component of the longitudinal virtual photon amplitude computed in the FDH scheme at NLO accuracy can be written as

$$|\gamma_{\mathrm{L}}^{*}(q^{+},Q^{2},\lambda)\rangle_{q\bar{q}} = \sum_{h}\sum_{\text{color}} \mathcal{PS}_{(2)}^{+}\int_{\mathbf{xy}}\left(\widetilde{\psi}_{\mathrm{LO}}^{\gamma_{\mathrm{L}}^{*}\to q\bar{q}}\Big|_{\mathrm{FDH}} + \widetilde{\psi}_{\mathrm{NLO}}^{\gamma_{\mathrm{L}}^{*}\to q\bar{q}}\Big|_{\mathrm{FDH}}\right) \times |q(p^{+},\mathbf{x},h,\alpha)\bar{q}(p'^{+},\mathbf{y},-h,\beta)\rangle, \tag{140}$$

where the two particle plus momentum phase space factor, $\mathcal{PS}_{(2)}^{+}$, defined in Eq. (56) is given by

$$\mathcal{PS}_{(2)}^{+} = \frac{1}{8\pi q^{+}}\int_{0}^{1}\frac{\mathrm{d}z}{z(1-z)}. \tag{141}$$

The transverse Fourier transformed LO and NLO light cone wave functions for longitudinal virtual photon in the mixed space are given by

$$\widetilde{\psi}_{\mathrm{LO/NLO}}^{\gamma_{\mathrm{L}}^{*}\to q\bar{q}}\Big|_{\mathrm{FDH}} = \int\frac{\mathrm{d}^{2}\mathbf{p}}{(2\pi)^{2}}\left(\psi_{\mathrm{LO/NLO}}^{\gamma_{\mathrm{L}}^{*}\to q\bar{q}}\Big|_{\mathrm{FDH}}\right)e^{i\mathbf{p}\cdot\mathbf{r}_{xy}} \tag{142}$$

with $\mathbf{r}_{xy}\equiv\mathbf{x}-\mathbf{y}$. Using Eq. (68) together with Eq. (C4) we get

$$\begin{aligned}\widetilde{\psi}_{\mathrm{LO}}^{\gamma_{\mathrm{L}}^{*}\to q\bar{q}}\Big|_{\mathrm{FDH}} &= 4q^{+}ee_{f}Q\delta_{\alpha\beta}[z(1-z)]^{3/2}\int\frac{\mathrm{d}^{2}\mathbf{p}}{(2\pi)^{2}}\frac{e^{i\mathbf{p}\cdot\mathbf{r}_{xy}}}{\left[\mathbf{p}^{2}+\overline{Q}^{2}\right]}\\ &= \frac{4ee_{f}Q\delta_{\alpha\beta}}{(2\pi)}[z(1-z)]^{3/2}K_{0}\left(\overline{Q}|\mathbf{r}_{xy}|\right).\end{aligned} \tag{143}$$

Correspondingly, using Eqs. (109), (C4) and (C5) gives

$$\widetilde{\psi}_{\mathrm{NLO}}^{\gamma_{\mathrm{L}}^{*}\to q\bar{q}}\Big|_{\mathrm{FDH}} = \frac{4q^{+}ee_{f}Q\delta_{\alpha\beta}}{(2\pi)}\left(\frac{g_{r}^{2}C_{\mathrm{F}}}{8\pi^{2}}\right)[z(1-z)]^{3/2}K_{0}\left(\overline{Q}|\mathbf{r}_{xy}|\right)\mathcal{K}^{\gamma_{\mathrm{L}}^{*}}\Big|_{\mathrm{FDH}}, \tag{144}$$

where the NLO kernel for longitudinal virtual photon written in the mixed space reads

$$\begin{aligned}\mathcal{K}^{\gamma_{\mathrm{L}}^{*}}\Big|_{\mathrm{FDH}} &= \left[\frac{3}{2}+\log\left(\frac{\alpha}{z}\right)+\log\left(\frac{\alpha}{1-z}\right)\right]\left\{\frac{1}{\varepsilon_{\overline{\mathrm{MS}}}}+\log\left(\frac{\mathbf{r}_{xy}^{2}\mu^{2}}{4}\right)-2\Psi_{0}(1)\right\}\\ &\quad+\frac{1}{2}\log^{2}\left(\frac{z}{1-z}\right)-\frac{\pi^{2}}{6}+\frac{5}{2}+\mathcal{O}(\varepsilon).\end{aligned} \tag{145}$$

Note again that in the CDR scheme (see [30]) there is an extra factor of 1/2 in the expression of NLO kernel defined in Eq. (145), which is the scheme dependent part of the one-loop computation of longitudinal virtual photon LCWF.

Next, operating on the amplitude in Eq. (140) with the eikonal scattering operator $(1-\hat{S}_E)$ and finally squaring the expression and simplifying the color algebra as in Eq. (D4) we find

$$
\begin{aligned}
{}_{q\bar{q}}\langle\gamma_{\mathrm{L}}^*(q'^+,Q^2,\lambda')|1-\hat{S}_E|\gamma_{\mathrm{L}}^*(q^+,Q^2,\lambda)\rangle_{q\bar{q}} &= 2q^+(2\pi)\delta(q'^+-q^+)\frac{8N_c\alpha_{em}e_f^2Q^2}{(2\pi)^2}\\
\times\int_{\mathbf{xy}}\int_0^1 \mathrm{d}z z^2(1-z)^2[K_0\left(|\mathbf{r}_{xy}|\overline{Q}\right)]^2&\left[1+\left(\frac{\alpha_s C_{\mathrm{F}}}{\pi}\right)\mathcal{K}^{\gamma_{\mathrm{L}}^*}\Big|_{\mathrm{FDH}}\right]\left(1-\mathcal{S}_{xy}\right)+\mathcal{O}(\alpha_{em}\alpha_s^2),
\end{aligned}
\tag{146}
$$

where we have summed over the helicity and color, introduced the fine structure constants $\alpha_s = g_r^2/4\pi$ and $\alpha_{em} = e^2/4\pi$ and the notation

$$
\mathcal{S}_{xy} = \frac{1}{N_c}\mathrm{Tr}\left(U[A](\mathbf{x})U^\dagger[A](\mathbf{y})\right). \tag{147}
$$

Similarly, using Eqs. (55), (56), and (137) the mixed space expression for the $q\bar{q}g$-component of the longitudinal virtual photon amplitude computed in the FDH scheme at NLO accuracy simplifies to

$$
\begin{aligned}
|\gamma_{\mathrm{L}}^*(q^+,Q^2,\lambda)\rangle_{q\bar{q}g} = \sum_{h,\sigma}\sum_{\text{color}}\mathcal{PS}^+_{(3)}\int_{\mathbf{xy}[\mathbf{z}]}&\left(\widetilde{\psi}^{\gamma_{\mathrm{L}}^*\to q\bar{q}g}\Big|_{\mathrm{FDH}}\right)\\
\times\ |q(p^+,\mathbf{x},h,\alpha)\bar{q}(p'^+,\mathbf{y},-h,\beta)&g(k^+,\mathbf{z},\sigma,a)\rangle,
\end{aligned}
\tag{148}
$$

where we have denoted by

$$
\int_{[\mathbf{z}]} = \int \mathrm{d}^{d-2}\mathbf{z} \tag{149}
$$

the integral over the gluon phase space, which must be done in d dimensional spacetime. The quark and antiquark are "observed" particles in the FDH scheme, and thus the integrals over $\mathbf{x}$, $\mathbf{y}$ can be kept in 2 dimensions, simplifying the final state phase space integrations. The three particle plus momentum phase space factor, $\mathcal{PS}^+_{(3)}$, is given by

$$
\mathcal{PS}^+_{(3)} = \frac{1}{8q^+(2\pi)^2}\int_0^\infty \mathrm{d}z_1\int_0^\infty \mathrm{d}z_2\int_0^\infty \mathrm{d}z_3\frac{1}{z_1z_2z_3}\delta(z_1+z_2+z_3-1), \tag{150}
$$

and

$$
\begin{aligned}
\widetilde{\psi}^{\gamma_{\mathrm{L}}^*\to q\bar{q}g}\Big|_{\mathrm{FDH}} &= 8q^+ee_fQg_rt^a_{\alpha\beta}z_1z_3\Big\{\Sigma^{ij}_{(\mathrm{l})}\mathcal{I}^i(\mathbf{r}_{yxz},\mathbf{r}_{zx},\overline{Q}^2_{(\mathrm{l})},\omega_{(\mathrm{l})})\\
&\quad-\Sigma^{ij}_{(\mathrm{m})}\mathcal{I}^i(\mathbf{r}_{xyz},\mathbf{r}_{zy},\overline{Q}^2_{(\mathrm{m})},\omega_{(\mathrm{m})})\Big\}\boldsymbol{\varepsilon}^{*j}_\sigma.
\end{aligned}
\tag{151}
$$

Here we have defined the function $\mathcal{I}^i(\mathbf{b},\mathbf{r},\overline{Q}^2,\omega)$ as

$$
\mathcal{I}^i(\mathbf{b},\mathbf{r},\overline{Q}^2,\omega) = \mu^{2-\frac{d}{2}}\int\frac{\mathrm{d}^2\mathbf{P}}{(2\pi)^2}\int\frac{\mathrm{d}^{d-2}\mathbf{K}}{(2\pi)^{d-2}}\frac{\mathbf{K}^i e^{i\mathbf{P}\cdot\mathbf{b}}e^{i\mathbf{K}\cdot\mathbf{r}}}{\left[\mathbf{P}^2+\overline{Q}^2\right]\left[\mathbf{K}^2+\omega\left(\mathbf{P}^2+\overline{Q}^2\right)\right]} \tag{152}
$$

and introduced the notation

$$
\mathbf{r}_{yxz} = \mathbf{r}_{yx}-\left(\frac{z_2}{z_1+z_2}\right)\mathbf{r}_{zx},\qquad \mathbf{r}_{xyz} = \mathbf{r}_{xy}-\left(\frac{z_2}{z_2+z_3}\right)\mathbf{r}_{zy}. \tag{153}
$$

The evaluation of the integral defined in Eq. (152) is outlined in Appendix C, leading to

$$
\mathcal{I}^i(\mathbf{b},\mathbf{r},\overline{Q}^2,\omega) = \mu^{2-\frac{d}{2}}\frac{i}{8}\pi^{-d/2}\mathbf{r}^i(\mathbf{r}^2)^{1-d/2}\int_0^\infty\frac{\mathrm{d}u}{u}e^{-u\overline{Q}^2}e^{-\frac{\mathbf{b}^2}{4u}}\Gamma\left(\frac{d}{2}-1,\frac{\omega\mathbf{r}^2}{4u}\right). \tag{154}
$$

Unfortunately, the remaining u-integral in Eq. (154) cannot be done analytically for arbitrary dimension d. In order to proceed further, we first square the amplitude in Eq. (148) with the operator $(1-\hat{S}_E)$,

$$
\begin{aligned}
&{}_{q\bar{q}g}\langle\gamma_{\mathrm{L}}^{*}(q'^{+},Q^2,\lambda')|1-\hat{S}_E|\gamma_{\mathrm{L}}^{*}(q^{+},Q^2,\lambda)\rangle_{q\bar{q}g} \\
&=\sum_{h,h',\sigma,\sigma'}\sum_{\text{color}}\mathcal{P}\mathcal{S}^{+}_{(3)}\mathcal{P}\mathcal{S}'^{+}_{(3)}\int_{\mathbf{xy[z]x'y'[z']}}\left(\widetilde{\psi}^{\gamma_{\mathrm{L}}^{*}\to q\bar{q}g}\Big|_{\mathrm{FDH}}\right)\left(\widetilde{\psi}^{\gamma_{\mathrm{L}}^{*}\to q\bar{q}g}\Big|_{\mathrm{FDH}}\right)^{*} \\
&\quad\times\langle g(k'^{+},\mathbf{z}',\sigma',b)\bar{q}(\ell'^{+},\mathbf{y}',-h',\beta')q(p'^{+},\mathbf{x}',h',\alpha')|1 \\
&\quad-\hat{S}_E|q(p^{+},\mathbf{x},h,\alpha)\bar{q}(\ell^{+},\mathbf{y},-h,\beta)g(k^{+},\mathbf{z},\sigma,a)\rangle.
\end{aligned}
\tag{155}
$$

The color algebra is written out in detail in Appendix D. Using the result Eq. (D6) from the appendix we obtain

$$
\begin{aligned}
&{}_{q\bar{q}g}\langle\gamma_{\mathrm{L}}^{*}(q'^{+},Q^2,\lambda')|1-\hat{S}_E|\gamma_{\mathrm{L}}^{*}(\vec{q},Q^2,\lambda)\rangle_{q\bar{q}g} \\
&=2q^{+}(2\pi)\delta(q'^{+}-q^{+})\frac{16(2\pi)^3N_{\mathrm{c}}\alpha_{em}e_f^2Q^2}{(2\pi)^2}\left(\frac{\alpha_s C_{\mathrm{F}}}{\pi}\right)\int_{\mathbf{xy[z]}} \\
&\quad\times\int_0^{\infty}\mathrm{d}z_1\int_0^{\infty}\mathrm{d}z_3\int_0^{\infty}\mathrm{d}z_2\,\delta(z_1+z_2+z_3-1)\frac{z_1z_3}{z_2}\Theta(z_1,z_2,z_3)\left(1-\mathcal{S}_{xyz}\right),
\end{aligned}
\tag{156}
$$

where the function Θ is given by

$$
\begin{aligned}
\Theta=&\left[\Sigma^{ij}_{(\mathrm{l})}\mathcal{I}^{i}(\mathbf{r}_{yxz},\mathbf{r}_{zx},\overline{\mathrm{Q}}^2_{(\mathrm{l})},\omega_{(\mathrm{l})})-\Sigma^{ij}_{(\mathrm{m})}\mathcal{I}^{i}(\mathbf{r}_{xyz},\mathbf{r}_{zy},\overline{\mathrm{Q}}^2_{(\mathrm{m})},\omega_{(\mathrm{m})})\right] \\
&\times\left[\Sigma^{kl}_{(\mathrm{l})}\mathcal{I}^{k}(\mathbf{r}_{yxz},\mathbf{r}_{zx},\overline{\mathrm{Q}}^2_{(\mathrm{l})},\omega_{(\mathrm{l})})-\Sigma^{kl}_{(\mathrm{m})}\mathcal{I}^{k}(\mathbf{r}_{xyz},\mathbf{r}_{zy},\overline{\mathrm{Q}}^2_{(\mathrm{m})},\omega_{(\mathrm{m})})\right]^{*}\sum_{\sigma}\boldsymbol{\varepsilon}^{*j}_{\sigma}\boldsymbol{\varepsilon}^{l}_{\sigma}
\end{aligned}
\tag{157}
$$

and $\mathcal{S}_{xyz}$ is defined as

$$
\mathcal{S}_{xyz}=\frac{{N_{\mathrm{c}}}^2}{2C_{\mathrm{F}}N_{\mathrm{c}}}\left[\mathcal{S}_{xz}\mathcal{S}_{zy}-\frac{1}{{N_{\mathrm{c}}}^2}\mathcal{S}_{xy}\right].
\tag{158}
$$

It is important that $\mathcal{S}_{xyz}$ must satisfy the condition $\mathcal{S}_{xyz}\to\mathcal{S}_{xy}$, when $\mathbf{z}\to\mathbf{x}$ or $\mathbf{z}\to\mathbf{y}$. This guarantees that the UV divergence in the real and virtual corrections has the same color structure from the target side, and can thus cancel between the contributions. Performing the sum over the d_s-dimensional gluon transverse polarization vectors and making some algebra Eq. (157) simplifies to

$$
\begin{aligned}
\Theta=&\frac{(\mu^2)^{2-d/2}}{8^2\pi^d}\Bigg\{\left(\frac{z_3}{z_1}\right)\left(z_1(z_1+z_2)+\frac{z_2^2}{2}\right)(\mathbf{r}_{zx}^2)^{3-d}\mathcal{J}^2(\mathbf{r}_{yxz}^2,\mathbf{r}_{zx}^2,\overline{\mathrm{Q}}^2_{(\mathrm{l})},\omega_{(\mathrm{l})}) \\
&+\left(\frac{z_1}{z_3}\right)\left(z_3(z_2+z_3)+\frac{z_2^2}{2}\right)(\mathbf{r}_{zy}^2)^{3-d}\mathcal{J}^2(\mathbf{r}_{xyz}^2,\mathbf{r}_{zy}^2,\overline{\mathrm{Q}}^2_{(\mathrm{m})},\omega_{(\mathrm{m})}) \\
&-((z_1+z_2)z_3+(z_2+z_3)z_1)\frac{(\mathbf{r}_{zx}\cdot\mathbf{r}_{zy})}{(\mathbf{r}_{zx}^2)^{\frac{d}{2}-1}(\mathbf{r}_{zy}^2)^{\frac{d}{2}-1}}\mathcal{J}(\mathbf{r}_{yxz}^2,\mathbf{r}_{zx}^2,\overline{\mathrm{Q}}^2_{(\mathrm{l})},\omega_{(\mathrm{l})}) \\
&\times\mathcal{J}(\mathbf{r}_{xyz}^2,\mathbf{r}_{zy}^2,\overline{\mathrm{Q}}^2_{(\mathrm{m})},\omega_{(\mathrm{m})})\Bigg\},
\end{aligned}
\tag{159}
$$

where we have taken the limit $d_s \to 4$ and defined the function $\mathcal{J}$ as

$$\mathcal{J}(\mathbf{b}^2, \mathbf{r}^2, \overline{Q}^2, \omega) = \int_0^\infty \frac{\mathrm{d}u}{u} e^{-u\overline{Q}^2} e^{-\frac{\mathbf{b}^2}{4u}} \Gamma\left(\frac{d}{2} - 1, \frac{\omega \mathbf{r}^2}{4u}\right). \tag{160}$$

Now equation (156) can be expressed in a more compact form by introducing the notation

$$\overline{\Theta} = \overline{\Theta}_{(\mathrm{l})} + \overline{\Theta}_{(\mathrm{m})} + \overline{\Theta}_{(\mathrm{l})(\mathrm{m})}, \tag{161}$$

where

$$\begin{aligned}
\overline{\Theta}_{(\mathrm{l})} &= \frac{(\mu^2)^{2-d/2}}{8^2\pi^d} \left(\frac{z_3}{z_1}\right)\left(z_1(z_1+z_2) + \frac{z_2^2}{2}\right) \int_{[\mathbf{z}]} (\mathbf{r}_{zx}^2)^{3-d} \mathcal{J}^2(\mathbf{r}_{yxz}^2, \mathbf{r}_{zx}^2, \overline{Q}_{(\mathrm{l})}^2, \omega_{(\mathrm{l})}) \left(1 - \mathcal{S}_{xyz}\right) \\
\overline{\Theta}_{(\mathrm{m})} &= \frac{(\mu^2)^{2-d/2}}{8^2\pi^d} \left(\frac{z_1}{z_3}\right)\left(z_3(z_2+z_3) + \frac{z_2^2}{2}\right) \\
&\quad \times \int_{[\mathbf{z}]} (\mathbf{r}_{zy}^2)^{3-d} \mathcal{J}^2(\mathbf{r}_{xyz}^2, \mathbf{r}_{zy}^2, \overline{Q}_{(\mathrm{m})}^2, \omega_{(\mathrm{m})}) \left(1 - \mathcal{S}_{xyz}\right)
\end{aligned} \tag{162}$$

and

$$\begin{aligned}
\overline{\Theta}_{(\mathrm{l})(\mathrm{m})} &= -\frac{(\mu^2)^{2-d/2}}{8^2\pi^d} \left((z_1+z_2)z_3 + (z_2+z_3)z_1\right) \int_{[\mathbf{z}]} \frac{(\mathbf{r}_{zx} \cdot \mathbf{r}_{zy})}{(\mathbf{r}_{zx}^2)^{\frac{d}{2}-1} (\mathbf{r}_{zy}^2)^{\frac{d}{2}-1}} \\
&\quad \times \mathcal{J}(\mathbf{r}_{yxz}^2, \mathbf{r}_{zx}^2, \overline{Q}_{(\mathrm{l})}^2 \omega_{(\mathrm{l})}) \mathcal{J}(\mathbf{r}_{xyz}^2, \mathbf{r}_{zy}^2, \overline{Q}_{(\mathrm{m})}^2, \omega_{(\mathrm{m})}) \left(1 - \mathcal{S}_{xyz}\right).
\end{aligned} \tag{163}$$

Thus we obtain the following expression

$$\begin{aligned}
{}_{q\bar{q}g}\langle \gamma_{\mathrm{L}}^*(q'^+, Q^2, \lambda') | \hat{S}_E | \gamma_{\mathrm{L}}^*(q^+, Q^2, \lambda) \rangle_{q\bar{q}g} &= 2q^+(2\pi)\delta(q'^+ - q^+) \frac{16(2\pi)^3 N_{\mathrm{c}} \alpha_{em} e_f^2 Q^2}{(2\pi)^2} \left(\frac{\alpha_{\mathrm{s}} C_{\mathrm{F}}}{\pi}\right) \\
&\quad \times \int_{\mathbf{xy}} \int_0^\infty \mathrm{d}z_1 \int_0^\infty \mathrm{d}z_2 \int_0^\infty \mathrm{d}z_3 \delta(z_1 + z_2 + z_3 - 1) \frac{z_1 z_3}{z_2} \\
&\quad \times \left[\overline{\Theta}_{(\mathrm{l})} + \overline{\Theta}_{(\mathrm{m})} + \overline{\Theta}_{(\mathrm{l})(\mathrm{m})}\right].
\end{aligned} \tag{164}$$

In Eq. (164), the first and second term are UV-divergent when $\mathbf{z} \to \mathbf{x}$ and $\mathbf{z} \to \mathbf{y}$, respectively. The third (cross) term is UV-finite and thus one can immediately take the limit $d \to 4$. In order to make the UV subtraction between the real $q\bar{q}g$-component and the virtual $q\bar{q}$-term (which has an explicit $1/\varepsilon$) we must add and subtract a term to make this cancellation manifest. Ideally we would subtract from Eq. (164) the same expression with the Wilson line structure $\left(1 - \mathcal{S}_{xyz}\right)$ replaced by its UV limit $\left(1 - \mathcal{S}_{xy}\right)$. This is, however not possible analytically since we have not been able to find an analytical expression for the required integral (160). However, there is no unique choice for the subtraction term. Indeed, since the only requirement for the subtraction is that the UV divergence needs to cancel, it is sufficient for the subtraction to approximate $\mathcal{J}(\mathbf{b}^2, \mathbf{r}^2, \overline{Q}^2, \omega)$ by any function that has the same value in the UV limit $\mathbf{r}^2 \to 0$ (for any d). Here we find it convenient to use the UV approximation

$$\begin{aligned}
\mathcal{J}(\mathbf{b}^2, \mathbf{r}^2, \overline{Q}^2, \omega)\Big|_{\mathrm{UV}} &= \int_0^\infty \frac{\mathrm{d}u}{u} e^{-u\overline{Q}^2} e^{-\frac{\mathbf{b}^2}{4u}} \Gamma\left(\frac{d}{2} - 1\right) e^{-\frac{\mathbf{r}^2}{2\mathbf{b}^2 \xi}} \\
&= 2K_0\left(\overline{Q}|\mathbf{b}|\right) \Gamma\left(\frac{d}{2} - 1\right) e^{-\frac{\mathbf{r}^2}{2\mathbf{b}^2 \xi}}, \qquad \xi \in \Re,
\end{aligned} \tag{165}$$

for which

$$\mathcal{J}(\mathbf{b}^2, \mathbf{r}^2, \overline{Q}^2, \omega)\Big|_{\mathrm{UV}, \mathbf{r} \to \mathbf{0}} = \mathcal{J}(\mathbf{b}^2, \mathbf{r}^2, \overline{Q}^2, \omega)\Big|_{\mathbf{r} \to \mathbf{0}}. \tag{166}$$

A natural way to think of this expression is that in the u-integral (160) the exponential sets $u \sim \mathbf{b}^2$. Our approximation replaces $\Gamma\left(\frac{d}{2}-1, \frac{\omega \mathbf{r}^2}{4u}\right)$ by $\Gamma\left(\frac{d}{2}-1\right) e^{-\frac{\mathbf{r}^2}{2\mathbf{b}^2\xi}}$ which (a) is independent of u, allowing for an analytical calculation of the u-integral, (b) has the same value in the UV limit $\mathbf{r} \to \mathbf{0}$ and (c) is also good and smooth approximation for large $\mathbf{r}^2$. The choice of the constant ξ is somewhat arbitrary, here we adopt the value $\xi = e^{\gamma_E}$ that leads to simpler expressions in the following. Our choice is slightly different than that of [30] concerning point (c) above; this difference is discussed in Appendix E.

Using our choice of $\mathcal{J}|_{\mathrm{UV}}$ we now define the UV-subtraction terms as

$$\begin{aligned}
\overline{\Theta}_{(\mathrm{l})}\Big|_{\mathrm{UV};\mathbf{z}\to\mathbf{x}} &= \frac{(\mu^2)^{2-d/2}}{8^2\pi^d}\left(\frac{z_3}{z_1}\right)\left(z_1(z_1+z_2)+\frac{z_2^2}{2}\right) \\
&\quad\times \int_{[\mathbf{z}]} (\mathbf{r}_{zx}^2)^{3-d}\mathcal{J}^2(\mathbf{r}_{xy}^2, \mathbf{r}_{zx}^2, \overline{\mathrm{Q}}_{(\mathrm{l})}^2, \omega_{(\mathrm{l})})\Big|_{\mathrm{UV}}\left(1-\mathcal{S}_{xy}\right) \\
\overline{\Theta}_{(\mathrm{m})}\Big|_{\mathrm{UV};\mathbf{z}\to\mathbf{y}} &= \frac{(\mu^2)^{2-d/2}}{8^2\pi^d}\left(\frac{z_1}{z_3}\right)\left(z_3(z_2+z_3)+\frac{z_2^2}{2}\right) \\
&\quad\times \int_{[\mathbf{z}]} (\mathbf{r}_{zy}^2)^{3-d}\mathcal{J}^2(\mathbf{r}_{xy}^2, \mathbf{r}_{zy}^2, \overline{\mathrm{Q}}_{(\mathrm{m})}^2, \omega_{(\mathrm{m})})\Big|_{\mathrm{UV}}\left(1-\mathcal{S}_{xy}\right).
\end{aligned} \tag{167}$$

Performing the subtraction

$$\begin{aligned}
&{}_{q\bar{q}g}\langle\gamma_{\mathrm{L}}^*(q'^+, Q^2, \lambda')|1-\hat{S}_E|\gamma_{\mathrm{L}}^*(q^+, Q^2, \lambda)\rangle_{q\bar{q}g} \\
&= 2q^+(2\pi)\delta(q'^+-q^+)\frac{16(2\pi)^3 N_c\alpha_{em}e_f^2Q^2}{(2\pi)^2}\left(\frac{\alpha_s C_{\mathrm{F}}}{\pi}\right) \\
&\quad\times\int_{\mathbf{xy}}\int_0^\infty \mathrm{d}z_1\int_0^\infty \mathrm{d}z_2\int_0^\infty \mathrm{d}z_3\,\delta(z_1+z_2+z_3-1)\frac{z_1z_3}{z_2} \\
&\quad\times\left[\left(\overline{\Theta}_{(\mathrm{l})}-\overline{\Theta}_{(\mathrm{l})}\Big|_{\mathrm{UV};\mathbf{z}\to\mathbf{x}}\right)+\left(\overline{\Theta}_{(\mathrm{m})}-\overline{\Theta}_{(\mathrm{m})}\Big|_{\mathrm{UV};\mathbf{z}\to\mathbf{y}}\right)\right. \\
&\quad\left.+\overline{\Theta}_{(\mathrm{l})(\mathrm{m})}+\overline{\Theta}_{(\mathrm{l})}\Big|_{\mathrm{UV};\mathbf{z}\to\mathbf{x}}+\overline{\Theta}_{(\mathrm{m})}\Big|_{\mathrm{UV};\mathbf{z}\to\mathbf{y}}\right],
\end{aligned} \tag{168}$$

we can split the result into UV-finite terms and a divergent one as

$$\begin{aligned}
&{}_{q\bar{q}g}\langle\gamma_{\mathrm{L}}^*(q'^+, Q^2, \lambda')|1-\hat{S}_E|\gamma_{\mathrm{L}}^*(q^+, Q^2, \lambda)\rangle_{q\bar{q}g} \\
&= {}_{q\bar{q}g}\langle\gamma_{\mathrm{L}}^*(q'^+, Q^2, \lambda')|1-\hat{S}_E|\gamma_{\mathrm{L}}^*(q^+, Q^2, \lambda)\rangle_{q\bar{q}g}\Big|_{\text{UV-fin}} \\
&\quad+{}_{q\bar{q}g}\langle\gamma_{\mathrm{L}}^*(q'^+, Q^2, \lambda')|1-\hat{S}_E|\gamma_{\mathrm{L}}^*(q^+, Q^2, \lambda)\rangle_{q\bar{q}g}\Big|_{\text{UV-div}}.
\end{aligned} \tag{169}$$

The UV-finite part simplifies to

$$
\begin{aligned}
&{}_{q\bar{q}g}\langle\gamma_{\mathrm{L}}^{*}(q'^{+},Q^{2},\lambda')|1-\hat{S}_{E}|\gamma_{\mathrm{L}}^{*}(q^{+},Q^{2},\lambda)\rangle_{q\bar{q}g}\Big|_{\text{UV-fin}}\\
&=2q^{+}(2\pi)\delta(q'^{+}-q^{+})\frac{8N_{c}\alpha_{em}e_{f}^{2}Q^{2}}{(2\pi)^{3}}\left(\frac{\alpha_{s}C_{\mathrm{F}}}{\pi}\right)\int_{\mathbf{xyz}}\\
&\quad\times\int_{0}^{1}\mathrm{d}z_{1}\int_{0}^{1-z_{1}}\frac{\mathrm{d}z_{2}}{z_{2}}\Bigg\{\\
&\quad+z_{3}^{2}\left(2z_{1}(z_{1}+z_{2})+z_{2}^{2}\right)\frac{1}{\mathbf{r}_{zx}^{2}}\left([K_{0}(\overline{Q}_{(\mathrm{l})}|\mathbf{R}_{(\mathrm{l})}|)]^{2}(1-\mathcal{S}_{xyz})\right.\\
&\quad\left.-[K_{0}(\overline{Q}_{(\mathrm{l})}|\mathbf{r}_{xy}|)]^{2}e^{-\mathbf{r}_{zx}^{2}/(\mathbf{r}_{xy}^{2}e^{\gamma_{E}})}(1-\mathcal{S}_{xy})\right)\\
&\quad+z_{1}^{2}\left(2z_{3}(z_{2}+z_{3})+z_{2}^{2}\right)\frac{1}{\mathbf{r}_{zy}^{2}}\left([K_{0}(\overline{Q}_{(\mathrm{m})}|\mathbf{R}_{(\mathrm{m})}|)]^{2}(1-\mathcal{S}_{xyz})\right.\\
&\quad\left.-[K_{0}(\overline{Q}_{(\mathrm{m})}|\mathbf{r}_{xy}|)]^{2}e^{-\mathbf{r}_{zy}^{2}/(\mathbf{r}_{xy}^{2}e^{\gamma_{E}})}(1-\mathcal{S}_{xy})\right)\\
&\quad-2\left((z_{1}+z_{2})z_{1}z_{3}^{2}+(z_{2}+z_{3})z_{3}z_{1}^{2}\right)\frac{\mathbf{r}_{zx}\cdot\mathbf{r}_{zy}}{(\mathbf{r}_{zx}^{2})(\mathbf{r}_{zy}^{2})}K_{0}(\overline{Q}_{(\mathrm{l})}|\mathbf{R}_{(\mathrm{l})}|)K_{0}(\overline{Q}_{(\mathrm{m})}|\mathbf{R}_{(\mathrm{m})}|)(1-\mathcal{S}_{xyz})\Bigg\}
\end{aligned}
\tag{170}
$$

with $z_3 = 1 - z_1 - z_2$ and

$$
\mathbf{R}_{(\mathrm{l})}^{2}=\mathbf{r}_{yxz}^{2}+\omega_{(\mathrm{l})}\mathbf{r}_{zx}^{2},\qquad\mathbf{R}_{(\mathrm{m})}^{2}=\mathbf{r}_{xyz}^{2}+\omega_{(\mathrm{m})}\mathbf{r}_{zy}^{2}.
\tag{171}
$$

Here the coefficients for the $\overline{Q}$'s and ω's are given by Eqs. (133) and (136). The arguments of the Bessel functions in Eq. (170) can be expressed in a more compact form by noting that

$$
\overline{Q}_{(\mathrm{l})}^{2}\mathbf{R}_{(\mathrm{l})}^{2}=\overline{Q}_{(\mathrm{m})}^{2}\mathbf{R}_{(\mathrm{m})}^{2}=Q^{2}\mathbf{R}^{2},
\tag{172}
$$

where $\mathbf{R}^2 = z_1 z_3 \mathbf{r}_{xy}^2 + z_1 z_2 \mathbf{r}_{zx}^2 + z_2 z_3 \mathbf{r}_{zy}^2$, leading to

$$
\begin{aligned}
&{}_{q\bar{q}g}\langle\gamma_{\mathrm{L}}^{*}(q'^{+},Q^{2},\lambda')|1-\hat{S}_{E}|\gamma_{\mathrm{L}}^{*}(\vec{q},Q^{2},\lambda)\rangle_{q\bar{q}g}\Big|_{\text{UV-fin}}=2q^{+}(2\pi)\delta(q'^{+}-q^{+})\frac{8N_{c}\alpha_{em}e_{f}^{2}Q^{2}}{(2\pi)^{3}}\\
&\quad\times\left(\frac{\alpha_{s}C_{\mathrm{F}}}{\pi}\right)\int_{\mathbf{xyz}}\int_{0}^{1}\mathrm{d}z_{1}\int_{0}^{1-z_{1}}\frac{\mathrm{d}z_{2}}{z_{2}}\Bigg\{+z_{3}^{2}\left(2z_{1}(z_{1}+z_{2})+z_{2}^{2}\right)\\
&\quad\times\frac{1}{\mathbf{r}_{zx}^{2}}\left([K_{0}(Q|\mathbf{R}|)]^{2}(1-\mathcal{S}_{xyz})-[K_{0}(\overline{Q}_{(\mathrm{l})}|\mathbf{r}_{xy}|)]^{2}e^{-\mathbf{r}_{zx}^{2}/(\mathbf{r}_{xy}^{2}e^{\gamma_{E}})}(1-\mathcal{S}_{xy})\right)\\
&\quad+z_{1}^{2}\left(2z_{3}(z_{2}+z_{3})+z_{2}^{2}\right)\frac{1}{\mathbf{r}_{zy}^{2}}\left([K_{0}(Q|\mathbf{R}|)]^{2}(1-\mathcal{S}_{xyz})-[K_{0}(\overline{Q}_{(\mathrm{m})}|\mathbf{r}_{xy}|)]^{2}e^{-\mathbf{r}_{zy}^{2}/(\mathbf{r}_{xy}^{2}e^{\gamma_{E}})}(1-\mathcal{S}_{xy})\right)\\
&\quad-2\left((z_{1}+z_{2})z_{1}z_{3}^{2}+(z_{2}+z_{3})z_{3}z_{1}^{2}\right)\frac{\mathbf{r}_{zx}\cdot\mathbf{r}_{zy}}{(\mathbf{r}_{zx}^{2})(\mathbf{r}_{zy}^{2})}[K_{0}(Q|\mathbf{R}|)]^{2}(1-\mathcal{S}_{xyz})\Bigg\}.
\end{aligned}
\tag{173}
$$

In the UV-divergent term one can now analytically perform the **z**-integral and the z_2-integral, which results in

$$
\begin{aligned}
{}_{q\bar{q}g}\langle\gamma_{\mathrm{L}}^{*}(q'^{+},Q^2,\lambda')|1-\hat{S}_E|\gamma_{\mathrm{L}}^{*}(\vec{q},Q^2,\lambda)\rangle_{q\bar{q}g}\Big|_{\text{UV-div}} &= -2q^{+}(2\pi)\delta(q'^{+}-q^{+})\frac{8N_c\alpha_{em}e_f^2Q^2}{(2\pi)^2} \\
\times\left(\frac{\alpha_s C_{\mathrm{F}}}{\pi}\right)\int_{\mathbf{xy}}\int_0^1 \mathrm{d}z z^2(1-z)^2[K_0(\overline{Q}|\mathbf{r}_{xy}|)]^2&\left[\frac{3}{2}+\log\left(\frac{\alpha}{z}\right)+\log\left(\frac{\alpha}{1-z}\right)\right] \\
\times\left\{\frac{1}{\varepsilon_{\overline{\mathrm{MS}}}}+\log\left(\frac{\mathbf{r}_{xy}^2\mu^2}{4}\right)-2\Psi_0(1)\right\}&(1-\mathcal{S}_{xy}).
\end{aligned}
\tag{174}
$$

This expression precisely cancels the term in square brackets in Eq. (145). After this cancellation we can write the total cross section for longitudinal virtual photon at NLO accuracy as a sum of two finite terms

$$
\sigma^{\gamma_{\mathrm{L}}^{*}}[A]=\sigma^{\gamma_{\mathrm{L}}^{*}}\Big|_{q\bar{q}}+\sigma^{\gamma_{\mathrm{L}}^{*}}\Big|_{q\bar{q}g}, \tag{175}
$$

where the finite contribution to the cross section coming from the $q\bar{q}$-component is

$$
\begin{aligned}
\sigma^{\gamma_{\mathrm{L}}^{*}}\Big|_{q\bar{q}} &= 4N_c\frac{4\alpha_{em}e_f^2Q^2}{(2\pi)^2}\int_{\mathbf{xy}}\int_0^1 \mathrm{d}z z^2(1-z)^2[K_0\left(\overline{Q}|\mathbf{r}_{xy}|\right)]^2 \\
&\times\left\{1+\left(\frac{\alpha_s C_{\mathrm{F}}}{\pi}\right)\left[\frac{1}{2}\log^2\left(\frac{z}{1-z}\right)-\frac{\pi^2}{6}+\frac{5}{2}\right]\right\}\left(1-\mathcal{S}_{xy}\right)
\end{aligned}
\tag{176}
$$

and the subtracted $q\bar{q}g$-component

$$
\begin{aligned}
\sigma^{\gamma_{\mathrm{L}}^{*}}\Big|_{q\bar{q}g} &= 4N_c\frac{4\alpha_{em}e_f^2Q^2}{(2\pi)^3}\left(\frac{\alpha_s C_{\mathrm{F}}}{\pi}\right)\int_{\mathbf{xyz}}\int_0^1 \mathrm{d}z_1\int_0^{1-z_1}\frac{\mathrm{d}z_2}{z_2} \\
&\times\Bigg\{+z_3^2\left(2z_1(z_1+z_2)+z_2^2\right)\frac{1}{\mathbf{r}_{zx}^2}\Big([K_0(Q|\mathbf{R}|)]^2(1-\mathcal{S}_{xyz})-[K_0(\overline{Q}_{(1)}|\mathbf{r}_{xy}|)]^2e^{-\mathbf{r}_{zx}^2/(\mathbf{r}_{xy}^2e^{\gamma_E})} \\
&\times(1-\mathcal{S}_{xy})\Big)+z_1^2\left(2z_3(z_2+z_3)+z_2^2\right)\frac{1}{\mathbf{r}_{zy}^2}\left([K_0(Q|\mathbf{R}|)]^2(1-\mathcal{S}_{xyz})\right. \\
&\left.-[K_0(\overline{Q}_{(\mathrm{m})}|\mathbf{r}_{xy}|)]^2e^{-\mathbf{r}_{zy}^2/(\mathbf{r}_{xy}^2e^{\gamma_E})}(1-\mathcal{S}_{xy})\right)-2\left((z_1+z_2)z_1z_3^2+(z_2+z_3)z_3z_1^2\right) \\
&\times\frac{\mathbf{r}_{zx}\cdot\mathbf{r}_{zy}}{(\mathbf{r}_{zx}^2)(\mathbf{r}_{zy}^2)}[K_0(Q|\mathbf{R}|)]^2(1-\mathcal{S}_{xyz})\Bigg\}.
\end{aligned}
\tag{177}
$$

Now that these expressions are UV finite, all the coordinate integrals can be performed in 2 transverse dimensions.

Here we should emphasize that the scheme dependent UV contribution in Eq. (174) precisely cancels the scheme dependent UV part obtained in Eq. (146), and the remaining finite contribution in Eq. (146) leads to the scheme independent final result for $q\bar{q}$-part in Eq. (176). We have confirmed both analytically and also numerically that our final results for the cross section in Eq. (176) and Eq. (177) agree with those of G. Beuf [30].

In addition, we should note that in the $z_2 \to 0$ limit the part inside the curly brackets in Eq. (177) reduces to

$$2z_1^2 z_3^2 [K_0(Q|\mathbf{r}_{xy}|)]^2 \left[\frac{\mathbf{r}_{xy}^2}{\mathbf{r}_{zx}^2 \mathbf{r}_{zy}^2}(1 - \mathcal{S}_{xyz}) - \frac{1}{\mathbf{r}_{zx}^2} e^{-\mathbf{r}_{zx}^2/(\mathbf{r}_{xy}^2 e^{\gamma_E})}(1 - \mathcal{S}_{xy}) \right. \\ \left. - \frac{1}{\mathbf{r}_{zy}^2} e^{-\mathbf{r}_{zy}^2/(\mathbf{r}_{xy}^2 e^{\gamma_E})}(1 - \mathcal{S}_{xy}) \right]. \tag{178}$$

Noting that $(1 - \mathcal{S}_{xy})$ does not depend on $\mathbf{z}$ and using the integral (this is the same integral that is studied in Appendix E)

$$\int_{\mathbf{z}} \left[\frac{\mathbf{r}_{xy}^2}{\mathbf{r}_{zx}^2 \mathbf{r}_{zy}^2} - \frac{1}{\mathbf{r}_{zx}^2} e^{-\mathbf{r}_{zx}^2/(\mathbf{r}_{xy}^2 e^{\gamma_E})} - \frac{1}{\mathbf{r}_{zy}^2} e^{-\mathbf{r}_{zy}^2/(\mathbf{r}_{xy}^2 e^{\gamma_E})} \right] = 0 \tag{179}$$

the form Eq. (178) can, under the integral over $\mathbf{z}$ in Eq. (177), be replaced by

$$2z_1^2 z_3^2 [K_0(Q|\mathbf{r}_{xy}|)]^2 \frac{\mathbf{r}_{xy}^2}{\mathbf{r}_{zx}^2 \mathbf{r}_{zy}^2} \left[(1 - \mathcal{S}_{xyz}) - (1 - \mathcal{S}_{xy}) \right], \tag{180}$$

which is recognized as the leading order wave function times the r.h.s. of the BK equation (or the first equation in the Balitsky hierarchy). Note that it is precisely to achieve the cancellation Eq. (179) and thus to obtain the conventional BK equation that we chose the constant ξ (see Eq. (165)) to have the value e^{γ_E}. Thus we see that the z_2-integral exhibits a small-x divergence that must be absorbed into a renormalization group evolution of the target, and that this can be done using the BK equation e.g. similarly as is done in [31].

7.2. Transverse photon

Let us then consider the case of transverse virtual photon. Similarly as in the longitudinal photon case, the mixed space expression for the $q\bar{q}$-component of the transverse virtual photon amplitude computed in the FHD scheme at NLO accuracy is given by

$$|\gamma_{\mathrm{T}}^*(q^+, Q^2, \lambda)\rangle_{q\bar{q}} = \sum_{h,\lambda} \sum_{\text{color}} \mathcal{PS}_{(2)}^+ \int \mathrm{d}^2\mathbf{x} \int \mathrm{d}^2\mathbf{y} \left(\widetilde{\psi}_{\mathrm{LO}}^{\gamma_{\mathrm{T}}^* \to q\bar{q}} \Big|_{\mathrm{FDH}} + \widetilde{\psi}_{\mathrm{NLO}}^{\gamma_{\mathrm{T}}^* \to q\bar{q}} \Big|_{\mathrm{FDH}} \right) \\ \times |q(p^+, \mathbf{x}, h, \alpha)\bar{q}(p'^+, \mathbf{y}, -h, \beta)\rangle. \tag{181}$$

Here the factor $\mathcal{PS}_{(2)}^+$ is given in Eq. (141), and the transverse Fourier transformed LO and NLO LCWF's for transverse virtual photon in the mixed space can be written as

$$\widetilde{\psi}_{\mathrm{LO/NLO}}^{\gamma_{\mathrm{T}}^* \to q\bar{q}} \Big|_{\mathrm{FDH}} = \int \frac{\mathrm{d}^2\mathbf{p}}{(2\pi)^2} \left(\psi_{\mathrm{LO/NLO}}^{\gamma_{\mathrm{T}}^* \to q\bar{q}} \Big|_{\mathrm{FDH}} \right) e^{i\mathbf{p}\cdot\mathbf{r}_{xy}}. \tag{182}$$

The momentum space expressions for the LO and NLO wave functions are given in Eqs. (65) and (95), respectively. Using the result given in Eqs. (C4), (C6) and (C7) we obtain for the LO part

$$\widetilde{\psi}_{\mathrm{LO}}^{\gamma_{\mathrm{T}}^* \to q\bar{q}} \Big|_{\mathrm{FDH}} = \frac{4iq^+ e e_f Q \delta_{\alpha\beta}}{(2\pi)} z(1-z) \left[\left(z - \frac{1}{2} \right) \delta^{ij} - ih \frac{1}{2} \epsilon^{ij} \right] \frac{(\mathbf{r}_{xy})^i \boldsymbol{\epsilon}_\lambda^j}{|\mathbf{r}_{xy}|} K_1\left(\overline{Q}|\mathbf{r}_{xy}|\right) \tag{183}$$

and similarly for the NLO part

$$\widetilde{\psi}_{\mathrm{NLO}}^{\gamma_{\mathrm{T}}^* \to q\bar{q}} \Big|_{\mathrm{FDH}} = \frac{4iq^+ e e_f Q \delta_{\alpha\beta}}{(2\pi)} \left(\frac{\alpha_s C_{\mathrm{F}}}{2\pi} \right) \left\{ z(1-z) \left[\left(z - \frac{1}{2} \right) \delta^{ij} - ih \frac{1}{2} \epsilon^{ij} \right] \mathcal{K}^{\gamma_{\mathrm{T}}^*} \Big|_{\mathrm{FDH}} \right\} \\ \times \frac{(\mathbf{r}_{xy})^i \boldsymbol{\epsilon}_\lambda^j}{|\mathbf{r}_{xy}|} K_1\left(\overline{Q}|\mathbf{r}_{xy}|\right), \tag{184}$$

where the NLO kernel in the FDH scheme simplifies to

$$\mathcal{K}^{\gamma_{\mathrm{T}}^*}\Big|_{\mathrm{FDH}} = \left[\frac{3}{2} + \log\left(\frac{\alpha}{z}\right) + \log\left(\frac{\alpha}{1-z}\right)\right]\left\{\frac{1}{\varepsilon_{\overline{\mathrm{MS}}}} + \log\left(\frac{\mathbf{r}_{xy}^2\mu^2}{4}\right) - 2\Psi_0(1)\right\} + \frac{1}{2}\log^2\left(\frac{z}{1-z}\right) - \frac{\pi^2}{6} + \frac{5}{2} + \mathcal{O}(\varepsilon). \tag{185}$$

Note that after the Fourier transform to mixed space (but not before), the NLO correction $\mathcal{K}^{\gamma_{\mathrm{T}}^*}$ for transverse photons is the same one as for the longitudinal ones in Eq. (145). Squaring the LCWF in Eq. (181) (summed over the helicity) together with the eikonal scattering operator $(1-\hat{S}_E)$ we find the final (unsubtracted) result for the $q\bar{q}$ part of the cross section as

$$\begin{aligned}{}_{q\bar{q}}\langle\gamma_{\mathrm{T}}^*(q'^+, Q^2, \lambda')|1-\hat{S}_E|\gamma_{\mathrm{T}}^*(q^+, Q^2, \lambda)\rangle_{q\bar{q}} &= 2q^+(2\pi)\delta(q'^+ - q^+)\frac{4N_c\alpha_{em}e_f^2Q^2}{(2\pi)^2} \\ &\times \int_{\mathbf{xy}}\int_0^1 \mathrm{d}z[K_1\left(\overline{Q}|\mathbf{r}_{xy}|\right)]^2 z(1-z)\Big\{1-2z(1-z)\Big\}\left[1+\left(\frac{\alpha_s C_{\mathrm{F}}}{\pi}\right)\mathcal{K}^{\gamma_{\mathrm{T}}^*}\Big|_{\mathrm{FDH}}\right] \\ &\times \left(1-\mathcal{S}_{xy}\right) + \mathcal{O}(\alpha_{em}\alpha_s^2).\end{aligned} \tag{186}$$

The mixed space expression for the $q\bar{q}g$-component of the transverse virtual photon amplitude computed in the FDH scheme at NLO accuracy is given by

$$\begin{aligned}|\gamma_{\mathrm{T}}^*(q^+, Q^2, \lambda)\rangle_{q\bar{q}g} = \sum_{h,\sigma,\lambda}\sum_{\text{color}}\mathcal{PS}^+_{(3)}\int_{\mathbf{xy}[\mathbf{z}]}\left(\tilde{\psi}^{\gamma_{\mathrm{T}}^*\to q\bar{q}g}\Big|_{\mathrm{FDH}}\right) \\ \times |q(p^+, \mathbf{x}, h, \alpha)\bar{q}(p'^+, \mathbf{y}, -h, \beta)g(k^+, \mathbf{z}, \sigma, a)\rangle,\end{aligned} \tag{187}$$

where $\mathcal{PS}^+_{(3)}$ is given in Eq. (150), and from Eq. (126) the NLO expression of transverse virtual photon LCWF in the mixed space simplifies to

$$\begin{aligned}\widetilde{\psi}^{\gamma_{\mathrm{T}}^*\to q\bar{q}g}\Big|_{\mathrm{FDH}} = -8ee_f g_r t^a_{\alpha\beta}(z_1z_3)^{1/2}\Big\{&\Sigma^{ijkl}_{(\mathrm{h})}\mathcal{I}^{ik}(\mathbf{r}_{yxz}, \mathbf{r}_{zx}, \overline{Q}^2_{(\mathrm{h})}, \omega_{(\mathrm{h})})\boldsymbol{\varepsilon}^{*l}_\sigma \\ &+ \Sigma^{ijkl}_{(\mathrm{i})}\mathcal{I}^{ik}(\mathbf{r}_{xyz}, \mathbf{r}_{zy}, \overline{Q}^2_{(\mathrm{i})}, \omega_{(\mathrm{i})})\boldsymbol{\varepsilon}^{*l}_\sigma \\ &+ \Sigma^{ij}_{(\mathrm{j})}\mathcal{I}(\mathbf{r}_{yxz}, \mathbf{r}_{zx}, \overline{Q}^2_{(\mathrm{j})}, \omega_{(\mathrm{j})})\boldsymbol{\varepsilon}^{*i}_\sigma \\ &- \Sigma^{ij}_{(\mathrm{k})}\mathcal{I}(\mathbf{r}_{xyz}, \mathbf{r}_{zy}, \overline{Q}^2_{(\mathrm{k})}, \omega_{(\mathrm{k})})\boldsymbol{\varepsilon}^{*i}_\sigma\Big\}\boldsymbol{\varepsilon}^j_\lambda.\end{aligned} \tag{188}$$

Similarly as in the case of longitudinal photon, we have introduced the notation

$$\mathcal{I}^{ik}(\mathbf{b}, \mathbf{r}, \overline{Q}^2, \omega) = \mu^{2-\frac{d}{2}}\int\frac{\mathrm{d}^2\mathbf{P}}{(2\pi)^2}\int\frac{\mathrm{d}^{d-2}\mathbf{K}}{(2\pi)^{d-2}}\frac{\mathbf{P}^i\mathbf{K}^k e^{i\mathbf{P}\cdot\mathbf{b}}e^{i\mathbf{K}\cdot\mathbf{r}}}{\left[\mathbf{P}^2+\overline{Q}^2\right]\left[\mathbf{K}^2+\omega\left(\mathbf{P}^2+\overline{Q}^2\right)\right]} \tag{189}$$

and

$$\mathcal{I}(\mathbf{b}, \mathbf{r}, \overline{Q}^2, \omega) = \mu^{2-\frac{d}{2}}\int\frac{\mathrm{d}^2\mathbf{P}}{(2\pi)^2}\int\frac{\mathrm{d}^{d-2}\mathbf{K}}{(2\pi)^{d-2}}\frac{e^{i\mathbf{P}\cdot\mathbf{b}}e^{i\mathbf{K}\cdot\mathbf{r}}}{\left[\mathbf{K}^2+\omega\left(\mathbf{P}^2+\overline{Q}^2\right)\right]}. \tag{190}$$

Squaring the amplitude in Eq. (187) with the eikonal operator $(1-\hat{S}_E)$, and using the result Eq. (D6) we get

$$
\begin{aligned}
{}_{q\bar{q}g}\langle\gamma_{\mathrm{T}}^{*}(q'^{+},Q^2,\lambda')|1-\hat{S}_E|\gamma_{\mathrm{T}}^{*}(q^{+},Q^2,\lambda)\rangle_{q\bar{q}g} &= 2q^{+}(2\pi)\delta(q'^{+}-q^{+})\frac{16(2\pi)^3N_{\mathrm{c}}\alpha_{em}e_f^2}{(2\pi)^2}\left(\frac{\alpha_s C_{\mathrm{F}}}{\pi}\right)\\
&\int_{\mathbf{xy[z]}}\int_0^\infty \mathrm{d}z_1\int_0^\infty \mathrm{d}z_3\int_0^\infty\frac{\mathrm{d}z_2}{z_2}\delta(z_1+z_2+z_3-1)\Theta(z_1,z_2,z_3)\left(1-\mathcal{S}_{xyz}\right).
\end{aligned}
\tag{191}
$$

Here, following the same notation as in Section 7.1, we have defined the function Θ as

$$
\begin{aligned}
\Theta=\sum_{\sigma,\lambda}\Big[&\Sigma^{ijkl}_{(\mathrm{h})}\mathcal{I}^{ik}(\mathbf{r}_{yxz},\mathbf{r}_{zx},\overline{\mathrm{Q}}^2_{(\mathrm{h})},\omega_{(\mathrm{h})})\boldsymbol{\varepsilon}^{*l}_{\sigma}+\Sigma^{ijkl}_{(\mathrm{i})}\mathcal{I}^{ik}(\mathbf{r}_{xyz},\mathbf{r}_{zy},\overline{\mathrm{Q}}^2_{(\mathrm{i})},\omega_{(\mathrm{i})})\boldsymbol{\varepsilon}^{*l}_{\sigma}\\
&+\Sigma^{ij}_{(\mathrm{j})}\mathcal{I}(\mathbf{r}_{yxz},\mathbf{r}_{zx},\overline{\mathrm{Q}}^2_{(\mathrm{j})},\omega_{(\mathrm{j})})\boldsymbol{\varepsilon}^{*i}_{\sigma}-\Sigma^{ij}_{(\mathrm{k})}\mathcal{I}(\mathbf{r}_{xyz},\mathbf{r}_{zy},\overline{\mathrm{Q}}^2_{(\mathrm{k})},\omega_{(\mathrm{k})})\boldsymbol{\varepsilon}^{*i}_{\sigma}\Big]\\
&\times\Big[\Sigma^{mnrs}_{(\mathrm{h})}\mathcal{I}^{mr}(\mathbf{r}_{yxz},\mathbf{r}_{zx},\overline{\mathrm{Q}}^2_{(\mathrm{h})},\omega_{(\mathrm{h})})\boldsymbol{\varepsilon}^{*s}_{\sigma}+\Sigma^{mnrs}_{(\mathrm{i})}\mathcal{I}^{mr}(\mathbf{r}_{xyz},\mathbf{r}_{zy},\overline{\mathrm{Q}}^2_{(\mathrm{i})},\omega_{(\mathrm{i})})\boldsymbol{\varepsilon}^{*s}_{\sigma}\\
&+\Sigma^{mn}_{(\mathrm{j})}\mathcal{I}(\mathbf{r}_{yxz},\mathbf{r}_{zx},\overline{\mathrm{Q}}^2_{(\mathrm{j})},\omega_{(\mathrm{j})})\boldsymbol{\varepsilon}^{*m}_{\sigma}-\Sigma^{mn}_{(\mathrm{k})}\mathcal{I}(\mathbf{r}_{xyz},\mathbf{r}_{zy},\overline{\mathrm{Q}}^2_{(\mathrm{k})},\omega_{(\mathrm{k})})\boldsymbol{\varepsilon}^{*m}_{\sigma}\Big]^{*}\boldsymbol{\varepsilon}^{j}_{\lambda}\boldsymbol{\varepsilon}^{*n}_{\lambda}
\end{aligned}
\tag{192}
$$

which corresponds to the full $q\bar{q}g$-sector wave function (see Eq. (188)) squared and summed over the gluon and photon polarization vectors. The expression in (192) can be simplified further by introducing the notation

$$
\overline{\Theta}=\overline{\Theta}_{(\mathrm{h})}+\overline{\Theta}_{(\mathrm{i})}+\overline{\Theta}_{(\mathrm{j})}+\overline{\Theta}_{(\mathrm{k})}+\overline{\Theta}_{(\mathrm{h})(\mathrm{i})(\mathrm{j})(\mathrm{k})}
\tag{193}
$$

with

$$
\begin{aligned}
{}_{q\bar{q}g}\langle\gamma_{\mathrm{T}}^{*}(q'^{+},Q^2,\lambda')|1-\hat{S}_E|\gamma_{\mathrm{T}}^{*}(q^{+},Q^2,\lambda)\rangle_{q\bar{q}g} &= 2q^{+}(2\pi)\delta(q'^{+}-q^{+})\frac{16(2\pi)^3N_{\mathrm{c}}\alpha_{em}e_f^2}{(2\pi)^2}\left(\frac{\alpha_s C_{\mathrm{F}}}{\pi}\right)\\
&\int_{\mathbf{xy}}\int_0^\infty \mathrm{d}z_1\int_0^\infty \mathrm{d}z_3\int_0^\infty\frac{\mathrm{d}z_2}{z_2}\delta(z_1+z_2+z_3-1)\overline{\Theta}(z_1,z_2,z_3),
\end{aligned}
\tag{194}
$$

where the individual terms coming from the wave function squared are given by

$$
\overline{\Theta}_{(\mathrm{h})}=\int_{[\mathbf{z}]}\left\{\Sigma^{ijkl}_{(\mathrm{h})}\mathcal{I}^{ik}(\mathbf{r}_{yxz},\mathbf{r}_{zx},\overline{\mathrm{Q}}^2_{(\mathrm{h})},\omega_{(\mathrm{h})})\Big(\Sigma^{mjrl}_{(\mathrm{h})}\mathcal{I}^{mr}(\mathbf{r}_{yxz},\mathbf{r}_{zx},\overline{\mathrm{Q}}^2_{(\mathrm{h})},\omega_{(\mathrm{h})})\Big)^{*}\right\}\left(1-\mathcal{S}_{xyz}\right)
\tag{195}
$$

$$
\overline{\Theta}_{(\mathrm{i})}=\int_{[\mathbf{z}]}\left\{\Sigma^{ijkl}_{(\mathrm{i})}\mathcal{I}^{ik}(\mathbf{r}_{xyz},\mathbf{r}_{zy},\overline{\mathrm{Q}}^2_{(\mathrm{i})},\omega_{(\mathrm{i})})\Big(\Sigma^{mjrl}_{(\mathrm{i})}\mathcal{I}^{mr}(\mathbf{r}_{xyz},\mathbf{r}_{zy},\overline{\mathrm{Q}}^2_{(\mathrm{i})},\omega_{(\mathrm{i})})\Big)^{*}\right\}\left(1-\mathcal{S}_{xyz}\right)
\tag{196}
$$

$$
\overline{\Theta}_{(\mathrm{j})}=\int_{[\mathbf{z}]}\left\{\Sigma^{ij}_{(\mathrm{j})}\mathcal{I}(\mathbf{r}_{yxz},\mathbf{r}_{zx},\overline{\mathrm{Q}}^2_{(\mathrm{j})},\omega_{(\mathrm{j})})\Big(\Sigma^{ij}_{(\mathrm{j})}\mathcal{I}(\mathbf{r}_{yxz},\mathbf{r}_{zx},\overline{\mathrm{Q}}^2_{(\mathrm{j})},\omega_{(\mathrm{j})})\Big)^{*}\right\}\left(1-\mathcal{S}_{xyz}\right)
\tag{197}
$$

$$
\overline{\Theta}_{(\mathrm{k})}=\int_{[\mathbf{z}]}\left\{\Sigma^{ij}_{(\mathrm{k})}\mathcal{I}(\mathbf{r}_{xyz},\mathbf{r}_{zy},\overline{\mathrm{Q}}^2_{(\mathrm{k})},\omega_{(\mathrm{k})})\Big(\Sigma^{ij}_{(\mathrm{k})}\mathcal{I}(\mathbf{r}_{xyz},\mathbf{r}_{zy},\overline{\mathrm{Q}}^2_{(\mathrm{k})},\omega_{(\mathrm{k})})\Big)^{*}\right\}\left(1-\mathcal{S}_{xyz}\right)
\tag{198}
$$

and the possible cross terms:

$$\begin{aligned}\overline{\Theta}_{(\mathrm{h})(\mathrm{i})(\mathrm{j})(\mathrm{k})} =& 2\int_{[\mathbf{z}]} \Re e\Big[\Sigma^{ijkl}_{(\mathrm{h})}\mathcal{I}^{ik}(\mathbf{r}_{yxz},\mathbf{r}_{zx},\overline{\mathrm{Q}}^2_{(\mathrm{h})},\omega_{(\mathrm{h})})\Big(\Sigma^{mjrl}_{(\mathrm{i})}\mathcal{I}^{mr}(\mathbf{r}_{xyz},\mathbf{r}_{zy},\overline{\mathrm{Q}}^2_{(\mathrm{i})},\omega_{(\mathrm{i})})\Big)^* \\ &+\Big(\Sigma^{ijkl}_{(\mathrm{h})}\mathcal{I}^{ik}(\mathbf{r}_{yxz},\mathbf{r}_{zx},\overline{\mathrm{Q}}^2_{(\mathrm{h})},\omega_{(\mathrm{h})})+\Sigma^{ijkl}_{(\mathrm{i})}\mathcal{I}^{ik}(\mathbf{r}_{xyz},\mathbf{r}_{zy},\overline{\mathrm{Q}}^2_{(\mathrm{i})},\omega_{(\mathrm{i})})\Big) \\ &\times\Big(\Sigma^{lj}_{(\mathrm{j})}\mathcal{I}(\mathbf{r}_{yxz},\mathbf{r}_{zx},\overline{\mathrm{Q}}^2_{(\mathrm{j})},\omega_{(\mathrm{j})})-\Sigma^{lj}_{(\mathrm{k})}\mathcal{I}(\mathbf{r}_{xyz},\mathbf{r}_{zy},\overline{\mathrm{Q}}^2_{(\mathrm{k})},\omega_{(\mathrm{k})})\Big)^* \\ &-\Sigma^{ij}_{(\mathrm{j})}\mathcal{I}(\mathbf{r}_{yxz},\mathbf{r}_{zx},\overline{\mathrm{Q}}^2_{(\mathrm{j})},\omega_{(\mathrm{j})})\Big(\Sigma^{ij}_{(\mathrm{k})}\mathcal{I}(\mathbf{r}_{xyz},\mathbf{r}_{zy},\overline{\mathrm{Q}}^2_{(\mathrm{k})},\omega_{(\mathrm{k})})\Big)^*\Big]\big(1-\mathcal{S}_{xyz}\big)\,.\end{aligned} \tag{199}$$

The contributions in Eqs. (195), (196), (197) and (198) correspond to the squared amplitudes from diagrams (h), (i), (j) and (k) respectively, and the contribution in Eq. (199) contains the cross terms of these diagrams.

In order to simplify the individual contributions above we note that

$$\overline{\mathrm{Q}}^2_{(\mathrm{h})}=\overline{\mathrm{Q}}^2_{(\mathrm{j})}=\overline{\mathrm{Q}}^2_{(\mathrm{l})},\quad \overline{\mathrm{Q}}^2_{(\mathrm{i})}=\overline{\mathrm{Q}}^2_{(\mathrm{k})}=\overline{\mathrm{Q}}^2_{(\mathrm{m})}, \tag{200}$$

and

$$\omega_{(\mathrm{h})}=\omega_{(\mathrm{j})}=\omega_{(\mathrm{l})},\quad \omega_{(\mathrm{i})}=\omega_{(\mathrm{k})}=\omega_{(\mathrm{m})}. \tag{201}$$

This implies that

$$\overline{\mathrm{Q}}^2_{(\mathrm{h})}\mathbf{R}^2_{(\mathrm{h})}=\overline{\mathrm{Q}}^2_{(\mathrm{i})}\mathbf{R}^2_{(\mathrm{i})}=Q^2\mathbf{R}^2,\quad \overline{\mathrm{Q}}^2_{(\mathrm{j})}\mathbf{R}^2_{(\mathrm{j})}=\overline{\mathrm{Q}}^2_{(\mathrm{k})}\mathbf{R}^2_{(\mathrm{k})}=Q^2\mathbf{R}^2, \tag{202}$$

where $\mathbf{R}^2$ is defined in Eq. (172). Using the definitions in Eq. (126) and result derived in Eq. (C17) we obtain

$$\Theta_{(\mathrm{h})}=\frac{F(z_1,z_2,z_3)(\mu^2)^{2-d/2}}{16^2\pi^d}\int_{[\mathbf{z}]}(\mathbf{r}_{yxz}\cdot\mathbf{r}_{yxz})(\mathbf{r}^2_{zx})^{3-d}\mathcal{L}^2(\mathbf{r}^2_{yxz},\mathbf{r}^2_{zx},\overline{\mathrm{Q}}^2_{(\mathrm{h})},\omega_{(\mathrm{h})})\big(1-\mathcal{S}_{xyz}\big) \tag{203}$$

and

$$\Theta_{(\mathrm{i})}=\frac{G(z_1,z_2,z_3)(\mu^2)^{2-d/2}}{16^2\pi^d}\int_{[\mathbf{z}]}(\mathbf{r}_{xyz}\cdot\mathbf{r}_{xyz})(\mathbf{r}^2_{zy})^{3-d}\mathcal{L}^2(\mathbf{r}^2_{xyz},\mathbf{r}^2_{zy},\overline{\mathrm{Q}}^2_{(\mathrm{i})},\omega_{(\mathrm{i})})\big(1-\mathcal{S}_{xyz}\big)\,, \tag{204}$$

where

$$\begin{aligned}(\mathbf{r}_{yxz}\cdot\mathbf{r}_{yxz})&=\frac{\mathbf{R}^2}{z_3(z_1+z_2)}-\frac{z_1z_2}{z_3(z_1+z_2)^2}\mathbf{r}^2_{zx}\\ (\mathbf{r}_{xyz}\cdot\mathbf{r}_{xyz})&=\frac{\mathbf{R}^2}{z_1(z_2+z_3)}-\frac{z_3z_2}{z_1(z_2+z_3)^2}\mathbf{r}^2_{zy}.\end{aligned} \tag{205}$$

The two functions F and G above are given by

$$\begin{aligned}F(z_2,z_3)&=\left[\left(z_1+z_2-\frac{1}{2}\right)^2+\frac{1}{4}\right]\left[\left(1-\frac{1}{2}\left(\frac{z_2}{z_1+z_2}\right)\right)^2+\frac{1}{4}\left(\frac{z_2}{z_1+z_2}\right)^2\right]\\ &=\frac{1}{4(z_1+z_2)^2}\Big[1-2z_3(1-z_3)\Big]\Big[2z_1(z_1+z_2)+z_2^2\Big]\end{aligned} \tag{206}$$

and

$$G(z_2,z_1)=\left[\left(z_1-\frac{1}{2}\right)^2+\frac{1}{4}\right]\left[\left(1-\frac{1}{2}\left(\frac{z_2}{z_2+z_3}\right)\right)^2+\frac{1}{4}\left(\frac{z_2}{z_2+z_3}\right)^2\right] \\ =\frac{1}{4(z_2+z_3)^2}\Big[1-2z_1(1-z_1)\Big]\Big[2z_3(z_2+z_3)+z_2^2\Big], \tag{207}$$

and, similarly as in the longitudinal case, we have defined the function

$$\mathcal{L}(\mathbf{b}^2,\mathbf{r}^2,\overline{Q}^2,\omega)=\int_0^\infty\frac{\mathrm{d}u}{u^2}e^{-u\overline{Q}^2}e^{-\frac{\mathbf{b}^2}{4u}}\Gamma\left(\frac{d}{2}-1,\frac{\omega\mathbf{r}^2}{4u}\right). \tag{208}$$

Now the UV divergences in the $\Theta_{(\mathrm{h})}$ and $\Theta_{(\mathrm{i})}$ terms can be subtracted in the same way as in the longitudinal photon case. Introducing the subtraction terms

$$\overline{\Theta}_{(\mathrm{h})}\Big|_{\mathrm{UV};\mathbf{z}\to\mathbf{x}}=\frac{F(z_1,z_2,z_3)(\mu^2)^{2-d/2}}{16^2\pi^d}\int_{[\mathbf{z}]}\Big[\mathbf{r}_{xy}^2(\mathbf{r}_{zx}^2)^{3-d}\Big]\mathcal{L}^2(\mathbf{r}_{xy}^2,\mathbf{r}_{zx}^2,\overline{Q}_{(\mathrm{h})}^2,\omega_{(\mathrm{h})})\Big|_{\mathrm{UV}}\left(1-\mathcal{S}_{xy}\right) \tag{209}$$

and

$$\overline{\Theta}_{(\mathrm{i})}\Big|_{\mathrm{UV};\mathbf{z}\to\mathbf{y}}=\frac{G(z_1,z_2,z_3)(\mu^2)^{2-d/2}}{16^2\pi^d}\int_{[\mathbf{z}]}\Big[\mathbf{r}_{xy}^2(\mathbf{r}_{zy}^2)^{3-d}\Big]\mathcal{L}^2(\mathbf{r}_{xy}^2,\mathbf{r}_{zy}^2,\overline{Q}_{(\mathrm{i})}^2,\omega_{(\mathrm{i})})\Big|_{\mathrm{UV}}\left(1-\mathcal{S}_{xy}\right), \tag{210}$$

where

$$\mathcal{L}(\mathbf{b}^2,\mathbf{r}^2,\overline{Q}^2,\omega)\Big|_{\mathrm{UV}}=\int_0^\infty\frac{\mathrm{d}u}{u^2}e^{-u\overline{Q}^2}e^{-\frac{\mathbf{b}^2}{4u}}\Gamma\left(\frac{d}{2}-1\right)e^{-\frac{\mathbf{r}^2}{2\mathbf{b}^2\xi}} \\ =\frac{4\overline{Q}}{|\mathbf{b}|}K_1\left(\overline{Q}|\mathbf{b}|\right)\Gamma\left(\frac{d}{2}-1\right)e^{-\frac{\mathbf{r}^2}{2\mathbf{b}^2\xi}},\quad \xi\in\Re \tag{211}$$

we can write down the UV subtracted contributions for (203) and (204)

$$\overline{\Theta}_{(\mathrm{h})}-\overline{\Theta}_{(\mathrm{h})}\Big|_{\mathrm{UV};\mathbf{z}\to\mathbf{x}}=\frac{Q^2}{4(2\pi)^4}f(z_1,z_2,z_3)\int_{\mathbf{z}}\Bigg[\left(\frac{1}{\mathbf{r}_{zx}^2}-\frac{z_1z_2}{(z_1+z_2)}\frac{1}{\mathbf{R}^2}\right)[K_1(Q|\mathbf{R}|)]^2\left(1-\mathcal{S}_{xyz}\right) \\ -\frac{1}{\mathbf{r}_{zx}^2}[K_1(\overline{Q}_{(\mathrm{h})}|\mathbf{r}_{xy}|)]^2e^{-\mathbf{r}_{zx}^2/(\mathbf{r}_{xy}^2\xi)}\left(1-\mathcal{S}_{xy}\right)\Bigg] \tag{212}$$

and

$$\overline{\Theta}_{(\mathrm{i})}-\overline{\Theta}_{(\mathrm{i})}\Big|_{\mathrm{UV};\mathbf{z}\to\mathbf{y}}=\frac{Q^2}{4(2\pi)^4}g(z_1,z_2,z_3)\int_{\mathbf{z}}\Bigg[\left(\frac{1}{\mathbf{r}_{zy}^2}-\frac{z_3z_2}{(z_2+z_3)}\frac{1}{\mathbf{R}^2}\right)[K_1(Q|\mathbf{R}|)]^2\left(1-\mathcal{S}_{xyz}\right) \\ -\frac{1}{\mathbf{r}_{zy}^2}[K_1(\overline{Q}_{(\mathrm{i})}|\mathbf{r}_{xy}|)]^2e^{-\mathbf{r}_{zy}^2/(\mathbf{r}_{xy}^2\xi)}\left(1-\mathcal{S}_{xy}\right)\Bigg] \tag{213}$$

with

$$f(z_1,z_2)=\frac{z_3}{(z_1+z_2)}\Big[1-2z_3(1-z_3)\Big]\Big[2z_1(z_1+z_2)+z_2^2\Big] \\ g(z_1,z_2)=\frac{z_1}{(z_2+z_3)}\Big[1-2z_1(1-z_1)\Big]\Big[2z_3(z_2+z_3)+z_2^2\Big]. \tag{214}$$

The contributions in Eqs. (197), (198) and (199) are all UV-finite and hence one can perform the computation in four dimension. The calculation of these terms is lengthy but straightforward. Thus in

here we only show the final result and include the detailed derivation in Appendix F:

$$\begin{aligned}\overline{\Theta}\Big|_{\text{UV-finite}} = \frac{Q^2}{4(2\pi)^4}\int_{\mathbf{z}}\frac{[K_1(Q|\mathbf{R}|)]^2}{\mathbf{R}^2}\Bigg[-2z_1z_3\Bigg\{\Big[(1-z_1)^2+z_1^2\Big]+\Big[(1-z_3)^2+z_3^2\Big]\Bigg\}\\ \times\frac{\mathbf{R}^2(\mathbf{r}_{zx}\cdot\mathbf{r}_{zy})}{\mathbf{r}_{zx}^2\mathbf{r}_{zy}^2}+\frac{2z_1(z_2z_3)^2}{(z_1+z_2)}\frac{(\mathbf{r}_{zx}\cdot\mathbf{r}_{zy})}{\mathbf{r}_{zx}^2}+\frac{2z_3(z_2z_1)^2}{(z_2+z_3)}\frac{(\mathbf{r}_{zx}\cdot\mathbf{r}_{zy})}{\mathbf{r}_{zy}^2}\\ +z_1z_2z_3\Bigg\{(z_1+z_2)^2+(z_2+z_3)^2+2z_1^2+2z_3^2+\frac{(z_1z_3)^2}{(z_1+z_2)^2}\\ +\frac{(z_1z_3)^2}{(z_2+z_3)^2}-z_2\Bigg[\frac{(z_1+z_2)}{(z_2+z_3)}+\frac{(z_2+z_3)}{(z_1+z_2)}\Bigg]\Bigg\}\Bigg]\big(1-\mathcal{S}_{xyz}\big)\,.\end{aligned} \tag{215}$$

Adding all the pieces together gives the result

$$\begin{aligned}{}_{q\bar{q}g}\langle\gamma_{\mathrm{T}}^*(q'^+,Q^2,\lambda')|1-\hat{S}_E|\gamma_{\mathrm{T}}^*(q^+,Q^2,\lambda)\rangle_{q\bar{q}g} = 2q^+(2\pi)\delta(q'^+-q^+)\frac{16(2\pi)^3N_c\alpha_{em}e_f^2}{(2\pi)^2}\\ \times\left(\frac{\alpha_sC_{\mathrm{F}}}{\pi}\right)\int_{\mathbf{xy}}\int_0^\infty \mathrm{d}z_1\int_0^\infty \mathrm{d}z_3\int_0^\infty\frac{\mathrm{d}z_2}{z_2}\delta(z_1+z_2+z_3-1)\\ \times\Bigg\{\Bigg[\overline{\Theta}_{(\mathrm{h})}-\overline{\Theta}_{(\mathrm{h})}\Big|_{\mathrm{UV};\mathbf{z}\to\mathbf{x}}\Bigg]+\Bigg[\overline{\Theta}_{(\mathrm{i})}-\overline{\Theta}_{(\mathrm{i})}\Big|_{\mathrm{UV};\mathbf{z}\to\mathbf{y}}\Bigg]\\ +\overline{\Theta}\Big|_{\text{UV-finite}}+\overline{\Theta}_{(\mathrm{h})}\Big|_{\mathrm{UV};\mathbf{z}\to\mathbf{x}}+\overline{\Theta}_{(\mathrm{i})}\Big|_{\mathrm{UV};\mathbf{z}\to\mathbf{y}}\Bigg\}.\end{aligned} \tag{216}$$

Dividing this expression into finite and UV-divergent parts as

$$\begin{aligned}&{}_{q\bar{q}g}\langle\gamma_{\mathrm{T}}^*(q'^+,Q^2,\lambda')|1-\hat{S}_E|\gamma_{\mathrm{T}}^*(q^+,Q^2,\lambda)\rangle_{q\bar{q}g}\\ &={}_{q\bar{q}g}\langle\gamma_{\mathrm{T}}^*(q'^+,Q^2,\lambda')|1-\hat{S}_E|\gamma_{\mathrm{T}}^*(q^+,Q^2,\lambda)\rangle_{q\bar{q}g}\Big|_{\text{UV-fin}}\\ &\quad+{}_{q\bar{q}g}\langle\gamma_{\mathrm{T}}^*(q'^+,Q^2,\lambda')|1-\hat{S}_E|\gamma_{\mathrm{T}}^*(q^+,Q^2,\lambda)\rangle_{q\bar{q}g}\Big|_{\text{UV-div}}\end{aligned} \tag{217}$$

and carrying out some algebra we obtain

$$\begin{aligned}{}_{q\bar{q}g}\langle\gamma_{\mathrm{T}}^*(q'^+,Q^2,\lambda')|1-\hat{S}_E|\gamma_{\mathrm{T}}^*(q^+,Q^2,\lambda)\rangle_{q\bar{q}g}\Big|_{\text{UV-fin}} = 2q^+(2\pi)\delta(q'^+-q^+)\frac{4N_c\alpha_{em}Q^2e_f^2}{(2\pi)^3}\left(\frac{\alpha_sC_{\mathrm{F}}}{\pi}\right)\\ \times\int_{\mathbf{xyz}}\int_0^1\mathrm{d}z_1\int_0^{1-z_1}\frac{\mathrm{d}z_2}{z_2}\Bigg\{\frac{f}{\mathbf{r}_{zx}^2}\Big[[K_1(Q|\mathbf{R}|)]^2\big(1-\mathcal{S}_{xyz}\big)-[K_1(\overline{Q}_{(\mathrm{h})}|\mathbf{r}_{xy}|)]^2e^{-\mathbf{r}_{zx}^2/(\mathbf{r}_{xy}^2\xi)}\big(1-\mathcal{S}_{xy}\big)\Big]\\ +\frac{g}{\mathbf{r}_{zy}^2}\Big[[K_1(Q|\mathbf{R}|)]^2\big(1-\mathcal{S}_{xyz}\big)-[K_1(\overline{Q}_{(\mathrm{i})}|\mathbf{r}_{xy}|)]^2e^{-\mathbf{r}_{zy}^2/(\mathbf{r}_{xy}^2\xi)}\big(1-\mathcal{S}_{xy}\big)\Big]+\frac{[K_1(Q|\mathbf{R}|)]^2}{\mathbf{R}^2}\Pi\big(1-\mathcal{S}_{xyz}\big)\Bigg\},\end{aligned} \tag{218}$$

where

$$\begin{aligned}\Pi =& -2z_1z_3\Bigg\{\Big[(1-z_1)^2+z_1^2\Big]+\Big[(1-z_3)^2+z_3^2\Big]\Bigg\}\frac{\mathbf{R}^2(\mathbf{r}_{zx}\cdot\mathbf{r}_{zy})}{\mathbf{r}_{zx}^2\mathbf{r}_{zy}^2}+\frac{2z_1(z_2z_3)^2}{(z_1+z_2)}\frac{(\mathbf{r}_{zx}\cdot\mathbf{r}_{zy})}{\mathbf{r}_{zx}^2}\\&+\frac{2z_3(z_2z_1)^2}{(z_2+z_3)}\frac{(\mathbf{r}_{zx}\cdot\mathbf{r}_{zy})}{\mathbf{r}_{zy}^2}+z_1z_2z_3\Bigg\{(z_1+z_2)^2+(z_2+z_3)^2+2z_1^2+2z_3^2+\frac{(z_1z_3)^2}{(z_1+z_2)^2}\\&+\frac{(z_1z_3)^2}{(z_2+z_3)^2}-z_2\Bigg[\frac{(z_1+z_2)}{(z_2+z_3)}+\frac{(z_2+z_3)}{(z_1+z_2)}\Bigg]-\frac{\Big[1-2z_3(1-z_3)\Big]\Big[2z_1(z_1+z_2)+z_2^2\Big]}{(z_1+z_2)^2}\\&-\frac{\Big[1-2z_1(1-z_1)\Big]\Big[2z_3(z_2+z_3)+z_2^2\Big]}{(z_2+z_3)^2}\Bigg\}\end{aligned}\tag{219}$$

and

$$\begin{aligned}{}_{q\bar{q}g}\langle\gamma_{\mathrm{T}}^*(q'^+,Q^2,\lambda')|1-\hat{S}_E|\gamma_{\mathrm{T}}^*(q^+,Q^2,\lambda)\rangle_{q\bar{q}g}\Big|_{\text{UV-div}}&=-2q^+(2\pi)\delta(q'^+-q^+)\frac{4N_c\alpha_{em}e_f^2Q^2}{(2\pi)^2}\\\times\left(\frac{\alpha_sC_{\mathrm{F}}}{\pi}\right)\int_{\mathbf{xy}}\int_0^1\mathrm{d}z[K_1(\overline{Q}|\mathbf{r}_{xy}|)]^2z(1-z)&\Bigg\{1-2z(1-z)\Bigg\}\Bigg[\frac{3}{2}+\log\left(\frac{\alpha}{z}\right)\\+\log\left(\frac{\alpha}{1-z}\right)\Bigg]\Bigg\{\frac{1}{\varepsilon_{\overline{\mathrm{MS}}}}+\log\left(\frac{\mathbf{r}_{xy}^2\mu^2}{4}\right)-2\Psi_0(1)\Bigg\}&\left(1-\mathcal{S}_{xy}\right).\end{aligned}\tag{220}$$

Like in the longitudinal photon case, the last expression above cancels the UV-divergent term in square brackets in Eq. (186). Finally thanks to Eq. (60), the total cross section for transverse virtual photon (averaged over the two incoming transverse virtual photon polarization states) at NLO accuracy is given by

$$\sigma^{\gamma_{\mathrm{T}}^*}[A]=\sigma^{\gamma_{\mathrm{T}}^*}\Big|_{q\bar{q}}+\sigma^{\gamma_{\mathrm{T}}^*}\Big|_{q\bar{q}g},\tag{221}$$

where the $q\bar{q}$-term is

$$\begin{aligned}\sigma^{\gamma_{\mathrm{T}}^*}\Big|_{q\bar{q}}=4N_c\frac{\alpha_{em}e_f^2Q^2}{(2\pi)^2}\int_{\mathbf{xy}}\int_0^1\mathrm{d}z[K_1\left(\overline{Q}|\mathbf{r}_{xy}|\right)]^2z(1-z)&\Bigg\{1-2z(1-z)\Bigg\}\\\times\Bigg\{1+\left(\frac{\alpha_sC_{\mathrm{F}}}{\pi}\right)\Bigg[\frac{1}{2}\log^2\left(\frac{z}{1-z}\right)-\frac{\pi^2}{6}+\frac{5}{2}\Bigg]\Bigg\}&\left(1-\mathcal{S}_{xy}\right)\end{aligned}\tag{222}$$

and for the $q\bar{q}g$-component we find

$$\sigma^{\gamma^*_{\mathrm{T}}}\Big|_{q\bar{q}g} = 4N_{\mathrm{c}}\frac{\alpha_{em}e_f^2Q^2}{(2\pi)^3}\left(\frac{\alpha_s C_{\mathrm{F}}}{\pi}\right)\int_{\mathbf{xyz}}\int_0^1 \mathrm{d}z_1\int_0^{1-z_1}\frac{\mathrm{d}z_2}{z_2}$$

$$\times\left\{\frac{f}{\mathbf{r}_{zx}^2}\left[[K_1(Q|\mathbf{R}|)]^2\left(1-\mathcal{S}_{xyz}\right)-[K_1(\overline{Q}_{(\mathrm{h})}|\mathbf{r}_{xy}|)]^2 e^{-\mathbf{r}_{zx}^2/(\mathbf{r}_{xy}^2\xi)}\left(1-\mathcal{S}_{xy}\right)\right]\right. \tag{223}$$

$$+\frac{g}{\mathbf{r}_{zy}^2}\left[[K_1(Q|\mathbf{R}|)]^2\left(1-\mathcal{S}_{xyz}\right)-[K_1(\overline{Q}_{(\mathrm{i})}|\mathbf{r}_{xy}|)]^2 e^{-\mathbf{r}_{zy}^2/(\mathbf{r}_{xy}^2\xi)}\left(1-\mathcal{S}_{xy}\right)\right]$$

$$\left.+\frac{[K_1(Q|\mathbf{R}|)]^2}{\mathbf{R}^2}\Pi\left(1-\mathcal{S}_{xyz}\right)\right\}.$$

Again, as for the longitudinal case the scheme dependent UV contribution in Eq. (220) cancels the scheme dependent UV part obtained in Eq. (186), and the remaining finite contribution in Eq. (186) leads to the scheme independent final result for $q\bar{q}$-part in Eq. (222). In addition, like in the longitudinal case, we have confirmed both analytically and also numerically that our final results for the cross section in Eq. (222) and Eq. (223) agree with [30], and we have checked that the part inside the curly brackets in Eq. (223) reduces to the r.h.s. of the BK equation.

8. Conclusions and outlook

As a concrete result, we have in this paper derived the NLO cross section for deep inelastic scattering in the dipole picture, with the final results given in Eq. (175) (with Eqs. (176) and (177)) for the longitudinal and in Eq. (221) (with Eqs. (222) and (223)) for the transverse virtual photon polarization. We have confirmed both analytically and numerically that our results agree with those of G. Beuf in [30]. Being derived in a different regularization scheme, they are an indication of the scheme-independence of this result. As a small difference, we believe that our choice of the subtraction term to cancel the UV divergence is, while equivalent, somewhat more benign numerically.

Nevertheless, the most important purpose of this paper has been to develop calculational techniques that should enable further NLO calculations to be more efficiently performed in LCPT. We have demonstrated how to express the elementary vertices of the theory systematically in terms of their natural variables, the center-of-mass splitting momentum, splitting momentum fraction and the helicities of the particles involved. Using our expressions the evaluation of the scheme-independent parts of the cross section reduces to multiplications of 2-dimensional vectors and tensors, and simple scalar integrations over longitudinal momentum fractions. They can be easily automated by symbolic manipulation programs such as FORM [42] or FeynCalc [43]. The scheme dependent parts require some more work, where at one point one must reduce expressions of Dirac matrices contracted with (d_s-2)- and $(d-2)$-dimensional Kronecker deltas. However, this procedure also is readily automated. We hope that the method developed here can be useful in future work. As an immediate future application with clear phenomenological relevance, the next step is to include quark masses in the DIS cross section calculation.

Acknowledgments

We thank G. Beuf for numerous discussions and providing his results in [30] to us already prior to publication. This work has been supported by the Academy of Finland, projects 273464 and 303756, and by the European Research Council, grants ERC-2015-CoG-681707 and ERC-2016-CoG-725369.

Appendix A. Decomposition of LC vertices

In this section we show how to decompose the general LC vertex to the symmetric and antisymmetric parts as discussed in Section 2.2. The most general form for the LC vertex (without the coupling and color structure) in the LC gauge is given by

$$\bar{\chi}_h(p')\not{\epsilon}_\lambda(q)\omega_s(p) = \frac{\mathbf{q}^i \boldsymbol{\epsilon}^j_\lambda}{q^+}\delta^{ij}\bar{\chi}_h(p')\gamma^+\omega_s(p) - \boldsymbol{\epsilon}^i_\lambda \bar{\chi}_h(p')\gamma^i\omega_s(p), \tag{A1}$$

where χ and ω can be either positive or negative energy massless spinors, i.e. u or v. For massless quarks the spinors χ and ω satisfy the Dirac equations:

$$\begin{aligned} \not{p}\omega_s(p) &= \left(\gamma^+ p^- + \gamma^- p^+ - \gamma^j \mathbf{p}^j\right)\omega_s(p) = 0, \\ \bar{\chi}_h(p')\not{p}' &= \bar{\chi}_h(p')\left(\gamma^+ p'^- + \gamma^- p'^+ - \gamma^j \mathbf{p}'^j\right) = 0. \end{aligned} \tag{A2}$$

Applying the Clifford algebra one can write

$$\bar{\chi}_h(p')\gamma^+\gamma^i\gamma^-\omega_s(p) = -\bar{\chi}_h(p')\gamma^+\gamma^-\gamma^i\omega_s(p) = -2\bar{\chi}_h(p')\gamma^i\omega_s(p) + \bar{\chi}_h(p')\gamma^-\gamma^+\gamma^i\omega_s(p) \tag{A3}$$

which gives

$$-2\bar{\chi}_h(p')\gamma^i\omega_s(p) = \bar{\chi}_h(p')\gamma^+\gamma^i\gamma^-\omega_s(p) - \bar{\chi}_h(p')\gamma^-\gamma^+\gamma^i\omega_s(p). \tag{A4}$$

Furthermore, using the Dirac equation (A2) we find

$$\begin{aligned} \bar{\chi}_h(p')\gamma^+\gamma^i\gamma^-\omega_s(p) &= \frac{1}{p^+}\bar{\chi}_h(p')\gamma^+\gamma^i\gamma^- p^+\omega_s(p) \\ &= -\frac{1}{p^+}\bar{\chi}_h(p')\gamma^+\gamma^i\left(\gamma^+ p^- - \gamma^j\mathbf{p}^j\right)\omega_s(p) \end{aligned} \tag{A5}$$

and

$$\begin{aligned} \bar{\chi}_h(p')\gamma^-\gamma^+\gamma^i\omega_s(p) &= \frac{1}{p'^+}\bar{\chi}_h(p')\gamma^- p'^+\gamma^+\gamma^i\omega_s(p) \\ &= -\frac{1}{p'^+}\bar{\chi}_h(p')\left(\gamma^+ p'^- - \gamma^j\mathbf{p}'^j\right)\gamma^+\gamma^i\omega_s(p). \end{aligned} \tag{A6}$$

Since $\gamma^+\gamma^+ = 0$, these simplify to

$$\begin{aligned} \bar{\chi}_h(p')\gamma^+\gamma^i\gamma^-\omega_s(p) &= \frac{\mathbf{p}^j}{p^+}\bar{\chi}_h(p')\gamma^+\gamma^i\gamma^j\omega_s(p) \\ \bar{\chi}_h(p')\gamma^-\gamma^+\gamma^i\omega_s(p) &= -\frac{\mathbf{p}'^j}{p'^+}\bar{\chi}_h(p')\gamma^+\gamma^j\gamma^i\omega_s(p). \end{aligned} \tag{A7}$$

Combining Eqs. (A4) and (A7) we obtain

$$-2\bar{\chi}_h(p')\gamma^i\omega_s(p) = \frac{\mathbf{p}^j}{p^+}\bar{\chi}_h(p')\gamma^+\gamma^i\gamma^j\omega_s(p) + \frac{\mathbf{p}'^j}{p'^+}\bar{\chi}_h(p')\gamma^+\gamma^j\gamma^i\omega_s(p). \tag{A8}$$

In order to separate the symmetric and anti-symmetric parts in Eq. (A8) we use the identity

$$\gamma^i\gamma^j = -\delta^{ij} + \frac{1}{2}[\gamma^i, \gamma^j], \tag{A9}$$

which gives

$$\bar{\chi}_h(p')\gamma^i\omega_s(p) = \left[\frac{\mathbf{p}^j}{2p^+} + \frac{\mathbf{p}'^j}{2p'^+}\right]\delta^{ij}\bar{\chi}_h(p')\gamma^+\omega_s(p) - \left[\frac{\mathbf{p}^j}{4p^+} - \frac{\mathbf{p}'^j}{4p'^+}\right] \times \bar{\chi}_h(p')\gamma^+[\gamma^i, \gamma^j]\omega_s(p). \tag{A10}$$

Inserting the above expression into Eq. (A1) gives

$$\bar{\chi}_h(p')\not{\epsilon}_\lambda(q)\omega_s(p) = \left[\frac{\mathbf{q}^i}{q^+} - \frac{\mathbf{p}^i}{2p^+} - \frac{\mathbf{p}'^i}{2p'^+}\right]\boldsymbol{\epsilon}^j_\lambda\delta^{ij}\bar{\chi}_h(p')\gamma^+\omega_s(p) - \left[\frac{\mathbf{p}^j}{4p^+} - \frac{\mathbf{p}'^i}{4p'^+}\right] \times \boldsymbol{\epsilon}^j_\lambda\bar{\chi}_h(p')\gamma^+[\gamma^i, \gamma^j]\omega_s(p). \tag{A11}$$

This equation is valid in arbitrary spacetime dimensions and automatically includes the plus and transverse momentum conservation.

In the particular case $d = 4$, this expression can be very compactly expressed in the helicity basis by first nothing that the commutator of Dirac transverse gamma matrices can be expressed as

$$[\gamma^i, \gamma^j] = -4i\epsilon^{ij}S^3, \tag{A12}$$

where ϵ^{ij} is the anti-symmetric rank-two Levi-Civita tensor, and S^3 is the light cone helicity operator acting on the good component of the spinors[3]

$$S^3 u_h^{(G)}(p^+) = \frac{h}{2}u_h^{(G)}(p^+)$$
$$S^3 v_h^{(G)}(p^+) = -\frac{h}{2}v_h^{(G)}(p^+), \tag{A13}$$

where we denote the two fermion spin states $\pm 1/2$ by $h = \pm$ for notational simplicity. In addition, it is easy to show that the following relation between the complete spinors and good component of the spinors is satisfied

$$\bar{\chi}_h(p')\gamma^+\omega_s(p) = \bar{\chi}_h^{(G)}(p'^+)\gamma^+\omega_s^{(G)}(p^+). \tag{A14}$$

Therefore, in four dimensions we find a very useful simplification of the Dirac algebra in Eq. (6)

$$\bar{u}_{h'}(p')\gamma^+[\gamma^i, \gamma^j]u_h(p) = -4i\epsilon^{ij}\bar{u}_{h'}(p')\gamma^+S^3u_h(p) = -2ih\epsilon^{ij}\bar{u}_{h'}(p')\gamma^+u_h(p). \tag{A15}$$

Appendix B. Transverse integrals

B.1. Transversely polarized photon

In order to compute the vertex corrections for the transversely polarized virtual photon one must evaluate the following rank-3 (r3) tensor integral

$$I^{(r3)}(\mathbf{r}, \hat{\mathbf{p}}, \hat{\mathbf{q}}; M_1, M_2) = (4\pi)\int_{\mathbf{m}} \frac{m^i(m-\hat{p})^j(m-\hat{q})^k}{D_0D_1}, \tag{B1}$$

[3] The projections to the good (G) and bad (B) components of a complete spinor field Ψ are defined as $P_{G/B}\Psi = \Psi_{G/B}$, where $P_G = \gamma^-\gamma^+/2$ and $P_B = \gamma^+\gamma^-/2$ (see e.g. [4]).

where the denominators D_0 and D_1 are defined as

$$D_0 = \mathbf{m}^2 + M_1, \quad D_1 = (\mathbf{m} - \mathbf{r})^2 + M_2 \tag{B2}$$

and the integral measure in $d_\perp = 2 - 2\varepsilon$ dimensions is

$$\int_{\mathbf{m}} = (\mu^2)^{1-d_\perp/2} \int \frac{d^{d_\perp}\mathbf{m}}{(2\pi)^{d_\perp}} = \mu^{2\varepsilon} \int \frac{d^{2-2\varepsilon}\mathbf{m}}{(2\pi)^{2-2\varepsilon}}. \tag{B3}$$

Using the standard Feynman parametrization with

$$(1-x)D_0 + xD_1 = (\mathbf{m} - x\mathbf{r})^2 + x(1-x)\mathbf{r}^2 + (1-x)M_1 + xM_2, \tag{B4}$$

and performing the change of variables $\mathbf{n} = \mathbf{m} - x\mathbf{r}$ gives

$$I^{(r3)}(\mathbf{r}, \hat{\mathbf{p}}, \hat{\mathbf{q}}; M_1, M_2) = (4\pi) \int_0^1 \mathrm{d}x \int_{\mathbf{n}} \frac{(n + xr)^i (n + xr - \hat{p})^i (n + xr - \hat{q})^k}{(\mathbf{n}^2 + M)^2}, \tag{B5}$$

where

$$M = x(1-x)\mathbf{r}^2 + (1-x)M_1 + xM_2. \tag{B6}$$

Upon the integration over transverse momentum $\mathbf{n}$ the numerator simplifies to

$$\begin{aligned}(n + xr)^i (n + xr - \hat{p})^j (n + xr - \hat{q})^k = \frac{\mathbf{n}^2}{d_\perp} \Big\{ & xr^i \delta^{jk} + (xr - \tilde{p})^j \delta^{ik} + (xr - \tilde{q})^k \delta^{ij} \Big\} \\ & + xr^i (xr - \hat{p})^j (xr - \hat{q})^k + \mathcal{O}(\mathbf{n} \text{ and } \mathbf{n}^3),\end{aligned} \tag{B7}$$

where the linear and cubic terms in $\mathbf{n}$ goes to zero in dimensional regularization framework. Performing the transverse integrals over $\mathbf{n}$ with standard momentum integrals that we have listed in [35], and expanding in power of ε we obtain

$$I^{(r3)}(\mathbf{r}, \hat{\mathbf{p}}; M_1, M_2) = I^{(r3)}\Big|_{\mathrm{UV}} + I^{(r3)}\Big|_{\mathrm{f}} + I^{(r3)}\Big|_{\mathrm{F}} + \mathcal{O}(\varepsilon), \tag{B8}$$

where the UV-divergent part of the integrals becomes

$$\begin{aligned} I^{(r3)}\Big|_{\mathrm{UV}} &= \frac{1}{2}\left[\frac{1}{\varepsilon_{\overline{\mathrm{MS}}}} + \log\left(\frac{\mu^2}{\overline{Q}^2}\right)\right] \int_0^1 \mathrm{d}x \left(xr^i\delta^{jk} + (xr - \tilde{p})^j \delta^{ik} + (xr - \tilde{q})^k \delta^{ij}\right) \\ &= \frac{1}{4}\left[\frac{1}{\varepsilon_{\overline{\mathrm{MS}}}} + \log\left(\frac{\mu^2}{\overline{Q}^2}\right)\right] \left(r^i\delta^{jk} + (r - 2\tilde{p})^j \delta^{ik} + (r - 2\tilde{q})^k \delta^{ij}\right) \end{aligned} \tag{B9}$$

and the UV-finite parts

$$I^{(r3)}\Big|_{\mathrm{f}} = \frac{1}{2} \int_0^1 \mathrm{d}x \left(x\Delta_{\mathrm{f1}}^{(r3)} + \Delta_{\mathrm{f2}}^{(r3)}\right) \log\left(\frac{\overline{Q}^2}{M}\right), \tag{B10}$$

$$I^{(r3)}\Big|_{\mathrm{F}} = \int_0^1 \mathrm{d}x \frac{x^3 \Delta_{\mathrm{F1}}^{(r3)} + x^2 \Delta_{\mathrm{F2}}^{(r3)} + x\Delta_{\mathrm{F3}}^{(r3)}}{M}. \tag{B11}$$

Here the coefficients $\Delta_{\mathrm{Fi}}^{(r3)}$ and $\Delta_{\mathrm{fj}}^{(r3)}$ are given by

$$\begin{aligned}
\Delta_{\mathrm{F1}}^{(r3)} &= r^i r^j r^k \\
\Delta_{\mathrm{F2}}^{(r3)} &= -r^i(r^j \hat{q}^k + r^k \hat{p}^j) \\
\Delta_{\mathrm{F3}}^{(r3)} &= r^i \hat{p}^j \hat{q}^k \\
\Delta_{\mathrm{f1}}^{(r3)} &= r^i \delta^{jk} + r^j \delta^{ik} + r^k \delta^{ij} \\
\Delta_{\mathrm{f2}}^{(r3)} &= -\hat{p}^j \delta^{ik} - \hat{q}^k \delta^{ij}.
\end{aligned} \tag{B12}$$

B.2. Longitudinally polarized photon

In order to compute the vertex corrections for the longitudinally polarized virtual photon one must evaluate the following rank-2 (r2) tensor integral

$$I^{(r2)}(\mathbf{r}, \hat{\mathbf{p}}; M_1, M_2) = (4\pi) \int_{\mathbf{m}} \frac{m^i (m - \hat{p})^j}{D_0 D_1} \tag{B13}$$

where the denominators D_0 and D_1 are given by Eq. (B2). Performing the Feynman parametrization and the transverse integrals as in the transverse photon case we obtain

$$I^{(r2)}(\mathbf{r}, \hat{\mathbf{p}}; M_1, M_2) = I^{(r2)}\Big|_{\mathrm{UV}} + I^{(r2)}\Big|_{\mathrm{f}} + I^{(r2)}\Big|_{\mathrm{F}} + \mathcal{O}(\varepsilon) \tag{B14}$$

where the UV and finite parts simplify to

$$I^{(r2)}\Big|_{\mathrm{UV}} = \frac{\delta^{ij}_{(d_\perp)}}{2}\left[\frac{1}{\varepsilon_{\overline{\mathrm{MS}}}} + \log\left(\frac{\mu^2}{\overline{Q}^2}\right)\right] \tag{B15}$$

$$I^{(r2)}\Big|_{\mathrm{f}} = \frac{\delta^{ij}_{(d_\perp)}}{2} \int_0^1 \mathrm{d}x \log\left(\frac{\overline{Q}^2}{M}\right) \tag{B16}$$

and

$$I^{(r2)}\Big|_{\mathrm{F}} = \int_0^1 \mathrm{d}x \frac{x^2 \Delta_{\mathrm{F1}}^{(r2)} + x \Delta_{\mathrm{F2}}^{(\mathrm{r2})}}{M} \tag{B17}$$

with the coefficients $\Delta_{\mathrm{F1}}^{(r2)} = r^i r^j$ and $\Delta_{\mathrm{F2}}^{(r2)} = -r^i \hat{p}^j$. The remaining integrals over x are straightforward to perform, but yield complicated expressions that we will not write out here.

Appendix C. Transverse Fourier integrals

In this appendix, we present the integrals that are needed to calculate the Fourier transformed LCWF's for transverse and longitudinal virtual photon in the mixed space up to NLO. The Fourier transform momentum integrals obtained in this paper can be computed by applying the Schwinger parametrization

$$\frac{1}{A^\beta} = \frac{1}{\Gamma(\beta)} \int_0^\infty \mathrm{d}t t^{\beta-1} e^{-tA}, \quad A, \beta > 0. \tag{C1}$$

For the $q\bar{q}$-component of the longitudinal and transverse virtual photon, the two basic momentum integrals expressed in the mixed space (see Section 7) can be written as

$$\int \frac{\mathrm{d}^{d-2}\mathbf{P}}{(2\pi)^{d-2}} \frac{e^{i\mathbf{P}\cdot\mathbf{x}}}{\left[\mathbf{P}^2+\overline{Q}^2\right]} = (4\pi)^{1-d/2} \int_0^\infty \mathrm{d}t t^{1-d/2} e^{-t\overline{Q}^2} e^{-\frac{\mathbf{x}^2}{4t}}$$

$$\int \frac{\mathrm{d}^{d-2}\mathbf{P}}{(2\pi)^{d-2}} \frac{e^{i\mathbf{P}\cdot\mathbf{x}}}{\left[\mathbf{P}^2+\overline{Q}^2\right]} \mathbf{P}^i = \frac{i}{2}\mathbf{x}^i (4\pi)^{1-d/2} \int_0^\infty \mathrm{d}t t^{-d/2} e^{-t\overline{Q}^2} e^{-\frac{\mathbf{x}^2}{4t}}, \tag{C2}$$

where the $(d-2)$-dimensional Gaussian integrals are performed over $\mathbf{P}$. Using the formula

$$\int_0^\infty \mathrm{d}t t^{\beta-1} e^{-tA} e^{-\frac{B}{t}} = 2\left(\frac{B}{A}\right)^{\beta/2} K_{-\beta}\left(2\sqrt{AB}\right), \quad A, B > 0 \tag{C3}$$

where $K_\alpha(z)$ is the modified Bessel function of the second kind, the integrals in Eq. (C2) simplify to

$$\int \frac{\mathrm{d}^{d-2}\mathbf{P}}{(2\pi)^{d-2}} \frac{e^{i\mathbf{P}\cdot\mathbf{x}}}{\left[\mathbf{P}^2+\overline{Q}^2\right]} = \frac{1}{2\pi}\left(\frac{\overline{Q}}{2\pi|\mathbf{x}|}\right)^{d/2-2} K_{\frac{d}{2}-2}\left(|\mathbf{x}|\overline{Q}\right)$$

$$\int \frac{\mathrm{d}^{d-2}\mathbf{P}}{(2\pi)^{d-2}} \frac{e^{i\mathbf{P}\cdot\mathbf{x}}}{\left[\mathbf{P}^2+\overline{Q}^2\right]} \mathbf{P}^i = i\mathbf{x}^i \left(\frac{\overline{Q}}{2\pi|\mathbf{x}|}\right)^{d/2-1} K_{\frac{d}{2}-1}\left(|\mathbf{x}|\overline{Q}\right). \tag{C4}$$

In addition, we also need the integrals (see derivation in [29])

$$\int \frac{\mathrm{d}^{d-2}\mathbf{P}}{(2\pi)^{d-2}} \frac{e^{i\mathbf{P}\cdot\mathbf{x}}}{\left[\mathbf{P}^2+\overline{Q}^2\right]} \log\left(\frac{\mathbf{P}^2+\overline{Q}^2}{\overline{Q}^2}\right) = \frac{1}{2\pi}\left(\frac{\overline{Q}}{2\pi|\mathbf{x}|}\right)^{d/2-2} K_{\frac{d}{2}-2}\left(|\mathbf{x}|\overline{Q}\right)$$

$$\times \left\{\left[-\frac{1}{2}\log\left(\frac{\mathbf{x}^2\overline{Q}^2}{4}\right)+\Psi_0(1)\right]+\mathcal{O}(d-4)\right\} \tag{C5}$$

$$\int \frac{\mathrm{d}^{d-2}\mathbf{P}}{(2\pi)^{d-2}} \frac{e^{i\mathbf{P}\cdot\mathbf{x}}}{\left[\mathbf{P}^2+\overline{Q}^2\right]} \mathbf{P}^i \log\left(\frac{\mathbf{P}^2+\overline{Q}^2}{\overline{Q}^2}\right)$$

$$= i\mathbf{x}^i \left(\frac{\overline{Q}}{2\pi|\mathbf{x}|}\right)^{d/2-1} \left\{\left[-\frac{1}{2}\log\left(\frac{\mathbf{x}^2\overline{Q}^2}{4}\right)+\Psi_0(1)\right]\right. \tag{C6}$$

$$\left. \times K_{\frac{d}{2}-1}\left(|\mathbf{x}|\overline{Q}\right) + \frac{1}{|\mathbf{x}|\overline{Q}} K_0\left(|\mathbf{x}|\overline{Q}\right) + \mathcal{O}(d-4)\right\},$$

where $\Psi_0(x)$ is the digamma function with $\Psi_0(1) = -\gamma_E$, and

$$\int \frac{\mathrm{d}^{d-2}\mathbf{P}}{(2\pi)^{d-2}} \frac{e^{i\mathbf{P}\cdot\mathbf{x}}}{\left[\mathbf{P}^2+\overline{Q}^2\right]} \mathbf{P}^i \frac{\left(\mathbf{P}^2+\overline{Q}^2\right)}{\mathbf{P}^2} \log\left(\frac{\mathbf{P}^2+\overline{Q}^2}{\overline{Q}^2}\right) \tag{C7}$$

$$= 2i\mathbf{x}^i \left(\frac{\overline{Q}}{2\pi|\mathbf{x}|}\right)^{d/2-1} \left\{\frac{1}{|\mathbf{x}|\overline{Q}} K_0\left(|\mathbf{x}|\overline{Q}\right) + \mathcal{O}(d-4)\right\}.$$

For the $q\bar{q}g$-component of the longitudinal virtual photon we need the following integral

$$\mathcal{I}^i(\mathbf{x},\mathbf{y},\overline{Q}^2,\omega) = \mu^{2-\frac{d}{2}} \int \frac{\mathrm{d}^2\mathbf{P}}{(2\pi)^2} \int \frac{\mathrm{d}^{d-2}\mathbf{K}}{(2\pi)^{d-2}} \frac{\mathbf{K}^i e^{i\mathbf{P}\cdot\mathbf{x}} e^{i\mathbf{K}\cdot\mathbf{y}}}{\left[\mathbf{P}^2+\overline{Q}^2\right]\left[\mathbf{K}^2+\omega\left(\mathbf{P}^2+\overline{Q}^2\right)\right]}. \tag{C8}$$

Using Eqs. (C2) and (C1) we get

$$\mathcal{I}^i(\mathbf{x},\mathbf{y},\overline{Q}^2,\omega) = \mu^{2-\frac{d}{2}} \frac{i}{2}(4\pi)^{1-d/2}\mathbf{y}^i \int_0^\infty \mathrm{d}t\, t^{-d/2} e^{-\frac{-\mathbf{y}^2}{4t}} \int_0^\infty \mathrm{d}s e^{-(s+t\omega)\overline{Q}^2} \tag{C9}$$

$$\times \int \frac{\mathrm{d}^2\mathbf{P}}{(2\pi)^2} e^{-(s+t\omega)\mathbf{P}^2} e^{i\mathbf{P}\cdot\mathbf{x}},$$

where the Gaussian integral over the transverse momentum $\mathbf{P}$ is

$$\int \frac{\mathrm{d}^2\mathbf{P}}{(2\pi)^2} e^{-(s+t\omega)\mathbf{P}^2} e^{i\mathbf{P}\cdot\mathbf{x}} = (4\pi)^{-1}(s+t\omega)^{-1} e^{-\frac{\mathbf{x}^2}{4(s+t\omega)}}. \tag{C10}$$

By making the change of variables $u = s + t\omega$,

$$\mathcal{I}^i(\mathbf{x},\mathbf{y},\overline{Q}^2,\omega) = \mu^{2-\frac{d}{2}} \frac{i}{2}(4\pi)^{-d/2}\mathbf{y}^i \int_0^\infty \mathrm{d}t\, t^{-d/2} e^{-\frac{-\mathbf{y}^2}{4t}} \int_{t\omega}^\infty \frac{\mathrm{d}u}{u} e^{-u\overline{Q}^2} e^{-\frac{\mathbf{x}^2}{4u}} \tag{C11}$$

and changing the order of integration we obtain

$$\mathcal{I}^i(\mathbf{x},\mathbf{y},\overline{Q}^2,\omega) = \mu^{2-\frac{d}{2}} \frac{i}{2}(4\pi)^{-d/2}\mathbf{y}^i \int_0^\infty \frac{\mathrm{d}u}{u} e^{-u\overline{Q}^2} e^{-\frac{\mathbf{x}^2}{4u}} \int_0^{u/\omega} \mathrm{d}t\, t^{-d/2} e^{-\frac{-\mathbf{y}^2}{4t}}. \tag{C12}$$

Finally, performing the outer integral with respect to t we obtain the result

$$\mathcal{I}^i(\mathbf{x},\mathbf{y},\overline{Q}^2,\omega) = \mu^{2-\frac{d}{2}} \frac{i}{8}\pi^{-d/2}\mathbf{y}^i(\mathbf{y}^2)^{1-d/2} \int_0^\infty \frac{\mathrm{d}u}{u} e^{-u\overline{Q}^2} e^{-\frac{\mathbf{x}^2}{4u}} \Gamma\left(\frac{d}{2}-1, \frac{\omega\mathbf{y}^2}{4u}\right), \tag{C13}$$

where $\Gamma(s,x)$ is the upper incomplete gamma function. For the case $d = 4$,

$$\mathcal{I}^i(\mathbf{x},\mathbf{y},\overline{Q}^2,\omega) = \frac{i}{(2\pi)^2}\frac{\mathbf{y}^i}{\mathbf{y}^2} K_0\left(\overline{Q}\sqrt{\mathbf{x}^2+\omega\mathbf{y}^2}\right). \tag{C14}$$

Similarly, for the $q\bar{q}g$-component of the transverse virtual photon we need the integrals

$$\mathcal{I}^{ik}(\mathbf{x},\mathbf{y},\overline{Q}^2,\omega) = \mu^{2-\frac{d}{2}} \int \frac{\mathrm{d}^2\mathbf{P}}{(2\pi)^2} \int \frac{\mathrm{d}^{d-2}\mathbf{K}}{(2\pi)^{d-2}} \frac{\mathbf{P}^i\mathbf{K}^k e^{i\mathbf{P}\cdot\mathbf{x}} e^{i\mathbf{K}\cdot\mathbf{y}}}{\left[\mathbf{P}^2+\overline{Q}^2\right]\left[\mathbf{K}^2+\omega\left(\mathbf{P}^2+\overline{Q}^2\right)\right]} \tag{C15}$$

and

$$\mathcal{I}(\mathbf{x},\mathbf{y},\overline{Q}^2,\omega) = \mu^{2-\frac{d}{2}} \int \frac{\mathrm{d}^2\mathbf{P}}{(2\pi)^2} \int \frac{\mathrm{d}^{d-2}\mathbf{K}}{(2\pi)^{d-2}} \frac{e^{i\mathbf{P}\cdot\mathbf{x}} e^{i\mathbf{K}\cdot\mathbf{y}}}{\left[\mathbf{K}^2+\omega\left(\mathbf{P}^2+\overline{Q}^2\right)\right]}. \tag{C16}$$

Following the same steps described previously we find

$$\mathcal{I}^{ik}(\mathbf{x},\mathbf{y},\overline{Q}^2,\omega)=-\mu^{2-d/2}\frac{\pi^{-d/2}}{16}\mathbf{x}^i\mathbf{y}^k(\mathbf{y}^2)^{1-d/2}\int_0^\infty\frac{\mathrm{d}u}{u^2}e^{-u\overline{Q}^2}e^{-\frac{\mathbf{x}^2}{4u}}\Gamma\left(\frac{d}{2}-1,\frac{\omega\mathbf{y}^2}{4u}\right) \tag{C17}$$

and

$$\mathcal{I}(\mathbf{x},\mathbf{y},\overline{Q}^2,\omega)=(2\pi)^{-d/2}\left(\frac{\mu}{\omega}\right)^{2-d/2}\left(\frac{\overline{Q}}{\sqrt{\mathbf{x}^2+\omega\mathbf{y}^2}}\right)^{d/2-1}K_{\frac{d}{2}-1}\left(\overline{Q}\sqrt{\mathbf{x}^2+\omega\mathbf{y}^2}\right). \tag{C18}$$

For the case $d=4$

$$\mathcal{I}^{ik}(\mathbf{x},\mathbf{y},\overline{Q}^2,\omega)=-\frac{1}{(2\pi)^2}\frac{\mathbf{x}^i\mathbf{y}^k}{\mathbf{y}^2}\left(\frac{\overline{Q}}{\sqrt{\mathbf{x}^2+\omega\mathbf{y}^2}}\right)K_1\left(\overline{Q}\sqrt{\mathbf{x}^2+\omega\mathbf{y}^2}\right)$$

$$\mathcal{I}(\mathbf{x},\mathbf{y},\overline{Q}^2,\omega)=\frac{1}{(2\pi)^2}\left(\frac{\overline{Q}}{\sqrt{\mathbf{x}^2+\omega\mathbf{y}^2}}\right)K_1\left(\overline{Q}\sqrt{\mathbf{x}^2+\omega\mathbf{y}^2}\right). \tag{C19}$$

Appendix D. Wilson line color algebra

For the cross section we need the following $q\bar{q}$ and $q\bar{q}g$ matrix elements with eikonal operator $\hat{S}_E$:

$$\delta_{\alpha\beta}\delta_{\alpha'\beta'}\langle\bar{q}(\ell^+,\mathbf{x}',h,\alpha')q(\ell'^+,\mathbf{y}',-h,\beta')|1-\hat{S}_E|q(p^+,\mathbf{x},h,\alpha)\bar{q}(p'^+,\mathbf{y},-h,\beta)\rangle \tag{D1}$$

and

$$t^a_{\alpha\beta}t^b_{\beta'\alpha'}\langle\bar{q}(\ell^+,\mathbf{x}',h,\alpha')q(\ell'^+,\mathbf{y}',-h,\beta')g(w^+,\mathbf{z}',\sigma',b)|1 - \hat{S}_E|q(p^+,\mathbf{x},h,\alpha)\bar{q}(p'^+,\mathbf{y},-h,\beta)g(k^+,\mathbf{z},\sigma,a)\rangle. \tag{D2}$$

Using the definition of eikonal scattering operator Eq. (51) together with the normalization conditions in Eq. (50) one obtain

$$\begin{aligned}&\langle\bar{q}(\ell^+,\mathbf{x}',h,\alpha')q(\ell'^+,\mathbf{y}',-h,\beta')|1-\hat{S}_E|q(p^+,\mathbf{x},h,\alpha)\bar{q}(p'^+,\mathbf{y},-h,\beta)\rangle\\ &=\left[\delta_{\alpha'\alpha}\delta_{\beta'\beta}-\sum_{\tilde{\alpha},\tilde{\beta}}[U[A](\mathbf{x})]_{\tilde{\alpha}\alpha}[U^\dagger[A](\mathbf{y})]_{\beta\tilde{\beta}}\delta_{\alpha'\tilde{\alpha}}\delta_{\beta'\tilde{\beta}}\right]4p^+p'^+(2\pi)^2\delta(p^+-\ell^+)\\ &\quad\times\ \delta(p'^+-\ell'^+)\delta^{(2)}(\mathbf{x}-\mathbf{x}')\delta^{(2)}(\mathbf{y}-\mathbf{y}').\end{aligned} \tag{D3}$$

On the cross section level this expression is multiplied with $\delta_{\alpha\beta}\delta_{\alpha'\beta'}$, and thus

$$\begin{aligned}&\delta_{\alpha\beta}\delta_{\alpha'\beta'}\langle\bar{q}(\ell^+,\mathbf{x}',h,\alpha')q(\ell'^+,\mathbf{y}',-h,\beta')|1-\hat{S}_E|q(p^+,\mathbf{x},h,\alpha)\bar{q}(p'^+,\mathbf{y},-h,\beta)\rangle\\ &=\left[N_c-\mathrm{Tr}\left(U[A](\mathbf{x})U^\dagger[A](\mathbf{y})\right)\right]4p^+p'^+(2\pi)^2\delta(p^+-\ell^+)\delta(p'^+-\ell'^+)\delta^{(2)}(\mathbf{x}-\mathbf{x}')\delta^{(2)}(\mathbf{y}-\mathbf{y}').\end{aligned} \tag{D4}$$

Similarly, for the $q\bar{q}g$-term one obtain

$$\langle \bar{q}(\ell^+, \mathbf{x}', h, \alpha')q(\ell'^+, \mathbf{y}', -h, \beta')g(w^+, \mathbf{z}', \sigma', b)|1 - \hat{S}_E|q(p^+, \mathbf{x}, h, \alpha)\bar{q}(p'^+, \mathbf{y}, -h, \beta)g(k^+, \mathbf{z}, \sigma, a)\rangle$$

$$= \left[\delta_{\alpha'\alpha}\ \delta_{\beta'\beta}\delta_{ba} - \sum_{\bar{\alpha},\bar{\beta},c,a} [U[A](\mathbf{x})]_{\bar{\alpha}\alpha}[U^\dagger[A](\mathbf{y})]_{\beta\bar{\beta}}[V[A](\mathbf{z})]_{ca}(\delta_{\alpha'\bar{\alpha}}\delta_{\beta'\bar{\beta}}\delta_{bc})\right] \tag{D5}$$

$$\times\ 8p^+p'^+k^+(2\pi)^3\delta(p^+ - \ell^+)\delta(p'^+ - \ell'^+)\delta(k^+ - w^+)\delta^{(2)}(\mathbf{x} - \mathbf{x}')\delta^{(2)}(\mathbf{y} - \mathbf{y}')\delta^{(2)}(\mathbf{z} - \mathbf{z}')\delta_{\sigma,\sigma'}.$$

On the cross section level this expression is multiplied with $t^a_{\alpha\beta}t^b_{\beta'\alpha'}$, and thus

$$t^a_{\alpha\beta}t^b_{\beta'\alpha'}\langle \bar{q}(\ell^+, \mathbf{x}', h, \alpha')q(\ell'^+, \mathbf{y}', -h, \beta')g(w^+, \mathbf{z}', \sigma', b)|\hat{S}_E|q(p^+, \mathbf{x}, h, \alpha)\bar{q}(p'^+, \mathbf{y}, -h, \beta)g(k^+, \mathbf{z}, \sigma, a)\rangle$$

$$= \left[N_cC_F - \sum_{b,a} \mathrm{Tr}\left(U[A](\mathbf{x})t^aU^\dagger[A](\mathbf{y})t^b\right)[V[A](\mathbf{z})]_{ba}\right] \tag{D6}$$

$$\times\ 8p^+p'^+k^+(2\pi)^3\delta(p^+ - \ell^+)\delta(p'^+ - \ell'^+)\delta(k^+ - w^+)\delta^{(2)}(\mathbf{x} - \mathbf{x}')\delta^{(2)}(\mathbf{y} - \mathbf{y}')\delta^{(2)}(\mathbf{z} - \mathbf{z}')\delta_{\sigma,\sigma'}.$$

Rewriting the adjoint Wilson line as

$$[V[A](\mathbf{z})]_{ba} = 2\mathrm{Tr}\left(U[A](\mathbf{z})t^aU^\dagger[A](\mathbf{z})t^b\right) \tag{D7}$$

and applying the Fierz identity

$$t^a_{\alpha\beta}t^a_{\bar{\alpha}\bar{\beta}} = \frac{1}{2}\left(\delta_{\alpha\bar{\beta}}\delta_{\beta\bar{\alpha}} - \frac{1}{N_c}\delta_{\alpha\beta}\delta_{\bar{\alpha}\bar{\beta}}\right) \tag{D8}$$

together with the unitarity condition, $U[A](\mathbf{z})U^\dagger[A](\mathbf{z}) = \mathbf{1}_{N_c}$, one finds the expression

$$\sum_{b,a} \mathrm{Tr}\left(U[A](\mathbf{x})t^aU^\dagger[A](\mathbf{y})t^b\right)[V[A](\mathbf{z})]_{ba} = \frac{1}{2}\Bigg[\mathrm{Tr}\left(U[A](\mathbf{x})U^\dagger[A](\mathbf{z})\right)\mathrm{Tr}\left(U[A](\mathbf{z})U^\dagger[A](\mathbf{y})\right) - \frac{1}{N_c}\mathrm{Tr}\left(U[A](\mathbf{x})U^\dagger[A](\mathbf{y})\right)\Bigg]. \tag{D9}$$

Appendix E. Subtraction procedures

The polynomial subtraction term in [30] is taken as proportional to

$$S_{\mathrm{pol}} = \frac{\Gamma(d/2-1)^2}{\pi^{d/2-1}}\int \mathrm{d}^{d-2}\mathbf{x}_2(\mathbf{x}_{20})^m(\mathbf{x}^2_{20})^{1-d/2}\left\{\mathbf{x}^m_{20}(\mathbf{x}^2_{20})^{1-d/2} - \mathbf{x}^m_{21}(\mathbf{x}^2_{21})^{1-d/2}\right\}, \tag{E1}$$

where the first term corresponds to the desired UV divergence in the limit $\mathbf{x}_{20} \to \mathbf{0}$ and the second term is added in order to cancel the IR divergence introduced by the first term. We use here the notations of [30], which are related to ours by $\mathbf{x}_0 \to \mathbf{x}$, $\mathbf{x}_1 \to \mathbf{y}$, $\mathbf{x}_2 \to \mathbf{z}$ and $\mathbf{x}_{02} \to \mathbf{r}_{xz}$ etc. Using

$\mathbf{x}_{21} = \mathbf{x}_{20} + \mathbf{x}_{01}$ and $\mathbf{x}_{21}^2 = \mathbf{x}_{20}^2 + \mathbf{x}_{01}^2 + 2\mathbf{x}_{20}\cdot\mathbf{x}_{01}$ we have

$$S_{\text{pol}} = \frac{\Gamma(d/2-1)^2}{\pi^{d/2-1}} \int \mathrm{d}^{d-2}\mathbf{x}_2 \Big\{ \mathbf{x}_{20}^2 (\mathbf{x}_{20}^2)^{2-d} - \mathbf{x}_{20}^2 (\mathbf{x}_{20}^2)^{1-d/2} (\mathbf{x}_{21}^2)^{1-d/2} - \mathbf{x}_{20}^m \mathbf{x}_{01}^m (\mathbf{x}_{20}^2)^{1-d/2} (\mathbf{x}_{21}^2)^{1-d/2} \Big\} \tag{E2}$$

and performing the Feynman parametrization one finds the result

$$S_{\text{pol}} = -(\mathbf{x}_{01}^2)^{2-d/2}\Gamma(d/2-2). \tag{E3}$$

Note that this result is valid when $\varepsilon < 0$. Thus one has to analytically continue this to $\varepsilon > 0$ and the result is

$$S_{\text{pol}} = +\left(\frac{1}{\varepsilon} + \gamma_E + \log(\mathbf{x}_{01}^2)\right). \tag{E4}$$

Our subtraction term uses the integral

$$S_{\text{exp}} = \frac{\Gamma(d/2-1)^2}{\pi^{d/2-1}} \int \mathrm{d}^{d-2}\mathbf{r}_{zx} (\mathbf{r}_{zx}^2)^{3-d} e^{-\mathbf{r}_{zx}^2/(\mathbf{r}_{xy}^2\xi)}, \tag{E5}$$

which has the same divergent behavior in the limit $\mathbf{r}_{zx} \to \mathbf{0}$, but moderated by an exponential function so that there is no IR divergence. The constant ξ is taken as $\xi = e^{\gamma_E}$. This gives

$$S_{\text{exp}} = (\mathbf{r}_{xy}^2\xi)^{2-d/2}\Gamma(d/2-1)\Gamma(2-d/2). \tag{E6}$$

This result is valid when $\varepsilon > 0$ and we get

$$S_{\text{exp}} = +\left(\frac{1}{\varepsilon} + \gamma_E + \log(\mathbf{x}_{01}^2)\right). \tag{E7}$$

It can be illustrative to go to $d = 4$ dimensions and perform the angular integral. Doing this one gets

$$S_{\text{pol}} = 2\int \frac{\mathrm{d}|\mathbf{x}_{20}|}{|\mathbf{x}_{20}|}\theta\left(|\mathbf{x}_{10}| - |\mathbf{x}_{20}|\right) \tag{E8}$$

$$S_{\text{exp}} = 2\int \frac{\mathrm{d}|\mathbf{r}_{zx}|}{|\mathbf{r}_{zx}|} e^{-\mathbf{r}_{zx}^2/(\mathbf{r}_{xy}^2\xi)}. \tag{E9}$$

This shows that indeed both functions subtract the same UV divergence in the small daughter dipole limit, but at larger values of $|\mathbf{x}_{20}| = |\mathbf{r}_{zx}|$ the behavior is different. Although both choices lead to a perfectly finite final result, we believe that the discontinuous theta function in (E8) can be somewhat inconvenient from a numerical point of view in the multidimensional numerical integration required to evaluate the cross section in practice.

Appendix F. Derivation of UV-finite terms for $\sigma^{\gamma_T^*}$

Here we present the detailed computation of individual UV-finite contributions to the transverse virtual photon cross section appearing in Eq. (215).

The full cross term given in Eq. (199) is divided into three parts: The contribution coming from the instantaneous diagrams simply gives

$$2\Re e\Big[(\mathrm{j})(\mathrm{k})^*\Big] = 0. \tag{F1}$$

The interference terms between the radiative diagrams (h), (i) and instantaneous diagrams (j), (k) simplifies to

$$2\Re e\Big[((\mathrm{h})+(\mathrm{i}))\,((\mathrm{j})--(\mathrm{k}))^*\Big] = \frac{2}{4(2\pi)^4}\frac{Q^2}{\mathbf{R}^2}[K_1(Q|\mathbf{R}|)]^2\Bigg[\frac{z_1^2z_2z_3^3}{z_1+z_2}\frac{\mathbf{r}_{yxz}\cdot\mathbf{r}_{zx}}{\mathbf{r}_{zx}^2}+\frac{z_1z_2z_3^2(z_1+z_2)^2}{z_2+z_3}\frac{\mathbf{r}_{yxz}\cdot\mathbf{r}_{zx}}{\mathbf{r}_{zx}^2} + \frac{z_2z_3z_1^2(z_2+z_3)^2}{z_1+z_2}\frac{\mathbf{r}_{xyz}\cdot\mathbf{r}_{zy}}{\mathbf{r}_{zy}^2}+\frac{z_2z_3^2z_1^3}{z_2+z_3}\frac{\mathbf{r}_{xyz}\cdot\mathbf{r}_{zy}}{\mathbf{r}_{zy}^2}\Bigg], \tag{F2}$$

where

$$\mathbf{r}_{yxz}\cdot\mathbf{r}_{zx} = \mathbf{r}_{zx}^2\left(\frac{z_1}{z_1+z_2}\right)-\mathbf{r}_{zx}\cdot\mathbf{r}_{zy} \tag{F3}$$

$$\mathbf{r}_{xyz}\cdot\mathbf{r}_{zy} = \mathbf{r}_{zy}^2\left(\frac{z_3}{z_2+z_3}\right)-\mathbf{r}_{zx}\cdot\mathbf{r}_{zy}.$$

Thanks to the above identities, Eq. (F2) can be further simplified to

$$2\Re e\Big[((\mathrm{h})+(\mathrm{i}))\,((\mathrm{j})--(\mathrm{k}))^*\Big] = \frac{2}{4(2\pi)^4}\frac{Q^2}{\mathbf{R}^2}[K_1(Q|\mathbf{R}|)]^2\frac{z_1z_2z_3}{(z_1+z_2)(z_2+z_3)}\Bigg[\left(\frac{z_1}{z_1+z_2}\right)A + \left(\frac{z_3}{z_2+z_3}\right)B - A\frac{(\mathbf{r}_{zx}\cdot\mathbf{r}_{zy})}{\mathbf{r}_{zx}^2}-B\frac{(\mathbf{r}_{zx}\cdot\mathbf{r}_{zy})}{\mathbf{r}_{zy}^2}\Bigg] \tag{F4}$$

with the coefficients

$$A = z_3\Big\{(z_1+z_2)^3+z_1z_3(z_2+z_3)\Big\} \tag{F5}$$

$$B = z_1\Big\{(z_2+z_3)^3+z_1z_3(z_1+z_2)\Big\}.$$

Finally, the interference term between radiative diagrams (h) and (i) can be cast in the following form

$$2\Re e\Big[(\mathrm{h})(\mathrm{i})^*\Big] = \frac{2}{4(2\pi)^4}\frac{Q^2}{\mathbf{R}^2}[K_1(Q|\mathbf{R}|)]^2\frac{z_1z_3}{(z_1+z_2)(z_2+z_3)}\Bigg[z_2^2(z_1-z_3)^2 - \Big[z_1(z_1+z_2)+z_3(z_2+z_3)\Big]\Big[z_1(z_2+z_3)+z_3(z_1+z_2)\Big] \tag{F6}$$

$$\times\frac{\mathbf{R}^2(\mathbf{r}_{zx}\cdot\mathbf{r}_{zy})}{\mathbf{r}_{zx}^2\mathbf{r}_{zy}^2}+2z_1z_2z_3\Big[(z_1+z_2)^2+(z_2+z_3)^2\Big]\frac{(\mathbf{r}_{zx}\cdot\mathbf{r}_{zy})^2}{\mathbf{r}_{zx}^2\mathbf{r}_{zy}^2}\Bigg],$$

where we have used the identity

$$\mathbf{r}_{xyz}\cdot\mathbf{r}_{yxz} = -\frac{\mathbf{R}^2}{(z_1+z_2)(z_2+z_3)}+\frac{z_2}{(z_1+z_2)(z_2+z_3)}(\mathbf{r}_{zx}\cdot\mathbf{r}_{zy}). \tag{F7}$$

The term proportional to $(\mathbf{r}_{zx}\cdot\mathbf{r}_{zy})^2$ can be further simplified by noticing that

$$\mathbf{r}_{zx}\cdot\mathbf{r}_{zy} = \frac{1}{2}\Bigg[\left(\frac{z_2+z_3}{z_3}\right)\mathbf{r}_{zx}^2+\left(\frac{z_1+z_2}{z_2}\right)\mathbf{r}_{zy}^2-\frac{\mathbf{R}^2}{z_1z_3}\Bigg]. \tag{F8}$$

Straightforward algebra leads to

$$2\Re e\Big[(\mathrm{h})(\mathrm{i})^*\Big] = \frac{2}{4(2\pi)^4}\frac{Q^2}{\mathbf{R}^2}[K_1(Q|\mathbf{R}|)]^2\frac{z_1z_2z_3}{(z_1+z_2)(z_2+z_3)}\Bigg[-C\frac{\mathbf{R}^2(\mathbf{r}_{zx}\cdot\mathbf{r}_{zy})}{\mathbf{r}_{zx}^2\mathbf{r}_{zy}^2} + D\Bigg[\left(\frac{z_1+z_2}{z_1}\right)\frac{(\mathbf{r}_{zx}\cdot\mathbf{r}_{zy})}{\mathbf{r}_{zx}^2} + \left(\frac{z_2+z_3}{z_3}\right)\frac{(\mathbf{r}_{zx}\cdot\mathbf{r}_{zy})}{\mathbf{r}_{zy}^2}\Bigg] + E\Bigg], \tag{F9}$$

where we have defined the coefficients

$$C = \frac{(z_1+z_2)(z_2+z_3)}{z_2}\left\{\left[(1-z_1)^2+z_1^2\right] + \left[(1-z_3)^2+z_3^2\right]\right\}$$

$$D = z_1z_3\left\{(z_1+z_2)^2+(z_2+z_3)^2\right\} \tag{F10}$$

$$E = z_2(z_1-z_3)^2.$$

Summing the contributions in (F4) and (F9) together we find for equation

$$(199) = \frac{2Q^2}{4(2\pi)^4}\frac{z_1z_2z_3}{(z_1+z_2)(z_2+z_3)}\int_{\mathbf{z}}\frac{[K_1(Q|\mathbf{R}|)]^2}{\mathbf{R}^2}\Bigg[-C\frac{\mathbf{R}^2(\mathbf{r}_{zx}\cdot\mathbf{r}_{zy})}{\mathbf{r}_{zx}^2\mathbf{r}_{zy}^2} + \frac{(\mathbf{r}_{zx}\cdot\mathbf{r}_{zy})}{\mathbf{r}_{zx}^2}\left\{D\left(\frac{z_1+z_2}{z_1}\right)-A\right\} + \frac{(\mathbf{r}_{zx}\cdot\mathbf{r}_{zy})}{\mathbf{r}_{zy}^2}\left\{D\left(\frac{z_2+z_3}{z_3}\right)-B\right\} + \left(\frac{z_1}{z_1+z_2}\right)A + \left(\frac{z_3}{z_2+z_3}\right)B + E\Bigg]\left(1-\mathcal{S}_{xyz}\right). \tag{F11}$$

The sum of contributions coming from the two instantaneous diagrams squared Eqs. (197) and Eqs. (198) can be simplified to the following form

$$\overline{\Theta}_{(\mathrm{j})} + \overline{\Theta}_{(\mathrm{k})} = \frac{2Q^2}{4(2\pi)^4}\frac{z_1z_2z_3}{(z_1+z_2)(z_2+z_3)}H\int_{\mathbf{z}}\frac{[K_1(Q|\mathbf{R}|)]^2}{\mathbf{R}^2}\left(1-\mathcal{S}_{xyz}\right), \tag{F12}$$

where

$$H = \frac{z_1z_2z_3}{2}\left\{\frac{(z_2+z_3)}{(z_1+z_2)}+\frac{(z_1+z_2)}{(z_2+z_3)}\right\}. \tag{F13}$$

Finally, combining the contributions in Eqs. (F11) and (F12) give the result shown in Eq. (215).

References

[1] J.B. Kogut, D.E. Soper, Phys. Rev. D 1 (1970) 2901.
[2] J. Bjorken, J.B. Kogut, D.E. Soper, Phys.Rev. D 3 (1971) 1382.
[3] G.P. Lepage, S.J. Brodsky, Phys. Rev. D 22 (1980) 2157.
[4] S.J. Brodsky, H.-C. Pauli, S.S. Pinsky, Phys. Rep. 301 (1998) 299. arXiv:hep-ph/9705477 [hep-ph].
[5] F. Gelis, E. Iancu, J. Jalilian-Marian, R. Venugopalan, Ann. Rev. Nucl. Part. Sci. 60 (2010) 463. arXiv:1002.0333 [hep-ph].
[6] I. Balitsky, Nuclear Phys. B 463 (1996) 99. arXiv:hep-ph/9509348.
[7] Y.V. Kovchegov, Phys. Rev. D 61 (2000) 074018. arXiv:hep-ph/9905214.
[8] Y.V. Kovchegov, Phys. Rev. D 60 (2) (1999) 034008. arXiv:hep-ph/9901281.
[9] I. Balitsky, G.A. Chirilli, Phys. Rev. D 77 (2008) 014019. arXiv:0710.4330 [hep-ph].
[10] I. Balitsky, G.A. Chirilli, Phys. Rev. D 88 (2013) 111501. arXiv:1309.7644 [hep-ph].
[11] A. Kovner, M. Lublinsky, Y. Mulian, 89 (2014) 061704. arXiv:1310.0378 [hep-ph].
[12] I. Balitsky, A.V. Grabovsky, J. High Energy Phys. 01 (2015) 009. arXiv:1405.0443 [hep-ph].
[13] G. Beuf, Phys. Rev. D 89 (2014) 074039. arXiv:1401.0313 [hep-ph].
[14] T. Lappi, H. Mäntysaari, Phys. Rev. D 91 (2015) 074016. arXiv:1502.02400 [hep-ph].

[15] E. Iancu, J.D. Madrigal, A.H. Mueller, G. Soyez, D.N. Triantafyllopoulos, Phys. Lett. B 744 (2015) 293. arXiv:1502.05642 [hep-ph].
[16] E. Iancu, J.D. Madrigal, A.H. Mueller, G. Soyez, D.N. Triantafyllopoulos, Phys. Lett. B 750 (2015) 643. arXiv:1507.03651 [hep-ph].
[17] J.L. Albacete, Nuclear Phys. A 957 (2017) 71. arXiv:1507.07120 [hep-ph].
[18] T. Lappi, H. Mäntysaari, Phys. Rev. D 93 (2016) 094004. arXiv:1601.06598 [hep-ph].
[19] M. Lublinsky, Y. Mulian, arXiv:1610.03453 [hep-ph].
[20] T. Altinoluk, A. Kovner, Phys. Rev. D 83 (2011) 105004. arXiv:1102.5327 [hep-ph].
[21] J. Jalilian-Marian, A.H. Rezaeian, Phys. Rev. D 85 (2012) 014017. arXiv:1110.2810 [hep-ph].
[22] G.A. Chirilli, B.-W. Xiao, F. Yuan, Phys. Rev. D 86 (2012) 054005. arXiv:1203.6139 [hep-ph].
[23] A.M. Stasto, B.-W. Xiao, D. Zaslavsky, Phys. Rev. Lett. 112 (2014) 012302. arXiv:1307.4057 [hep-ph].
[24] Z.-B. Kang, I. Vitev, H. Xing, Phys. Rev. Lett. 113 (2014) 062002. arXiv:1403.5221 [hep-ph].
[25] T. Altinoluk, N. Armesto, G. Beuf, A. Kovner, M. Lublinsky, Phys. Rev. D 91 (2015) 094016. arXiv:1411.2869 [hep-ph].
[26] A. Ayala, M. Hentschinski, J. Jalilian-Marian, M.E. Tejeda-Yeomans, Phys. Lett. B 761 (3) (2016) 229. arXiv:1604.08526 [hep-ph].
[27] G. Beuf, Phys. Rev. D 85 (2012) 034039. arXiv:1112.4501 [hep-ph].
[28] I. Balitsky, G.A. Chirilli, Phys. Rev. D 87 (2013) 014013. arXiv:1207.3844 [hep-ph].
[29] G. Beuf, Phys. Rev. D 94 (2016) 054016. arXiv:1606.00777 [hep-ph].
[30] G. Beuf, arXiv:1708.06557 [hep-ph].
[31] B. Ducloué, H. Hänninen, T. Lappi, Y. Zhu, arXiv:1708.07328 [hep-ph].
[32] R. Boussarie, A.V. Grabovsky, L. Szymanowski, S. Wallon, J. High Energy Phys. 09 (2014) 026. arXiv:1405.7676 [hep-ph].
[33] R. Boussarie, A.V. Grabovsky, D. Yu. Ivanov, L. Szymanowski, S. Wallon, Phys. Rev. Lett. 119 (2017) 072002. arXiv:1612.08026 [hep-ph].
[34] R. Boussarie, A.V. Grabovsky, L. Szymanowski, S. Wallon, J. High Energy Phys. 11 (2016) 149. arXiv:1606.00419 [hep-ph].
[35] T. Lappi, R. Paatelainen, Ann. Physics 379 (2017) 34. arXiv:1611.00497 [hep-ph].
[36] J.C. Collins, Renormalization, in: Cambridge Monographs on Mathematical Physics, vol. 26, Cambridge University Press, Cambridge, 1986.
[37] G. 't Hooft, M.J.G. Veltman, Nuclear Phys. B 44 (1972) 189.
[38] W. Siegel, Phys. Lett. 84B (1979) 193.
[39] Z. Bern, D.A. Kosower, Nuclear Phys. B 379 (1992) 451.
[40] Z. Bern, A. De Freitas, L.J. Dixon, H.L. Wong, Phys. Rev. D 66 (2002) 085002. arXiv:hep-ph/0202271 [hep-ph].
[41] H. Weigert, Prog. Part. Nucl. Phys. 55 (2005) 461. arXiv:hep-ph/0501087.
[42] J.A.M. Vermaseren, arXiv:math-ph/0010025 [math-ph].
[43] V. Shtabovenko, R. Mertig, F. Orellana, Phys. Commun. 207 (2016) 432. arXiv:1601.01167 [hep-ph].

III

COLOR GLASS CONDENSATE AT NEXT-TO-LEADING ORDER MEETS HERA DATA

by

G. Beuf, H. Hänninen, T. Lappi and H. Mäntysaari 2020

Physical Review D 102, 074028

DOI: 10.1103/PhysRevD.102.074028

Color glass condensate at next-to-leading order meets HERA data

G. Beuf

Department of Physics, University of Jyväskylä, P.O. Box 35, 40014 University of Jyväskylä, Finland and Helsinki Institute of Physics, P.O. Box 64, 00014 University of Helsinki, Finland and National Centre for Nuclear Research, 02-093, Warsaw, Poland

H. Hänninen, T. Lappi, and H. Mäntysaari

Department of Physics, University of Jyväskylä, P.O. Box 35, 40014 University of Jyväskylä, Finland and Helsinki Institute of Physics, P.O. Box 64, 00014 University of Helsinki, Finland

(Received 30 July 2020; accepted 24 September 2020; published 30 October 2020)

We perform the first dipole picture fit to HERA inclusive cross section data using the full next-to-leading order (NLO) impact factor combined with an improved Balitsky-Kovchegov evolution including the dominant effects beyond leading logarithmic accuracy at low x. We find that three different formulations of the evolution equation that have been proposed in the recent literature result in a very similar description of HERA data and robust predictions for future deep inelastic scattering experiments. We find evidence pointing toward a significant nonperturbative contribution to the structure function for light quarks, which stresses the need to extend the NLO impact factor calculation to massive quarks.

DOI: 10.1103/PhysRevD.102.074028

I. INTRODUCTION

The inner structure of protons and nuclei can be accurately determined in deep inelastic scattering (DIS) experiments, where the target structure is probed by a simple pointlike electron via the exchange of a virtual photon. For proton targets, the combined structure function data from the H1 and ZEUS experiments at HERA [1–4] have made it possible to extract the parton densities with an excellent precision.

At small momentum fraction x the gluon densities rise rapidly, and one eventually expects nonlinear high-occupancy effects to be important and become visible in the weak coupling regime. At high gluon densities, these nonlinear effects tame the growth of the gluon density, and a dynamical scale known as the saturation scale Q_s^2 is generated. This scale characterizes the region of phase space where the nonlinear saturation effects dominate. To describe QCD in this high-energy regime an effective theory known as the color glass condensate (CGC) has been developed; see Refs. [5,6] for a review.

The precise DIS data can provide a crucial test for the saturation picture. Theoretically the inclusive DIS cross section is a relatively simple observable, as the probe has no internal structure and one does not need to consider e.g., fragmentation effects. As the proton structure is not perturbatively calculable, some input from experimental data is needed. In the CGC framework, one can calculate the energy dependence of various observables, e.g., the total photon-proton cross section, perturbatively by resumming contributions enhanced by a large logarithms of energy or $\ln 1/x$. The nonperturbative input in this case is the proton structure at an initial (and smallish) Bjorken x, which is a parametrized input fitted to the data. The leading-order CGC calculations have been able to obtain a good description of the precise HERA data by fitting the initial condition with only a few free parameters [7–9]. However, in all these fits one needs to introduce an additional fit parameter to slow down the x evolution to be compatible with the HERA measurements.

To precisely test the saturation picture of CGC, it is crucial to move beyond leading-order accuracy. In recent years the theory has been rapidly developing toward full next-to-leading-order (NLO) accuracy. The impact factors, describing the photon-proton interaction, have been calculated at this order in case of massless quarks [10–15], and the first numerical results were reported in Ref. [16]. The impact factors need to be combined with evolution equations that describe the Bjorken-x dependence and resum contributions enhanced by large logarithms of energy, $(\alpha_s \ln 1/x)^n$ at leading order and $\alpha_s(\alpha_s \ln 1/x)^n$ at next-to-leading order. The Balitsky-Kovchegov (BK) equation describing the evolution of the dipole-target interaction [17,18] is available at NLO accuracy [19] with the higher-order contributions enhanced by large transverse logarithms

resummed in Refs. [20–23] and numerical solutions reported in Refs. [24,25].

An additional complication in the small-x evolution is that the Coulomb tails obtained from a perturbative calculation result in the proton size growing much faster than seen in the data and faster than suggested by the Froissart bound [26] for hadronic collisions. It has been argued [27,28] on the theoretical level that including some nonperturbative damping of the gluon emission at large transverse distance is necessary and sufficient to recover a Froissart behavior for the virtual photon-proton cross section. This idea has been studied [29,30] in fits to the HERA data using the impact-parameter-dependent BK equation supplemented by either a nonperturbative cutoff or collinear resummations. In addition to the BK equation, one can solve the more general Jalilian-Marian–Iancu–McLerran–Weigert–Leonidov–Kovner (JIMWLK) evolution equation [31–37] (available at NLO accuracy [38,39], but no numerical solution exists for the NLO equation). The JIMWLK evolved proton structure was compared with the HERA data in Ref. [40] (see also Refs. [41,42]), where again large nonperturbative contributions were needed to describe the system with a finite proton geometry. Due to these additional complications, we only study an impact-parameter-independent evolution here and assume that the transverse area of the proton can be factorized in the cross section calculations.

In addition to testing the saturation conjecture, an accurate description of the DIS data is important for other phenomenological applications. As we will discuss later, the DIS cross section is written in terms of the quark dipole-target scattering amplitude. The exactly same degrees of freedom are needed to describe other scattering processes, such as particle production in proton-nucleus collisions (see e.g., [9,43–53]) or diffractive DIS (e.g., [54–62]). Although most of the current phenomenological applications are performed at leading-order accuracy, the NLO calculations are developing rapidly [63–74]. A necessary input for the phenomenological applications at NLO accuracy is the initial condition for the NLO evolution, which can be obtained by fitting the DIS data as presented in this paper.

This paper is structured as follows. First, in Sec. II, we will briefly introduce the dipole picture of DIS at leading and next-to-leading order. Then, in Sec. III, we will review the necessary details of the different variants of the BK equation used in this work. Section IV reviews the datasets used in the fits, and Sec. V discusses the results of the fits.

II. DEEP INELASTIC SCATTERING IN THE DIPOLE PICTURE AT NLO

The photon-proton cross section is parametrized in terms of the structure functions F_2 and F_L, that are related to the virtual photon-proton cross sections $\sigma^{\gamma^* p}$ as

$$F_2(x_{\mathrm{Bj}}, Q^2) = \frac{Q^2}{4\pi^2\alpha_{\mathrm{em}}}(\sigma_L^{\gamma^* p} + \sigma_T^{\gamma^* p}) \tag{1}$$

and

$$F_L(x_{\mathrm{Bj}}, Q^2) = \frac{Q^2}{4\pi^2\alpha_{\mathrm{em}}}\sigma_L^{\gamma^* p}. \tag{2}$$

Here the subscripts T and L refer to the transverse and longitudinal polarizations, respectively, of the virtual photon. The experimental data are often reported as a reduced cross section:

$$\sigma_r(x_{\mathrm{Bj}}, y, Q^2) = F_2(x_{\mathrm{Bj}}, Q^2) - \frac{y^2}{1+(1-y)^2}F_L(x_{\mathrm{Bj}}, Q^2). \tag{3}$$

Here $-Q^2$ is the photon virtuality, x_{Bj} is the Bjorken variable and y is the inelasticity.

The focus in this paper is on the next-to-leading-order corrections to the total DIS cross section in the dipole picture. As an introduction, let us first briefly describe the process in the leading-order dipole picture.

At leading order, the virtual photon-proton scattering in the dipole picture is understood in the following way (see e.g., [75]). First, the incoming photon fluctuates into a quark-antiquark pair. This splitting is described by the photon light-cone wave function $\psi^{\gamma^* \to q\bar{q}}$. Subsequently, the produced dipole interacts with the target. At high energy, the quark-target interaction is eikonal, and the transverse position of the quark does not change during the scattering. Instead, the quark goes through a color rotation in the target color field and picks up a Wilson line $V(\mathbf{x}_0)$ in the fundamental representation, where $\mathbf{x}_0$ is the transverse coordinate of the quark. Similarly, the antiquark at point $\mathbf{x}_1$ picks up a conjugate Wilson line $V^\dagger(\mathbf{x}_1)$.

To calculate the total cross section, one applies the optical theorem and calculates the imaginary part of the forward elastic scattering amplitude for the process $\gamma^* p \to \gamma^* p$. The resulting cross section reads

$$\sigma_{T,L}^{\gamma^* p} = 2\int \mathrm{d}^2\mathbf{b}\mathrm{d}^2\mathbf{r}\mathrm{d}z|\psi^{\gamma^* \to q\bar{q}}(\mathbf{r}, Q^2, z)|^2 \times (1 - S(\mathbf{r}, \mathbf{b}, x)). \tag{4}$$

Here, z is the light-cone momentum fraction of the photon carried by the quark. The dipole size is $\mathbf{r} = \mathbf{x}_0 - \mathbf{x}_1$ and its impact parameter is $\mathbf{b} = (\mathbf{x}_0 + \mathbf{x}_1)/2$. In the following, $S(\mathbf{r}, \mathbf{b}, x)$ is assumed to depend only slowly on $\mathbf{b}$. Thus we will drop this dependence on $\mathbf{b}$ and replace the integration over $\mathbf{b}$ by a constant $\int \mathrm{d}^2\mathbf{b} \to \sigma_0/2$. The dipole scattering matrix S is defined as a two-point function of the Wilson lines that the quarks pick up in the scattering process:

$$S(\mathbf{r},\mathbf{b},x) \equiv \left\langle \frac{1}{N_c}\mathrm{Tr}V(\mathbf{x}_0)V^\dagger(\mathbf{x}_1)\right\rangle_x. \tag{5}$$

The brackets $\langle\rangle$ refer to the average over the target color charge configurations. Here the momentum fraction x in the subscript stands for the fact that the Wilson lines are evaluated at some energy or rapidity scale corresponding to the kinematics of the process. This dependence is given by the Balitsky-Kovchegov equation which, at leading order, is usually used to evolve the Wilson lines up to an evolution rapidity $Y = \log 1/x_{\mathrm{Bj}}$. At NLO the question of the evolution rapidity becomes more complicated, as discussed in more detail in Sec. III.

At NLO the virtual photon-proton scattering involves Fock states of the photon that contain a gluon in addition to the quark and antiquark, which all scatter off the target. There are also other NLO contributions with only a quark-antiquark Fock state scattering off the target, which include a gluon loop correction to the photon splitting. These NLO $q\bar{q}g$ and $q\bar{q}$ contributions have been calculated independently using the conventional dimensional regularization [13,14] and four-dimensional helicity schemes [15]. The individual diagrams contain UV divergences that cancel each other in the sum. On top of these, there remains a divergence related to low-x gluons, which must be resummed into the evolution of the target. Subtraction schemes for this low-x gluon divergence in DIS were devised and tested in Refs. [14,16], and in our present paper we continue to refine the "unsub" scheme to enable a comparison between the theory and experimental data.

In Refs. [14,16] the low-x gluon divergence factorization from the NLO DIS cross sections (for a more detailed discussion in the context of single inclusive particle production see Refs. [67,76,77]) were written in two distinct but equivalent forms: a form where the factorization is implicit, and another where it was made explicit, named "unsubtracted" and "subtracted" schemes, respectively. In this work we use the unsubtracted form for the cross sections, which can be expressed as

$$\sigma_{L,T}^{\mathrm{NLO}} = \sigma_{L,T}^{\mathrm{IC}} + \sigma_{L,T}^{\mathrm{dip}} + \sigma_{L,T}^{qg,\mathrm{unsub}}. \tag{6}$$

Here the first term is the leading-order cross section (4) where the dipole scattering amplitude is evaluated at the chosen fixed initial rapidity scale of the target, corresponding to the initial condition of BK evolution. The other terms can be interpreted as arising from the NLO $q\bar{q}$ diagrams ($\sigma_{L,T}^{\mathrm{dip}}$) and from the NLO $q\bar{q}g$ diagrams ($\sigma_{L,T}^{qg,\mathrm{unsub}}$), up to subtraction terms used to make the cancellation of UV divergences between these diagrams explicit. In our scheme, the unsubtracted qg term is

$$\sigma_{L,T}^{qg,\mathrm{unsub}} = 8N_c\alpha_{\mathrm{em}}\frac{\alpha_s C_F}{\pi}\sum_f e_f^2\int_0^1 \mathrm{d}z_1\int_{z_{2,\min}}^{1-z_1}\frac{\mathrm{d}z_2}{z_2}\int_{\mathbf{x}_0,\mathbf{x}_1,\mathbf{x}_2}\mathcal{K}_{L,T}^{\mathrm{NLO}}(z_1,z_2,\mathbf{x}_0,\mathbf{x}_1,\mathbf{x}_2), \tag{7}$$

and the dipole term is

$$\sigma_{L,T}^{\mathrm{dip}} = 4N_c\alpha_{em}\frac{\alpha_s C_F}{\pi}\sum_f e_f^2\int_0^1 \mathrm{d}z_1\int_{\mathbf{x}_0,\mathbf{x}_1}\mathcal{K}_{L,T}^{\mathrm{LO}}(z_1,\mathbf{x}_0,\mathbf{x}_1)\left[\frac{1}{2}\ln^2\left(\frac{z_1}{1-z_1}\right)-\frac{\pi^2}{6}+\frac{5}{2}\right], \tag{8}$$

with the shorthand $\int_{\mathbf{x}_i} \coloneqq \int\frac{\mathrm{d}^2\mathbf{x}_i}{2\pi}$. The integrand kernels and dipole operators for the leading-order and dipole terms are

$$\mathcal{K}_L^{\mathrm{LO}}(z_1,\mathbf{x}_0,\mathbf{x}_1) = 4Q^2z_1^2(1-z_1)^2K_0^2(QX_2)(1-S(\mathbf{x}_{01})), \tag{9}$$

$$\mathcal{K}_T^{\mathrm{LO}}(z_1,\mathbf{x}_0,\mathbf{x}_1) = Q^2z_1(1-z_1)(z_1^2+(1-z_1)^2)K_1^2(QX_2)(1-S(\mathbf{x}_{01})), \tag{10}$$

where $X_2^2 \equiv z_1(1-z_1)\mathbf{x}_{01}^2$, $\mathbf{x}_{ij} \equiv \mathbf{x}_i - \mathbf{x}_j$ and $S(\mathbf{x}_{ij}) \equiv S(\mathbf{x}_{ij},\mathbf{b})$. Here, the rapidity scale which the dipole operator (5) is evaluated at is left implicit. It will be discussed together with the associated small-x evolution in Sec. III. However, we note already now that in the qg term this rapidity scale must be taken to depend on the gluon momentum fraction z_2, not just the external kinematical scales x_{Bj} and Q^2. This is essential for the stability of the factorization scheme, as discussed in great detail e.g., in Refs. [16,20,67,76,77].

For the qg terms that only appear at NLO, the kernels and Wilson line operators are

$$\mathcal{K}_L^{\mathrm{NLO}}(z_1,z_2,\mathbf{x}_0,\mathbf{x}_1,\mathbf{x}_2) = 4Q^2 z_1^2(1-z_1)^2\Bigg\{P\left(\frac{z_2}{1-z_1}\right)\frac{\mathbf{x}_{20}}{\mathbf{x}_{20}^2}\cdot\left(\frac{\mathbf{x}_{20}}{\mathbf{x}_{20}^2}-\frac{\mathbf{x}_{21}}{\mathbf{x}_{21}^2}\right)[K_0^2(QX_3)(1-S_{012})-(\mathbf{x}_2\to\mathbf{x}_0)] + \left(\frac{z_2}{1-z_1}\right)^2\frac{\mathbf{x}_{20}\cdot\mathbf{x}_{21}}{\mathbf{x}_{20}^2\mathbf{x}_{21}^2}K_0^2(QX_3)(1-S_{012})\Bigg\}, \tag{11}$$

$$\mathcal{K}_T^{\mathrm{NLO}}(z_1,z_2,\mathbf{x}_0,\mathbf{x}_1,\mathbf{x}_2) = Q^2 z_1(1-z_1)\Bigg\{P\left(\frac{z_2}{1-z_1}\right)(z_1^2+(1-z_1)^2)\frac{\mathbf{x}_{20}}{\mathbf{x}_{20}^2}\cdot\left(\frac{\mathbf{x}_{20}}{\mathbf{x}_{20}^2}-\frac{\mathbf{x}_{21}}{\mathbf{x}_{21}^2}\right)[K_1^2(QX_3)(1-S_{012})-(\mathbf{x}_2\to\mathbf{x}_0)] + \left(\frac{z_2}{1-z_1}\right)^2\left[(z_1^2+(1-z_1)^2)\frac{\mathbf{x}_{20}\cdot\mathbf{x}_{21}}{\mathbf{x}_{20}^2\mathbf{x}_{21}^2}+2z_0z_1\frac{\mathbf{x}_{20}\cdot\mathbf{x}_{21}}{\mathbf{x}_{20}^2X_3^2}-\frac{z_0(z_1+z_2)}{X_3^2}\right]K_1^2(QX_3)(1-S_{012})\Bigg\}. \tag{12}$$

Here z_0, z_1, and z_2 are the longitudinal momentum fractions of the quark, antiquark, and gluon, respectively, which satisfy $\sum_i z_i = 1$. The parton configuration factor QX_3 is interpreted as the ratio of the $q\bar{q}g$ state formation time to the γ^* lifetime [12]. It is defined as $X_3^2 := z_0z_1\mathbf{x}_{01}^2 + z_0z_2\mathbf{x}_{02}^2 + z_2z_1\mathbf{x}_{21}^2$. We have also defined a shorthand $P(z) := 1+(1-z)^2$. The $q\bar{q}g$ state-target scattering Wilson line operator is

$$S_{012} \equiv \frac{N_c}{2C_F}\left(S(\mathbf{x}_{02})S(\mathbf{x}_{21}) - \frac{1}{N_c{}^2}S(\mathbf{x}_{01})\right). \tag{13}$$

In Eq. (7) the lower limit $z_{2,\mathrm{min}}$ in the gluon longitudinal momentum fraction integral is yet undefined, and its proper value will be discussed in the next section.

III. HIGH-ENERGY EVOLUTION

A. Balitsky-Kovchegov equation

In the calculation of the photon-proton cross section at NLO, as discussed above, the dipole-target scattering amplitude depends on the energy or, equivalently, on Bjorken x. In the large N_c limit, the evolution is given by the BK equation [17,18]. At leading order, the BK equation reads

$$\frac{\partial S(\mathbf{x}_{01})}{\partial Y} = \int \mathrm{d}^2\mathbf{x}_2 K_{\mathrm{BK}}(\mathbf{x}_0,\mathbf{x}_1,\mathbf{x}_2) \times [S(\mathbf{x}_{02})S(\mathbf{x}_{21}) - S(\mathbf{x}_{01})]. \tag{14}$$

The kernel K_{BK} is proportional to the probability density to emit a gluon with transverse coordinate $\mathbf{x}_2$ from the dipole of size $\mathbf{x}_{01} = \mathbf{x}_0 - \mathbf{x}_1$. The evolution rapidity Y is discussed in detail later. When running coupling corrections following the Balitsky prescription [78] are included, it reads

$$K_{\mathrm{BK}}(\mathbf{x}_0,\mathbf{x}_1,\mathbf{x}_2) = \frac{N_c\alpha_s(\mathbf{x}_{01}^2)}{2\pi^2}\left[\frac{\mathbf{x}_{01}^2}{\mathbf{x}_{12}^2\mathbf{x}_{02}^2} + \frac{1}{\mathbf{x}_{02}^2}\left(\frac{\alpha_s(\mathbf{x}_{02}^2)}{\alpha_s(\mathbf{x}_{12}^2)}-1\right) + \frac{1}{\mathbf{x}_{12}^2}\left(\frac{\alpha_s(\mathbf{x}_{12}^2)}{\alpha_s(\mathbf{x}_{02}^2)}-1\right)\right]. \tag{15}$$

In principle we should use the next-to-leading-order BK equation when using the impact factors calculated to the order α_s. The required numerical solution of the NLO BK equation exists [24,25,79]. However, the equation is numerically burdensome due to the high-dimensional transverse integration (in the NLO BK equation one integrates over the transverse coordinates of the two emitted gluons, instead of just one gluon in the leading-order equation). Instead of the full equation, in this work we use prescriptions of BK evolution that capture an important subset of beyond leading-order effects. The difference between the studied evolutions reflects some of the uncertainty due to the missing full NLO evolution.

In practice we have chosen three related formulations of the BK equation that resum some or all of the large transverse momentum logarithms in the NLO equation. Firstly we consider the nonlocal evolution equation in terms of the projectile momentum fraction introduced in Ref. [20], where collinear double logarithms are resummed via the inclusion of a kinematical constraint: we denote this the KCBK equation. Secondly, we consider the local equation in the projectile momentum fraction of Ref. [21], where the same double logarithms, together with Dokshitzer-Gribov-Lipatov-Altarelli-Parisi (DGLAP)-like single logarithms, are explicitly resummed into a kernel that is a nontrivial function of α_s: we call this the ResumBK equation. Thirdly we study a nonlocal equation in the target momentum fraction, recently formulated in Ref. [23] and denoted here as the TBK equation. The first two are formulated in terms of the projectile momentum fraction, so that the rapiditylike

evolution variable in the BK equation is defined by the momentum fraction of the probe or, equivalently, by the plus component of the 4-momentum.[1] Since the projectile momentum fraction is the variable appearing explicitly in the NLO DIS impact factors, using these evolution equations is fairly straightforward. However the fact that the TBK equation is written in terms of the target momentum fraction, i.e., the minus component of 4-momentum, means that the evolution and the perturbative impact factors can only be matched approximatively, and the procedure requires more care.

As we will discuss in detail in the following, we solve the BK equation by taking a parametrized dipole amplitude as an initial condition at an initial rapidity scale. Starting from this initial condition the evolution predicts the behavior of the dipole at higher rapidities, i.e., energies, or correspondingly at smaller Bjorken x. The phase space available for the emission of the gluon grows with energy and determines the amount of BK evolution. Thus the evolution range is controlled by the lower limit of the gluon momentum fraction $z_{2,\min}$ in Eq. (7), with a smaller lower limit corresponding to longer evolution.

B. Evolution in projectile momentum fraction

Let us first consider the evolution written in projectile momentum fraction, which is the case for the KCBK and ResumBK equations. In this case the high-energy evolution is parametrized by the rapidity variable Y, which is defined using the plus components of the gluon momentum k^+ and a plus momentum scale P^+ associated with the target as

$$Y \equiv \ln\left(\frac{k^+}{P^+}\right). \tag{16}$$

Since the incoming photon energy q^+ (which is the maximal k^+) in the target rest frame is proportional to the photon-target c.m.s. energy W^2, one should think of evolution in the rapidity variable Y as evolution in $\ln W^2$, as we will see more explicitly below.

In the impact factor, Eq. (7), the gluon momentum is parametrized by the momentum fraction z_2 as $k^+ = z_2 q^+$. Both the probe momentum fraction evolution equations and the NLO impact factor are derived in terms of the same z_2. Thus it is straightforward to see that the dipole operators in the evaluation of the qg term in the cross section (7) are always evaluated at the projectile rapidity

$$Y = \ln z_2 + \ln\left(\frac{q^+}{P^+}\right), \tag{17}$$

depending on the integration variable z_2. We will specify the value of P^+ below.

First, we have to determine the lower limit $z_{2,\min}$ for the z_2 integral in the NLO impact factor, Eq. (7), which controls the amount of evolution. This limit is set by the overall kinematics of the process. One way to understand the existence of this limit is to note that in the limit $z_2 \to 0$ the invariant mass of the $q\bar{q}g$ system interacting with the target grows as $M^2_{q\bar{q}g} \sim 1/z_2$. The fact that this invariant mass cannot be larger than the c.m.s. collision energy results in a lower limit for kinematically allowed values of z_2. Since the validity of the eikonal approximation used to derive the dipole picture cross section requires in principle $M^2_{q\bar{q}g} \ll W^2$, one could require a more strict limit on z_2 than resulting from purely kinematics. Thus there is a choice in how close to the kinematical limit one allows the integral to go, which we quantify by the parameter $e^{Y_{0,\mathrm{if}}} \gtrsim 1$. In terms of this parameter we have the limit

$$z_2 q^+ > e^{Y_{0,\mathrm{if}}} P^+ = e^{Y_{0,\mathrm{if}}} \frac{Q_0^2}{2P^-} = e^{Y_{0,\mathrm{if}}} x_{\mathrm{Bj}} \frac{Q_0^2}{Q^2} q^+,$$
$$z_2 > e^{Y_{0,\mathrm{if}}} x_{\mathrm{Bj}} \frac{Q_0^2}{Q^2} \approx e^{Y_{0,\mathrm{if}}} \frac{Q_0^2}{W^2} \equiv z_{2,\min}. \tag{18}$$

Here we have introduced a nonperturbative target transverse momentum scale Q_0^2, for which in this work we use the value[2] $Q_0^2 = 1\ \mathrm{GeV}^2$. This allows us to write $P^+ = Q_0^2/(2P^-)$, and we used the fact that $x_{\mathrm{Bj}} = Q^2/(2P \cdot q) = Q^2/(2P^- q^+)$. This limit is already derived e.g., in Refs. [14,16,20]. In Ref. [16] the authors for simplicity set $Q_0^2/Q^2 = 1$ in practical evaluations of the NLO impact factors.

In principle also the limits $z_1 \to 0$, $z_1 \to 1$ in Eqs. (7) and (8) correspond to the invariant mass of the scattering state becoming infinite, similarly to the limit $z_2 \to 0$. Thus, as discussed in Ref. [14], one could also take the energy or rapidity scale at which the dipoles are evaluated to depend on the (anti)quark momentum fractions z_0, z_1 (see also Ref. [80]). This part of phase space does not, however, generate a contribution enhanced by a large logarithm of x to the cross section. Instead, this "aligned jet" configuration produces a large collinear logarithm which in principle should be included in the DGLAP evolution not included in the dipole picture applied in this work. Properly including this collinear logarithm is an important issue but separate from the factorization to the BK equation and is left for future work.

[1] We work in a frame where the target has a large minus momentum P^-, and the incoming photon has a large plus momentum q^+.

[2] Note that the two parameters $Y_{0,\mathrm{if}}$ and Q_0 only appear in one combination $e^{Y_{0,\mathrm{if}}} Q_0^2$ here; thus there is really only one independent parameter characterizing the limit $z_{2,\min}$. However, for the discussion that follows it is better to think in terms of a separate nonperturbative transverse momentum scale Q_0.

When the Bjorken x of the process is such that the smallest momentum fraction $z_{2,\min}$ is close to 1, i.e., when $x_{\mathrm{Bj}} \sim e^{-Y_{0,\mathrm{if}}}$ (with $Q^2 \sim Q_0^2$), the possible phase space for real gluon emission allowed in the expression for the cross section vanishes. Thus the qg contribution to the NLO cross section goes to zero at $x_{\mathrm{Bj}} \sim e^{-Y_{0,\mathrm{if}}}$ by construction. The NLO calculation does not fix any exact value for $Y_{0,\mathrm{if}}$. A possible choice to consider for $Y_{0,\mathrm{if}}$ would be to take $Y_{0,\mathrm{if}} \approx \ln 1/0.01$, corresponding to the limit where the dipole picture is usually considered applicable. This was the choice used in Ref. [16]. However, this choice leads to a transient effect in the NLO cross sections at the upper end of the x_{Bj} range $x_{\mathrm{Bj}} \sim e^{-Y_{0,\mathrm{if}}}$ since the positive virtual correction remains large, while the negative qg contribution vanishes, as demonstrated in Ref. [16].

To avoid this unphysical transient effect, we adopt here instead the maximal (or minimal depending on the point of view) choice $Y_{0,\mathrm{if}} = 0$. This means that the integral over z_2 in the cross section extends all the way to the kinematical limit, outside of the validity of the eikonal approximation. The contribution from this region is, however, only a parametrically small part of the cross section for small x_{Bj}, which is where we are comparing the cross section to experimental data. Also, since there is a cancellation between the real and virtual contributions to the cross section, and the latter includes a z_2 integral over the full range $0 < z_2 < 1$, one could in fact argue that this choice minimizes the net effect of very large invariant mass states in the photon on the cross section.

The above discussion only applies to the qg term (7) in the cross section. The virtual correction in Eq. (8) is already integrated over z_2 and cannot be evaluated at a z_2-dependent rapidity. Thus for this term dipole operators are taken to be independent of z_2 and evaluated at rapidity $Y = \ln 1/x_{\mathrm{Bj}}$. Using a z_2-independent dipole is justified, as the region $z_2 \ll 1$ gives only a negligible contribution to the virtual correction. Including these formally subleading effects, namely the z_2-dependent dipole operator, in the virtual term and improving the approximation $Y \approx \ln 1/x_{\mathrm{Bj}}$ is left for future work.

The choice $Y_{0,\mathrm{if}} = 0$ removes the unphysical transient effect, but it forces us to confront another problem that the earlier formulation of Ref. [16] wanted to avoid by choosing a larger $Y_{0,\mathrm{if}}$. Namely, at the lower end of the z_2 range we are forced to evaluate also the (BK-evolved) dipoles at a rapidity scale that is lower (or x_{Bj} scale that is higher) than where the BK equation is normally used. Now we again have different options regarding the rapidity where we start the BK evolution. We parametrize this choice by another constant $Y_{0,\mathrm{BK}}$, whose value can also be chosen in different ways.

One way is to take $Y_{0,\mathrm{BK}} = Y_{0,\mathrm{if}} = 0$, in which case we simply start the BK evolution much earlier (much higher x_{Bj}) than where we are actually calculating the cross section. Here the contribution of the unphysical small rapidity or large x phase space to the cross section (7) is suppressed, because target gets more and more dilute following the evolution backward to smaller rapidities. This procedure changes the way the parametrization of the initial condition for the BK evolution should be interpreted. In this approach, the quantity that can meaningfully be compared to the initial dipole amplitude at $x = x_0 \sim 0.01$ in LO fits is not the actual initial condition at $Y = Y_{0,\mathrm{BK}} = 0$, but the result obtained after $Y = \ln 1/0.01$ units of rapidity evolution.

Another option is to take a more typical initial energy scale for the BK equation, which we here take as $Y_{0,\mathrm{BK}} = \ln 1/0.01$. In this latter case one has to model the dipole amplitude in the region $Y_{0,\mathrm{if}} < Y < Y_{0,\mathrm{BK}}$. In this case, we simply assume that the dipole operator is independent of Y in this region, which is "before the initial condition" in Y. Assuming an energy-independent dipole amplitude in this region is consistent within the accuracy of the framework.

To summarize, we have two parameters that we must choose, $Y_{0,\mathrm{if}}$ and $Y_{0,\mathrm{BK}}$. In this work we always take $Y_{0,\mathrm{if}} = 0$ to avoid the large transient effect at $x_{\mathrm{Bj}} \sim e^{-Y_{0,\mathrm{if}}}$ in the data region. We then apply two approaches for the parameter $Y_{0,\mathrm{BK}}$. The first option is to start the BK evolution at rapidity $Y_{0,\mathrm{BK}} = \ln 1/0.01$ and freeze the dipole amplitude at $Y < Y_{0,\mathrm{BK}}$. The second option is to also start the BK evolution at rapidity $Y_{0,\mathrm{BK}} = Y_{0,\mathrm{if}} = 0$.

We recall that the dipole amplitudes in the cross section Eq. (7) are evaluated at a rapidity

$$Y \equiv \ln \frac{k^+}{P^+} = \ln \frac{W^2 z_2}{Q_0^2}. \tag{19}$$

Note that the maximum rapidity $Y_{\max}$ encountered is obtained at the $z_2 \to 1$ limit

$$Y_{\max} = \ln \frac{W^2}{Q_0^2} = \ln \frac{1}{z_{2,\min}} + Y_{0,\mathrm{if}}, \tag{20}$$

corresponding to values of Y probed by the z_2 integral in the cross section ranging from $Y_{0,\mathrm{if}}$ to $Y_{\max}$, i.e., over a rapidity interval $\Delta Y = \ln 1/z_{2,\min}$. When $Y_{0,\mathrm{BK}} > Y_{0,\mathrm{if}}$, the actual range of BK evolution is smaller by $Y_{0,\mathrm{BK}}$, and for $Y_{0,\mathrm{if}} < Y < Y_{0,\mathrm{BK}}$ the dipole does not change. We emphasize that the evolution rapidity depends only on the total center-of-mass energy W^2 and not explicitly on x_{Bj} or Q^2. This is natural, as the scattering amplitude for a dipole with a fixed transverse size can only be sensitive to the total center-of-mass energy, and strictly speaking the dipole does not exactly know about the photon virtuality or the Bjorken x.

C. Kinematically constrained BK

As discussed previously, in order to keep the computational cost of the fit procedure manageable, we do not use the full NLO BK equation to obtain the rapidity dependence of the dipole scattering matrix S. Instead, we use modified versions of the leading-order evolution equation that resums the most important higher-order corrections, in particular the collinear double logarithms.

First, we use the KCBK equation [20] that is nonlocal in the projectile momentum fraction (i.e., the evolution variable Y):

$$\begin{aligned}&\partial_Y S(\mathbf{x}_{01}, Y)\\ &= \int \mathrm{d}^2\mathbf{x}_2 K_{\mathrm{BK}}(\mathbf{x}_0, \mathbf{x}_1, \mathbf{x}_2)\theta(Y - \Delta_{012} - Y_{0,\mathrm{if}})\\ &\quad \times [S(\mathbf{x}_{02}, Y - \Delta_{012})S(\mathbf{x}_{21}, Y - \Delta_{012}) - S(\mathbf{x}_{01}, Y)] \end{aligned} \tag{21}$$

with

$$\Delta_{012} = \max\left\{0, \ln\frac{\min\{\mathbf{x}_{02}^2, \mathbf{x}_{21}^2\}}{\mathbf{x}_{01}^2}\right\}. \tag{22}$$

This equation explicitly forces time ordering between subsequent gluon emissions. The theta function ensures that only dipoles in the range $Y > Y_{0,\mathrm{if}}$ are included.

D. Rapidity local resummed BK

The most important higher-order corrections to the BK equation that are enhanced by double large transverse logarithms can be resummed alternatively into a kernel that is local in the evolution rapidity Y by a method introduced in Ref. [21].[3] This procedure resums exactly the same contributions that are included in Ref. [20] to derive the kinematically constrained BK equation shown above in Eq. (21). A practical advantage of the approach taken in Ref. [21] is that the resulting equation is local in evolution (projectile) rapidity, and as such numerically easier to solve using standard Runge-Kutta methods. In addition to the double transverse logarithms resummation, the contribution of some of the single transverse logarithms present in the NLO BK equation can be included following Ref. [22], keeping the equation local in rapidity. In Ref. [81] it was shown that this resummed BK equation is in practice close to the kinematically constrained BK equation discussed previously. As the resulting resummed evolution equation is written in terms of the projectile rapidity Y, it can be used with the impact factors exactly as the kinematically constrained BK equation.

The resummed equation is obtained by multiplying the BK kernel (15) by $K_{\mathrm{DLA}}K_{\mathrm{STL}}$, where K_{DLA} is a resummation of double and K_{STL} single transverse logarithms. The kernel resumming the double transverse logarithms reads

$$K_{\mathrm{DLA}} = \frac{J_1(2\sqrt{\bar{\alpha}_s x^2})}{\sqrt{\bar{\alpha}_s x^2}}, \tag{23}$$

with $x = \sqrt{\ln \mathbf{x}_{02}^2/\mathbf{x}_{01}^2 \ln \mathbf{x}_{12}^2/\mathbf{x}_{01}^2}$ and $\bar{\alpha}_s = \alpha_s N_c/\pi$. If $\ln \mathbf{x}_{02}^2/\mathbf{x}_{01}^2 \ln \mathbf{x}_{12}^2/\mathbf{x}_{01}^2 < 0$, an absolute value of the argument is used and the Bessel function is changed to $J_1 \to I_1$; see Ref. [21]. The single transverse logarithms $\sim\alpha_s \ln 1/(\mathbf{x}_{ij}^2 Q_s^2)$ are included multiplying the kernel multiplied by

$$K_{\mathrm{STL}} = \exp\left\{-\frac{\alpha_s N_c A_1}{\pi}\left|\ln\frac{C_{\mathrm{sub}}\mathbf{x}_{01}^2}{\min\{\mathbf{x}_{02}^2, \mathbf{x}_{12}^2\}}\right|\right\}. \tag{24}$$

In Ref. [25] it was shown that the resummation of single transverse logarithms can be done such that the resummed equation is a good approximation to the full NLO BK evolution by adjusting the constant C_{sub} whose numerical value is not fixed by the resummation procedure. This renders the $\mathcal{O}(\alpha_s^2)$ contributions in the NLO BK equation that are not enhanced by large (single) transverse logarithms minimal. With this procedure, one obtains a rapidity local projectile momentum fraction resummed BK equation which we use as an approximation to the full NLO BK equation (with a resummation of large transverse logarithmic corrections), with $C_{\mathrm{sub}} = 0.65$ determined in Ref. [25].

The resummation of the single transverse logarithms is completely independent of the resummation of the double transverse logarithms and thus could be included in the same way also in the other studied evolution equations. In this work, however, we only include this contribution in the ResumBK evolution, as we prefer to work with the established versions of the BK evolution. We will discuss the effect of the single transverse logarithm resummation on our fits in Sec. V.

E. Target momentum fraction evolution

As discussed in detail in Ref. [23], it is possible to formulate the evolution in terms of the target rapidity η defined as a logarithm of the minus component of the momentum. This corresponds to a fraction of the total longitudinal momentum of the target, which is the variable used in its DGLAP evolution, and also the usual physical interpretation of x_{Bj} in the parton model. In order to translate a plus momentum to a minus, one needs to have access to the correct transverse momentum scale. In the case of the whole DIS process this would naturally be Q^2. Thus we would want to define things in such a way that the largest evolution rapidity reached in the process is

[3]The double log resummation was further developed in Ref. [23]; in this work we however use the result from Ref. [21] numerically implemented in Ref. [25].

$$\eta_{\max} \sim Y_{\max} - \ln\frac{Q^2}{Q_0^2} = \ln\frac{1}{x_{\mathrm{Bj}}}, \tag{25}$$

with $Y_{\max}$ from Eq. (20). Here we see that the target rapidity η is directly related to the Bjorken x in DIS, as expected. Thus, similarly as one can think of evolution in Y as evolution in $\ln W^2$, evolution in η corresponds to evolution in $\ln 1/x_{\mathrm{Bj}}$.

The complication in using the target momentum fraction is that both the evolution equation and the impact factors are written in transverse coordinate space, which is natural for the eikonal interaction with the target. Thus the gluon transverse momentum is not very explicit in either. The usual procedure is to use an uncertainty principle argument and estimate the transverse momentum as the inverse of the corresponding transverse distance. In both the BK equation and the impact factor one integrates over transverse distances up to infinity, which would correspond to zero transverse momentum and infinite η (for a fixed Y). Distances longer than some nonperturbative scale should, however, not have a significant effect on the physics. Thus we do not want large dipoles with sizes above a (soft) target transverse momentum scale $1/Q_0^2$ (the same Q_0^2 that we have already used) to appear in the relation between the rapidities Y and η. In practice we are thus led to consider a dipole of size r at a projectile momentum fraction corresponding to Y, to have a target evolution rapidity η given by

$$\eta \equiv Y - \ln\frac{1}{\min\{1, r^2Q_0^2\}} = \ln\frac{W^2 z_2 \min\{1, r^2Q_0^2\}}{Q_0^2}. \tag{26}$$

We see that with this definition we always have $\eta < Y$, which corresponds to the fact that for perturbative size dipoles $r^2 < 1/Q_0^2$ we always have less evolution in η than in Y [see Eq. (25)].

The evolution equation for the dipole amplitude in terms of the target rapidity η was derived in Ref. [23] as[4]

$$\partial_\eta \bar{S}(\mathbf{x}_{01},\eta) = \int \mathrm{d}^2\mathbf{z} K_{\mathrm{BK}}(\mathbf{x}_0,\mathbf{x}_1,\mathbf{x}_2)\theta(\eta-\eta_{0,\mathrm{BK}}-\delta) \times [\bar{S}(\mathbf{x}_{02},\eta-\delta_{02})\bar{S}(\mathbf{x}_{21},\eta-\delta_{21}) - \bar{S}(\mathbf{x}_{01},\eta)], \tag{27}$$

where $\bar{S}$ refers to the dipole scattering matrix depending on the target rapidity η, instead of projectile rapidity Y. This evolution equation then needs to be provided with an initial condition at the initial rapidity $\eta_{0,\mathrm{BK}}$. We include running coupling corrections and use the kernel $K_{\mathrm{BK}}(\mathbf{x}_0,\mathbf{x}_1,\mathbf{x}_2)$ from Eq. (15). The rapidity shift reads

$$\delta_{kl} = \max\left\{0, \ln\frac{\mathbf{x}_{01}^2}{\mathbf{x}_{kl}^2}\right\}. \tag{28}$$

The step function with $\delta \equiv \max\{\delta_{02}, \delta_{21}\}$ ensures that the equation is a well-defined initial value problem and no information about the dipole amplitude for $\eta < \eta_{0,\mathrm{BK}}$ affects the evolution. When calculating the cross section, we use $\bar{S}(\mathbf{r},\eta) = \bar{S}(\mathbf{r},\eta_{0,\mathrm{BK}})$ for $\eta < \eta_{0,\mathrm{BK}}$.

Equation (27) is the "canonical" BK equation from [23], which contains an all-order resummation of the double collinear logarithm enhanced corrections, and thus is perturbatively correct up to an error of $\mathcal{O}(\bar{\alpha}_s^2)$. The full NLO BK evolution in target rapidity has not been solved numerically so it is not known in practice how well this resummation captures the NLO effects. In Ref. [23] a comparison is made between two formulations of the equation with double logarithm resummations, and the differences are minor and mostly in the early evolution. The resummed evolution is also compared to the LO BK evolution formulated in target rapidity, and the resummed evolution is found to be notably slower.

To use the target rapidity dependent dipole amplitudes in the NLO impact factors, we simply need to replace the dipoles in the impact factor with the η-dependent dipoles. The rapidity argument is determined by using z_2 to obtain Y with Eq. (19), which is then transformed into η using Eq. (26), i.e.,

$$S(\mathbf{x}_{ij},Y) \to \bar{S}\left(\mathbf{x}_{ij}, \eta = Y - \ln\frac{1}{\min\{1,\mathbf{x}_{ij}^2Q_0^2\}}\right) \tag{29}$$

with Y defined in Eq. (19). The regulator ensures that the rapidity shift is always negative, consistent with the definition (26) and with the rapidity shift in the TBK evolution equation (28).

Let us finally discuss the kinematical limits in the z_2 integral and their connection to the target momentum fraction probed by the process. The lower limit $z_2 > z_{2,\min}$ of the z_2 integral (18) corresponds to the lower limit of the η values probed by the impact factor

$$\eta > Y_{0,\mathrm{if}} + \ln\ \min\{1, r^2Q_0^2\}. \tag{30}$$

With our choice $Y_{0,\mathrm{if}} = 0$ the values of η needed in the cross section always extend down to evolution rapidities before the initial condition that is imposed at $\eta_{0,\mathrm{BK}}$. In this region $\eta < \eta_{0,\mathrm{BK}}$ the dipole operators are, as in Ref. [82], just frozen to the initial value: $\bar{S}(r,\eta < \eta_{0,\mathrm{BK}}) \equiv \bar{S}(r,\eta_{0,\mathrm{BK}})$. At the upper limit $z_2 = 1$, on the other hand, the largest values of η are reached for $r > 1/Q_0$, with the range in η extending up to

$$\eta < \ln\frac{W^2}{Q_0^2}, \tag{31}$$

[4]Compared to the recent analysis in Ref. [82], we include the step function $\theta(\eta-\eta_{0,\mathrm{BK}}-\delta)$ and leave the resummation of the single transverse logarithms for future work.

which is the same as the maximum Y reached in projectile momentum fraction evolution. Here let us note two things. Firstly, the min function used in defining the target momentum fraction rapidity (26) prohibits η from getting infinitely large (which would require an infinite amount of evolution) for very large dipoles $r > 1/Q_0$ that are not expected to contribute significantly to the cross section. Secondly, the amount of evolution, or largest rapidity reached, in target momentum fraction given by x_{Bj}, as in Eq. (25), strictly speaking applies only to typical dipole sizes $r \sim 1/Q$. For larger dipoles $1/Q \lesssim r \lesssim 1/Q_0$ one actually evolves further in the target momentum fraction.

F. Running coupling

For the strong coupling constant in coordinate space we use the expression

$$\alpha_{\mathrm{s}}(\mathbf{x}_{ij}^2) = \frac{4\pi}{\beta_0 \ln\left[\left(\frac{\mu_0^2}{\Lambda_{\mathrm{QCD}}^2}\right)^{1/c} + \left(\frac{4C^2}{\mathbf{x}_{ij}^2\Lambda_{\mathrm{QCD}}^2}\right)^{1/c}\right]^c}, \tag{32}$$

with $\beta = (11N_{\mathrm{c}} - 2N_{\mathrm{F}})/3$ and $N_{\mathrm{F}} = 3$, $\Lambda_{\mathrm{QCD}} = 0.241$ GeV. The parameter C^2 controls the running coupling scale in the transverse coordinate space, i.e., $\alpha_s(k^2 \sim C^2/r^2)$. From Fourier analysis it has the expected value of $C^2 = e^{-2\gamma_E}$ [83,84]. In this work, however, we take C^2 to be a fit parameter to absorb missing nonperturbative or higher-order contributions in the modified evolution speed, similarly to previous LO fit studies [8,9]. The parameters μ_0 and c control how the coupling is frozen in the infrared, and we choose $\mu_0/\Lambda_{\mathrm{QCD}} = 2.5$ and $c = 0.2$. With this choice, the coupling freezes to $\alpha_{\mathrm{s}} = 0.762$ in the infrared.

We have performed fits with two different running coupling prescriptions. The first one is denoted *Balitsky + smallest dipole* (Bal + SD) scheme below. In this scheme, we use the Balitsky prescription from Ref. [78] in the BK evolution as in Eq. (15). In the NLO impact factor, Eq. (7), and in the terms resumming large transverse logarithms, Eqs. (23) and (24) in the ResumBK evolution equation, the scale is set by the smallest dipole

$$\alpha_{s,\mathrm{sd}}(\mathbf{x}_{01}^2, \mathbf{x}_{02}^2, \mathbf{x}_{21}^2) = \alpha_{\mathrm{s}}(\min\{\mathbf{x}_{01}^2, \mathbf{x}_{02}^2, \mathbf{x}_{21}^2\}). \tag{33}$$

Note that the Balitsky prescription reduces to the smallest dipole one when one of the dipoles is much smaller than the others. For comparison we also use another scheme denoted as *parent dipole*. Here, the scale is always set by the size of the parent dipole, both in the evolution equation and in the impact factor.

In the LO-like $\sigma_{L,T}^{\mathrm{dip}}$ term of the impact factor, Eq. (8), there are no daughter dipoles in the scattering state. For this term the smallest dipole scheme is equivalent with the parent dipole scheme.

G. Initial conditions

The initial condition for the (projectile momentum fraction) BK evolution is parametrized at rapidity $Y = Y_{0,\mathrm{BK}}$. We use the MV$^\gamma$ parametrization used previously in similar fits [7,8] and write the initial condition as

$$S(\mathbf{x}_{ij}, Y = Y_{0,\mathrm{BK}}) = \exp\left[1 - \frac{(\mathbf{x}_{ij}^2 Q_{s,0}^2)^\gamma}{4} \ln\left(\frac{1}{|\mathbf{x}_{ij}|\Lambda_{\mathrm{QCD}}} + e\right)\right]. \tag{34}$$

The fit parameters in the initial condition are Q_{s0}^2, which controls the saturation scale at the initial x, and the anomalous dimension γ, which determines the shape of the dipole amplitude at small $|\mathbf{x}_{ij}|$. We note that this parametrization results in both a negative unintegrated gluon distribution and negative particle production cross sections in proton-nucleus collisions at high transverse momenta if $\gamma > 1$. As the inclusive DIS measurements are not sensitive to asymptotically small dipoles, we do not consider our dipole amplitude to be valid in that region and as such, having an anomalous dimension $\gamma > 1$ is acceptable. The practical interpretation of γ in our fit is that it controls the shape of the dipole amplitude in the transient region $r \sim 1/Q_s$. The leading-order BK fits to HERA data generally prefer $\gamma \sim 1.1$ [8,9], and similar results were found in recent fits where the BK equation with some higher-order corrections resummed [82] was used. For a detailed discussion related to the Fourier positivity of the dipole amplitude, the reader is referred to Ref. [85].

For the local resummed projectile momentum fraction (ResumBK) evolution, the resummation should also in principle affect the initial condition [21]. However, as the initial condition is in any case a nonperturbative input, we will use the same parametrization of Eq. (34) also for solving the ResumBK equation.

For target momentum fraction evolution, the initial condition for the evolution (27) corresponds to the scattering amplitude $\tilde{S}(r, \eta = \eta_{0,\mathrm{BK}})$ at some rapidity $\eta_{0,\mathrm{BK}}$. We use the same parametrization, Eq. (34), as in the case of projectile rapidity evolution.

IV. AVAILABLE DIS DATA

The HERA experiments H1 and ZEUS have published their combined measurements for the reduced cross section σ_r in Refs. [1,2]. Additionally, the charm and bottom quark contributions to the fully inclusive data are available [3,4]. As the impact factors at next-to-leading-order accuracy in the massive quark case are not available, we only calculate the light-quark contribution to the photon-proton cross section. In the leading-order fits [8,9] it has been possible to obtain a good description of the fully inclusive data with only light quarks, even though the charm contribution is significant (parametrically up to ~40% at $Q^2 \gg m_c^2$). On

the other hand, the leading-order fits aiming to simultaneously describe the total and charm structure function data require separate parameters (e.g., different transverse areas) for the light and charm quarks [8] or an additional effective soft and nonperturbative contribution [29,40].

In this work we consider two different setups. First, we follow the strategy that has been successfully used at leading order, calculate the light-quark contribution to the structure functions, and compare with the inclusive HERA data from Ref. [1]. We note that the newer combined dataset containing data from the HERA-II run is also available [2], but at low x and moderate Q^2 the two datasets result in very similar fits (see e.g., Ref. [86]).

As a second approach, we construct an interpolated dataset that only contains the light-quark contribution. Since the charm and bottom data are not measured in the same kinematical x, Q^2 bins as the inclusive data, it is not possible to just subtract the heavy quark contribution from the fully inclusive cross section. Instead, we use a leading-order dipole model fit from Ref. [86], where the Bjorken-x and dipole size $\mathbf{r}$ dependence is described using the so-called IPsat parametrization [87]. This parametrization includes a smooth matching to the DGLAP evolution [88–91] in the dilute region, and at large dipoles or densities the scattering amplitude saturates to unity. The advantage of this parametrization is that it results in an excellent description of both inclusive and heavy quark datasets. Consequently, it can be used to interpolate the charm and bottom contributions to the structure functions. We use this parametrization to subtract the heavy quark contributions from the measured reduced cross section. We then use this interpolated light-quark-only data in the NLO fits. In our procedure we do not modify the uncertainties of the inclusive data in the subtraction (another possible approach would be to reduce the uncertainties proportionally). This is not really a consistent treatment for the errors; ultimately only the experimental collaborations would be in a position to correctly take into account the correlation between errors in the total and heavy quark data. Thus the errors and consequently χ^2 values in the light-quark fits are not correct statistically. However, we expect the magnitude of the uncertainties to only affect the final fit qualities and to have only a limited effect on the extracted best fit parameter values and the interpretation in terms of physics. This detail must be kept in mind for the interpretation of the χ^2 values from the light-quark fits.

The total reduced cross section for some Q^2 bins from HERA [1] is shown in Fig. 1 and compared with the result obtained by the IPsat fit mentioned above. The description of the data is excellent. The interpolated light-quark data in the same kinematics are also shown and compared to the light-quark reduced cross section computed using the same IPsat fit.

When fitting the initial condition for the BK evolution, we consider data points in the region

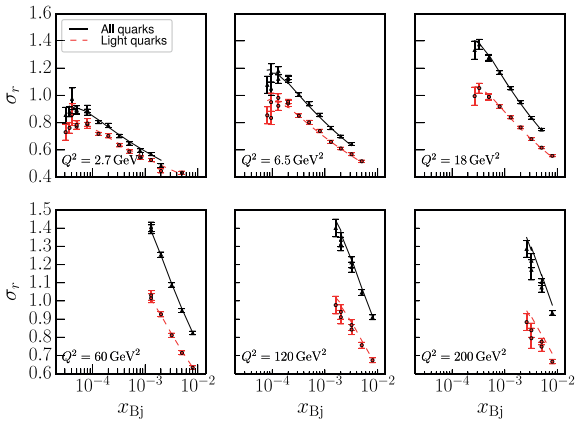

FIG. 1. Total reduced cross section (black triangles) from Ref. [1] and interpolated light quark pseudodata (red circles) in a few Q^2 bins. The solid and dashed lines show the calculated cross sections from the IPsat fit that are used to generate the pseudodata.

$0.75 < Q^2 < 50\ \mathrm{GeV}^2$ at $x < 0.01$. This results in $N = 187$ data points to be included in the fit. Although the correlation matrix for the experimental uncertainties is available [1], we do not take these correlations into account as we expect it to have only a negligible effect in our fits.

V. FIT RESULTS

In this section we will look at our fit results. The discussion is divided first by the data that are being fitted, followed by a comparison of the evolution prescriptions in the kinematical domain accessible in future DIS experiments, which lies outside the HERA region included in the fits.

Let us first recall the essential details of our fit schemes. The choice of a fit scheme consists of the version of the BK evolution equation (discussed in Secs. III C–III E), the running coupling scheme (see Sec. III F), and the starting point of the BK evolution, parametrized in terms of $Y_{0,\mathrm{BK}}$ or $\eta_{0,\mathrm{BK}}$. The fit results in values for the free parameters characterizing the initial condition as discussed in Sec. III G: Q_{s0}^2, σ_0 and γ, and in a value for the parameter C^2 in the scale of the running coupling; see Sec. III F.

Our main fit results are presented in Tables I–III classified by the BK equation used, with secondary and tertiary grouping keys being the running coupling scheme and $Y_{0,\mathrm{BK}}$ (or $\eta_{0,\mathrm{BK}}$) controlling the rapidity scale of the BK initial condition used in the fits. The saturation scale Q_s^2 defined as $N(r^2 = 2/Q_s^2) = 1 - e^{-1/2}$ is also shown at fixed projectile rapidity $Y = \ln\frac{1}{0.01}$. We will first discuss in the next subsection the fits to the full HERA reduced cross section data, and in the following subsection the fits to the interpolated light-quark pseudodata presented in Sec. IV and labeled as *light-q* in the tables where the fit results are

TABLE I. Fits to HERA and light-quark data with the KCBK evolution.

Data	α_s	$Y_{0,\mathrm{BK}}$	χ^2/N	$Q_{s,0}^2$ [GeV^2]	C^2	γ	$\sigma_0/2$ [mb]	$Q_s^2(Y=\ln\frac{1}{0.01})$ [GeV^2]
HERA	Parent	$\ln\frac{1}{0.01}$	1.85	0.0833	3.49	0.98	9.74	0.11
Light-q	Parent	$\ln\frac{1}{0.01}$	1.58	0.0753	37.7	1.25	18.41	0.11
HERA	Parent	0	1.24	0.0680	79.9	1.21	18.39	0.20
Light-q	Parent	0	1.18	0.0664	1340	1.47	27.12	0.14
HERA	Bal + SD	$\ln\frac{1}{0.01}$	1.89	0.0905	0.846	1.21	8.68	0.13
Light-q	Bal + SD	$\ln\frac{1}{0.01}$	2.63	0.0720	1.91	1.55	12.44	0.11
HERA	Bal + SD	0	1.49	0.1114	0.846	1.94	8.53	0.26
Light-q	Bal + SD	0	1.69	0.1040	2.87	7.70	12.09	0.14

TABLE II. Fits to HERA and light-quark data with local projectile momentum fraction evolution (ResumBK).

Data	α_s	$Y_{0,\mathrm{BK}}$	χ^2/N	$Q_{s,0}^2$ [GeV^2]	C^2	γ	$\sigma_0/2$ [mb]	$Q_s^2(Y=\ln\frac{1}{0.01})$ [GeV^2]
HERA	Parent	$\ln\frac{1}{0.01}$	2.24	0.0964	1.21	0.98	7.66	0.13
Light-q	Parent	$\ln\frac{1}{0.01}$	1.62	0.0755	11.7	1.24	16.53	0.11
HERA	Parent	0	1.12	0.0721	89.5	1.37	19.68	0.21
Light-q	Parent	0	1.18	0.0794	1480	1.92	26.69	0.18
HERA	Bal + SD	$\ln\frac{1}{0.01}$	2.37	0.0950	0.313	1.24	7.85	0.14
Light-q	Bal + SD	$\ln\frac{1}{0.01}$	2.21	0.0796	0.684	1.81	11.34	0.13
HERA	Bal + SD	0	2.35	0.0530	0.486	1.56	10.10	0.23
Light-q	Bal + SD	0	3.19	0.0566	1.27	9.35	14.27	0.13

TABLE III. Fits to HERA and light-quark data with TBK evolution. Note that the saturation scale Q_s^2 is extracted at fixed projectile rapidity Y to allow comparisons with the projectile momentum fraction evolutions.

Data	α_s	$\eta_{0,\mathrm{BK}}$	χ^2/N	$Q_{s,0}^2$ [GeV^2]	C^2	γ	$\sigma_0/2$ [mb]	$Q_s^2(Y=\ln\frac{1}{0.01})$ [GeV^2]
HERA	Parent	$\ln\frac{1}{0.01}$	2.76	0.0917	0.641	0.90	6.19	0.11
Light-q	Parent	$\ln\frac{1}{0.01}$	1.61	0.0729	14.4	1.19	16.45	0.10
HERA	Parent	0	1.03	0.0820	209	1.44	19.78	0.23
Light-q	Parent	0	1.26	0.0731	8050	1.86	29.84	0.16
HERA	Bal + SD	$\ln\frac{1}{0.01}$	2.48	0.0678	1.23	1.13	10.43	0.09
Light-q	Bal + SD	$\ln\frac{1}{0.01}$	1.90	0.0537	3.55	1.59	16.85	0.08
HERA	Bal + SD	0	2.77	0.0645	3.67	6.37	14.14	0.15
Light-q	Bal + SD	0	1.82	0.0690	822	8.35	29.26	0.14

shown. The two datasets differ enough to warrant their own discussion.

A. Fitting the HERA reduced cross section

Before we discuss the results and their systematic features in more detail we show in Fig. 2 that all three BK evolutions combined with next-to-leading-order impact factors are capable of describing the HERA data equally well. The results shown are obtained using the Bal + SD running coupling, and $Y_{0,\mathrm{BK}} = \eta_{0,\mathrm{BK}} = \ln 1/0.01$, but excellent fit results are obtained with other scheme choices, too. Even though the resulting parametrizations for the dipole at initial rapidity can differ significantly, the resulting reduced cross sections are mostly indistinguishable.

We first present in Table I the fit results obtained using the kinematically constrained BK equation as discussed in Sec. III C. We find a very good description ($\chi^2/N = 1.49$) of the HERA data using our main setup with the Bal + SD prescription and $Y_{0,\mathrm{BK}} = 0$. We consider this as our preferred HERA data fit, with a BK equation derived in the same framework as the impact factor, a theoretically preferred running coupling scheme, and only one starting scale $Y_{0,\mathrm{if}} = Y_{0,\mathrm{BK}} = 0$. We note that starting the BK

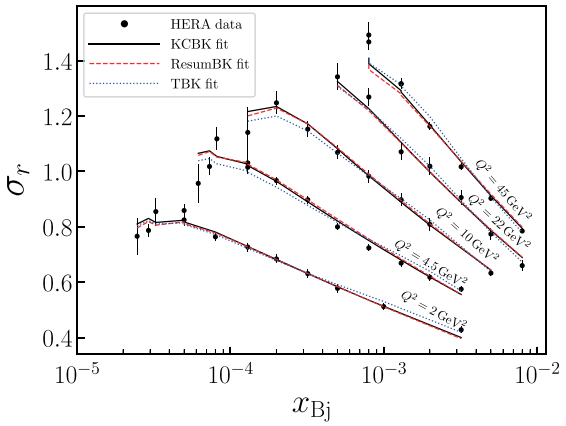

FIG. 2. Reduced cross section obtained using the fits with different BK evolutions compared with the HERA data [1]. Balitsky + smallest dipole running coupling is used, with $Y_{0,\mathrm{BK}} = \ln 1/0.01$.

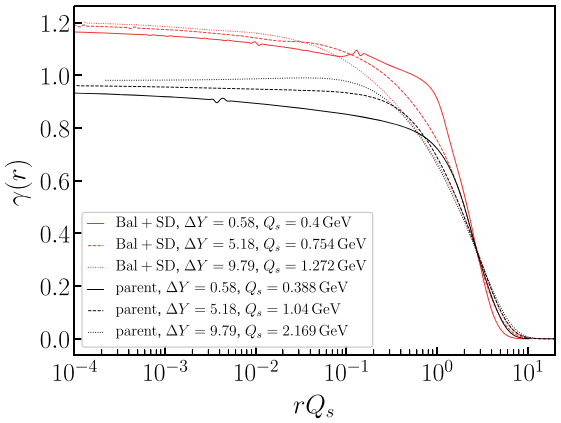

FIG. 3. Anomalous dimension evolution with KCBK, $Y_{0,\mathrm{BK}} = \ln 1/0.01$. Computed from fits to HERA data.

evolution at $Y_{0,\mathrm{BK}} = \ln\frac{1}{0.01}$ (and freezing the dipole at smaller rapidities) results in an equally good fit. This suggests that we are only weakly sensitive to the details of extrapolation scheme used to describe the dipole amplitude in the region $Y_{0,\mathrm{if}} < Y < Y_{0,\mathrm{BK}}$. The parameter C^2 controlling the evolution speed is not required to be large as it is in the case of leading-order fits, where one generally finds $C^2 \sim 10$ [8,9]. Instead, we find $C^2 \approx 0.85$, which is of the same ballpark as the general estimate $C^2 = e^{-2\gamma_E} \approx 0.3$ [83,84].

As seen in Table I, larger values of C^2 are required in the parent dipole scheme fits. This is expected, as C^2 maps the coordinate space scale $\mathbf{x}_{ij}^2$ to momentum space $C^2/\mathbf{x}_{ij}^2$, and in the parent dipole scheme the coordinate space scale is generically larger. Consequently a larger C^2 is needed to render the strong coupling values and the resulting evolution speeds, comparable between the coupling constant scheme choices.

We generically find $\gamma > 1$ at the initial condition, with the exception $\gamma \approx 1$ found in the case where the evolution starts at $Y_{0,\mathrm{BK}} = \ln\frac{1}{0.01}$ and the parent dipole prescription for the running coupling is used. We note that $\gamma > 1$ is also required in the leading-order fits to obtain a Q^2 dependence at the initial condition compatible with the HERA data [8,9]. The disadvantage of an initial condition with $\gamma > 1$ is that, as discussed in Sec. III G, it results in the unintegrated gluon distribution not being positive definite at large transverse momenta.

To understand why different running coupling prescriptions result in different initial anomalous dimensions, we study the slope of the dipole defined as

$$\gamma(r) = \frac{\mathrm{d}\ln N(r)}{\mathrm{d}\ln r^2}. \tag{35}$$

For the KCBK fits this is shown in Fig. 3 as a function of dimensionless dipole size rQ_s. The kinematically constrained BK equation is found to keep the anomalous dimension (slope at small r) approximatively constant at very small r, unlike the leading-order BK equation. A similar effect was found in case of the ResumBK equation in Ref. [25].

At intermediate $r \sim 1/Q_s$ which dominates the cross section, there is clear evolution toward an asymptotic shape. Let us first focus on results where the smallest dipole Bal + SD coupling is used. Here, the anomalous dimension is large at the initial condition and the evolution decreases the slope at intermediate rQ_s, which results in the cross section growing more rapidly with Q^2. If the BK evolution is started at the rapidity scale from which there is a long evolution before entering the data region (i.e., $Y_{0,\mathrm{BK}} = 0$), a larger initial anomalous dimension is required in order to obtain the shape dictated by the Q^2 dependence of the HERA structure function data around $r \sim 1/Q_s$.

Let us then consider the evolution with the parent dipole prescription. In this case, we start from a relatively small $\gamma = 0.98$, and the evolution increases the slope at small (but not asymptotically small) r. This can be seen to stem from the fact that in the parent dipole prescription the coupling, and consequently the evolution speed of the dipole amplitude $N(r)$, grows more as a function of parent dipole size r in comparison to other running coupling prescriptions. At larger r, the slope evolves only slightly. After a few units of rapidity evolution, the dipole amplitudes have the same shape in the $r \sim 1/Q_s$ region independently of the running coupling prescription. This is expected, as $r \sim 1/Q_s$ size dipoles dominate when calculating the structure functions in HERA kinematics.

Next we move to the local projectile momentum fraction (ResumBK) fits, the results of which are shown in Table II. In general, the results are close to the ones previously

discussed in case of the kinematically constrained BK equation. This is not surprising, as both equations are designed to include the same subset of higher-order corrections enhanced by large double transverse logarithms. Similarly to the preferred fit with KCBK, in the ResumBK fit to HERA data with Bal + SD and $Y_{0,\mathrm{BK}} = 0$ the obtained C^2 is quite small at $C^2 \approx 0.49 \sim e^{-2\gamma_E}$ and the anomalous dimension is large, $\gamma = 1.56$. The obtained anomalous dimension values behave similarly as in the case of KCBK, and there similarly seems to be a systematic preference for smaller $\sigma_0/2$ with the Balitsky + smallest dipole coupling.

The ResumBK equation evolves generically more slowly than the KCBK equation, which is reflected in the required C^2 values being smaller (except in the case $Y_{0,\mathrm{BK}} = 0$ with parent dipole prescription when the C^2 values are comparable). This is a consequence of the ResumBK equation including an additional resummation of some single transverse logarithms. The main effect of this resummation is that it results in a slower evolution; see discussion in Sec. III D. We have confirmed numerically that if the resummation of single transverse logarithms is not included, our fit results are almost intact, except that a larger value for the parameter C^2 is obtained.

In both ResumBK and KCBK fits with Bal + SD running coupling, the obtained values for the proton transverse area $\sigma_0/2$ are generally smaller than what is found in leading-order fits with similar running coupling schemes, with or without a resummation of large transverse logarithms [8,9,82]. The obtained saturation scales at $Y = \ln\frac{1}{0.01}$, on the other hand, are comparable to the leading-order fit results. In the LO fits, one typically obtains $\sigma_0/2 \sim 16$ mb (proton sizes comparable to our results were found in the leading-order fit presented in Ref. [81] where double logarithmic corrections were resummed in the BK equation similarly as in our setup).

We note that the proton transverse area can in principle be obtained by studying the squared momentum transfer t dependence of exclusive vector meson production. If the cross section is written as $e^{-B_D|t|}$ at small $|t|$, the HERA measurements on J/ψ production [92,93] give $B_D \approx 4\ \mathrm{GeV}^{-2}$. Depending on the assumed proton density profile, this corresponds to $\sigma_0/2 \approx 9.8\ldots19.6$ mb (using Gaussian or a step function profile). As the vector meson t spectra are not measured precisely enough especially at large $|t|$, the exact form of the proton density profile cannot be deduced. Consequently, we find that all obtained values for the proton transverse size $\sigma_0/2$ in our fits to HERA reduced cross section data are compatible with the J/ψ spectra. However, we also note that the step function profile is not really favored by the HERA data [94]. Thus one would prefer values that are in the lower part of the range $\sigma_0/2 \approx 9.8\ldots19.6$ mb. Indeed, especially with the Balitsky + smallest dipole running coupling, our fit results for the proton size also favor such smaller target sizes for the proton.

As we are neglecting the impact parameter dependence, we cannot compute the evolution of the proton transverse area and consequently use a fixed $\sigma_0/2$ at all x_{Bj}. We note that the HERA vector meson production data [93,95] suggest that the transverse area depends logarithmically on the center-of-mass energy. This growth is effectively included in the energy dependence of the proton saturation scale in our framework.

Let us finally discuss the results obtained with the third evolution equation considered in this work, the BK equation formulated in terms of the target momentum fraction (TBK). The fit results in this case are shown in Table III. While the fit qualities overall are quite similar to the projectile momentum fraction setups, we find some departures from the shared qualitative features of the KCBK and ResumBK fits. With the Balitsky + smallest dipole running coupling the TBK evolution needs to be slowed down more with a larger values of C^2 compared to KCBK and ResumBK equations. The TBK fit with parent dipole coupling is more mixed in this respect: with $\eta_{0,\mathrm{BK}} = 0$ setups the C^2 values are quite a bit larger but then with $\eta_{0,\mathrm{BK}} = \ln\frac{1}{0.01}$ the HERA data fit is found to require only a small C^2.

Comparing the initial conditions with $\eta_{0,\mathrm{BK}} = 0$ and $\eta_{0,\mathrm{BK}} = \ln\frac{1}{0.01}$ we see that every evolution starts from a significantly larger anomalous dimension when $\eta_{0,\mathrm{BK}} = 0$. This difference is more pronounced compared to the previously studied KCBK and ResumBK equations. This is because the TBK evolution drives the dipole toward the asymptotic shape with a small anomalous dimension $\gamma \sim 0.6$ [23]. This behavior is similar to the leading-order BK equation, in which case it is already known that the asymptotic shape cannot be used to parametrize the initial condition [8].[5] Indeed the development of the geometric scaling regime independently of the initial condition is a theoretically attractive feature of the TBK formulation. However, HERA data seem to prefer to lie in the pre-asymptotic regime in the fits. Thus, especially in the fits with more evolution before the data region (smaller $\eta_{0,\mathrm{BK}}$), one needs to slow down the evolution more and start with a significantly larger anomalous dimension in order to still have a transient form of the dipole amplitude in the data regime.

The evolution of the dipole slope in TBK evolution is shown in Fig. 4 at different evolution rapidities η. Unlike in the case of KCBK equation discussed earlier and shown in Fig. 3, the slope of the dipole from the TBK evolution is decreasing with both running couplings in the $r \sim 1/Q_s$ regime. As shown in Ref. [23], the asymptotic anomalous dimension $\gamma \sim 0.6$ is obtained only at very large rapidities, and at least the Bal + SD coupling case can be seen to be

[5] In [96] an asymptotic form of the initial condition produces working results only when a significant additional "energy conservation" correction in the BK evolution is used.

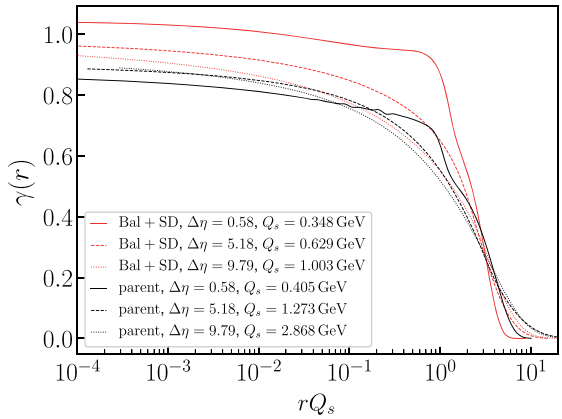

FIG. 4. Anomalous dimension evolution with TBK, using the initial conditions parametrized at $\eta_{0,\mathrm{BK}} = \ln\frac{1}{0.01}$. The evolved rapidity range from the initial condition is denoted by $\Delta\eta$.

evolving toward this asymptotic value. In the rapidity range relevant in HERA or even LHeC kinematics the asymptotic anomalous dimension is not reached. With the parent dipole coupling, a significantly longer evolution is needed before evolution toward the asymptotic shape at small r becomes visible in the best fit case with a small anomalous dimension $\gamma = 0.9$ in the initial condition.

The dipole amplitudes at different evolution rapidities as a function of dipole size are shown in Fig. 5. Here, results obtained using all three considered evolution equations are shown at fixed projectile rapidity $Y = Y_{0,\mathrm{BK}} + \Delta Y$. The solution to the TBK evolution is shifted from the target rapidity η to the projectile rapidity Y by performing the shift (29). The shifted TBK solutions are shown in the region

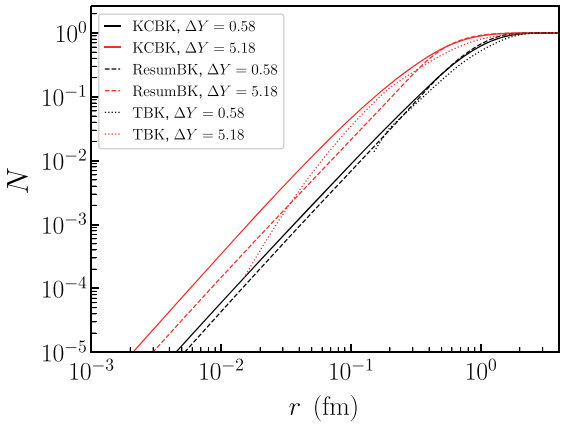

FIG. 5. Dipole amplitudes of the three BK equations at an early and later stage in the evolution at constant evolution rapidities $Y = Y_{0,\mathrm{BK}} + \Delta Y$, with TBK solutions in η shifted into Y. Balitsky + smallest dipole running coupling is used, with the initial conditions from the fits with $Y_{0,\mathrm{BK}} = \eta_{0,\mathrm{BK}} = \ln\frac{1}{0.01}$.

where $\eta > \eta_{0,\mathrm{BK}}$. In the region where the dipole amplitude is not small, all evolution equations result in comparable dipole amplitudes. This is expected, as all the shown dipoles result in a compatible description of the HERA structure function data.

At small dipole sizes that do not significantly contribute to the structure functions some differences appear. Despite the fact that KCBK and ResumBK equations have very similar initial conditions the resulting amplitudes differ significantly for small dipoles. This is mostly driven by the resummation of the single transverse logarithms not included in the kinematically constrained BK equation, as this resummation is more important at small parent dipole size r. At very small dipoles the TBK evolved dipole also differs significantly from the other dipoles when the shift from target rapidity, Eq. (28), results in the dipole being evaluated close to the initial condition. If the parent dipole scheme for the running coupling were used, the differences between the dipoles obtained from the different evolution equations would be significantly reduced, as in that scheme the coupling constant is generically smaller at small r and differences between the evolution equations are suppressed by the small α_s.

B. Fitting the interpolated light-quark reduced cross section

Next we consider fits to our interpolated light-quark dataset. The fit results are also shown in Tables I–III. Figure 6 shows a comparison between the HERA and interpolated light-quark data with one of the fits, obtained with the KCBK equation with the Balitsky + smallest dipole running coupling and initial condition parametrized at $Y_{0,\mathrm{BK}} = \ln 1/0.01$.

The light-quark-only fits have quite distinct systematics in comparison to the actual HERA data fits. Every single fit

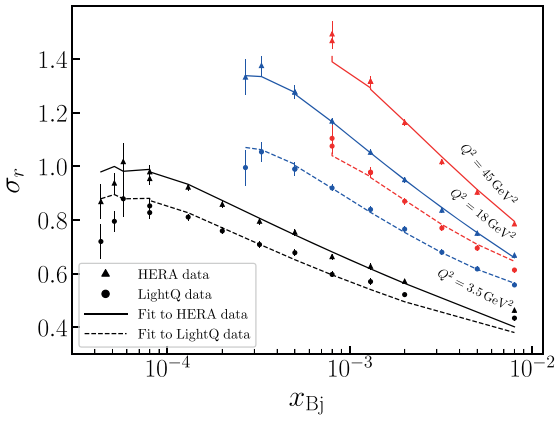

FIG. 6. Total and light-quark reduced cross sections computed from KCBK fit compared with the light-quark pseudodata data and HERA reduced cross section data [1]. Balitsky + smallest dipole running coupling is used with $Y_{0,\mathrm{BK}} = \ln 1/0.01$.

setup used needs a substantially larger C^2 and to a varying degree larger anomalous dimensions. Lastly, and importantly, light-quark fits need larger values of σ_0 compared to the corresponding total HERA cross section fit.

The slow evolution speed (visible as a large C^2 especially when using the parent dipole prescription) and a large σ_0 in the light-quark pseudodata fits can be understood to result from an effective description of nonperturbative effects. We expect that there is a nonperturbative hadronic contribution in the light-quark production cross section which is large (resulting in a large σ_0) and evolves more slowly as a function of Bjorken x_{Bj} than the fully perturbative cross sections, like charm production. In our framework, these nonperturbative effects correspond to large dipoles, with sizes larger than roughly the inverse pion mass. In this case, quark-antiquark dipoles are not the right degrees of freedom, and one should in principle use an another effective description for the nonperturbative physics, e.g., the vector meson dominance [97–100] model.

The same nonperturbative effects are there also in the total reduced cross section and, consequently, in our fits to full HERA data. However, the full reduced cross section also includes the more reliably perturbative charm production contribution (and a small b quark one), with a much faster x evolution and a smaller magnitude (σ_0). Consequently, when performing our (massless) NLO fits to the full HERA data more weight is given to perturbative contributions compared to light-quark fits, and there is less need for the fit parameters to adjust to nonperturbative effects with unnatural values.

These observations are compatible with some of the previous analyses. In the study by the AAMQS Collaboration [8] it was found that a combined fit to both charm and total reduced cross section requires one to introduce separate fit parameters for the charm quarks, especially the charm quarks require a smaller σ_0. A slowly evolving nonperturbative contribution to the light-quark production was also found to be necessary in Refs. [29,40]. In the dipole picture applied here, one finds that very large dipoles up to a few femtometers contribute significantly to the light-quark structure function [86]. In reality, nonperturbative confinement scale effects not included in our perturbative calculation are expected to dominate in these cases as discussed above.

To arrive at one of our central points of this article, we make the observation that even though the HERA DIS data has been described well with leading-order dipole picture fits with the BK equation in the past, simultaneous fits to the full data and charm quark data have not been successful with a single BK-evolved amplitude (note however the existence of fits [94,101,102] using parametrizations that mimic BK evolution). Similar results are found in the recent study with the target rapidity BK prescription as well [82]: fits to the full data are excellent but the fit parametrizations do not describe the heavy-quark data. Our next-to-leading-order analysis, where we separately consider the light-quark production only, results in similar conclusions. This indicates that the description of the light-quark contribution has a large theoretical uncertainty as well in any such fit to the full DIS data.

Thus we find that it would be preferable to fit the charm quark structure function $F_{2,c}$ separately (or inclusive F_L data, as the longitudinal photon splits generally to smaller dipoles, resulting in smaller nonperturbative contributions). The F_L measurements from HERA [103] are however not precise enough for our purposes (see the next section). Very precise F_L data (among with inclusive and charm structure functions) can be expected from the future Electron Ion Collider [104,105] or from the LHeC [106].

C. Beyond HERA

Given the equality in the capabilities of the different versions of the BK equation in describing the HERA and light-quark data, a question arises if it is possible to distinguish the different fit schemes and find the preferred form of the BK equation. In general, one might expect to see differences in the Q^2 dependence of the structure functions at small x (in the HERA kinematics, the fit procedure ensures a compatible evolution). This is because the Q^2 dependence is controlled by the anomalous dimension, which behaves differently in ResumBK and KCBK evolutions, when compared to the BK equation formulated in the target momentum fraction as shown in Figs. 3 and 4.

At asymptotically small x both approaches can result in the same Q^2 dependence of the cross section in spite of the different anomalous dimensions. This can be seen as follows. Let us first consider the BK equation formulated in the target rapidity and write the dipole amplitude as $N \sim (Q_s^2 r^2)^\gamma$. The TBK equation results in the saturation scale scaling as $Q_s^2 \sim x^{-\lambda}$, as the evolution range is $\ln 1/x_{\mathrm{Bj}}$. This gives $N \sim {x_{\mathrm{Bj}}}^{-\lambda\gamma}(Q^2)^{-\gamma}$, and consequently the structure functions behave as

$$\frac{1}{|\psi^{\gamma^* \to q\bar{q}}|^2} F_{2,L}(Q^2) \sim (Q^2)^{-\gamma}, \tag{36}$$

where we have scaled out the Q^2 dependence originating from the virtual photon wave function $\psi^{\gamma^* \to q\bar{q}}$. Substituting an asymptotic anomalous dimension $\gamma \sim 0.7$ we get

$$\frac{1}{|\psi^{\gamma^* \to q\bar{q}}|^2} F_{2,L}(Q^2) \sim (Q^2)^{-0.7}. \tag{37}$$

On the other hand, when applying the KCBK or ResumBK equations formulated in terms of the projectile momentum fraction, the evolution range is controlled by $\ln W^2 = \ln(Q^2/x_{\mathrm{Bj}})$. Consequently, we get $Q_s^2 \sim (W^2)^\lambda \sim (Q^2/x_{\mathrm{Bj}})^\lambda$. This gives

$$\frac{1}{|\psi^{\gamma^*\to q\bar{q}}|^2} F_{2,L} \sim (Q^2)^{\gamma(\lambda-1)}. \tag{38}$$

In general, in the case of ResumBK and KCBK we expect $\gamma \sim 1$ as the evolution does not change the asymptotic anomalous dimension. Using $\lambda \sim 0.3$ for the generic evolution speed we get

$$F_{2,L} \sim |\psi^{\gamma^*\to q\bar{q}}|^2 (Q^2)^{-0.7}, \tag{39}$$

which is the same Q^2 scaling as obtained in case of TBK equation; see Eq. (37).

In practice, however, in HERA or even LHeC kinematics the TBK evolution has not reached its asymptotic form, and the anomalous dimension is still close to unity as shown in Fig. 4. Consequently, the Q^2 dependence is expected to be slower in the TBK evolution in realistic kinematics. We note that the structure functions are not actually sensitive to the slope of the dipole at asymptotically small r but in the region $r \sim 1/Q_s$ or $r \sim 1/Q$, which makes it in practice difficult to compare Q^2 dependences analytically. We also note that when computing the structure function at low x_{Bj}, also dipole amplitudes at higher x_{Bj} are probed when performing the z_2 integral.

The numerically calculated Q^2 dependence of the structure functions F_2 and F_L is shown in Fig. 7. The results are shown at small $x_{\mathrm{Bj}} = 5.6 \times 10^{-5}$ corresponding to the LHeC kinematics using each of the BK equations, employing the fit to the full HERA data with the Bal + SD running coupling prescription and $Y_{0,\mathrm{BK}} = \eta_{0,\mathrm{BK}} = \ln\frac{1}{0.01}$. For comparison, the leading-order result based on Ref. [9] is shown. Compared to the leading-order fit, the Q^2 dependence is weaker at next-to-leading order, due to the different asymptotic shape of the dipole amplitude (the leading-order BK equation develops a small anomalous dimension γ which results in faster Q^2 dependence).

The different fit schemes that result in an equally good description of the HERA data start to differ slightly at large Q^2 when considering the Bjorken-x_{Bj} region not included in the fits. The longitudinal structure function F_L is more sensitive to small dipole sizes, and as such it can be expected to be more sensitive on the details of the evolution. This is especially visible when the ResumBK evolution is compared to other approaches: the Q^2 dependence is much weaker at large Q^2. This is due to the resummation of single transverse logarithms not included in other evolution schemes, which has the largest effect at small parent dipole sizes probed at large Q^2. However, in the realistic kinematical range considered here, the difference between the fits is moderate. This suggests that our next-to-leading-order predictions for the structure functions in the future collider experiments are robust. Future high-energy DIS data from e.g., LHeC will be extremely precise, with the expected uncertainties in the structure function

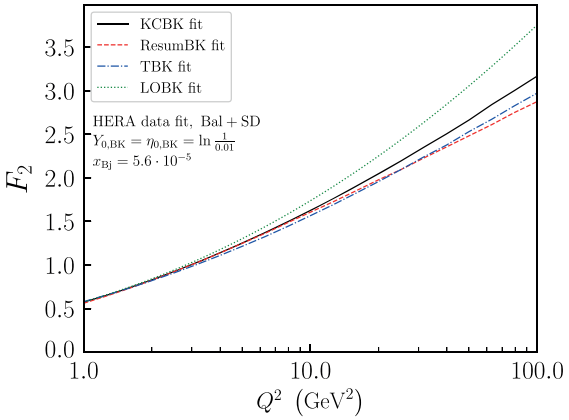

(a) Structure function F_2

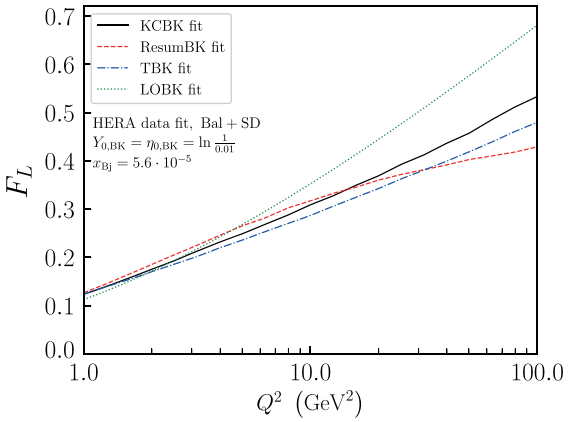

(b) Structure function F_L

FIG. 7. Structure functions F_2 and F_L computed from HERA data fit parametrizations extrapolated to the LHeC kinematics. For comparison, the corresponding leading-order predictions from Ref. [9] are shown.

measurements being even at the per mill level [106]. As such one could be sensitive to details in NLO BK evolution, even though the effects are not large. Ultimately more differential measurements in addition to the reduced cross section will be needed.

The most precise measurement of the proton longitudinal structure function F_L up to date is performed by the H1 Collaboration at HERA [103] (with compatible results obtained by the ZEUS Collaboration [107]). In Fig. 8 we compare the F_L computed from our fits to the H1 data. Due to the limited statistics, the most precise results are not reported as a function of both x and Q^2, but at fixed x, Q^2 combinations. Consequently, it is crucial to note that the higher Q^2 points are measured at higher x. All three fit setups result in almost identical F_L, as expected as the F_L is measured in the kinematical domain mostly included in our

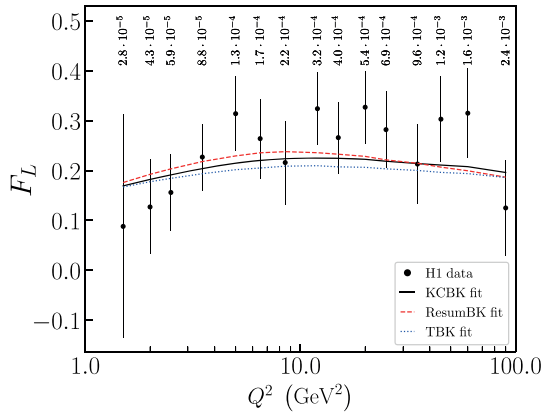

FIG. 8. NLO fit predictions of F_L compared to averaged H1 data [103]. Fits are to HERA data, with smallest dipole coupling and $Y_{0,\mathrm{BK}} = \eta_{0,\mathrm{BK}} = \ln\frac{1}{0.01}$.

reduced cross section fits. Even though the future Electron Ion Collider [104] will not reach as small Bjorken-x values as the LHeC, the F_L measurements it can perform will be very useful as the HERA measurement has large uncertainties and it only covers a small fraction of the phase space where the details of the evolution cannot be accessed.

VI. CONCLUSIONS

We have performed, for the first time, a fit to the HERA structure function data in the color glass condensate framework at next-to-leading-order accuracy in the case of massless quarks. As the full next-to-leading-order BK equation is computationally demanding, we approximate it by employing evolution equations that resum higher-order corrections enhanced by large transverse logarithms. As a result of the fits, we obtain the initial condition for the perturbative BK evolution. The resulting dipole-target scattering amplitude can be used in other phenomenological applications, for example when calculating particle production in proton-nucleus collisions at next-to-leading order in α_s.

Similarly as in the leading-order fits previously studied in the literature, we find that it is possible to obtain an excellent description of the precise combined HERA structure function data. Equally good fits are obtained when using both the BK equation formulated in terms of the projectile momentum fraction, and the recently proposed BK equation where the evolution rapidity is dictated by the fraction of the target longitudinal momentum. When extrapolated to LHeC energies, the different BK evolution prescriptions are found to result in moderate differences in the Q^2 dependence of the structure functions. This suggests that the NLO calculation presented here is robust, and has a strong predictive power for future DIS measurements in new experimental facilities such as the EIC or LHeC.

As next-to-leading-order impact factors for massive quarks are not yet available, it is not possible to compute charm and bottom contribution to the structure functions. To perform consistent fits, we also generated an interpolated light-quark dataset by subtracting the interpolated charm and bottom contribution from the HERA reduced cross section data. Fits to these light-quark data require a much slower Bjorken-x evolution than we naturally get from the perturbative evolution equations applied. Additionally, the apparent proton transverse size obtained is significantly larger than seen when fitting the full HERA data. These features we interpret to result from a nonperturbative hadronic component in the light-quark production cross section. This component is large (resulting in a large proton transverse area) and evolves more slowly as a function of Bjorken x, as expected for a hadronic component.

Our results demonstrate the need for massive quark impact factors at next-to-leading-order accuracy in the CGC framework, which would allow fits to fully perturbative charm cross section separately. Precise measurements of the charm structure function over a wide range of x and Q^2, in addition to the longitudinal structure function, from future experiments will also be useful. The fits to the generated light-quark data should in principle be considered our principal preferred fits as there the agreement between the data and the massless theory should be on the most solid footing. However, if used for QCD phenomenology in other observables where the presumed nonperturbative contribution is smaller, the best one can do is use the full HERA data fits.

In addition to inclusion of the quark masses and the usage of the full NLO BK, the NLO DIS calculation can be improved by relaxing some of the kinematical assumptions. First, in addition to the gluon momentum fraction z_2, the quark momentum fraction z_1 should not be allowed to get arbitrary close to end points $z_1 \to 0, 1$ in order to avoid production of $q\bar{q}$ pairs with invariant mass larger than the center-of-mass energy. Additionally, in the virtual correction one should also perform the integral over the gluon momentum fraction and evaluate the dipole operator at the same rapidity as in the real term. This would make it possible to also consistently include a Q^2-dependent evolution range in the virtual contribution. Finally, when the Balitsky prescription for the running coupling is used in the BK evolution, there is a mismatch in the running coupling schemes between the impact factor and the evolution equation which could be improved. We plan to address these issues in future work.

ACKNOWLEDGMENTS

We thank B. Ducloué for discussions. This work was supported by the Academy of Finland, Projects No. 314764 (H. M.) and No. 321840 (T. L.). G. B., H. H. and T. L. are supported under the European Union's Horizon 2020

research and innovation program by the European Research Council (ERC, Grant Agreement No. ERC-2015-CoG-681707) and by the STRONG-2020 project (Grant Agreement No. 824093). The content of this article does not reflect the official opinion of the European Union and responsibility for the information and views expressed therein lies entirely with the authors. Computing resources from CSC–IT Center for Science in Espoo, Finland and from the Finnish Grid and Cloud Infrastructure (persistent identifier urn:nbn:fi:research-infras-2016072533) were used in this work.

[1] F. D. Aaron *et al.* (H1 and ZEUS Collaborations), Combined measurement and QCD analysis of the inclusive $e^{\pm}p$ scattering cross sections at HERA, J. High Energy Phys. 01 (2010) 109.

[2] H. Abramowicz *et al.* (H1 and ZEUS Collaborations), Combination of measurements of inclusive deep inelastic $e^{\pm}p$ scattering cross sections and QCD analysis of HERA data, Eur. Phys. J. C **75**, 580 (2015).

[3] H. Abramowicz *et al.* (H1 and ZEUS Collaborations), Combination and QCD analysis of charm and beauty production cross-section measurements in deep inelastic ep scattering at HERA, Eur. Phys. J. C **78**, 473 (2018).

[4] H. Abramowicz *et al.* (H1 and ZEUS Collaborations), Combination and QCD analysis of charm production cross section measurements in deep-inelastic ep scattering at HERA, Eur. Phys. J. C **73**, 2311 (2013).

[5] F. Gelis, E. Iancu, J. Jalilian-Marian, and R. Venugopalan, The color glass condensate, Annu. Rev. Nucl. Part. Sci. **60**, 463 (2010).

[6] J. L. Albacete and C. Marquet, Gluon saturation and initial conditions for relativistic heavy ion collisions, Prog. Part. Nucl. Phys. **76**, 1 (2014).

[7] J. L. Albacete, N. Armesto, J. G. Milhano, and C. A. Salgado, Non-linear QCD meets data: A global analysis of lepton-proton scattering with running coupling BK evolution, Phys. Rev. D **80**, 034031 (2009).

[8] J. L. Albacete, N. Armesto, J. G. Milhano, P. Quiroga-Arias, and C. A. Salgado, AAMQS: A non-linear QCD analysis of new HERA data at small-x including heavy quarks, Eur. Phys. J. C **71**, 1705 (2011).

[9] T. Lappi and H. Mäntysaari, Single inclusive particle production at high energy from HERA data to proton-nucleus collisions, Phys. Rev. D **88**, 114020 (2013).

[10] I. Balitsky and G. A. Chirilli, Photon impact factor in the next-to-leading order, Phys. Rev. D **83**, 031502 (2011).

[11] I. Balitsky and G. A. Chirilli, Photon impact factor and k_T-factorization for DIS in the next-to-leading order, Phys. Rev. D **87**, 014013 (2013).

[12] G. Beuf, NLO corrections for the dipole factorization of DIS structure functions at low x, Phys. Rev. D **85**, 034039 (2012).

[13] G. Beuf, Dipole factorization for DIS at NLO: Loop correction to the $\gamma^*_{T,L} \to q\bar{q}$ light-front wave functions, Phys. Rev. D **94**, 054016 (2016).

[14] G. Beuf, Dipole factorization for DIS at NLO: Combining the $q\bar{q}$ and $q\bar{q}g$ contributions, Phys. Rev. D **96**, 074033 (2017).

[15] H. Hänninen, T. Lappi, and R. Paatelainen, One-loop corrections to light cone wave functions: The dipole picture DIS cross section, Ann. Phys. (Amsterdam) **393**, 358 (2018).

[16] B. Ducloué, H. Hänninen, T. Lappi, and Y. Zhu, Deep inelastic scattering in the dipole picture at next-to-leading order, Phys. Rev. D **96**, 094017 (2017).

[17] I. Balitsky, Operator expansion for high-energy scattering, Nucl. Phys. **B463**, 99 (1996).

[18] Y. V. Kovchegov, Small x F(2) structure function of a nucleus including multiple Pomeron exchanges, Phys. Rev. D **60**, 034008 (1999).

[19] I. Balitsky and G. A. Chirilli, Next-to-leading order evolution of color dipoles, Phys. Rev. D **77**, 014019 (2008).

[20] G. Beuf, Improving the kinematics for low-x QCD evolution equations in coordinate space, Phys. Rev. D **89** (2014) 074039.

[21] E. Iancu, J. D. Madrigal, A. H. Mueller, G. Soyez, and D. N. Triantafyllopoulos, Resumming double logarithms in the QCD evolution of color dipoles, Phys. Lett. B **744**, 293 (2015).

[22] E. Iancu, J. D. Madrigal, A. H. Mueller, G. Soyez, and D. N. Triantafyllopoulos, Collinearly-improved BK evolution meets the HERA data, Phys. Lett. B **750**, 643 (2015).

[23] B. Ducloué, E. Iancu, A. H. Mueller, G. Soyez, and D. N. Triantafyllopoulos, Non-linear evolution in QCD at high-energy beyond leading order, J. High Energy Phys. 04 (2019) 081.

[24] T. Lappi and H. Mäntysaari, Direct numerical solution of the coordinate space Balitsky-Kovchegov equation at next to leading order, Phys. Rev. D **91**, 074016 (2015).

[25] T. Lappi and H. Mäntysaari, Next-to-leading order Balitsky-Kovchegov equation with resummation, Phys. Rev. D **93**, 094004 (2016).

[26] M. Froissart, Asymptotic behavior and subtractions in the Mandelstam representation, Phys. Rev. **123**, 1053 (1961).

[27] A. Kovner and U. A. Wiedemann, Nonlinear QCD evolution: Saturation without unitarization, Phys. Rev. D **66**, 051502 (2002).

[28] A. Kovner and U. A. Wiedemann, No Froissart bound from gluon saturation, Phys. Lett. B **551**, 311 (2003).

[29] J. Berger and A. M. Stasto, Small x nonlinear evolution with impact parameter and the structure function data, Phys. Rev. D **84**, 094022 (2011).

[30] D. Bendova, J. Cepila, J. G. Contreras, and M. Matas, Solution to the Balitsky-Kovchegov equation with the

collinearly improved kernel including impact-parameter dependence, Phys. Rev. D **100**, 054015 (2019).
[31] J. Jalilian-Marian, A. Kovner, L. D. McLerran, and H. Weigert, The intrinsic glue distribution at very small x, Phys. Rev. D **55**, 5414 (1997).
[32] J. Jalilian-Marian, A. Kovner, A. Leonidov, and H. Weigert, The BFKL equation from the Wilson renormalization group, Nucl. Phys. **B504**, 415 (1997).
[33] J. Jalilian-Marian, A. Kovner, A. Leonidov, and H. Weigert, The Wilson renormalization group for low x physics: Towards the high density regime, Phys. Rev. D **59**, 014014 (1998).
[34] E. Iancu and L. D. McLerran, Saturation and universality in QCD at small x, Phys. Lett. B **510**, 145 (2001).
[35] E. Ferreiro, E. Iancu, A. Leonidov, and L. McLerran, Nonlinear gluon evolution in the color glass condensate. 2., Nucl. Phys. **A703**, 489 (2002).
[36] E. Iancu, A. Leonidov, and L. D. McLerran, The Renormalization group equation for the color glass condensate, Phys. Lett. B **510**, 133 (2001).
[37] E. Iancu, A. Leonidov, and L. D. McLerran, Nonlinear gluon evolution in the color glass condensate. 1., Nucl. Phys. **A692**, 583 (2001).
[38] I. Balitsky and G. A. Chirilli, Rapidity evolution of Wilson lines at the next-to-leading order, Phys. Rev. D **88**, 111501 (2013).
[39] A. Kovner, M. Lublinsky, and Y. Mulian, Jalilian-Marian, Iancu, McLerran, Weigert, Leonidov, Kovner evolution at next to leading order, Phys. Rev. D **89**, 061704 (2014).
[40] H. Mäntysaari and B. Schenke, Confronting impact parameter dependent JIMWLK evolution with HERA data, Phys. Rev. D **98**, 034013 (2018).
[41] S. Schlichting and B. Schenke, The shape of the proton at high energies, Phys. Lett. B **739**, 313 (2014).
[42] H. Mäntysaari and B. Schenke, Accessing the gluonic structure of light nuclei at a future electron-ion collider, Phys. Rev. C **101**, 015203 (2020).
[43] J. L. Albacete and C. Marquet, Single inclusive hadron production at RHIC and the LHC from the color glass condensate, Phys. Lett. B **687**, 174 (2010).
[44] H. Fujii and K. Watanabe, Heavy quark pair production in high energy pA collisions: Quarkonium, Nucl. Phys. **A915**, 1 (2013).
[45] B. Ducloué, T. Lappi, and H. Mäntysaari, Forward J/ψ production in proton-nucleus collisions at high energy, Phys. Rev. D **91**, 114005 (2015).
[46] B. Ducloué, T. Lappi, and H. Mäntysaari, Forward J/ψ production at high energy: Centrality dependence and mean transverse momentum, Phys. Rev. D **94**, 074031 (2016).
[47] B. Ducloué, T. Lappi, and H. Mäntysaari, Forward J/ψ and D meson nuclear suppression at the LHC, Nucl. Part. Phys. Proc. **289–290**, 309 (2017).
[48] Y.-Q. Ma and R. Venugopalan, Comprehensive Description of J/ψ Production in Proton-Proton Collisions at Collider Energies, Phys. Rev. Lett. **113**, 192301 (2014).
[49] Y.-Q. Ma, R. Venugopalan, K. Watanabe, and H.-F. Zhang, $\psi(2S)$ versus J/ψ suppression in proton-nucleus collisions from factorization violating soft color exchanges, Phys. Rev. C **97** (2018) 014909.
[50] H. Mäntysaari and H. Paukkunen, Saturation and forward jets in proton-lead collisions at the LHC, Phys. Rev. D **100**, 114029 (2019).
[51] P. Tribedy and R. Venugopalan, Saturation models of HERA DIS data and inclusive hadron distributions in $p+p$ collisions at the LHC, Nucl. Phys. **A850**, 136 (2011); Erratum, Nucl. Phys. **A859**, 185 (2011).
[52] T. Lappi and H. Mantysaari, Forward dihadron correlations in deuteron-gold collisions with the Gaussian approximation of JIMWLK, Nucl. Phys. **A908**, 51 (2013).
[53] B. Ducloué, T. Lappi, and H. Mäntysaari, Isolated photon production in proton-nucleus collisions at forward rapidity, Phys. Rev. D **97**, 054023 (2018).
[54] C. Marquet, A unified description of diffractive deep inelastic scattering with saturation, Phys. Rev. D **76**, 094017 (2007).
[55] T. Lappi and H. Mantysaari, Incoherent diffractive J/ψ production in high energy nuclear DIS, Phys. Rev. C **83**, 065202 (2011).
[56] T. Lappi and H. Mantysaari, J/ψ production in ultra-peripheral Pb + Pb and p + Pb collisions at energies available at the CERN Large Hadron Collider, Phys. Rev. C **87**, 032201 (2013).
[57] H. Mäntysaari and B. Schenke, Evidence of Strong Proton Shape Fluctuations from Incoherent Diffraction, Phys. Rev. Lett. **117**, 052301 (2016).
[58] H. Mäntysaari and B. Schenke, Revealing proton shape fluctuations with incoherent diffraction at high energy, Phys. Rev. D **94**, 034042 (2016).
[59] H. Mäntysaari and R. Venugopalan, Systematics of strong nuclear amplification of gluon saturation from exclusive vector meson production in high energy electron–nucleus collisions, Phys. Lett. B **781**, 664 (2018).
[60] F. Salazar and B. Schenke, Diffractive dijet production in impact parameter dependent saturation models, Phys. Rev. D **100**, 034007 (2019).
[61] H. Mäntysaari, N. Mueller, and B. Schenke, Diffractive Dijet Production and Wigner Distributions from the Color Glass Condensate, Phys. Rev. D **99**, 074004 (2019).
[62] H. Mäntysaari, N. Mueller, F. Salazar, and B. Schenke, Multigluon Correlations and Evidence of Saturation from Dijet Measurements at an Electron-Ion Collider, Phys. Rev. Lett. **124**, 112301 (2020).
[63] G. A. Chirilli, B.-W. Xiao, and F. Yuan, Inclusive hadron productions in pA collisions, Phys. Rev. D **86**, 054005 (2012).
[64] A. M. Stasto, B.-W. Xiao, and D. Zaslavsky, Towards the Test of Saturation Physics Beyond Leading Logarithm, Phys. Rev. Lett. **112**, 012302 (2014).
[65] T. Altinoluk, N. Armesto, G. Beuf, A. Kovner, and M. Lublinsky, Single-inclusive particle production in proton-nucleus collisions at next-to-leading order in the hybrid formalism, Phys. Rev. D **91**, 094016 (2015).
[66] T. Altinoluk, N. Armesto, G. Beuf, A. Kovner, and M. Lublinsky, Heavy quarks in proton-nucleus collisions—The hybrid formalism, Phys. Rev. D **93**, 054049 (2016).
[67] B. Ducloué, T. Lappi, and Y. Zhu, Single inclusive forward hadron production at next-to-leading order, Phys. Rev. D **93**, 114016 (2016).

[68] R. Boussarie, A. Grabovsky, L. Szymanowski, and S. Wallon, On the one loop $\gamma^{(*)} \to q\bar{q}$ impact factor and the exclusive diffractive cross sections for the production of two or three jets, J. High Energy Phys. 11 (2016) 149.

[69] R. Boussarie, A. V. Grabovsky, D. Yu. Ivanov, L. Szymanowski, and S. Wallon, Next-to-Leading Order Computation of Exclusive Diffractive Light Vector Meson Production in a Saturation Framework, Phys. Rev. Lett. **119**, 072002 (2017).

[70] B. Ducloué, E. Iancu, T. Lappi, A. H. Mueller, G. Soyez, D. N. Triantafyllopoulos, and Y. Zhu, Use of a running coupling in the NLO calculation of forward hadron production, Phys. Rev. D **97**, 054020 (2018).

[71] H.-Y. Liu, Y.-Q. Ma, and K.-T. Chao, Improvement for color glass condensate factorization: Single hadron production in pA collisions at next-to-leading order, Phys. Rev. D **100**, 071503 (2019).

[72] M. A. Escobedo and T. Lappi, Dipole picture and the nonrelativistic expansion, Phys. Rev. D **101**, 034030 (2020).

[73] K. Roy and R. Venugopalan, NLO impact factor for inclusive photon + dijet production in $e + A$ DIS at small x, Phys. Rev. D **101**, 034028 (2020).

[74] H.-Y. Liu, Z.-B. Kang, and X. Liu, Threshold resummation for hadron production in the small-x region, arXiv: 2004.11990 [Phys. Rev. D (to be published)].

[75] Y. V. Kovchegov and E. Levin, Quantum chromodynamics at high energy, Cambridge Monogr. Part. Phys., Nucl. Phys., Cosmol. **33**, 1 (2012).

[76] E. Iancu, A. H. Mueller, and D. N. Triantafyllopoulos, CGC factorization for forward particle production in proton-nucleus collisions at next-to-leading order, J. High Energy Phys. 12 (2016) 041.

[77] B. Ducloué, T. Lappi, and Y. Zhu, Implementation of NLO high energy factorization in single inclusive forward hadron production, Phys. Rev. D **95**, 114007 (2017).

[78] I. Balitsky, Quark contribution to the small-x evolution of color dipole, Phys. Rev. D **75**, 014001 (2007).

[79] T. Lappi, H. Mäntysaari, and A. Ramnath, Next-to-leading order Balitsky-Kovchegov equation beyond large N_c, arXiv:2007.00751.

[80] A. Bialas, H. Navelet, and R. B. Peschanski, QCD dipole model and K(t) factorization, Nucl. Phys. **B593**, 438 (2001).

[81] J. L. Albacete, Resummation of double collinear logs in BK evolution versus HERA data, Nucl. Phys. **A957**, 71 (2017).

[82] B. Ducloué, E. Iancu, G. Soyez, and D. N. Triantafyllopoulos, HERA data and collinearly-improved BK dynamics, Phys. Lett. B **803**, 135305 (2020).

[83] Y. V. Kovchegov and H. Weigert, Triumvirate of running couplings in small-x evolution, Nucl. Phys. **A784**, 188 (2007).

[84] T. Lappi and H. Mäntysaari, On the running coupling in the JIMWLK equation, Eur. Phys. J. C **73**, 2307 (2013).

[85] B. G. Giraud and R. Peschanski, Fourier-positivity constraints on QCD dipole models, Phys. Lett. B **760**, 26 (2016).

[86] H. Mäntysaari and P. Zurita, In depth analysis of the combined HERA data in the dipole models with and without saturation, Phys. Rev. D **98**, 036002 (2018).

[87] H. Kowalski and D. Teaney, An impact parameter dipole saturation model, Phys. Rev. D **68**, 114005 (2003).

[88] V. N. Gribov and L. N. Lipatov, Deep inelastic e p scattering in perturbation theory, Yad. Fiz. **15**, 781 (1972) [Sov. J. Nucl. Phys. **15**, 438 (1972)].

[89] V. N. Gribov and L. N. Lipatov, e^+e^- pair annihilation and deep inelastic e p scattering in perturbation theory, Yad. Fiz. **15**, 1218 (1972) [Sov. J. Nucl. Phys. **15**, 675 (1972)].

[90] G. Altarelli and G. Parisi, Asymptotic freedom in parton language, Nucl. Phys. **B126**, 298 (1977).

[91] Y. L. Dokshitzer, Calculation of the structure functions for deep inelastic scattering and e^+e^- annihilation by perturbation theory in quantum chromodynamics, Zh. Eksp. Teor. Fiz. **73**, 1216 (1977) [Sov. Phys. JETP **46**, 641 (1977)].

[92] S. Chekanov *et al.* (ZEUS Collaboration), Exclusive electroproduction of J/ψ mesons at HERA, Nucl. Phys. **B695**, 3 (2004).

[93] C. Alexa *et al.* (H1 Collaboration), Elastic and proton-dissociative photoproduction of J/ψ Mesons at HERA, Eur. Phys. J. C **73**, 2466 (2013).

[94] H. Kowalski, L. Motyka, and G. Watt, Exclusive diffractive processes at HERA within the dipole picture, Phys. Rev. D **74**, 074016 (2006).

[95] S. Chekanov *et al.* (ZEUS Collaboration), Exclusive photoproduction of J/Ψ mesons at HERA, Eur. Phys. J. C **24**, 345 (2002).

[96] J. Kuokkanen, K. Rummukainen, and H. Weigert, HERA-data in the light of small x evolution with state of the art NLO input, Nucl. Phys. **A875**, 29 (2012).

[97] V. N. Gribov, Interaction of gamma quanta and electrons with nuclei at high-energies, Zh. Eksp. Teor. Fiz. **57**, 1306 (1969) [Sov. Phys. JETP **30**, 709 (1970)].

[98] S. J. Brodsky and J. Pumplin, Photon-nucleus total cross-sections, Phys. Rev. **182**, 1794 (1969).

[99] D. Ritson, Phenomenological predictions for deep inelastic electron scattering, Phys. Rev. D **3**, 1267 (1971).

[100] J. J. Sakurai and D. Schildknecht, Generalized vector dominance and inelastic electron-proton scattering, Phys. Lett. **40B**, 121 (1972).

[101] A. H. Rezaeian and I. Schmidt, Impact-parameter dependent color glass condensate dipole model and new combined HERA data, Phys. Rev. D **88**, 074016 (2013).

[102] G. Soyez, Saturation QCD predictions with heavy quarks at HERA, Phys. Lett. B **655**, 32 (2007).

[103] V. Andreev *et al.* (H1 Collaboration), Measurement of inclusive ep cross sections at high Q^2 at $\sqrt{s} = 225$ and 252 GeV and of the longitudinal proton structure function F_L at HERA, Eur. Phys. J. C **74** (2014) 2814.

[104] A. Accardi *et al.*, Electron ion collider: The next QCD frontier, Eur. Phys. J. A **52**, 268 (2016).

[105] E. C. Aschenauer, S. Fazio, J. H. Lee, H. Mantysaari, B. S. Page, B. Schenke, T. Ullrich, R. Venugopalan, and P. Zurita, The electron–ion collider: Assessing the energy dependence of key measurements, Rep. Prog. Phys. **82**, 024301 (2019).

[106] J. L. Abelleira Fernandez *et al.* (LHeC Study Group Collaboration), A large hadron electron collider at CERN: Report on the physics and design concepts for machine and detector, J. Phys. G **39**, 075001 (2012).

[107] H. Abramowicz *et al.* (ZEUS Collaboration), Deep inelastic cross-section measurements at large y with the ZEUS detector at HERA, Phys. Rev. D **90**, 072002 (2014).